THE UNIVERSITY *of* EDINBURGH

Massive Stars and Miniature Robots: Today's Research and Tomorrow's Technologies

William Taylor

A thesis submitted in fulfilment of the requirements
for the degree of Doctor of Philosophy to the
University of Edinburgh
Summer 2012

For Mum and Dad

Abstract

Due to their violent stellar winds, ionising radiation and famous deaths as supernovae, massive stars play a key role in galactic evolution. A complete understanding of these objects has been hindered by both their rarity and by the relatively limited volume of the Universe that is accessible with existing facilities.

Addressing the first of these limiting factors, the VLT-FLAMES Tarantula Survey (VFTS) has drawn from the 30 Doradus region an unprecedented sample of over 800 O- and B-type stars. The survey is beginning to uncover a wide range of global properties such as the region's binary fraction of massive stars and their dynamics, whilst also looking in detail at some of its more fascinating objects. This thesis documents the reduction of the VFTS data set, whilst also describing the analysis for one of the serendipitous discoveries: the massive binary R139. This high-mass binary will provide an excellent future calibration point for stellar models, in part as it seems to defy certain expectations about its evolution.

Outwith the VFTS, a search for binary companions around a trio of B-type supergiants is presented. These stars are surrounded by nebulae that closely resemble the triple-ring structure associated with the poorly-understood SN1987A. Do these stars share a similar evolutionary fate? While strong evidence is found for periodic pulsations in one of the stars, there appears to be no indication of a short-period binary companion suggested in the literature.

Gathering observations from a wide range of environments builds a fuller picture of massive stars, but the samples remain somewhat limited. The coming generation of extremely large telescopes will open new regions for studies like the VFTS. Fully utilising these remarkable telescopes will require many new technologies, and this thesis presents one such development project. For adaptive-optics corrected, multi-object instruments it will be necessary to position small pick-off mirrors in the telescope's focal plane to select the sub-fields on the sky. This could be most efficiently achieved if the mirrors were self-propelled, which has led to a miniature robot project called MAPS - the Micro Autonomous Positioning System.

A number of robots have been built with a footprint of only 30 x 30 mm. These

wirelessly-controlled robots draw their power from the floor on which they operate and have shown the potential to be positioned to an accuracy of tens of microns. This thesis details much of the early design work and testing of the robots, and also the development of the camera imaging system used to determine the position of the robots. The MAPS project is ongoing and a number of the potential future tests, and avenues for new research, are discussed.

This is a thesis that brings together an area of active astronomical research with cutting-edge technological development, highlighting how tomorrow's telescopes will be an essential tool to answer some of today's most puzzling research questions.

Declaration

Except where otherwise stated, the research undertaken in this thesis was the unaided work of the author. Where the work was done in collaboration with others, a significant contribution was made by the author.

William Taylor
August 2012

Acknowledgements

When I came to Edinburgh for a ten-week work placement, I did not envisage that five years later I'd be submitting a thesis. Such events don't occur without a huge amount of help and support, for which I'm extremely grateful. First and foremost thanks go to my two supervisors, Chris Evans and Hermine Schnetler. They have provided me with fantastic guidance and advice, not to mention showing a great deal of patience when I've found myself swallowed by the 'other-half' of the thesis.

I've been very fortunate to be part of the VLT-FLAMES Tarantula Survey, which is studying one of the most beautiful objects in the night sky - good choice Chris! This survey has allowed me to work with and learn from, a wide range of different scientists. In particular, I'd like to acknowledge the help of Hugues Sana and Selma de Mink. More locally, its been great to work with Vincent - a fellow low-redshift man!

MAPS has been a wonderfully entertaining project to be part of. Will Cochrane above anyone, has been through the highs and lows of these little robots with me, and it's always been a pleasure working with him - thanks mate! The project has accreted many new members; originally David Atkinson and Dave Montgomery, while more recently, Martin Black has found himself roped-in to provide fantastic help with the optical work. Tom Baillie and Brian Wilson should be mentioned for putting up with Will and me relentlessly pestering them. Special mention should go to Stewart McLay, who has helped so much in making the software more professional/work.

Thanks must also go to the University of Edinburgh and STFC for their support, both academically and financially. Naturally there are a host of peers, who have made this process so much more fun, but briefly; Trev, thanks for showing how writing-up should be done, and Vinod, its been such a pleasure sharing an office with you - even if it's been a haven for outreach daydreaming rather than academic rigour. Also, thanks to Ian for his proof reading skills and Paula for her continual help.

Finally to my family: Dad, who gave us all the drive to do things like this and Mum, who would have been so pleased to see me studying stars. Jenny and Pat, you've listened to many of my more-stressed moments and that matters so much. And finally we come to my Rachael, who has been there through thick and thin, patiently helping and understanding. Thank you one and all.

Contents

List of Figures

List of Tables

A VISTA image of the 30 Doradus star-forming region in the Large Magellanic Cloud.

Chapter 1

Introduction

If the stars should appear but one night every thousand years, how man would marvel and stare.

Ralph Waldo Emerson

1.1 Author's note

As its title suggests, this thesis covers a diverse range of topics and it would be a brave author who tried to present an introductory chapter which comprehensively addressed each of these. Instead, this chapter stands as a background framework to the work; beginning with an overview of the key aspects of massive-star research and the more fundamental questions that remain unanswered. The chapter then describes some of the current instruments available for studying massive stars, before looking ahead to the next generation of telescopes and their instruments. Finally, this leads to the introduction of the miniature robot concept that is proposed for use in future multi-object instruments. Each chapter which follows will also contain an introductory element to that area of research, particularly for the technology-related work.

1.2 Massive Stars

The study of stars has long been one of the chief corner-stones of astronomical research. While huge strides have been made towards an understanding of these objects, for the largest and hottest stars, many questions still remain. These 'Massive stars' have a significant influence on their surroundings at all stages of their lives; as young stars they ionise the nebulae from which they form, later in life they often exhibit strong stellar winds, and finally they will nearly all undergo violent deaths as supernovae, leading to metal enrichment of the interstellar medium.

1.2.1 Classification systems

It could be tentatively argued that the history of studying stellar spectra can be dated as far back as Newton's experiments with sunlight and prisms. However, more credit surely lies with Fraunhofer, who in the early 19th century used his remarkable technical skills to build prisms which allowed him to identify the dark absorption bands in the Sun's spectra. The true pioneers of non-solar stellar spectroscopy were to come later though, with work by men such as Donalti and Secchi. Secchi is particularly famed for developing the idea that certain stars could be grouped together in 'Classes', defined solely by similarities in their spectra.

This basic notion is still a fundamental tool in stellar astrophysics, and forms a key aspect of the VLT-FLAMES Tarantula Survey (VFTS) described in chapter 2. Today's classification system has evolved from work done at Harvard around the turn of the 20th century, where large numbers of stars were recorded in the Henry Draper catalogue (Cannon & Pickering 1918). These stars were grouped into alphabetical classes based on their spectra; subsequent adjustment and rejection of some groups gives today's classes of O, B, A, F, G, K and M.

These classes are themselves split into sub-divisions through the addition of a number between zero and nine. Lower case letters are also often added to denote certain spectral features, a currently comprehensive list of which is given in Sota et al. (2011). The hottest stars are O and B, and it is these which are generally referred to as massive stars, but the name can also encompass a diverse range of other, more evolved high-mass objects.

The spectrum of a star is primarily determined by its surface temperature, so it is therefore quite possible that stars with similar spectra can have different masses and therefore luminosities. To lift this degeneracy, Morgan and Keenan from the Yerkes Observatory developed the concept of Lumonsity Classes, which are shown in Table 1.1 (Morgan et al. 1943). Within this classification system, the fairly average sun is a G2 V, while the famous blue-supergiant, Rigel, which defines Orion's left foot, is a B8 I.

Table 1.1: The Yerkes Luminosity classes.

Name	Description
I	Supergiant
II	Bright giant
III	Giant
IV	Subgiant
V	Dwarf

1.2.2 Evolution

In 1912 Hertzsprung found that if the colour index of a star is plotted against its absolute magnitude, a relatively clear correlation emerges. This relationship was also found independently by Russell around the same time, and hence the Hertszprung-Russell (HR) diagram was born; it is one of the most commonly used tools in stellar studies.

The colour index used in the original diagram indicates the temperature of the star, which in turn relates to the stellar classification system. Interestingly, the connection between stellar class and temperature was not understood at the time of the class derivation, it was purely a means of ordering objects. The data shown in Figure 1.1 are from an early paper by Gyllenberg et al. (1926), in which the objects have been grouped by stellar class, hence the discrete sampling of the data in the x-axis. The

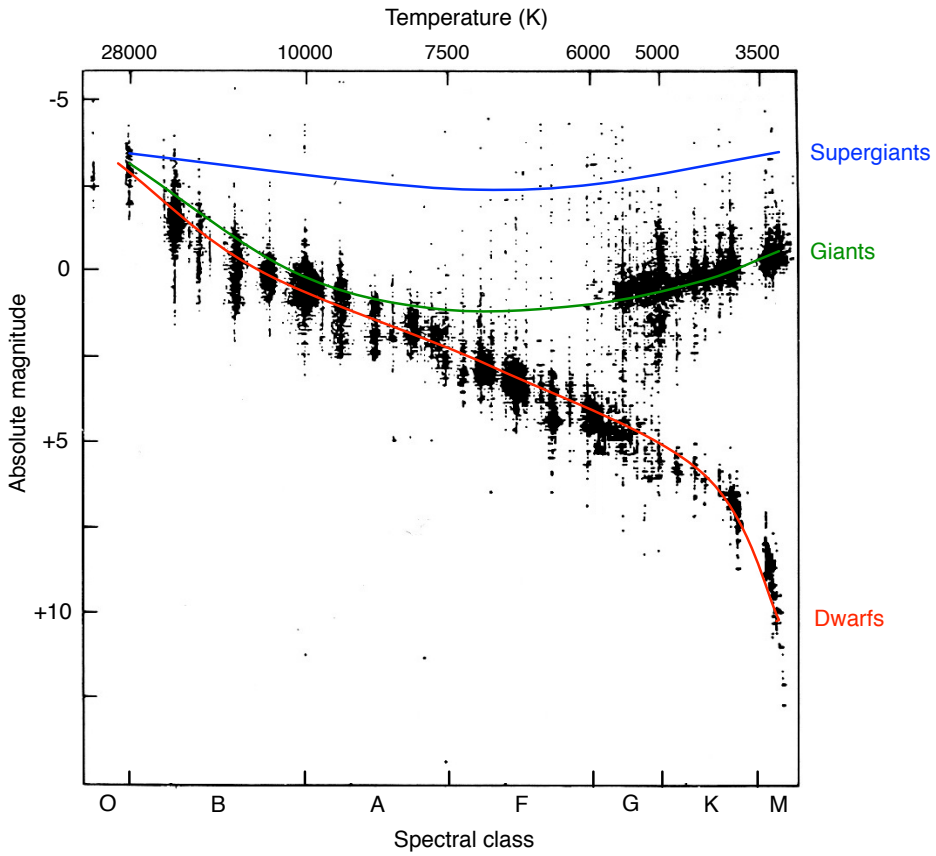

Figure 1.1: An example of a Hertzsprung-Russell Diagram with data from Gyllenberg et al. (1926). Overlaid on the diagram are the positions of the different Yerkes luminosity classes. The temperatures indicate a rough lower limit for that spectral class.

temperature scale has been added to give an indication of the temperatures associated with the different classes.

Overlaid on Gyllenberg's data are the now-known tracks of the different Yerkes luminosity classes. The diagonal band where the majority of stars are found represents the 'Main Sequence'. This period, when the star is burning hydrogen in its core, generally corresponds to the Dwarf luminosity class. For lower-mass stars, the vast majority of their life will be spent on the main sequence. Once the core-hydrogen supply is depleted, the star will expand, and cool, moving up through the luminosity classes as it does so. As an example, a star may begin its life as an O4 V on the main sequence and then as it ages, it will swell to become an O7 I.

If a complete census of the stars in a region can be obtained, the HR diagram can be used to infer many properties of that system. As a group of stars ages, the more massive stars leave the main sequence, and consequently the top of the main sequence appears to retreat to later type stars. This 'turn-off' point therefore provides a diagnostic of the age of a stellar population. It is often possible to infer multiple turn-off points, and thus build up a complete picture of the region's Star Formation History (SFH).

1.2.3 Formation and initial mass function

The formation of a massive star is intriguing in at least two ways: firstly because the process is not well understood but also, more broadly, because the relative fraction of stars that are 'massive' is also open to debate.

The conventional picture of star formation, whereby a cloud of material collapses in on itself, has difficulty fully explaining more massive star formation (McKee & Ostriker 2007). In such a system, a disk of material forms around the young star and is gradually accreted onto the core, thus increasing the density and leading to the point at which fusion occurs and the star begins its life on the main sequence. With large monolithically collapsing systems, the core will be immediately sufficiently dense for fusion to begin. This therefore leads to the production of high energy ionising radiation which could disrupt the accretion disk. How, therefore, is it possible to find stars of tens of solar masses? Do they form from large monolithic collapses, or does the process involve some period of accretion from the surrounding region? It has even been suggested that collisions or mergers of smaller stars could be responsible (Bonnell et al. 1998).

A recent observation of a massive star forming by Davies et al. (2010b), has suggested a similar formation process as that for smaller stars: both accretion disks and bi-polar outflows are present. However, this is only for a star of $\sim$15 $M_{\odot}$. Crowther et al. (2010) recently presented evidence that the centre of the R136 cluster in the Large

Magellanic Cloud (LMC) might contain stars as large as $300\,M_\odot$; whether conventional star-formation theories could explain these is uncertain. It is unfortunately difficult to witness the formation of such stars as they are very rare and the process is rapid. Questions also remain about the impact of rotation and magnetic fields on star-forming regions. For further discussion of massive-star formation, see the review by Zinnecker & Yorke (2007).

The Initial Mass Function (IMF) is used to describe the relative distribution of stars of different masses. Massive stars are rare - there are roughly 10 solar-mass stars born for every $8\,M_\odot$ star. In 1955 Salpeter published a seminal work which described the IMF. Debate rages about whether the IMF is truly constant and independent of factors such as cluster mass and/or metallicity; arguments have been found which appear to support both cases (Bastian et al. 2010). Understanding massive-star formation is important for predicting the IMF; if stars can form in relative isolation from a single monolithic collapse, there could be considerably more variation in the upper IMF than the tight relationship between cluster mass and population distribution that an accretion scenario would imply (Bressert et al. 2012).

The rarity and short lifetimes of massive stars often make them one of the most difficult aspects of the IMF to determine. However, when studying unresolved star-forming regions it is often only the tracers of star formation, such as H II regions, which are a direct result of massive stars, that can be studied. Without a complete understanding of massive stars inherent dangers remain in our ability to determine the properties of young star-forming regions (Weidner et al. 2010).

1.2.4 Stellar winds and metallicity

A massive star can lose up to 50% of its mass during its lifetime due to an out-flowing wind; this will clearly have a significant impact on its later evolutionary path. Massive stars will also contribute extremely large amounts of kinetic energy to their surrounding regions. In order to understand these two impacts of the wind, it is necessary to know the two most fundamental properties which describe all stellar winds: the mass loss rate, $\dot{M}$, and the terminal velocity, v_∞.

The basic principle of radiatively driven winds was put forward in the seventies by Castor et al. (1975). Radiation emitted from the stellar 'surface' is scattered by elements in the surrounding wind structure. The process is dominated by heavier elements, such C, N, O right up to Fe, as these ions have a large number of possible transitions. The range of photon frequencies that will be scattered is further enhanced by the very expansion of the wind itself, as the fast-moving ions further out in the wind will present Doppler-shifted transitions relative to those nearer to the star. This

large-scale absorption of photons, imparts to these ions considerable momentum. Many of the heavier ions will transfer this momentum to lighter particles through Coulomb interactions, and thus the material in the wind is composed of many kinds of species. This transfer of momentum is important, as it means that not all the heavy elements are lost from the star: this is necessary for the generation of a stable wind.

Since the momentum transferred is dependent on heavier elements, theory predicts that the strength of stellar winds is determined by the metallicity of the star. Predictions of such effects were made by Vink et al. (2001), and strong supporting evidence was seen by Mokiem et al. (2007), who found that $\dot{M} \propto Z^{0.78\pm0.17}$, where Z is the metallicity of the local environment. However, more recent examples potentially contradict this pattern. Tramper et al. (2011) studied a group of stars in a low metallicity environment, $Z = 0.14\,Z_{\odot}$, and found higher than expected mass loss estimates, as is shown in Figure 1.2.

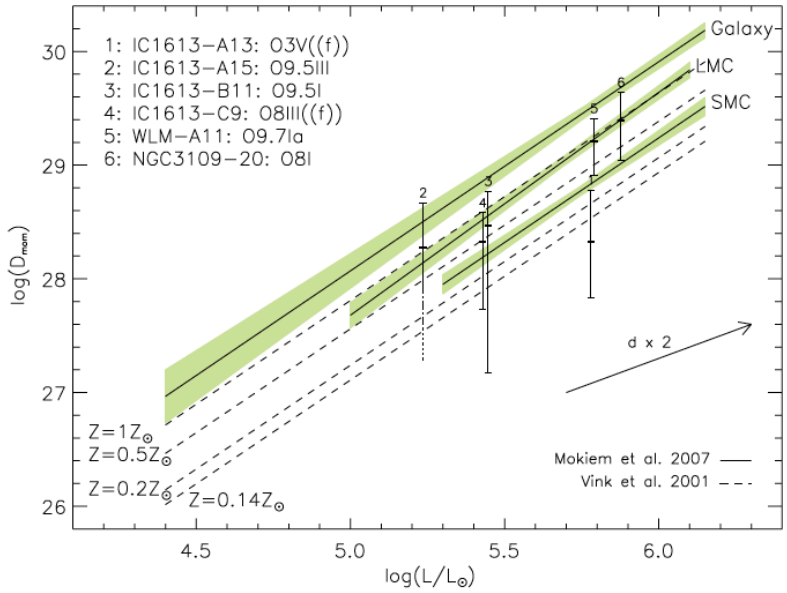

Figure 1.2: The dashed lines show the mass-loss estimates of Vink et al. (2001), while the green shaded regions show the results of Mokiem et al. (2007). While there is an offset between the two, the expected sequence for the different metallicity environments is clearly seen. The new results for lower metallicity galaxies from Tramper et al. (2011) are the over-plotted data points.

1.2.5 Rotation

Stars are structurally supported by the delicate balance between gravity and radiation pressure, but this can be disturbed by the presence of rotation, which adds an outward centrifugal force. This can cause the star to expand, especially around the equator

where the rotation is fastest, thus lowering the surface temperature of the star.

Rotation can also lead to two-way mixing of material: metals such as nitrogen can move outwards from the interior and appear as enrichment at the surface (Maeder 1987), while the converse of this can draw hydrogen into the core from the envelope. This can prolong the core hydrogen burning lifetime of the star thus delaying its evolution away from the main sequence (Meynet & Maeder 2000).

There is evidence suggesting that rotational rates in B stars might also be metallicity dependent (Hunter et al. 2008b). This could be due to angular momentum being lost in stellar winds, but in B-stars the mass-loss is relatively low, perhaps pointing to differences in the star-formation process. For O-stars such studies have not yet been performed for large samples of objects. Observing stars either early in their life or in low-metallicity environments, where the winds are weak, would give a better understanding of the initial rotation rates.

1.2.6 Binarity

The 'Demon Star' Algol, which lies in the constellation of Perseus, is seen to exhibit a significant and periodic reduction in its brightness every 2.8 days. This well-studied object is considered the first correctly identified binary system, having been confirmed as such in the 19th century. It has since been learnt that the majority of the higher-mass stars which adorn the night sky are members of binary systems or sometimes more complex, multiple systems, consisting of a few gravitationally bound stars. However, this is not the case for lower mass K and M stars, which are generally singular (Lada 2006).

If sufficient information is known about a binary system it is possible to use Keplerian dynamics to directly measure the mass of the stars in the system. This is a key element of stellar astronomy; there is no other way to directly measure mass, and it is mass which dictates the evolution of the star. There are four main types of binary system from which the orbital properties can be determined:

Visual binary: When it is possible to resolve the individual stars. This is clearly only possible for relatively nearby stars, which are widely separated.

Eclipsing binary: If one star passes in front of another it causes a diminishing of the light from the system, thus a variation in observed magnitude can be detected - as is the case for Algol.

Single-lined, spectroscopic binary, SB1: If one of the stars in the system is considerably more massive than the other, its spectral signature will dominate, and it is often not possible to reveal the smaller companion. However, small, periodic shifts in the star's position caused by its orbital motion, can be measured from the spectrum.

This is one of the most common methods for identifying short-period binary systems. Detection requires a number of repeated observations of the object; this forms a driving feature of the VFTS survey discussed in Chapter 2.

Double-lined, spectroscopic binary, SB2: When the spectrum of the system reveals the features of two distinct stars - this is often most apparent when the spectral features are seen to shift with respect to each other due to their relative motion. This is the case for the R139 system discussed in Chapter 3.

To completely describe the dynamics of a binary system, a number of orbital elements are needed. The orbits of the binary stars define an orbital plane and its intersection with the tangential plane of the sky is defined by two angles: the Inclination, i, and the Position Angle, Ω. This is shown schematically in Figure 1.3. The inclination defines how "edge-on" the system is to the observer, i.e. if $i = 0^o$ the orbital plane is parallel to the plane of the sky. Ω describes the orientation of the line of intersection between the two planes, it is measured relative to North. From spectroscopic observations alone it is not possible to determine either of these angles - eclipses are also needed. However, if i is too low, eclipses can never be observed. It is therefore common for system properties to be quoted as a function of $\sin i$ reflecting this uncertainty.

The eccentricity, e, and the semi-major axis, a, have their normal geometric meanings and thus describe the shape of the orbital path. T_0, is defined as the time the two stars are at their closest approach, which is known as *periastron* - with *apastron* the other extreme. The position of the periastron point is defined relative to the line of intersection of the planes (the line of ascending nodes), and is known as the *longitude of primary periastron,* ω. In the case of spectroscopic binaries, and in this work, ω, is defined from the point at which it intersects the line of ascending nodes while *receding* from the observer.

To put all these terms into practice, imagine a spectator in the Olympic stadium, with a seat which looks North along the finishing line - the same view as the photo-finish camera. For them, the running plane has an Ω of 270°, taking the periastron point to be the middle of the first bend, $\omega \approx 0°$, and the inclination will be (roughly) proportional to how much they spent on their seat.

With enough observations over a sufficient time-frame it is possible to determine the period of the binary system. This is sometimes not treated as a true orbital element, partly because it can be derived from the semi-major axis through Kepler's third Law:

$$a^3 = (M_1 + M_2)P^2 \tag{1.1}$$

where P is measured in years, a in Astronomical Units (AU), M_1 and M_2 are the masses

of the two stars in solar masses. The period is, nevertheless, one of the key properties of the binary system as it can dictate the type of interaction that can occur between the stars. Another important property which is often used is the maximum observed velocities of the components, K_1 and K_2.

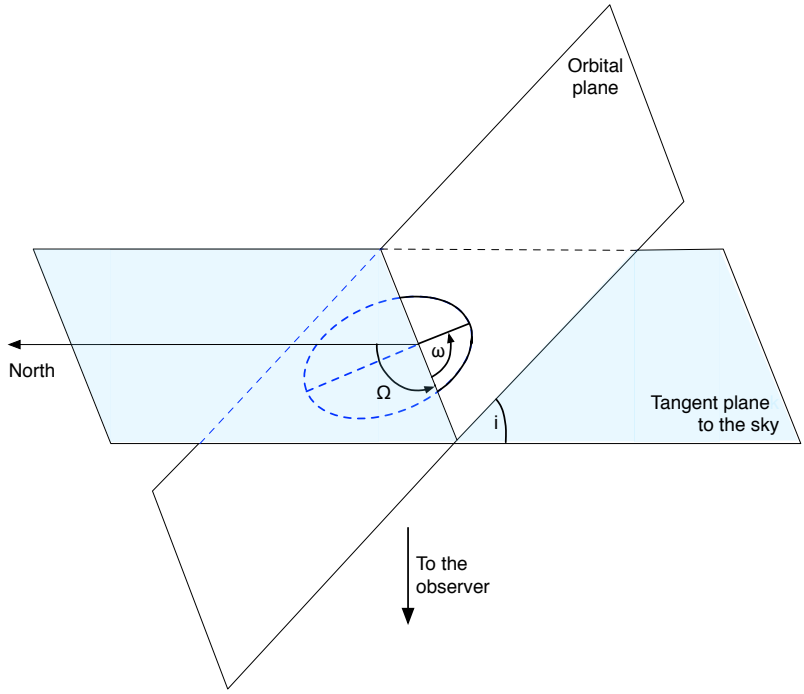

Figure 1.3: Definitions of the orbital parameters for a binary system.

1.2.6.1 Massive binaries

It has been said that 'Massive stars appear to love company' (Mason et al. 2009). Solar-type main sequence stars are often found in binary systems (Duquennoy & Mayor 1991), but it has been shown that a higher fraction of O and B stars are in binary or even multiple-star systems (Preibisch et al. 2001; Duchêne et al. 2001). When the observational effects are considered, some authors have even suggested that the observed binary fraction is not inconsistent with there being an intrinsic fraction of 100% (Pfalzner & Olczak 2007). It should be noted that attempts to study the binary fraction of massive stars are often significantly hindered by the limited sample sizes or the lack of homogeneity between data sets.

Understanding the true binary fraction has important implications for population synthesis of unresolved targets. It also affects estimates of the dynamical masses of clusters, where an unknown contribution from binary motions can be misinterpreted

as a high velocity dispersion (Gieles et al. 2010). Also, some X-ray sources can be attributed to massive binaries, where material is shock heated at the collision regions of the stellar winds.

There does appear to be evidence of a difference between the binary fraction of OB stars in clusters to that of stars in the field (Gies 1987). This would support the theory that the field stars did not originate there, but are the result of ejections from denser environments. In the study of Sana & Evans (2011) the authors looked for trends of different binary fractions for different cluster masses: the current data sets do not provide enough evidence for firm conclusions, but suggest that there is no such variation. From the studies considered, Sana & Evans found the average binary fraction to be $44 \pm 5\%$, but this an observational lower limit.

If the stars in a binary system are sufficiently close that they can interact, this can have a significant impact on their evolution. Interaction is dependent on the period of the system, and also the eccentricity, as this dictates the proximity at periastron. The interaction can take various forms, ranging from wind collisions, mass stripping and transfer of angular momentum, even to mergers of the two stars.

A recent study of a large sample of Galactic O stars by Sana et al. (2012b) observed a binary fraction of 56%, but when observational biases are considered, the intrinsic binary fraction is likely to be $69 \pm 9\%$. Of particular interest, though, is that the authors find a larger fraction of short-period binaries than had previously been observed. This considerably increases the chance of interaction during the star's lifetime. It is predicated that 71% of all O stars will interact with their companions, over half of these while still on the main sequence. They also predict that roughly 25% of stars will merge with their companion. These results suggest that the role of binarity in the evolution of the most massive stars cannot be overstated. It even questions the belief that an apparently single star has evolved in isolation and is not, in fact, the result of a merger of a previous binary system.

1.2.7 After the main sequence

The evolutionary tracks of evolved massive stars generally show little variation in luminosity, but rather move horizontally across the HR diagram undergoing variations in temperature. Massive stars are generally considered to be those over $8M_{\odot}$, which means they will end their lives in core-collapse supernova (SN).

The post main-sequence evolutionary tracks for a range of high-mass stars, along with an indication of their eventual fate, are shown in Figure 1.4; this is modified from Smith (2010). For stars below $40M_{\odot}$, after leaving the main-sequence the star cools, the envelope expands and the star enters the Yellow Supergiant phase (YSG). This is

seen as only a transitional period of evolution, with stars predicted to spend just a few thousand years here before cooling further and becoming a Red Supergiant (RSG).

At this stage the star will likely undergo a type-II SN, i.e. the spectrum of the SN will show the presence of hydrogen. However, it is also possible that the star will turn blue-wards again, prior to a SN. This is believed to occur if a substantial fraction of the star's envelope has been lost towards the end of the main-sequence, either through interaction with a binary companion or through strong stellar-winds. The star can pass into a Blue Supergiant (BSG) phase but, if the mass is large enough, more exotic forms of evolution are possible: the star can become a Luminous Blue Variable (LBV), before eventually becoming a Wolf-Rayet (W-R) star.

LBVs are a poorly understood period of stellar evolution. They are of interest as they are seen to exhibit periods of increased illumination, associated with excessive mass-loss episodes. These generally last a few years or decades and can lead to a 1 to 2 magnitude increase in brightness. Some LBVs have been seen to exhibit giant eruptions like that of η Carinae, which famously increased by around 3 magnitudes during its eruption in the mid-19th century. Such eruptions have even led to LBVs being dubbed 'supernova impostors.' The role which this period of evolution plays is discussed in more detail in Chapter 4.

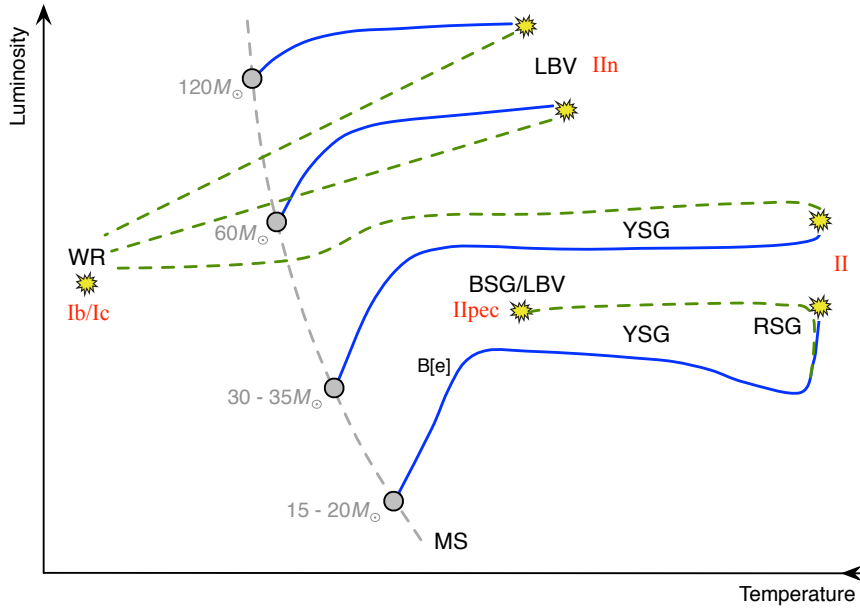

Figure 1.4: HR diagram showing evolutionary tracks (blue lines) for a number of high-mass stars, as they evolve away from the main sequence. The blue-wards paths of the stars are shown by the green dotted lines. Evolutionary stages are labelled in black, while the possible SN fates that await the stars, are shown in red.

W-R stars are generally considered to be the final stages of evolution for the most massive stars. These objects display very strong stellar winds (with v_∞ of order 1000km/s) which effectively strip the envelope from the star, revealing the hot core. Their spectra are characterised by very strong emission lines, which are formed in the dense stellar wind. Since they are stripped of their envelope, W-R stars will explode as type I SNe, which are deficient in hydrogen. For a review of W-R stars, see Crowther (2007).

In the 1970s Humphreys and Davidson observed that there is no evidence of very high mass stars evolving to cooler temperatures (Humphreys & Davidson 1979). This led to the now widely accepted Humphreys-Davidson Limit on the luminosity of stable stars: $\log(L/L_\odot) \approx 5.8$. Above this the star will not migrate red-wards and form RSGs, as is seen by the evolutionary paths for a $60M_\odot$ and $120M_\odot$ star in Figure 1.4

For completeness, Ofpe/WNs or 'Slash Stars' should also be mentioned. These have N and He enrichments similar to many LBVs, but also strong emission lines like W-Rs. They may represent a stage of evolution between LBVs and WN stars or perhaps dormant LBVs as they have not been seen to exhibit any variability. This divide will be discussed again in chapter 4.

Finally, an interesting subset of B stars are Be stars, which are generally near-main-sequence stars that show extremely strong H emission lines. It is believed that the emission comes from large, dense equatorial disks formed by mass lost from the star. From studies by Martayan et al. (2007) in the Magellanic clouds and the Milky Way it appears that the Be stars have higher initial rotation rates than normal B stars, this might be responsible for the ejection of the equatorial material.

1.2.8 The VLT-FLAMES Tarantula Survey

As this brief synopsis of massive-star research has highlighted, there are a large number of open and interesting questions that surround massive stars. Many of these uncertainties arise because of the difficulties in studying massive stars; they are rare, short-lived and generally sample sizes are small.

The Milky Way's largest satellite galaxy, the LMC hosts the 30 Doradus region. With a mass in excess of $10^4 M_\odot$, 30 Doradus is the largest star-forming region in the local universe and consequently provides a remarkable laboratory in which to study massive stars. It was therefore chosen as the target region for the VLT-FLAMES Tarantula Survey (Evans et al. 2011b), which forms a large part of this thesis and is discussed in more detail in chapters 2 and 3.

1.3 Instruments for studying stars

The early spectrometers of men like Secchi would have been based on a very simple concept: light passes through a narrow slit, is collimated and then dispersed to yield a spectrum. The technology used to achieve this effect today is somewhat different, but the basic principle is still exactly the same. Indeed, the slit aspect of the spectrometer has a direct influence on the nature of many observations, as it is often used to define a narrow region on the sky from which to gather data. It is common to place the object of interest in the centre of the slit, with surrounding 'sky' on either side. This technique has the advantage that it allows for extremely accurate treatment of the sky contribution through examination of the wings of the slit. It is also possible to vary the width of the slit depending on the nature of the source and/or the seeing conditions on the night of the observation, which has a corresponding impact on the effective spectral resolving power.

1.3.1 Multi-object instruments

It is occasionally possible to line-up more than one object of interest in the slit of a spectrometer. However, for more than two objects this is very rare and, in general, building up large surveys of spectra for many objects is time-consuming and inefficient. To rectify this situation multi-object instruments have been developed which allow for numerous targets to be simultaneously observed.

1.3.1.1 Slit mask instruments

The most simple, and therefore most common (see Figure 1.5), form of multi-object spectrograph is an extension of the basic slit spectrometer, which utilises a 'slit mask'. The 'slit mask' is a plate which has been cut with slits of various shapes and sizes. It is placed at the focal plane of the telescope, thus allowing only light from the desired regions to enter the spectrometer. Such spectrometers can obtain spectra of tens or even hundreds of objects simultaneously; for instance VIMOS on the VLT is capable of observing around 800 objects at once (Le Fèvre et al. 2003).

A major drawback of such designs, is that slit masks must be cut for each and every observation. Although many modern instruments now have a carriage of interchangeable masks, the requirement for pre-cut masks does limit the flexibility of observations. EMMI, an instrument on the New Technology Telescope in La Silla, attempted to provide an alternative method through an ability to 'punch' slit masks in real time within the instrument (Dekker et al. 1986). However, the precision is generally better for pre-made laser cut masks.

A more complex solution, is to use configurable slit masks, where the slits are created by moving micro-shutters or sliders inside the instrument. An early example of this was with FORS on the VLT (Appenzeller et al. 1998). However, due to the size of the mechanisms required for moving the slits, only a relatively modest multiplex of 19 slits was possible. Two excellent more recent examples are MOSFIRE on Keck, and the remarkable shutter-based NIRSpec which is being developed for JWST (McLean et al., 2010 and Bagnasco et al., 2007 respectively). However, all slit masks suffer the same problem: all the on-sky slits must be defined in the same on-sky direction, and they cannot overlap one-another in the direction in which the light will be dispersed. These restrictions greatly reduce the number of objects available for simultaneous observation.

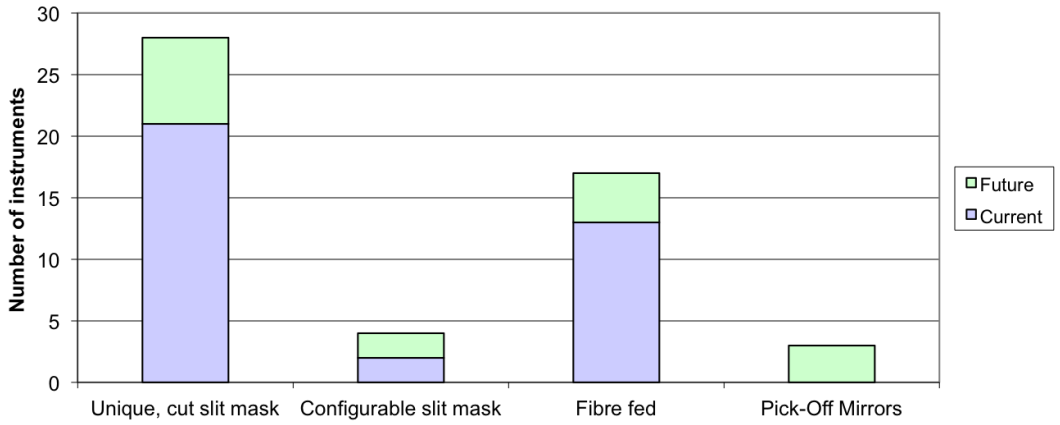

Figure 1.5: A census of current and future multi-object instruments on major research telescopes that are >2m in diameter. This currently includes over 70 telescopes.

1.3.1.2 Fibre-fed instruments

The next most common form of multi-object instruments are fibre-fed devices, which use optical fibres to couple the light from an object to the spectrograph. The first successful use of a fibre-feed in astronomy came in 1978 on the Stewart 36-inch telescope at Kitt Peak (Hubbard et al. 1979). Remarkably, within a year, a multi-object fibre device had also been deployed by Hill et al. (1980) at the Stewart observatory. MEDUSA, as this came to be known, used 26 fibres attached to a punched plate - much like the masks used in multi-slit spectrographs. The task of fixing each fibre to a pre-made hole, is clearly time consuming, but it is still the method of choice in some spectrographs; the Sloan Digital Sky Survey employs punch plates with 640 fibres (Uomoto et al. 1999).

There are two primary ways in which robotic devices can speed-up the positioning of fibres: use a robot for positioning all fibres or give each fibre some kind of personalised actuation. The latter of these ideas was first demonstrated with the MX spectrometer

(Hill & Lesser 1986), which had 32 fibres each carried on robotic arms distributed around the focal plane; objects were then picked-off using a 'fishermen-round-a-pond' technique. This concept of powering each fibre has been used in various different formats, and now the idea of focal planes covered in small actuated fibres is becoming increasingly common. One example of such a technique is the Echidna positioners used in FMOS, where each of the 400 fibres is connected to an individual spine that can be tilted to move the fibre tip around within the image (Akiyama et al. 2008). China's LAMOST spectrograph goes to the next level in multiplexing with 4000 fibres, again each driven into position individually, but this time with a pair of dedicated r and θ drives which translate the fibre across its small patrol field (Cui 2009).

AUTOFIB was the first system to use a single robot to position all the fibres (Parry & Gray 1986). A small pick-and-place machine was used to position the 64 magnetic fibre-carrying buttons at any location across the focal plane. From work on AUTOFIB the, then, Anglo Australian Observatory developed the 2dF positioner, a much faster robot which was capable of positioning over 400 fibres. This positioner for 2dF is similar to that which was later employed in FLAMES (Pasquini et al. 2002), the multi-object spectrograph for the VLT which will be discussed in more detail in Chapter 2. The OzPoz positoner used in FLAMES is shown in Figure 1.6; it shows the parked fibres around the edge of the soon-to-be populated focal surface. Both 2dF and OzPoz have two interchangeable focal surfaces, this allows one to be populated with fibres, while the other is observing.

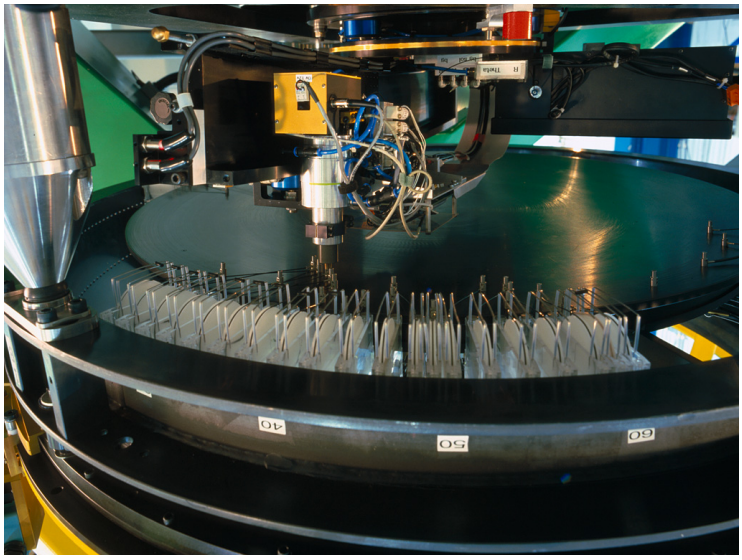

Figure 1.6: The OzPoz fibre positioner in FLAMES. One of the 1 m curved focal surfaces is shown surrounded by the banks of fibres ready to be pulled into position by the gripper. A few already-positioned fibres are visible on the right-hand edge of the image.

1.3.1.3 Integral field spectroscopy

Many of the fibre-fed instruments use a micro-lens to feed light into the fibres. The lenses are often designed to have an on-sky aperture of roughly 1"-2", this is generally matched or slightly larger than the normal atmospheric seeing. For studies of resolved stellar populations this is excellent, as light from a single star can be fed into each fibre. However, for more extended sources, this can be a drawback.

The Integral Field Unit (IFU) has been designed to obtain spatially resolved spectra of extended sources. The simplest form of an IFU is formed from bundles of tightly-packed optical fibres; often a micro-lens array is used to couple the light into the fibres and ensure there are no loses between fibres. These systems are not a large extension from the single optical fibre systems described above. Indeed FLAMES has two different observing modes which use IFUs; the ARGUS mode has a large central fixed IFU composed of 22 x 14 fibres, while there is also the option for simultaneously using 15 deployable 4 x 5 fibre IFUs.

Another method for performing IFU observations is to use an image slicer. This was first tested on-sky by Krabbe et al. (1997) with the 3D instrument, while the first common-user instrument to use an image slicer was UIST (Ramsay Howat et al. 2004). An image slicer is a small array of tilted mirrors that effectively reformats the focal-plane image into one long slice for entrance to the spectrograph. This process is illustrated in Figure 1.7. Out of interest, note that the slit entrance is still an essential part of the spectrograph's design, indeed, all the fibre systems described above, are also

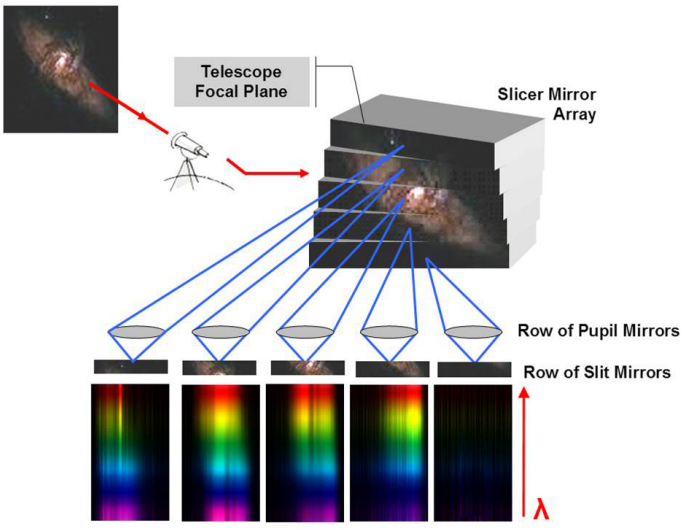

Figure 1.7: A schematic representation of an IFU image slicer; the image is sliced such that both spectral and spatial information is obtained.

eventually lined-up one above the other to feed the spectrograph.

As will be described in more detail in Chapter 5, KMOS is a new instrument for the VLT which employs multiple image-slicer based IFUs (Sharples et al. 2006). Just like the design of the MX Spectrometer thirty years ago, the areas of interest are selected through robotic arms extended across the focal plane, but KMOS's arms will carry small pick off mirrors (POMs) rather than optical fibres to feed the image slicers.

1.4 Next-generation instrumentation

Through studying in detail one relatively homogeneous cluster of massive stars, the VFTS will reveal many insights about the evolution of these elusive objects. However, the survey is pushing the limitations of current observing facilities. The LMC lies around 50 kpc away and at this distance the 1.2" FLAMES fibres subtend 0.29 pc. To put this scale in context, the famous Trapezium cluster in Orion, which contains at least five massive stars, spans roughly 0.5 pc, i.e., the entire region would almost appear to fit in a single fibre in FLAMES. It was only with observations using the *Hubble Space Telescope (HST)* that the core of R136 could be properly resolved, and the long held suspicion that R136 might contain a star of a few thousand solar masses was laid to rest (Campbell et al. 1992).

Adaptive Optics (AO), whereby the distorting effects of the atmosphere are corrected for through real-time analysis of nearby bright natural or laser guide stars, now means that the diffraction limit of ground-based telescopes can be approached. The diffraction limit, θ, is given by the equation $\theta \sim \lambda/D$, where λ is the wavelength and D is the telescope diameter. This means that an 8 m ground-based telescope, such as the VLT, can potentially reveal greater detail than the 2.4 m *HST*. This was shown by the Multi-conjugate Adaptive Optics Demonstrator, which was used to observe a small region of 30 Doradus in unprecedented detail by Campbell et al. (2010).

There are currently numerous designs for wide-field AO-corrected multi-object spectrographs for next-generation telescopes. A forerunner of these now exists on Gemini South, where the AO system of GeMS has been combined with the upgraded 'Flamingos2' spectrograph (Eikenberry et al. 2012). These instruments will be capable of creating considerably more detailed surveys than VFTS. In fact, it would be possible to investigate other, more massive star-burst regions in different galaxies - for instance the Antennae Galaxies contains star-forming knots that considerably exceed the mass of 30 Doradus. Currently, even with AO correction, the 8 m telescopes cannot resolve such distant clusters and so it is necessary to consider the new telescopes that are soon to be built.

1.4.1 Next generation telescopes

The power of hindsight allows the history of the telescope to be simplified into a series of distinct evolutionary epochs. For much of its early years in the 17th century, the telescope's design was dictated by the size of lenses that could be manufactured, with the added problems of achromatic effects greatly limiting any increase in aperture size. When, in 1668, Newton presented the world's first reflecting telescope to the Royal Society in London, the era of reflecting telescopes had tentatively begun. The arrival of the achromatic lens would give renewed life to the refracting telescope, but, by the end of the 18th century, the reflecting telescope's remarkable potential for ever-growing light collecting areas was being exploited - a trend which is still continuing.

In 1948 Hale constructed his masterpiece - the 200 inch telescope at Palomar, and astronomy entered the era of the 4-5 metre class telescope, an age which prevailed until the 1990s when the Keck telescopes in Hawaii ushered in the current epoch of the 8-10m class telescopes. All the world's great telescopes now occupy this elite class, including the four 8.2m telescopes of the Very Large Telescope which will be discussed in subsequent chapters. While there have been examples of telescopes that push this size limit, such as the South African Large Telescope (SALT) and the Large Binocular Telescope in the US, going to the next level of aperture size requires a considerable leap in telescope design. This will be the era of the Extremely Large Telescopes, and it is an era which is approaching rapidly.

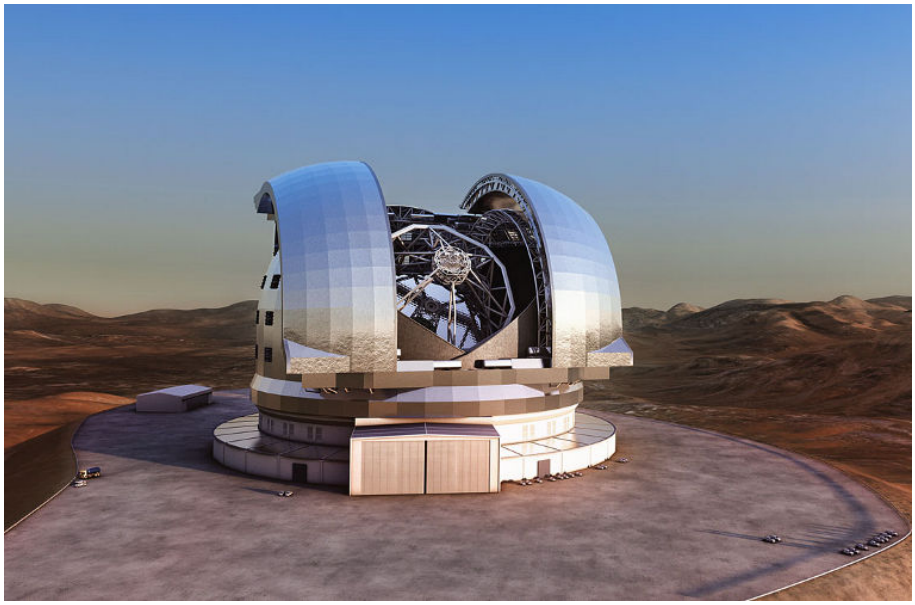

Figure 1.8: An artist's impression of the E-ELT sitting atop Cerro Armazones in the Atacama Desert, Chile.

Globally there are three independent projects which fall under this 'Extremely Large' moniker. The Thirty Metre Telescope (TMT) is an American-led project, which aims to build a telescope similar in design to the Keck telescopes, i.e. a Cassegrain telescope, which has a segmented primary mirror. The European-Extremely Large Telescope (E-ELT), shown in Figure 1.8 also employs a segmented mirror but is intended to be around 40 metres in diameter. Finally the Giant Magellan Telescope, which is another American project with contributions from Australia and South Korea, plans to utilise five off-axis 8 m mirrors (combined with a sixth on-axis) to form a collecting area which is equivalent to a 21.5 metre dish. These projects are currently at a similar stage, each with designs finalised but confirmation of the required budgets not yet in place. It is likely that first-light for any ELT will be seen in the early 2020s.

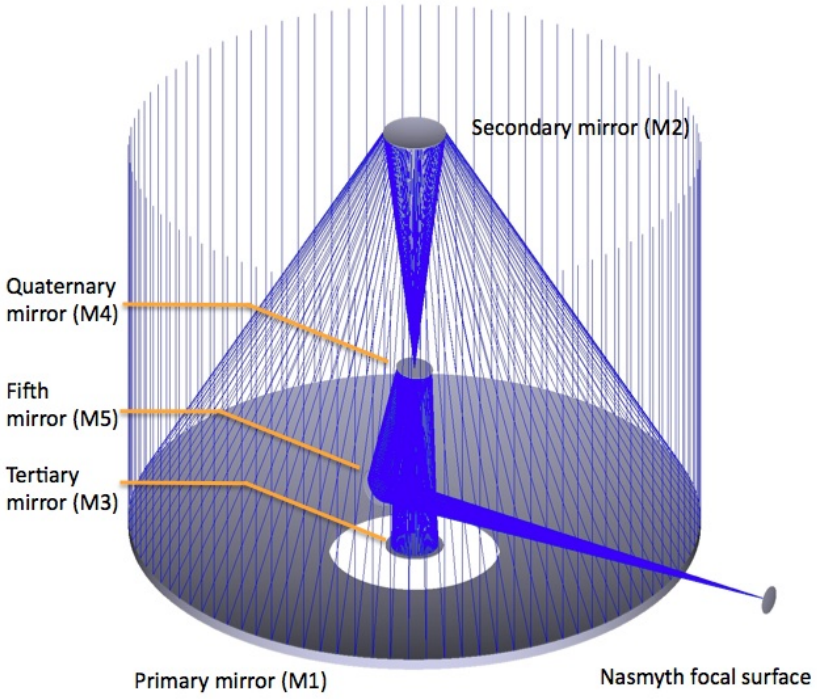

Figure 1.9: The five mirror design of the E-ELT. The primary mirror is composed of 786 hexagonal tiles, while M4 will be the largest deformable mirror yet built. There will be a further fold mirror immediately prior to the two Nasmyth focii to direct light into the different instruments.

The diffraction limit of the ELTs and indeed of most 4 m + class telescopes, is well below the atmospheric seeing limit; consequently, AO will be essential to fully exploit these telescopes. In current telescopes with an AO capability, the correction has always been performed within the instruments. The E-ELT differs from existing telescopes and from the other proposed ELTs, in that some of the AO correction will be performed

by the telescope itself, prior to light being passed to the instruments. This has led to the novel five mirror design of the telescope that is shown in Figure 1.9, within which M4 is a large Deformable Mirror (DM). It is anticipated that this mirror will correct for ground layer turbulence, whereas corrections for distortions from higher in the atmosphere will be performed within the instruments themselves. The possibility of some instruments sharing the same AO facility has also been considered.

1.4.2 E-ELT instrumentation

Although it is not possible to be certain what the fundamental science questions will be at the start of the next decade, the dramatic increase in light collection and spatial resolving power which the E-ELT promises, means it is appropriate to identify some questions that are unlikely to be addressed before then. The E-ELT's Science Working Group have therefore considered a wide range of areas to develop the primary science objectives for the E-ELT (Hook 2009); to address these, ESO has commissioned studies of nine separate instruments, as listed in Table 1.2. It is also important to consider that the telescope, and its suite of instruments, need to have sufficient versatility to be able to address questions that have not yet been conceived.

Table 1.2: Proposed instruments for the E-ELT.

Name	Description
CODEX	High-resolution, high-stability spectrograph
EAGLE	Multi-channel IFU spectrograph
EPICS	Planet imager
HARMONI	Single-channel IFU spectrograph
METIS	Mid-IR imager and spectrograph
MICADO	Imager and slit spectrograph
OPTIMOS-DIORAMAS	Wide-field imager and low-res spectrograph
OPTIMOS-EVE	Optical, near-IR fibre-fed MOS
SIMPLE	High-res near-IR echelle spectrograph

ESO has decided that its two first-light instruments will be a basic imager and a spectrograph, i.e. MICADO and HARMONI. These instruments have been selected for a number of reasons: they can both address a wide range of the E-ELT's science cases, they will both operate at the telescope's diffraction limit (thus maximising their potential scientific impact), and they carry fewer perceived technical risks than some of the other instruments.

Beyond these first two instruments, the intention is for a staggered delivery of a new instrument every two years. ESO have identified planetary imaging as a very high-

priority science case, however, the technical challenges required to build such a camera mean that it is likely that EPICS will be the last of the first generation instruments to be built. The third instrument has been identified as a Mid-IR imager and spectrograph such as METIS, while the four and fifth instruments will be either a MOS or a high-resolution spectrograph. For a fuller discussion of the instruments see Ramsay (2012).

1.4.2.1 EAGLE

The tremendously named E-ELT AO GaLactic Explorer, or EAGLE, has been designed by a European collaboration, with a great deal of work conducted by the UK Astronomy Technology Centre (Cuby et al. 2010). The robotic mirror positioning system described in this thesis has been developed with this instrument in mind. The EAGLE design has 20 near-IR IFUs, which will be fed through carefully positioned POMs on the focal plane (see Figure 1.10). Each of the channels will have an IFU which will deliver forty-two 37 mas slices. To achieve such high spatial resolution, EAGLE will employ Multi Object Adaptive Optics (MOAO), which will require use of the six laser guide stars (LGS) of the ELT and also five additional natural guide stars (NGS), selected from within the instrument's field-of-view (Rousset et al. 2010)[1]. Tailored corrections will then be calculated for each channel of the instrument and applied individually by a DM. A number of these design features directly influence the performance requirements of the robot system, as will be discussed in Chapter 5.

Like many of the proposed instruments, EAGLE is being planned around a primary science case - the physics of high redshift galaxies - but it will equally address other important cases. These are discussed in more detail in the EAGLE science requirements documentation delivered as part of Phase A study of EAGLE (Lehnert & Evans 2009)[2]. EAGLE will address three main science areas (Morris et al. 2012):

1. The physics of high redshift galaxies.

2. Spectroscopy of resolved stellar populations.

3. First light - the highest redshift galaxies.

From the science cases of EAGLE it is possible to determine the limiting values of the some of key instrument requirements, as listed in Table 1.3. For the E-ELT the aim is to better understand the formation of galaxies at $z > 2$. At this distance "clumpy" galaxies are seen that have bright knots which contribute a significant percentage of the

[1] An analysis of the likely availability of five bright NGS in the EAGLE field-of-view is given in Appendix A.

[2] A number of these Phase A documents are referenced throughout the thesis, but are not publicly available.

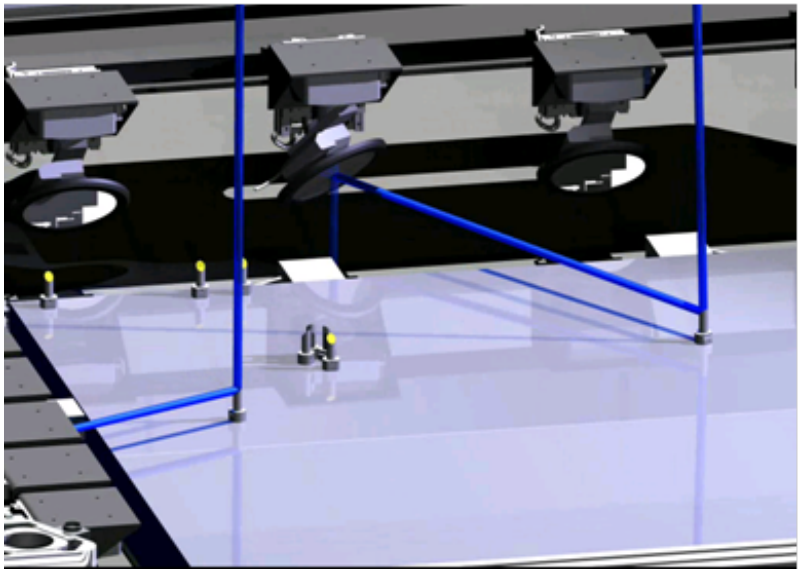

Figure 1.10: Pick-off mirrors in the focal plane of EAGLE selecting objects by feeding light onto the surrounding beam-steering mirrors, from which the light passes into the individual spectrographs.

galaxy's light (Elmegreen & Elmegreen 2005). The role of these clumps in the galaxy's evolution is not well understood, but it is possible they contribute to the formation of the bulge. These structures are of order 75 - 100 mas on the sky and it is partially this which sets the spatial resolving power of EAGLE. Smaller spatial resolutions could be sampled, but there is unlikely to be much scientific gain and therefore this presents a good compromise between signal-to-noise and resolution.

Table 1.3: Key properties of the EAGLE design.

Property	Specification
Effective field of view	Eqv. 7' diameter
IFU field of view	1.65 x 1.65 arcseconds
Number of IFUs	20
Spatial resolving power	30% Encircled Energy in 75 mas (H band)
Spectral resolving power (R)	4000 and 10 000
Wavelength range	0.8 - 2.5 μm

The size of the IFU field-of-view is set partially by the average size of the $z > 2$ galaxies and also by the technical requirements of manufacturing an image slicer. The relatively limited density of these sources also suggest that there is little advantage to increasing the IFU multiplex substantially. The science case for stellar populations pushes the wavelength range down to 0.8 μm as this then includes the Calcium triplet

which is an excellent diagnostic for metallicity determinations. This also leads to the requirement for the higher spectral resolution setting. Stellar studies would also nearly always desire high multiplexing. However, it is important to consider that it will often be possible to observe numerous stars with a single IFU, so upwards of one hundred stars could be observed with a single pointing of a 20-channel EAGLE.

1.4.2.2 Stellar research with the EAGLE

Evans et al. (2011a) have studied the potential of EAGLE to measure the metallicities of stars using both the Calcium triplet and diagnostics developed in the J-band (Davies et al. 2010a). They found that it should be possible to directly measure the metallicity for evolved red-giant branch (RGB) stars out to distances of ~ 2.5 Mpc and for RSGs out to beyond the Virgo cluster. Interestingly, they also found that robust estimates of these properties could be made from J-band spectra, without the use of the Calcium triplet. This is particularly relevant as, historically, stellar analyses have largely been carried out using visible data, in particular the 4000 - 5000 Å region. However, this will not be available for many of the AO-corrected instruments on the E-ELT that will operate in the IR.

Figure 1.11 shows the positions of all the nearby galaxies out to 8 Mpc. The over-plotted circles indicate the comparison between current and future facilities. It is clear that the E-ELT will open up many more galaxies for study. Note that this is not only for spectroscopic studies of massive stars; a similar impact for resolved stellar photometric work would also be expected. Indeed, Greggio et al. (2012) believe that they will be able to obtain a full description of the SFH in the last 1 Gyr for galaxies out to the Centaurus group (CenA in the 1.11).

One of the driving reasons for trying to sample a larger number of galaxies, is to increase the range of environments in which homogenous sets of massive stars can be studied. This will now include additional starburst regions, like 30 Doradus, and a wider range of different galaxy-types. It will increase the metallicity range available, for instance, the LMC and SMC have, respectively, metallicities of 0.5 and 0.2 times that of the Milky Way, whereas out to the Virgo cluster there are galaxies with metallicities as low as $\sim 1/20^{th}$ of the Milky Way. A complete understanding of this metallicity relationship is important for making any sort of predictions for the elusive Population III stars; these are predicted to be the first generation of stars which would therefore be expected to have extremely low metallicities.

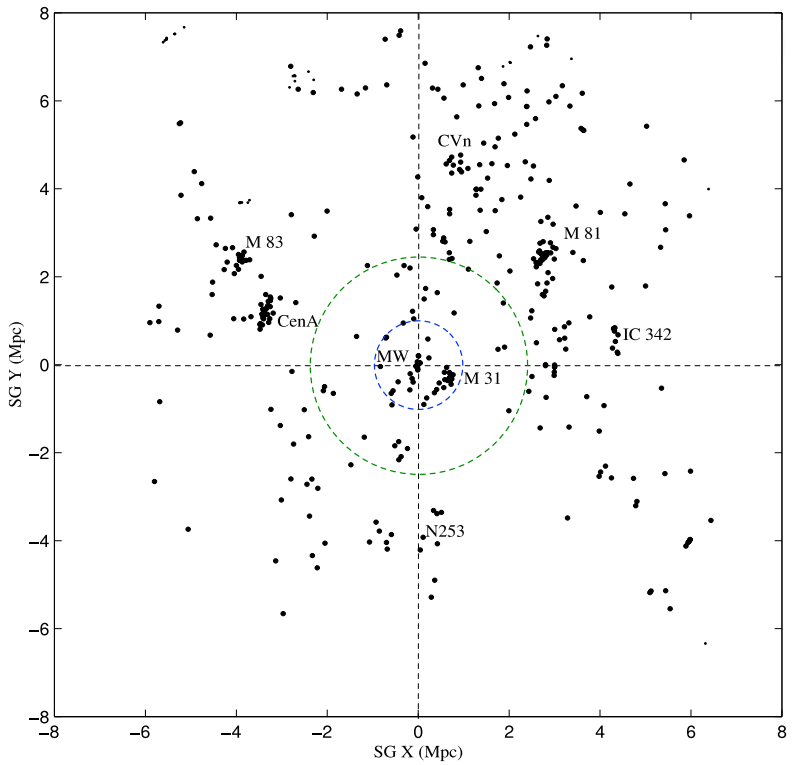

Figure 1.11: The local distribution of galaxies relative to the Milky Way (MW), from Karachentsev et al. (2004). The blue overlaid circle indicates the current reach of spectroscopic studies of resolved, evolved (i.e. low-mass) stellar populations. The green suggests the equivalent for EAGLE (Evans et al. 2011a). The Virgo cluster, for which work on RSGs will be possible lie beyond this figure, at around 16-17 Mpc. This shows how the age of the ELTs will dramatically increase the number and range of galaxies for which resolved stellar populations can be explored.

1.4.3 A fleet of Pick-off Mirrors - MAPS

EAGLE will require placement of at least 20 small POMs anywhere across its focal plane to select the target fields. There are a number of different methods which could be employed to do this, such as pick-and-place devices, robotic arms or a tiled focal plane with tilted mirrors. One of the more imaginative and perhaps more challenging methods would be to effectively give each mirror the ability to drive itself into position. Such a concept was first muted by McGrath & Moore (2004) as a means to position optical fibres.

This thesis presents research on a 'Micro Autonomous Positioning System' (MAPS) that has been carried out at the UK Astronomy Technology Centre (Taylor et al. 2010a;

Cochrane et al. 2012). The project involves small robots, each of which carries its own POM into position in the focal plane. Once in place the POM reflects the desired light onto the surrounding Beam Steering Mirrors which feed the light into the rest of the instrument; this concept is illustrated in Figure 1.12. Chapter 5 goes into more detail discussing the other possible POM placement methods, and fully introduces the development of the MAPS idea. Chapter 6 presents results of the testing carried out on the robots, while Chapter 7 concludes with a discussion of the effectiveness of MAPS, whilst also highlighting a number of areas of on-going research.

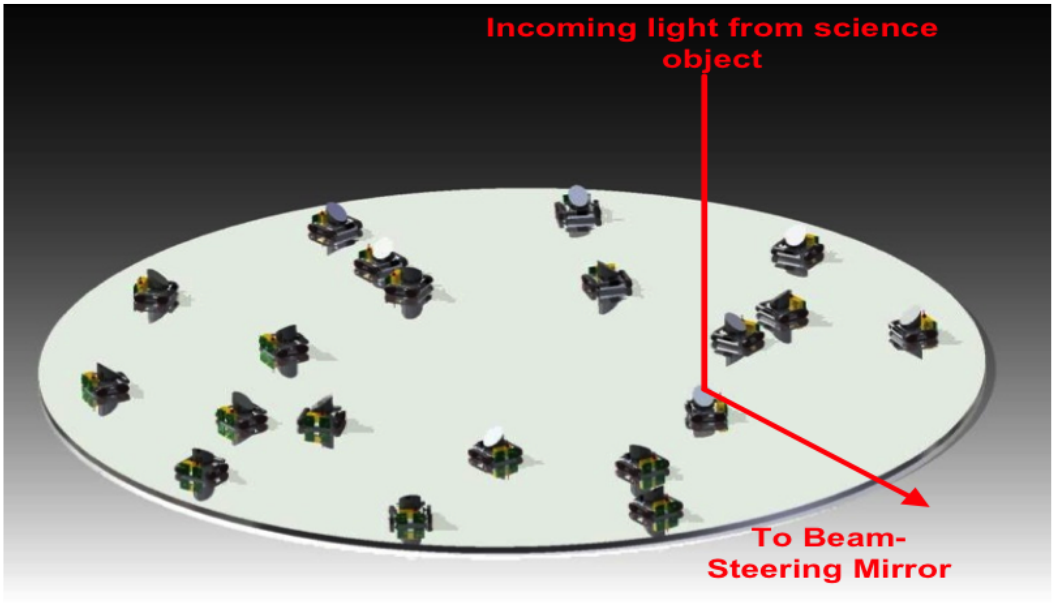

Figure 1.12: An artist's impression of MAPS robots populating a focal plane.

Chapter 2

The VLT-FLAMES Tarantula Survey

One could not count the moons that shimmer on her roofs, or the thousand splendid suns that hide behind her walls.

Saib Tabrizi, translated by Josephine Davis

2.1 Author's note

This chapter details the work carried out as part of the VLT-FLAMES Tarantula Survey (VTFS). This includes a description of the data reduction and some of the data quality checks performed, which included a quantitive analysis of the effects of atmospheric dispersion on the data set. The reduction work highlighted poorly understood scattering problems within the FLAMES spectrograph and an ongoing investigation into this is described here. Finally some of the early results of the VFTS project are presented.

2.2 Introduction to the VFTS

To gain a complete picture of stellar evolution it is necessary to study a large number of objects in a wide range of environments. However, this is difficult for massive stars as they are not only less common than lower mass stars, but there is less time to view them as they live relatively short lives (a few Myrs). As was discussed in the previous chapter, there are consequently numerous short-comings in the current theories of massive stars, some of which pertain to very basic concepts such as their formation, evolution and eventual fate.

Some larger surveys of B stars have been able to amass hundreds of objects, for instance the VLT-FLAMES Survey of Massive Stars (Evans et al. 2005, 2006) considered over 500 objects from seven clusters in the galaxy and Magellanic Clouds.

The survey helped to support some well-established theories, such as the metallicity dependence of stellar winds for O-type stars (Mokiem et al. 2007), but it also presented challenging results, such as the unexpected relationship between nitrogen abundances and the rotational velocities of the stars found by Hunter et al. (2008a). For the rarer O stars, surveys had previously been limited to much smaller sample sets (e.g. Herrero et al. 2000; Massey et al. 2009) with the result that it is often difficult to draw statistically valid conclusions from the available data.

The VFTS has assembled the largest spectroscopic sample ($\sim$ 1000 stars) to date of massive stars drawn from a single region (Evans et al. 2011b). There is only one region in which this is possible with current ground-based facilities: the Tarantula Nebula in the LMC, which is the largest star-forming region in the Local Group (it is also known as 30 Doradus and NGC 2070). This complex region is actually comprised of at least five distinct phases of star formation (Walborn & Blades 1997): the oldest of these is Hodge 301, a small group to the north-west of the central region, which is $\sim$20-25 Myrs old (Grebel & Chu 2000). All the other populations are younger, generally considered to be around 1-2 Myrs old; included in these is the famous central region R136. Results from Crowther et al. (2010) have been used to argue that, within this central cluster, a number of stars have masses in excess of 150 $M_{\odot}$; these are currently the most massive stars known. These central stars contribute a significant percentage of the ionising radiation in the region, and influence the shape of the surrounding nebula, possibly even triggering star-formation in some of the regions surrounding the core (Walborn & Blades 1997).

This extraordinary region provides a wide sample of different stellar populations beyond just the numerous O and B-type stars; there are a number of W-R stars, several transition Of/Wn stars and also some candidate young stellar objects (YSOs) suggesting relatively recent star formation. The scientific aims of the VFTS are consequently relatively broad, but a brief summary of some of the primary scientific motivations are outlined below. For comparison, some of the early results of the survey are given at the end of this chapter; these naturally include a few results which had not been anticipated.

2.2.1 Scientific motivations for the VFTS

Identification of massive binaries: One of the primary aims of the VFTS is to detect binary systems. The survey therefore employs a multi-epoch strategy whereby the same stars are viewed on numerous occasions and the radial velocity shifts associated with binarity can be identified between repeat observations. From a survey of 50 early-type stars Bosch et al. (2009) found evidence that the binary fraction in 30 Doradus is

$\geq 50\%$, but could not rule out a fraction of 100%. The VFTS provides a larger sample of both O and B stars, which enables more detailed analysis of other properties such as the distributions of the orbital period and the mass ratios.

Rotational velocities and their influence: The large sample of stars, from roughly the same population, provides insight into the distribution of $v \sin i$ values for a variety of different types of stars. The influence of rotation on the evolution of O-stars has never been well explored before due to limited sample sizes. The VFTS will provide excellent tests of the rotational models for O-stars which have, effectively, been derived from scaling up properties derived for B-type stars (Brott et al. 2011).

Stellar winds: Studying the winds of early O-stars, W-R stars and the 'slash' stars, will potentially reveal information about the differences (and similarities) between the mechanisms driving the weaker winds of O-stars and the much stronger winds found in W-Rs. The potential relationship between winds and rotation can also be explored.

Dynamical mass estimates: The dynamical mass provides an estimate of a cluster's mass through measurement of its velocity dispersion. This can be contrasted with the photometric stellar mass of the cluster to allow estimates of whether the cluster is in virial equilibrium. From this, predictions of the cluster's fate can be made - for instance, will R136 become a future Globular cluster?

Extra-galactic comparisons: For those whose research lies beyond that of individual stellar objects, perhaps one of the most important reasons for studying this local starburst region is to better understand more distant, unresolvable regions. Codes such as Starburst99 (Leitherer et al. 1999) are used to simulate entire populations of stars, such that the content of unresolved, distant regions can be estimated. The VFTS will provide a better understanding of both the dynamical and stellar properties of 30 Doradus. This can be used to inform population synthesis models by comparing the well-informed simulation results for 30 Doradus against unresolved observations of the cluster. Through such methods, knowledge of the more distant Universe can be improved through studying in detail the galactic backyard.

2.3 Observation strategy

The VFTS exploited three different observing modes of the FLAMES instrument. The majority of observations were obtained in the 'Medusa' mode. This mode was described

in the previous chapter, where 132 fibres are distributed across the field-of-view through use of a pick-and-place robot. To probe the more densely populated regions towards the core of R136, the 'ARGUS' IFU setting was also used. Finally, a small number of objects were observed in the 'UVES' mode, which can be used in parallel with ARGUS, providing higher resolution spectroscopy of a single object at a time. Both the Medusa and ARGUS observations and their data reduction are described below; the UVES reductions are not relevant to this thesis and are not discussed further. The settings used for the three different modes are shown in Table 2.1: note that all the observations were observed in back-to-back pairs, to form a single Observation Block (OB).

Table 2.1: Observational details of the different settings used for the different observing modes of FLAMES. The column on the right gives an indication of the *minimum* number of OBs taken for each setting.

Mode	Setting	Wavelength /Å	R	Exp. time / OB	No. of OBs
Medusa	LR02	3980-4525	6,500	2×1815s	6
Medusa	LR03	4505-5050	7,500	2×1815s	3
Medusa	HR15N	6470-6790	17,000	2×2265s	2
ARGUS	LR02	3980-4525	10,500	2×1815s	5
UVES	520	4175-6200	53,000	2×1815s	5

2.3.1 Medusa observations

The Medusa targets were selected from unpublished imaging of 30 Doradus taken with ESO's Wide-Field Imager on the 2.2m telescope at La Silla. Although the majority of targets sample the inner 5' of the cluster, they also extend out into the surrounding field stars and some of the nearby smaller associations/clusters, as shown in Figure 2.1. To avoid possible selection biases, no colour cuts were made, but a limiting magnitude of $V \leq 17$ was applied to ensure adequate signal-to-noise (S/N).

A total of nine fibre configurations (fields 'A' through to 'I') were used to build-up a sample of exactly 1000 stars. The targets were allocated to each field using ESO's Fibre Positioner Observation Support Software (FPOSS). Each field was observed at three of the standard Giraffe wavelength settings (LR02, LR03 and HR15N) thus providing coverage of the classical blue region used in the analysis of massive stars, combined with higher resolution observations of Hα, which provides a diagnostic of the intensity of the stellar winds. Each observation consisted of a pair of back-to-back exposures, to allow for cosmic removal and to ensure sufficient S/N ($\geq$50) in the combined spectra. For every field a minimum of ten fibres were deliberately not placed on objects to produce a number of 'sky fibres' - these were distributed relatively evenly across the field.

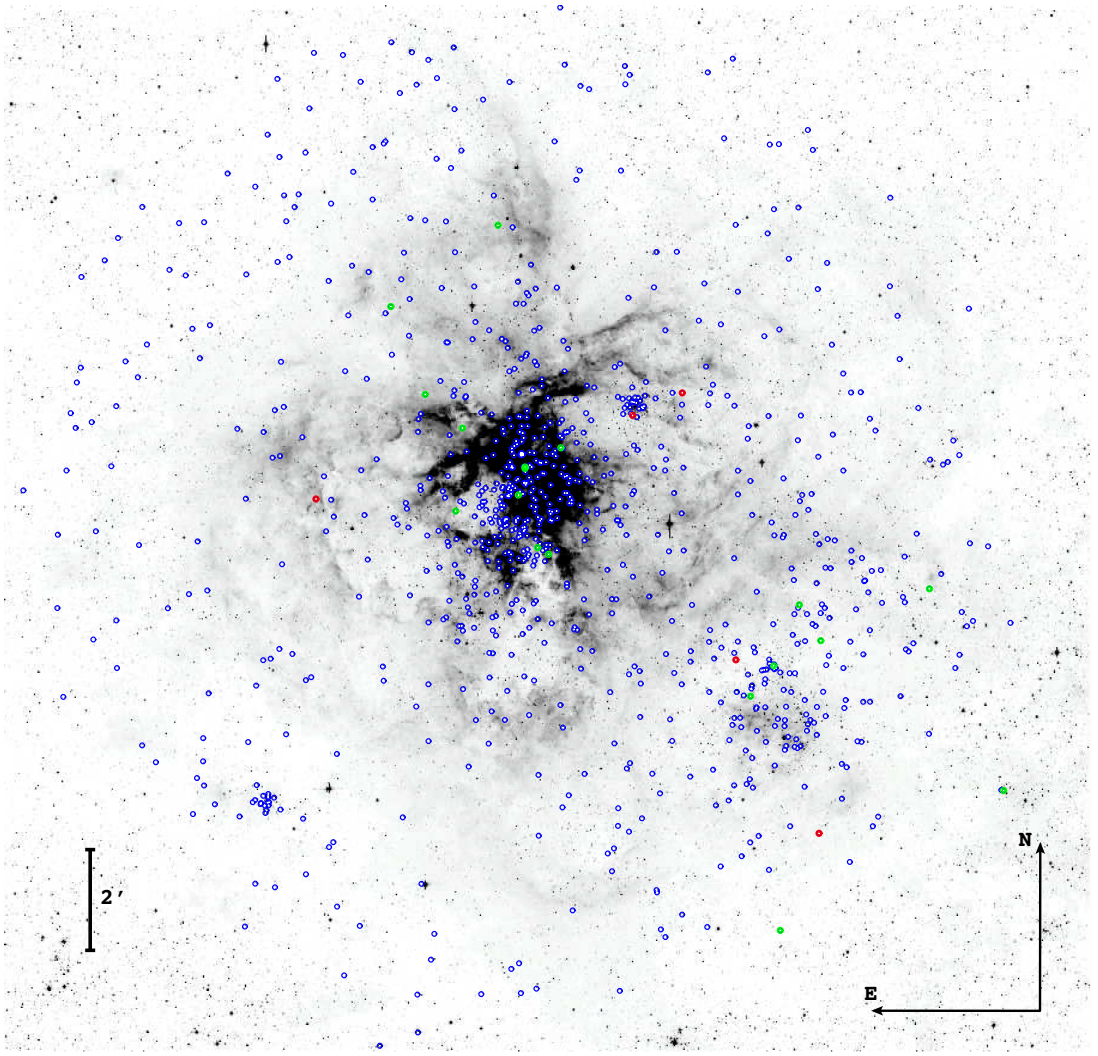

Figure 2.1: The Medusa targets overlaid on a a V-band WFI image of 30 Doradus. The majority of targets lie in the central region surrounding R136. Also of note are the surrounding regions of NGC 2060 to the south west, the tight group of Hodge 301 just to the north west and also the smaller group of SL 639 to the south east. The emission-line stars identified in the survey are shown in green while the luminous RSGs are appropriately in red.

The first three LR02 OBs, and all the LR03 and HR15 OBs were obtained with no strong time constraints - in practise, these were often obtained consecutively, or on sequential nights. For detection of massive binaries, a further three pairs of LR02 exposures were obtained. The fourth and fifth epochs were constrained such that a minimum of 28 days had expired since the previous LR02 observation, while the final (sixth) epoch was obtained in the equivalent observing season one year later.

This additional time-delayed sixth epoch considerably increases the chances of detecting binaries with periods greater than 100 days. Sana et al. (2009) presented methods to calculate the probabilities of detecting a binary companion around a star as a function of the orbital period, based on the time sampling of the observations. This is shown for one of the fields from the Tarantula survey in Figure 2.2, indicating the impact of the sixth, time-delayed OB. The survey should be fairly complete for orbits of tens of days. Quantifying the potential selection biases is a critical component of the work to inform the binarity results from the survey.

All of the VFTS data were observed in service-mode at the VLT. This had the slight disadvantage that many of the early OBs were observed consecutively - which decreases the chances of binary detection. However, it did bring the benefit that a number of OBs were repeated; this was due to a number of reasons such as poor seeing, or other operational difficulties. In many cases the data were still acceptable for use, and this therefore presented a few additional OBs taken at different times.

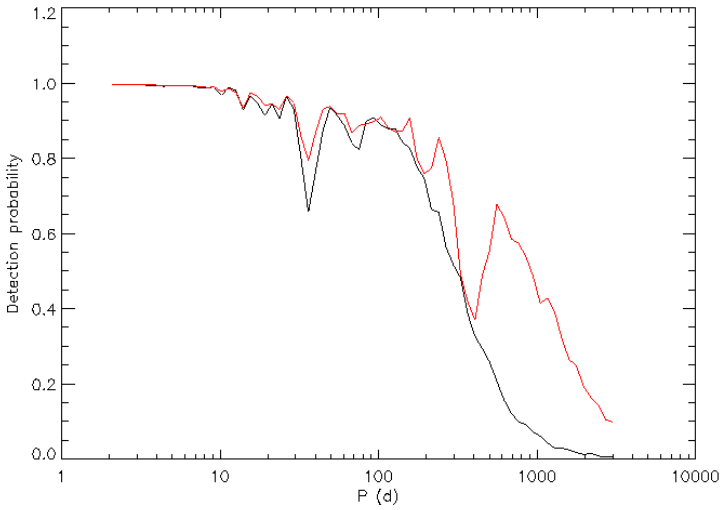

Figure 2.2: The black line indicates the detection probabilities for the first five epochs, with the red line demonstrating how inclusion of the sixth, delayed, epoch significantly increases the chance for detecting binaries with periods greater than 100 days.

2.3.2 ARGUS observations

The ARGUS observations were designed for studying the dynamics of the inner regions of the cluster, consequently all the pointings were within 1' of R136, as can be seen in Figure 2.3. Undetected binaries can alter dynamical measurements of a system, and consequently a similar multi-epoch strategy was employed for these frames, only with two unrestricted initial OBs rather than the three employed for Medusa.

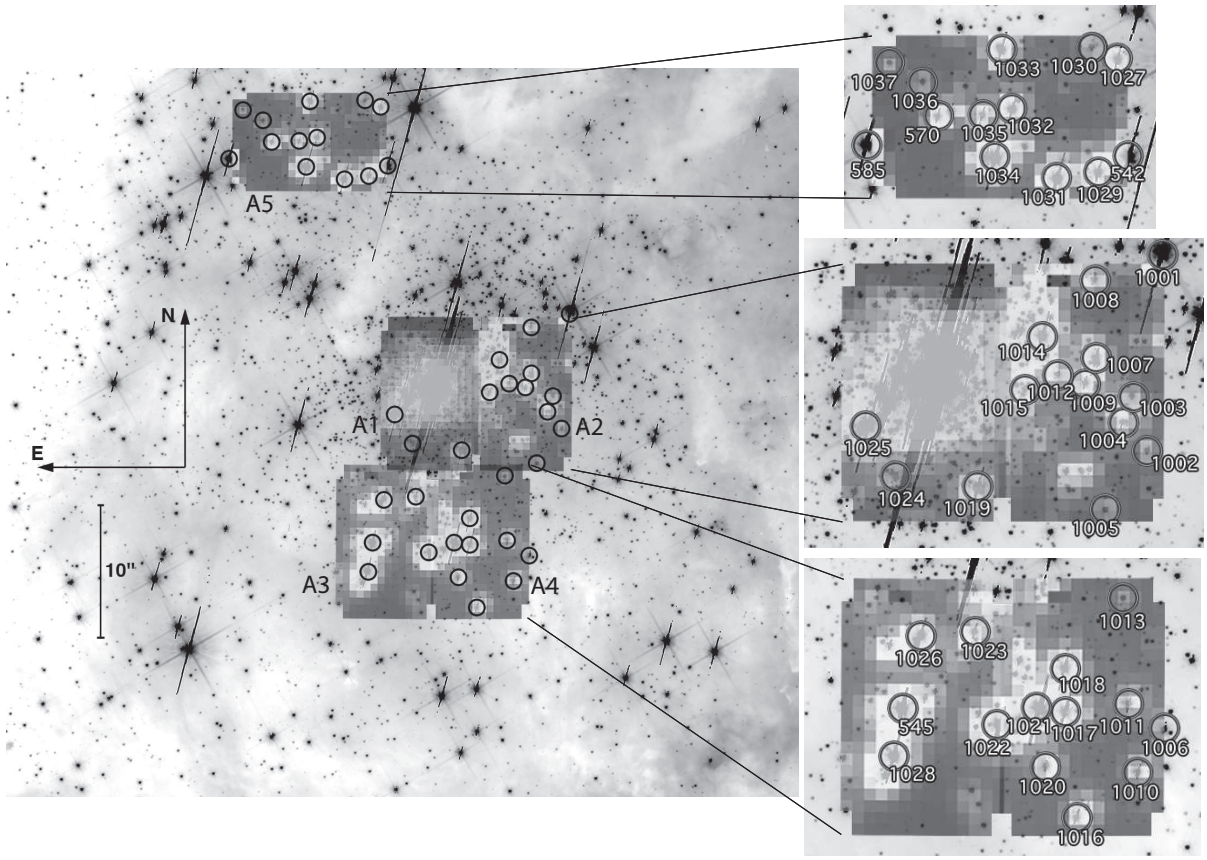

Figure 2.3: The left-hand image shows the five ARGUS pointings overlaid on an F555W HST-WFC3 image, with close-ups of each pointing on the right. The identified individual extracted sources are overlaid in white text.

2.4 Data Reduction

The VFTS gathered over 250 frames of data, leading to over 22,000 individual spectra and multiple ARGUS pointings. The primary data reduction was carried out using the FLAMES reduction routines from the ESO Common Pipeline Library (version 2.8.7). Before undertaking the reduction for the full data-set, quality checks were performed on an old data set by comparing the new pipeline reductions with previous reductions, performed using tailored codes for those frames. The quality of the pipeline reductions was found to be very similar to the previous work.

A typical raw Medusa frame is shown in Figure 2.4: the dispersed spectra of the 132 fibres can be seen running along the length of the image; the variation in the intensity of the brightness of the stars is also apparent. The ARGUS fibres are smaller than those of Medusa (0.8' on-sky compared to 1.2'), they are also packed closer together; this

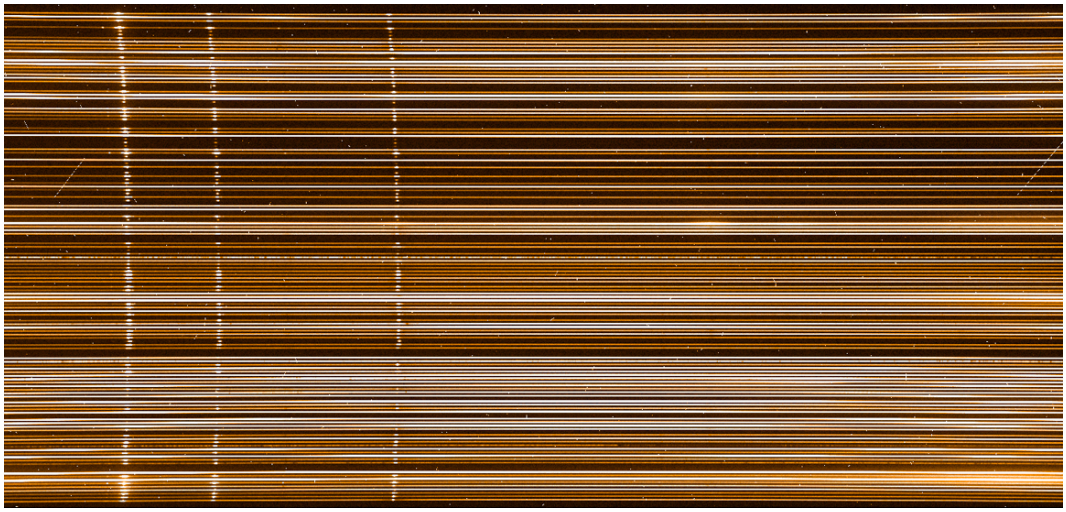

Figure 2.4: An example image of a raw Medusa frame for the LR02 setting. A number of common emission features are seen in every fibre, which originate from the surrounding nebula. It can be seen how these bow across the image due to natural distortions in the spectrograph camera. Also visible are bright spots which originate from cosmic ray events.

means there are over 300 spectra on a single ARGUS frame. However, the reduction techniques for both Medusa and ARGUS OBs are very similar.

The data reduction for FLAMES is not that dissimilar to other fibre-fed multi-object instruments. An overview of the key stages is given here, which will provide background for the reduction-related issues that will be discussed later in the chapter, in particular the later section on scattering.

2.4.1 Bias frames

The first stage of the reduction is to subtract the bias level of the detector. Numerous bias frames are taken each day as part of the standard day-time calibration of the instrument; the median of five frames is then calculated and subtracted from each raw science frame. The current detector on FLAMES has a very uniform bias and is relatively free from any distinguishing features. This is a considerable improvement on the original detector, which had a bright glow in one corner that significantly affected observations.

2.4.2 Flat-fields

The standard flat-fields are taken by positioning all the fibres in a spiral pattern on the focal plate. The positioning robot then sweeps continuously over the top of the fibre tips, illuminating each one with a featureless white light source. This builds up

a strong and even signal in each fibre, giving a very high S/N noise on the detector. Again a number of these frames are taken each day.

The flat field fulfils two primary functions; it gives both the positions of the fibres on the detector and also their throughput. The software searches though the flat-field image to make a map of the centres of all the fibres; this map can then be used to estimate the position of the fibres in the real science frames, where the S/N could be considerably lower and it may not be possible to successfully trace the fibre across the CCD. A measurement of the throughput of each fibre relative to the brightest fibre is also made at this stage. This can be used later to correct the relative flux levels of the final spectra for accurate sky subtraction. It was also necessary at this stage to specify if any fibres are broken, an up-to-date record of which is available from the ESO website.

A different kind of 'attached screen' flat-field is also available. This is created by back-illuminating the entrance (or Nasmyth) shutter of the VLT with halogen lamps and then taking an exposure. This technique has the advantage that it can be performed immediately before/after an observation with the fibres still in place - this minimises any errors that could be introduced to the throughput measurements when the fibres are moved into position. These were not used for the Medusa observations, as throughput is not a primary concern and this method increases observing overheads. Such flats are taken as standard for the ARGUS observations. It was found that there were noticeable differences between the 'normal' and the attached flats. It is believed this is a result of scattering within the instrument and is discussed further in section 2.7. In the end, the normal flats were used for the ARGUS reductions.

2.4.3 Wavelength calibration

Wavelength calibration frames are taken by passing the positioning robot over the fibre tips, illuminating it with a Th-Ar light source. This process is slower than that for the normal flats, as the robot dwells on each fibre. This provides a large number of emission lines that are analysed to provide a wavelength calibration, which is used to determine the wavelength scale across the CCD.

2.4.4 Extraction of data

The final stage of the reduction process is to 'extract' the data, i.e. use the results from the two previous reduction stages to turn a slightly-bowed 2-d band of illuminated pixels on a CCD, into a single 1-d wavelength-calibrated spectrum. This is done by moving along the dispersion for a fibre, and combining all the flux from that particular fibre. There are two primary methods of doing this to consider:

Summed extraction: The most simple method is a summation of all the flux across the width of the fibre profile for each column of the CCD.

Optimal extraction: In this method the flux across the fibre is fit to a fibre-profile model. All the fibres across the whole CCD column are fit simultaneously to the following equation:

$$m(x,y) = \sum_{j=0}^{N-1} f_j(x) P_j(x,y) + B(x,y), \tag{2.1}$$

where $f_j(x)$ is the flux in wavelength bin x of fibre j and $P_j(x,y)$ is the fibre-profile model. This model was created from the flat-field reduction.

By fitting to a model, it is possible to search for, and remove, unexpected spikes in the spectrum arising from cosmic hits. This is a distinct advantage of the optimal extraction over the summed method. Another advantage is that it is possible to model the background across the CCD arising from scattered light - the $B(x,y)$ term in the above equation. This is determined by fitting a Chebyshev polynomial to the inter-fibre flux values.

All the extracted spectra are then combined to form a FITS file containing 132 spectra. The spectra are truncated to a common wavelength grid, which is defined by the fibre that spans the shortest wavelength range. Wavelength, observational and reduction details are encoded in the corresponding FITS header. For the Medusa fibres this is the final stage of the reduction, while for ARGUS the data is reformed to create a 3-d 'cube' of data, with the 'spaxels' mapped onto their appropriate on-sky position.

2.4.5 Problems of apparently negative fibres

Many early frames were reduced using the optimal method. By design the sky fibres should contain the faintest signals, but it was quickly noted that some reduced sky spectra actually contained negative flux levels - this is clearly not possible. Initial investigation focussed on the possibility of over-subtraction during the correction for the bias frame, however, this was found to be within acceptable limits. A number of frames were re-reduced using the summed extraction and it was found that the problem was not present in these frames. A similar drop in the total flux was found in a number of the object fibres too.

The problem has not yet been definitively identified despite parallel investigations from individuals at ESO. However, it is believed that it is linked with the treatment of the background in the optimal extraction method. As discussed, the background is fit using polynomials, the order of which can be specified as part of the reduction

process (the default is 2). It was found that if this was very significantly increased (to ~ 50) the negative fibre problem could be improved but not fully removed. The high order required to improve the polynomial fit suggests the background varies on a small scale. Consequently, if too low an order is used, it is possible that in certain places the background will be significantly over estimated - this would lead to over subtraction in the adjacent fibres and would explain the negative fluxes.

Part of the target allocation process for the VFTS was to deliberately not be too selective about the targets. Consequently all fields contain objects which span magnitudes between $V \sim 12 - 17$, i.e. the brightest object can be as much as 100 times brighter than the faintest. For bright objects the wings of the fibre profile can be extremely broad, and this can significantly raise the inter-fibre flux. It is believed that this wide range of magnitudes is responsible for a varying background and therefore the negative sky fibres. All the VFTS reductions have therefore been carried out using the summed extraction.

2.4.6 Cross-contamination

The fibre wings for some of brighter objects, in particular the W-Rs and slash stars, were sufficiently broad that they extended into nearby fibres. Using the observations with the best seeing (and therefore strongest signal and broadest wings) the fibres adjacent to the brighter targets were examined. Five stars were found to have been significantly contaminated and were therefore rejected from the survey, while a further 22 showed some evidence of mild contamination and were flagged as being suspect in the catalogue paper (Evans et al. 2011b).

2.4.7 Cosmic-ray rejection

Since each OB consists of back-to-back exposures, this pair can be used to correct for cosmic-ray contamination. Rather than studying each spectrum, the ratio of the two was calculated, and a boxcar 4-sigma clip over 100 wavelength bins was performed. Any inconsistency that was flagged in the ratio points to a feature present in only one of the spectra, which is likely to be cosmic contamination. The offending region can then be replaced by the 'clean' region in the sister observation, appropriately scaled by the ratio of the surrounding region. This technique removed the majority of cosmic-hits. The threshold could be set lower to remove the final few, but there then becomes a danger that subtle, but real, differences between the frames could be misinterpreted and removed.

2.4.8 Sky subtraction

A median sky spectrum was created through combining all the sky fibres. An initial, visual check was performed to reject any sky fibres that showed signs of contamination either from an on-sky source or through proximity to a bright source on the detector. The median sky was then subtracted from all the objects in that frame.

Accurate sky subtraction is one of the major challenges for fibre spectrographs. In a slit spectrograph the sky can be calculated using the regions adjacent to the source. To recreate this for fibres, it would be necessary to have multiple fibres surrounding the source, but this would be an inefficient use of detector space. Consequently, the approach applied is the best available option. In 30 Doradus the nebula contamination is high, and a truly accurate treatment of nebula emission would be very difficult to achieve with any fibre instrument. Instead it is better to simply avoid lines in which nebula contamination is likely to affect any measurements.

2.4.9 Error files

The ESO reduction pipeline produces an error frame associated with every fibre. For each wavelength bin, this records the statistical uncertainties arising from each stage of the reduction process. The final data product released for each star needs to include this error frame and any contribution to it introduced through the sky subtraction.

Each sky fibre used to form the median sky also has an error frame associated with it. Figure 2.5 shows the results of three methods that were investigated to combine the individual sky error frames to form an appropriate error for the median sky (MSE).

The most simple option is to take the median of the sky error frames, this is shown by the red line in the figure. This is effectively a smoothed version of the error frame for a single fibre, and is therefore not a realistic reflection of the variation in the real flux of the sky fibres. Likewise simply adding in quadrature the error frames from each sky fibre, results in an unrealistically low value for the MSE - shown by the blue line.

To give a more representative error, it is necessary to include the variance in the real fluxes of the sky fibres used to create the median. The final MSE is given by;

$$MSE(i)^2 = \frac{\sum_{j=1}^{N} [f_j(i) - \bar{f}(i)]^2 / \sigma_j(i)^2}{\sum_{j=1}^{N} 1/\sigma_j(i)^2}, \tag{2.2}$$

where, i represents each wavelength bin, f_j describes the actual flux in the sky fibre j, while $\bar{f}(i)$ describes the median flux of all the sky fibres (N). This variance on the sky

fibre values is weighted by the error term associated with that fibre, given by σ_j. The denominator in the equation ensures that if only one fibre were used, the error would simply be the variance on a single fibre. As more fibres are introduced, the value of the MSE decreases.

One of the key advantages of this final technique is that the error for the nebula lines is considerably larger than the continuum. This is an accurate reflection of reality - as discussed, there is large variation in the nebula emission across 30 Doradus, and this should be reflected in the error frames.

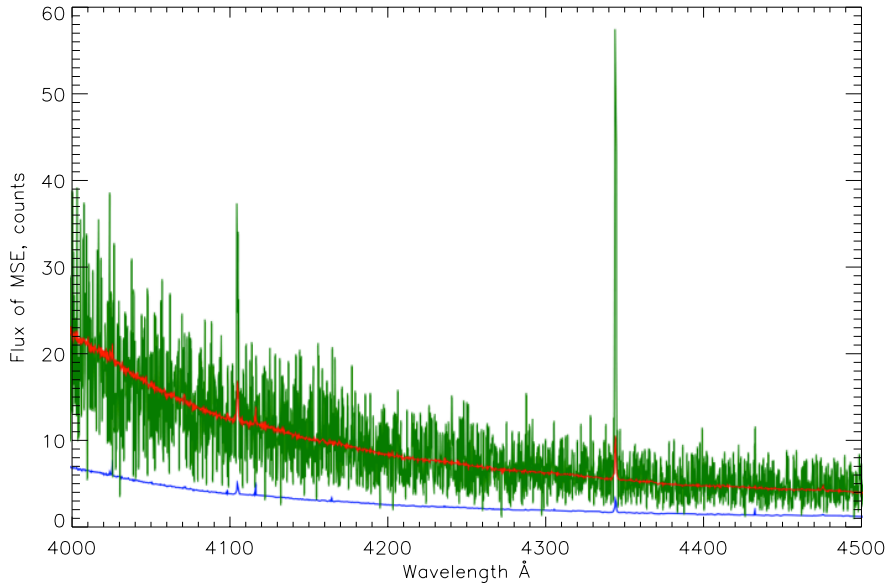

Figure 2.5: Example of the different possible methods to construct the median sky error frame. The green line represents the chosen method, described by equation 2.2, see text for more details.

2.5 Data products

The final data product released to the consortium was presented in a FITS file with numerous extensions, through which it was possible to trace all stages of the reduction process. These extensions are shown in Table 2.2. As can be seen, a user is able to quickly obtain the original spectrum by combining extensions [1] and [2], and its error frame will be extension [4].

Table 2.2: The FITS extensions of the final data product files.

Extension	Name	Description
[0]	PRIMARY	Final data product, sky subtracted and cleaned of cosmic contamination
[1]	SKY SUBTRACTED	Sky subtracted, but not cosmic clipped
[2]	MEDIAN SKY	The median sky associated with that OB
[3]	PROCESSED ERROR	Error spectrum associated with [0]
[4]	ORIGINAL ERROR	Original, untreated error spectrum
[5]	FIBRE SETUP	Fibre look-up table associated with that OB

2.5.1 Types of stars

It was necessary to remove any foreground objects that are not part of 30 Doradus but happen to lie along the line of sight. The LMC has an average recessional velocity of $\sim$270 kms^{-1} (Sana et al. 2012a); an estimate was made for the radial velocity of objects, and any object with $v < 100\,\mathrm{kms}^{-1}$ was rejected from the survey. Also, a handful of objects which had very low S/N and were likely cool stars in the LMC were also rejected. These two criteria led to the exclusion of 102 stars from the data-set.

In total the VFTS catalogued Medusa spectra for 893 objects. Based on ascending RA position each object was assigned an identifier of the form VFTS ###. There were an additional 41 ARGUS targets, 4 of which overlapped with the Medusa targets. To distinguish the objects, the ARGUS numbering began at VFTS 1001. An initial visual inspection was made of all the LR02 observations to determine loosely the type of objects; it was found that the survey contained:

- 20 W-R stars including some Of/WN
- $\sim$300 O-type stars
- $\sim$500 B-type stars
- $\sim$90 cooler-type stars

This is equivalent to the number of B-type stars from the original VLT-FLAMES Survey of Massive Stars (Evans et al. 2005), but has the advantage of multiple epochs of the same objects. Also this number of extra-galactic O-stars is unprecedented for a homogeneous data-set, taken from one region of space.

2.5.2 Data quality

As examples of the data quality, Figure 2.6 shows the normalised and rectified LR02 spectra for one of the faintest objects in the survey, VFTS 553 and one of the brightest,

VFTS 527 (which is the star R139 that will be discussed in the next chapter). For VFTS 553 the S/N *per resolution element* is ∼50 for all three wavelength settings, whereas for R139 the S/N is >400.

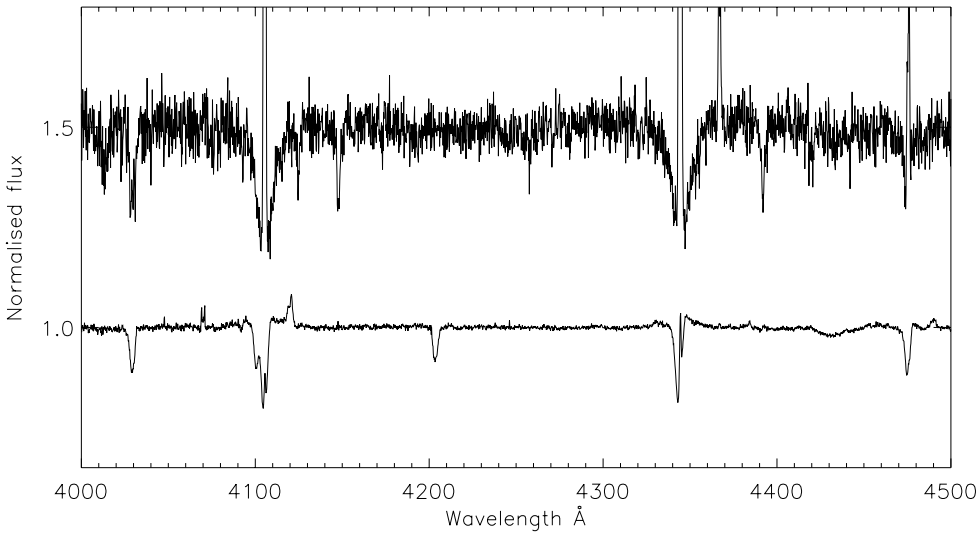

Figure 2.6: Examples of the LR02 region for highest and the lowest quality data. The top object is the late B-type star VFTS 553, while the lower object is the considerably brighter VFTS 527.

2.6 Atmospheric refraction effects

Throughout the course of the survey, numerous queries have arisen regarding the VFTS data-set. Many of these have been relatively simple to explain, but have highlighted interesting aspects of both survey and instrument design. One such problem, in this case relating to atmospheric diffraction, is described along with the discussion it generated.

It was noted that for many objects in the survey, repeat observations displayed distinctly different profile shapes. An extreme example of this is shown in the bottom half of Figure 2.7. This shows two OBs of VFTS 001 that were separated by only 15 minutes, yet the difference in shape is extremely pronounced. Initial checks were made in case such an effect was the result of the reduction process, but a difference in flux levels could be traced right back to the raw counts on the CCD.

The top panel of Figure 2.7 shows the ratios of the frames; they appear to vary linearly with wavelength. The effect was looked for in all the other stars which lie in the same field (Field H). It was found that for many there was little change in spectral shape, while for some the change was in the opposite sense to VFTS 001, i.e. the flux

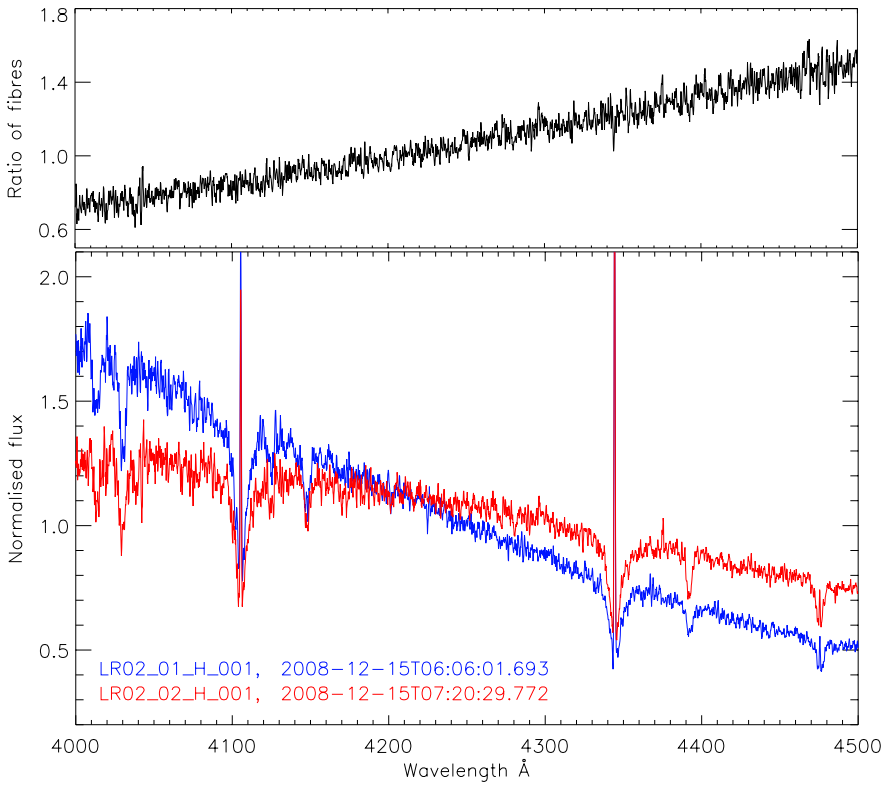

Figure 2.7: The impact of differential refraction on continuum profile shapes. The bottom panel shows the consecutive OBs. The observation name and its date are shown in the colour matching the line on the graph. The top panel shows the ratio of the OB1/OB2.

increased in the blue-end of the spectrum and decreased in the red-end. The gradient of the ratio can be used to measure the scale and direction of this change, and in Figure 2.8 the measured gradient is plotted against the position of the object in the field. If the field is split along a line of $\sim$15° anti-clockwise from the vertical, then one half generally shows a positive gradient, while the other half shows a negative one.

2.6.0.1 Atmospheric effects

As light from a distant star passes through the atmosphere it is refracted; this leads to an apparent shift in the on-sky position of a star. This shift can be described by:

$$dr(\lambda) = n(\lambda) \tan(z), \tag{2.3}$$

where dr is the shift in arc-seconds, n is the refractive index of the atmosphere and z is the zenith distance of the object. The variation in refractive index of the atmosphere

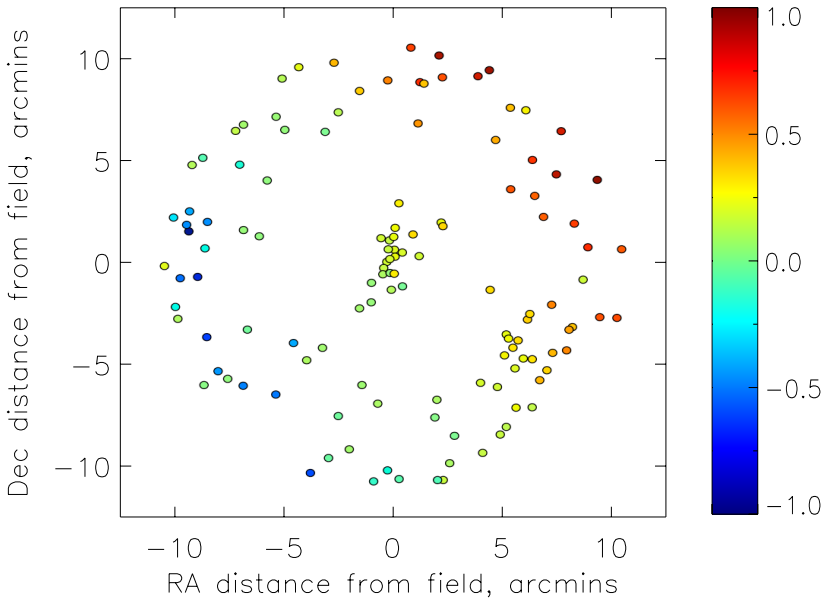

Figure 2.8: A comparison of the change in profile continuum shapes for the objects in Field H between two consecutive OBs. The colour represents the normalised gradients of the ratio of OB1/OB2 for each spactra.

is described by Filippenko (1982); crucially, it is a function of the wavelength (λ). This means that light of different colours is offset by varying amounts and a seeing-limited source can have subtly different colours across its dispersed image on the sky (i.e. at its 'top' and 'bottom').

The software that controls the FLAMES instrument accounts for the effects of atmospheric refraction by offsetting each fibres by an appropriate amount, dr. Since dr is a function of z this varies for each fibre across the field. As the telescope tracks a field across the sky, the zenith distance of the field changes, and so the telescope must compensate for the associated change in dr. However, the field is also rotating, which means that the variation in dr across the field is not constant. As a consequence the fibres gradually become mis-aligned with their intended objects.

Generally, observations can be designed such that these effects are relatively small and an object will never drift outside the collecting area of the fibre. However, it is possible that as the fibre becomes slightly mis-aligned, it will effectively move towards the 'top' or 'bottom' of the source. Since dr is wavelength dependent, this therefore means that the relative contribution of 'bluer' or 'redder' flux can vary depending on the relative alignment of the fibre and the source.

Returning to the observations of Field H, it is clear that this differential refraction effect has caused some of the fibres to selectively gather more of the different constituent

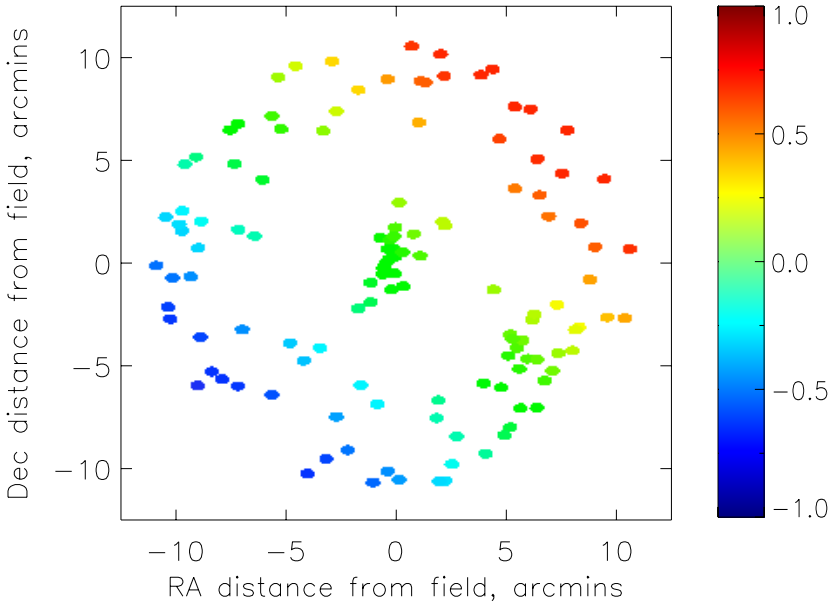

Figure 2.9: The offset between the on-sky position and the fibre position after a 2.5 hr observation for all the Field H objects. The scale has been normalised relative to the largest and smallest shifts.

colours of light, leading to the observed change in the profile continuum shape. The problem has become apparent in these observations, because they were carried out back-to-back - the magnitude of the drift over the longer observing period is more noticeable than for the normal observation blocks.

Based on the hour angle and the times of the observations, it is possible to calculate precisely the on-sky positions of all the objects in Field H. Figure 2.9 shows the offset between the on-sky position and the fibre position after a 2.5 hr observation. The colours represent the relative size of this shift, e.g. for the blue objects the fibre gets 'left behind' as the field rotates and begins to sample the 'bluer' end of the object, this leads to a negative gradient of the ratio described in Figure 2.7. These simulated shifts clearly correlate well with the observed changes in gradients shown in Figure 2.8.

The results of these problems on the data are not too serious for the work envisaged with the VFTS, where absolute flux levels are not important. The only real impact is that if spectra from different observations need to be stacked to increase the S/N, each spectrum must be normalised and rectified before stacking. This technique was particularly important in the ARGUS observations, where the effects of the atmospheric refraction were clearly visible - adjacent spaxels from the same source often appeared to have very different continuum profiles.

2.7 Scattered light investigation

2.7.1 Background

There are a number of sections throughout this chapter where unexpected features of the FLAMES data have been highlighted. It is believed that these may have arisen due to faint scattering within the instrument, partially caused by the range of magnitudes of objects observed in the VFTS. Despite a number of iterations with the instrument team associated with FLAMES, some of the problems could not be fully explained. A successful proposal was therefore made to visit the VLT and gather numerous calibration frames, with the intention of trying to quantify the observed features.

This section highlights the observed problems in the data, before detailing the calibration data-set that has been obtained and presenting some of the preliminary analysis.

2.7.2 Observed problems in the data

There are three distinct areas where problems have been observed, the first two are known to arise because of scattering and were described previously. The third is a more subtle problem, the origin of which is not completely clear.

2.7.2.1 Direct fibre-to-fibre cross talk

Figure 2.10 shows an extract from a raw FLAMES image. It is clear that there is a great deal of scattering from the brightest target in this field. These problems led to

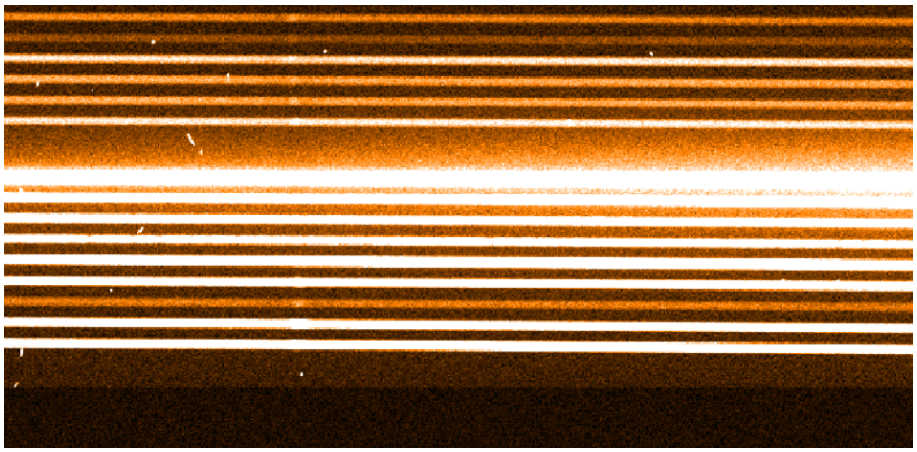

Figure 2.10: An extract from a raw FLAMES frame, showing evidence of the light scattered from the wings of a bright object, contaminating the surrounding region.

the rejection of a number of objects from the survey. This was carried out manually by visual inspection of the raw frames. It would be useful to know the width of the wings of the scattered light: from this the size of the contaminated region could be determined and the appropriate fibres automatically rejected or even corrected.

2.7.3 Modelling of background Levels

As outlined in section 2.4.5, the optimal extraction mode in the Medusa reductions attempts to model the background contribution across the detector. However, for OBs with a range of magnitudes, this is not well described by a polynomial fit and this can lead to over subtraction for some fibres.

A better background model is needed. Perhaps an alternative would be to convolve models of the line profiles with fibre fluxes to create a realistic model of how much erroneous flux is in the centre of adjacent fibres. This could then be subtracted from the appropriate fibres instead of the current broad-brush background model.

2.7.4 Spectral shape variations in ARGUS observations

It was noted that, depending on the type of flat-field being used for the ARGUS observations, unexpected spectral shapes were obtained, as demonstrated by Figure 2.11. The shape of the spectra reduced with the 'attached flat', shows quite a marked 'bend' at around 4200 Å, this is not present in the reduction from the 'normal flat', nor is this shape expected for a stellar spectrum. It was therefore believed the problem is a result of the attached rather than the normal flat.

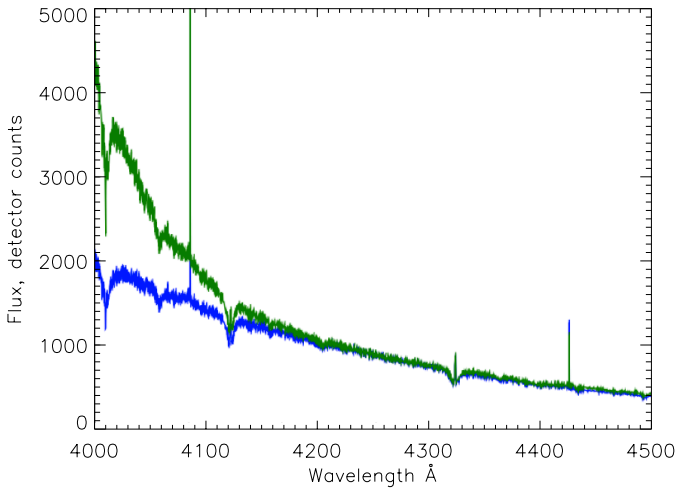

Figure 2.11: The same LR02 ARGUS spaxel reduced using the attached flat (green) and normal flat (blue).

The flat-field correction divides each extracted spectrum by the normalised throughput fibre profile for that particular fibre. The normalised fibre-profile is obtained from the flat-field observation, with its shape dominated by the instrument response from the blue to the red-end of the spectra. The peculiar response seen in the attached flat suggests that, compared to the normal flat, there is a relatively lower flux level in the blue part of the spectra. Thus, some unknown effect in the attached flat is either increasing the red-end flux in the raw flat-field frame, or decreasing the blue-end contribution.

Figure 2.12 shows a comparison of the red-end and blue-end fluxes from raw LR02 frames for both the normal and the attached flat. Both figures show clearly that the red-end flux is higher than the blue-end; this is to be expected as the quantum efficiency of the detector increases towards the red. It can also be seen that, on average, for both types of flat-field the *inter*-fibre values of the red-end are higher than the *in*-fibre values in the blue. It can be assumed therefore that there must be a larger contribution to red-end flux from cross-contamination of adjacent fibres. The blue-end flux does not change a great deal between the normal and the attached flat, but the red-end flux is considerably higher in the attached flat, leading to a much higher level of inter-fibre values. It is therefore proposed, that it is this cross-fibre scattering that leads to the artificially increased flux levels in the red-end attached flats, and subsequently the incorrect flat-field correction seen in Figure 2.11.

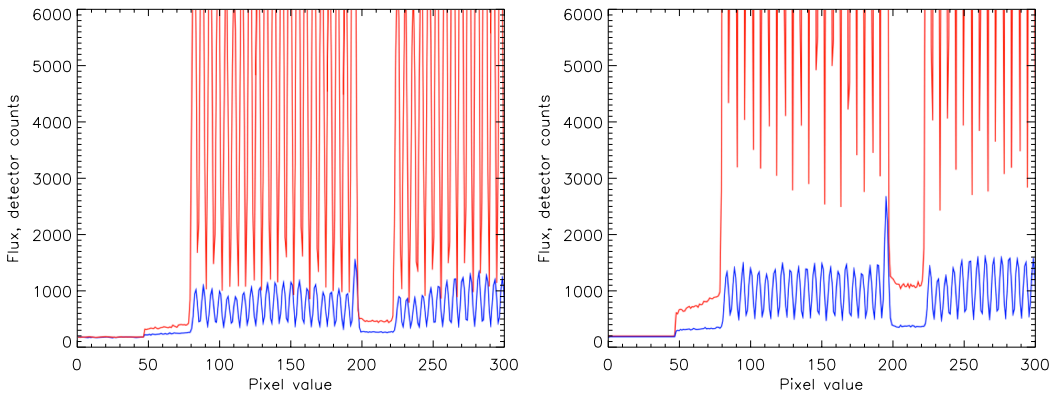

Figure 2.12: A cross-section through the fluxes from different flats: on the left is the normal flats, on the right the attached flats. For both graphs the blue lines are column 500 of the raw CCD image, i.e. the blue-end, while the red lines are column 3500, i.e. the red-end. N.B. The FLAMES spectrograph has a 2k x 4k detector.

2.7.5 Calibration data-set acquired for investigation

To explore the role of scattering a large set of different flat-field frames was acquired. The primary intention of this investigation was to try and characterise the behaviour of a single fibre on the CCD, and from this, see if it would be possible to accurately describe the background level that would be created by a whole range of fibres with varying intensities. The observations obtained are described below.

2.7.6 Medusa flat-fields

All the FLAMES observations contain five fibres that can optionally be used for simultaneous wavelength-calibration. These fibres are distributed evenly across the CCD, and can be illuminated at the start of an observation with the Th-Ar light source, to give a more precise wavelength scaling (this option was not employed in the VFTS). These fibres cannot be disabled for the flat-field frames and consequently, it was not possible to obtain the desired frames illuminated by only one single fibre. Instead, frames were acquired with a single fibre in an isolated portion of the CCD, as far from a simultaneous wavelength-calibration fibre as possible.

Frames were obtained for six different wavelength settings: LR02, LR03, LR08, HR06, HR15N and HR21. These were chosen to give a wide range of wavelengths, but also to include the same settings as the VFTS data. A number of different exposure times were used, allowing the flux in the central fibre to vary from a few thousand counts, up to sixty-thousand, at which point the CCD begins to saturate. Similar observations were also made of two adjacent fibres, this was to give a simple illustration of cross-talk between fibres.

2.7.7 'ARGUS' flat-fields

The ARGUS and Medusa fibres have different aperture sizes, and therefore need to be analysed independently. Ideally the same tests would be performed, but it is not possible to illuminate a single ARGUS fibre without some form of mask placed over the entrance lenslet array, which was not possible. The intention therefore was to obtain flat-fields using the IFU mode in FLAMES (this mode was not used at all in the VFTS). It provides the possibility to place up to 15 individual IFUs at any positions throughout the field (each IFU is comprised of 5 x 4 fibres). The fibres have the same on-sky size as the ARGUS fibres and could therefore serve as a proxy for analysis of these.

Observations were taken using one IFU bundle, again positioned on the detector between two simultaneous wavelength-calibration fibres. This did lead to illumination of twenty fibres, but it was still more informative than a traditional, full flat-field frame.

An attempt was also made to obtain attached flats for a single IFU bundle in the field centre. However, since the attached flats are obtained by illuminating the entire focal plane with light reflected from the Nasmyth shutter, even IFUs 'parked' on the edge of the field were still illuminated. It was unfortunately, therefore, not possible to obtain suitable frames to make the desired comparison between attached flats and normal flats. This therefore prevented further study of the problem highlighted in section 2.7.4.

2.7.8 Preliminary analysis of the Medusa fibres

Figure 2.13 shows the base of cross-sections through a single fibre; this slice was through the red-end of the LR02 observations. It can be seen that as the peak flux in the fibre increases, the width of the wings also increases. These may appear to be extreme cases, as the peak values are very high, but many of emission features for the bright stars in the VFTS data set had tens of thousands of counts. The important factor to consider here is that the distance between adjacent fibres is only ∼15 pixels; this illustrates why contamination for bright objects cannot be neglected.

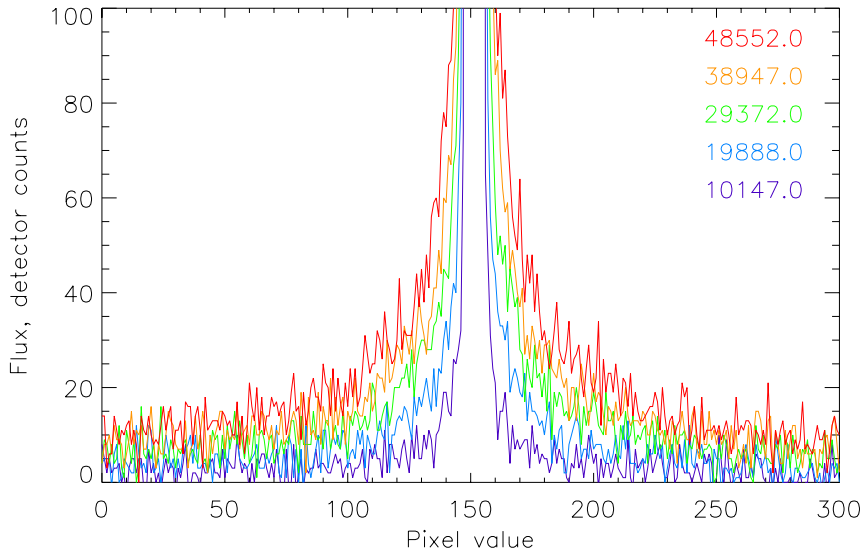

Figure 2.13: Cross-section through the base of a single fibre profile. The different coloured lines represent the same fibre observed with different exposure times. The peak fibre-value is shown in the corresponding colour for each of the observations.

Attempts were made to model the single fibre using a number of different known profile shapes. While these wings may appear severe in these plots, they were still a small fraction of the peak intensity. It was therefore found that no one function could accurately reproduce both the peak central value and these wings.

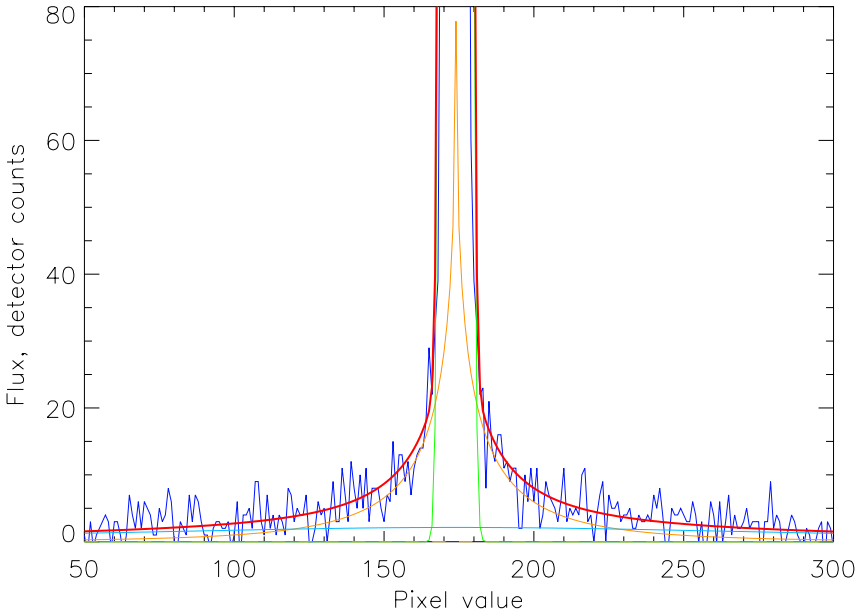

Figure 2.14: The three-component model used to fit an LR02 fibre-profile. The dark blue represents the original data, while the final fit is shown in red. The Gaussian core component is shown in green, the wing function in orange and the Lorentzian term in light blue.

Figure 2.14 shows a technique that was found to successfully model the fibre for parts of the LR02 frames. The fit was comprised of three different profiles, each of which described a different aspect of the fibre profile:

1. **Gaussian function:** the core flux of the fibre was well-described by a Gaussian function. This was used to define the central pixel value of all the profiles. Note, that in this work, less concern was paid to the quality of the fit to the peak value compared to the fit for the base.

2. **'Wing' function:** An ad hoc profile was defined to match the shape of the wings, this is given by:

$$f(x) = aP_0 \exp\left(-\frac{1}{2}\sqrt{\frac{|x - x_0|}{\sigma}}\right) \tag{2.4}$$

where x is the pixel number, x_0 is the pixel number of the fibre centre, a is a scaling factor to the peak intensity, P_0, and σ is the 'width' of the profile. Appropriate values were found for a and σ through fitting a wide range of fibre profiles with different peak intensities. The modulus component of this function

creates an unphysical sharp point to the profile centre, but it does accurately trace the broad shape of the wings.

3. **Lorentzian function:** It was found that the presence of any fibre introduced a low level increase in the background flux. This was low and broad, as it extended across almost the width of the whole CCD, but was only of order a few counts. This was best described by a broad Lorentzian function.

Using this three component model, the next step was to attempt to recreate the real data from a VFTS observation. An example fit to an LR02 observation is shown in Figure 2.15. Each individual fibre profile was created only through knowledge of the peak value; all the other fitting parameters were determined through the previous analysis of the single fibre frames. It can be seen that the model re-creates the data profile relatively well. There are a few regions where it could potentially be improved through additional adjustments of the fitting parameters beyond those automatically derived in relation to the peak value.

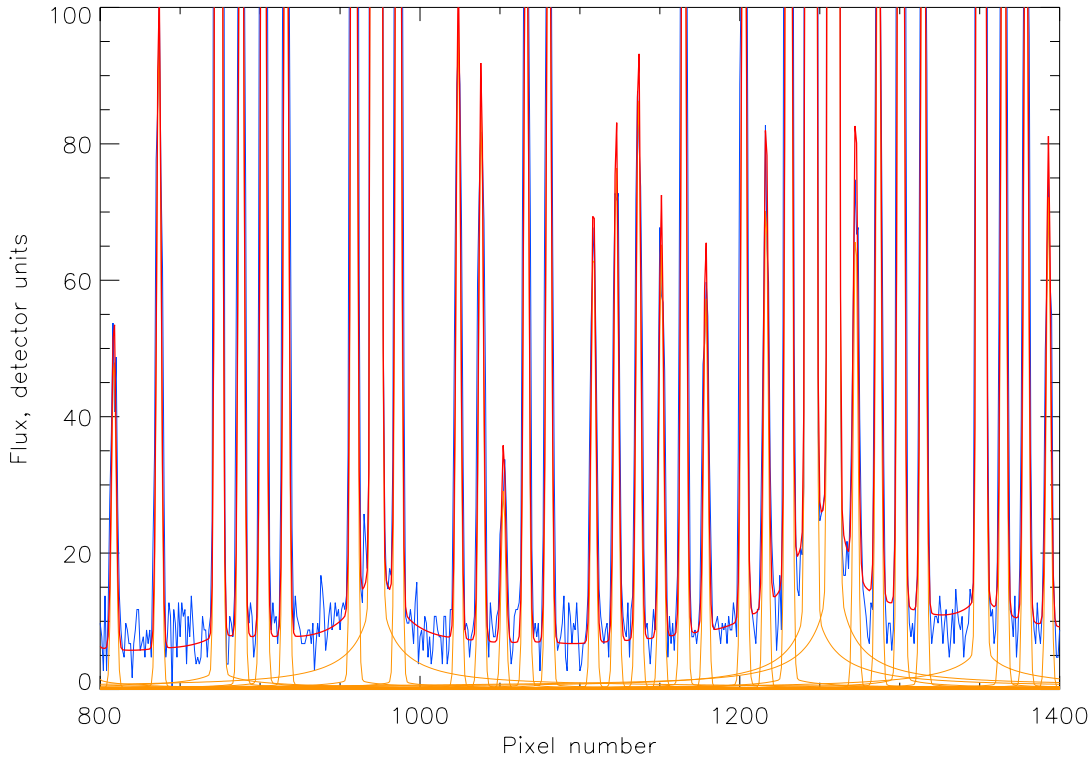

Figure 2.15: The blue line shows the cross-section through the base of a number of fibres for an LR02 observation from VFTS. The red line shows the fit to the data. This is formed from the summation of all the individual fibre profiles, which are shown in orange.

2.7.9 Discussion

It is possible that, for the region considered, a background model could be described which would be more accurate than that used in the optimal extraction of Medusa data. This could significantly aid the extraction of faint objects and sky fibres. Attempts could even be made to correct for contamination from bright objects, as estimates of the contribution from surrounding objects could now be more accurately estimated.

There are, however, strong caveats to consider. This fitting model has been derived only for the central regions of the LR02 frames. It was found that for the last ∼500 pixels at both ends of the detector, the scattering effect was different and the scaling laws described above could not be used. A different model would have to be determined for these regions. It was also found that the derived scaling values for a particular peak value are not successful for the LR03 frames or for the higher resolution settings. This suggests there is a wavelength dependence to the scattering which also must be accounted for. It would have to be determined if the variation with wavelength was a continuous, predictable pattern, or if it varied between the different grating settings. If the latter is true, then considerably more data than that obtained thus far would be required.

2.7.10 Conclusion

This brief investigation has shown that the effects of scattering are significant and that, at a low level, the wings of bright fibres can extend across many fibres. It has also shown that, in principle, it may be possible to construct an accurate 2d model of the scattering effects across the full extent of the CCD. However, to do this would require an extremely broad study, looking at a very large range of observations, paying particular attention to the edge effects of the CCD.

2.8 Early science results from the VFTS

Much of the information detailed in the first half of this chapter was published as part of the first paper in the VFTS series (Evans et al. 2011b). Many interesting results are starting to emerge from this large data-set and a brief summary of some of the highlights follows.

2.8.1 Intriguing objects

Whilst the main science-drivers behind the VFTS originate from the new insights that can be drawn from such a large data-set, some of the first papers have been on bizarre

and unexpected individual objects. One such case was the observation that the massive star R139 was actually a binary system comprised of two evolved Of supergiants (Taylor et al. 2011) - this result is described in the next chapter.

The late O-type star VFTS 102 has been shown to be rotating at the near-critical velocity of $\sim$600 kms^{-1} (Dufton et al. 2011). This alone would be fascinating as very fast rotation could lead to such efficient mixing of the star that it evolves homogeneously. However, VFTS 102 has caused added speculation as it is spatially very close to the rapid rotating X-ray pulsar J0537-6910. There is evidence that the two objects are moving away from each other - is it possible that these are from the same binary system, kicked apart during the supernova which formed the pulsar? If so, the rapid rotation of each star could be attributed to spin-up during accretion.

A new W-R star, VFTS 682, has been discovered, which is estimated to have a mass of $\sim 150 M_{\odot}$ (Bestenlehner et al. 2011). With such a large mass such a star would be expected to lie near the core of R136, however it is 29 pc away. The star must either be a runaway in the plane of the sky or, if not, then its large mass and relative isolation from the core challenge some star-formation theories.

2.8.2 Binary fraction of 30 Doradus

Sana et al. (2012a) calculate that the observed binary fraction of the O-type star population in 30 Doradus is 0.35 ± 0.03. Through a Monte Carlo method they estimate that the intrinsic binary fraction is 0.51 ± 0.04, which is in keeping with that observed for other Galactic clusters (Sana & Evans 2011). They find no evidence of statistically significant variation either spatially or between spectral types. The period-distribution appears to favour more short-period systems than that expected by the commonly used Öpik law - this again strengthens the argument that binary interaction is an important aspect of the lives of many stars (de Mink et al. 2011).

Due to the size of the sample, the analysis of the B-type stars has been undertaken independently, but early results show a similar binary fraction of these objects to their larger cousins (Dunstall et al. 2012).

2.8.3 Dynamical mass estimates

The ARGUS data, which probe the inner regions of the R136 cluster, have been used to study the dynamics of these stars. Any stars that showed signs of radial velocity variation, suggesting binarity, were rejected and the remaining 'single' stars were used to infer a velocity dispersion of $\sim$6 kms^{-1} (Hénault-Brunet et al. 2012a). This is an upper limit, as it may still include undetected binaries and yet the value is similar to that expected for a system in virial equilibrium. This suggests that the R136 cluster is

dynamically stable, and early cluster evolutionary stages, such as gas-expulsion, have not disrupted the system. An interesting additional measurement from this work, was the observation that R136 appears to be rotating slowly at $\sim$3 kms^{-1} (Hénault-Brunet et al. 2012b).

2.8.4 Isolated star formation?

As was outlined in the introduction, the formation-mechanism for massive stars is not well understood. One aspect of this is whether such stars can form in isolation, i.e. independently of a surrounding cluster. Bressert et al. (2012) report results from the VFTS of 15 stars which are earlier than O7, and appear to lie away from the central region. The stars have been selected as they do not show any evidence of binarity or being runaways along the line-of-sight, and their sight-lines are associated with gaseous filaments in the surrounding ISM. It has been suggested that these stars could therefore be examples of 'isolated' high-mass star formation.

The possibility that these stars are runaways in the plane of the sky from more dense regions cannot currently be ruled out. *HST*[1] time has been obtained to observe a large part of 30 Doradus with WFC3 over a number of years, with the intention of determining the proper motions of many stars, including the intriguing candidates of Bressert et al. (2012).

[1] P.I. Lennon, D. (ESA/STScI)

Chapter 3

R139 revealed as a massive binary

Two stars keep not their motion in one sphere.

William Shakespeare, Henry IV: Part 1

3.1 Author's note

This chapter details the discovery that the massive 'star' R139, is in fact two massive stars locked in a relatively wide binary orbit. The results were presented in Taylor et al. (2011). A fuller discussion of the analysis methods is presented here, with further interpretation given to the evolutionary conundrum which R139 now represents.

3.2 Background

Due to its high population of massive stars, 30 Doradus has been the site of numerous surveys searching for W-R stars. These massive stars exhibit extremely strong winds which effectively strip the star of its envelope, exposing the core. Within these winds strong emission lines form, thus giving W-R spectra very distinctive features. For a fuller discussion of W-R stars see the review by Crowther (2007).

Feast et al. (1960) carried out one of the earliest surveys of bright objects in the LMC, many of which turned out to be W-R stars. Each object was labelled in the R'x' running order hence the name R139 and also its more famous cousin, R136 - the region's core (see Figure 3.1). It has since been found that R136 hosts a number of extremely massive young stars, which exhibit strong emission lines and therefore resemble W-R stars (Crowther et al. 2010). Equally, there was debate on whether R139 was a W-R star by Walborn & Blades (1997), who suggested it was a late O-type star.

With a V-band magnitude of 12.04, Walborn & Blades (1997) also proposed that R139 might be the most massive star in the cluster outside of the central region. It

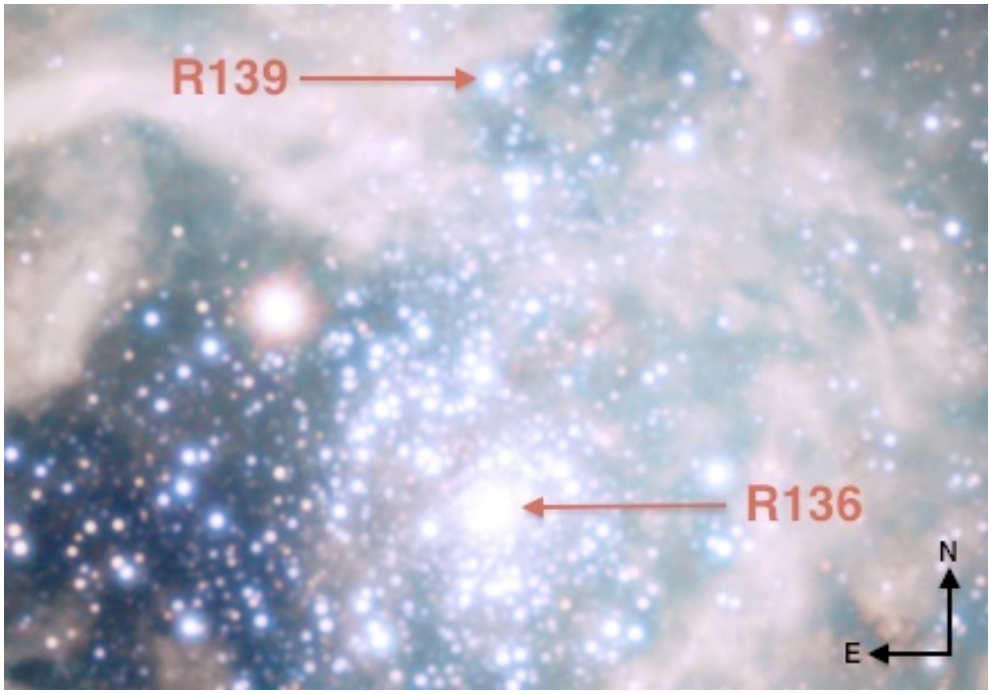

Figure 3.1: R139 shown relative to the central cluster R136, the separation in the plane of the sky is 16 pc. The image is a combination of the YJK images taken with VISTA, as part of the VMC Survey.

has been included in a number of other W-R surveys, where each has added its own moniker for the object: Brey 86 (Breysacher 1981), Parker 952 (Parker 1993), BAT99-107 (Breysacher et al. 1999), Selman 2 (Selman et al. 1999) and, most recently, VFTS 527 from this study. The VFTS study has finally been able to confirm that R139 is in fact not a W-R star at all, and although two stars, they are nearer to the classification of Walborn & Blades (1997).

Multi-epoch spectroscopy of R139 was obtained as part of the campaign by Moffat (1989). His mean radial velocity from observations in 1982 showed an offset of $\sim$100 kms^{-1} compared to the mean velocity from earlier data. He noted R139 as a single-lined binary, with a tentative period of 52.7 d adopted from a number of possible fits to the data. In contrast Schnurr et al. (2008) presented spectroscopy of R139 from three observing seasons (spanning 2001 to 2003). While noting that the system displayed a 'slightly variable radial velocity', it was concluded that R139 was single, citing the relatively large uncertainties in Moffat's past work for the conflicting scenarios. From the VFTS data is has been possible to show that R139 is a massive binary with a high eccentricity, and it is thus not surprising that Moffat and Schnurr drew contrasting opinions as, unless viewed relatively near to periastron passage, there are long periods when R139 would not show any significant shift in radial velocity.

3.3 Observations

R139 was observed as part of the VFTS within the field G fibre configuration and has the catalogue number VFTS 527. The data were reduced in the standard way, as discussed in chapter 2. As it is a bright source, the signal-to-noise was extremely high, of order 150 per observation, the pairs of back-to-back observations were not co-added, but were treated as individual exposures, thus maximising the number of observations.

R139 was quickly identified as a binary system merely through visual inspection of the data; it is a clear spectroscopic binary with two well-resolved components. As discussed below, it was not possible to confidently determine the orbital period of R139 from the VFTS data alone. The survey was always intended as a means to identify variability, rather than characterise orbits - a far greater number of observations would have been required to do this. Additional observations of R139 were therefore obtained from a number of different facilities; all the observations are summarised in Table 3.1. In the table an 'epoch' has been assigned to each observation, or in the case of back-to-back observations, a single number has been given to each pair of observations.

A single follow-up observation was obtained on the 6.5m Magellan Clay Telescope with the MagE instrument, followed by three more using X-Shooter on the VLT. These latter observations revealed the greatest velocity separation of components yet seen, and showed significant changes over the course of a single week - indicating a highly eccentric orbit. Finally, observations were obtained with FEROS on the MPG/ESO 2.2m telescope at La Silla[1]. These finally allowed confirmation of the orbital period. The tale of R139 highlights the need for a large number of observations to accurately determine orbital parameters if the system is eccentric.

All these follow-up observations are from instruments with a much wider spectral range than FLAMES, providing coverage across the entire visible spectrum and, in the case of X-Shooter, also into the infrared. This additional wavelength coverage has yet to be fully exploited, but will be useful for later studies which look in greater detail at the two components of this system. The data were all reduced using the standard reduction techniques associated with each instrument. No attempt was made to correct for the sky with these new observations - for the purposes of the radial velocity analysis and considering the signal-to-noise, it was not necessary. Each additional exposure yielded a typical signal-to-noise ratios of order 150 - although the FEROS data had to be degraded to $R \sim 9000$ to achieve this.

Figure 3.2 shows a montage of normalised spectra for a number of these observations which clearly illustrate how many of R139's prominent emission and absorption features separate into two distinct and similar components. This can be best seen in epoch 16,

[1]FEROS observations obtained as part of programme 086.D-0997.

which shows the maximum observed separation. Note that this was an additional frame observed with X-Shooter, however, the separation was clearly visible in the original FLAMES spectra, e.g. epochs 7 and 10.

Table 3.1: Observational epochs for R139 detailing: the instrument used, the resolving power (R), the date, and the time elapsed since the first epoch (Δ HJD). The FLAMES observations were comprised of back-to-back observations, so only the mid-exposure HJD is given. The resolving power quoted for X-Shooter is that of the UV-arm only, which overlaps the LR02-03 regions of the FLAMES data.

Epoch	Instrument / Setting	R	HJD +2400000	Δ HJD
1	FLAMES / LR02	7,000	54748.7769	-
2	FLAMES / LR02		54748.8228	0.046
3	FLAMES / LR02		54749.7233	0.946
4	FLAMES / HR15N	16,000	54749.7726	0.996
5	FLAMES / LR03	8,500	54755.6882	6.911
6	FLAMES / HR15N		54810.6697	61.893
7	FLAMES / LR03		54810.7374	61.961
8	FLAMES / LR03		54810.7808	62.004
9	FLAMES / LR03		54810.8357	62.059
10	FLAMES / LR02		54837.6332	88.856
11	FLAMES / LR02		54868.5569	119.780
12	FLAMES / LR02		55112.8129	364.036
13	MagE / 1" slit	4,500	55527.8017	779.025
14	X-Shooter / 0.5" slit	9,100	55580.5477	831.771
15	X-Shooter		55584.7076	835.931
16	X-Shooter		55588.6922	839.915
17	FEROS	48,000	55604.6909	855.936
18	FEROS		55605.5613	856.739

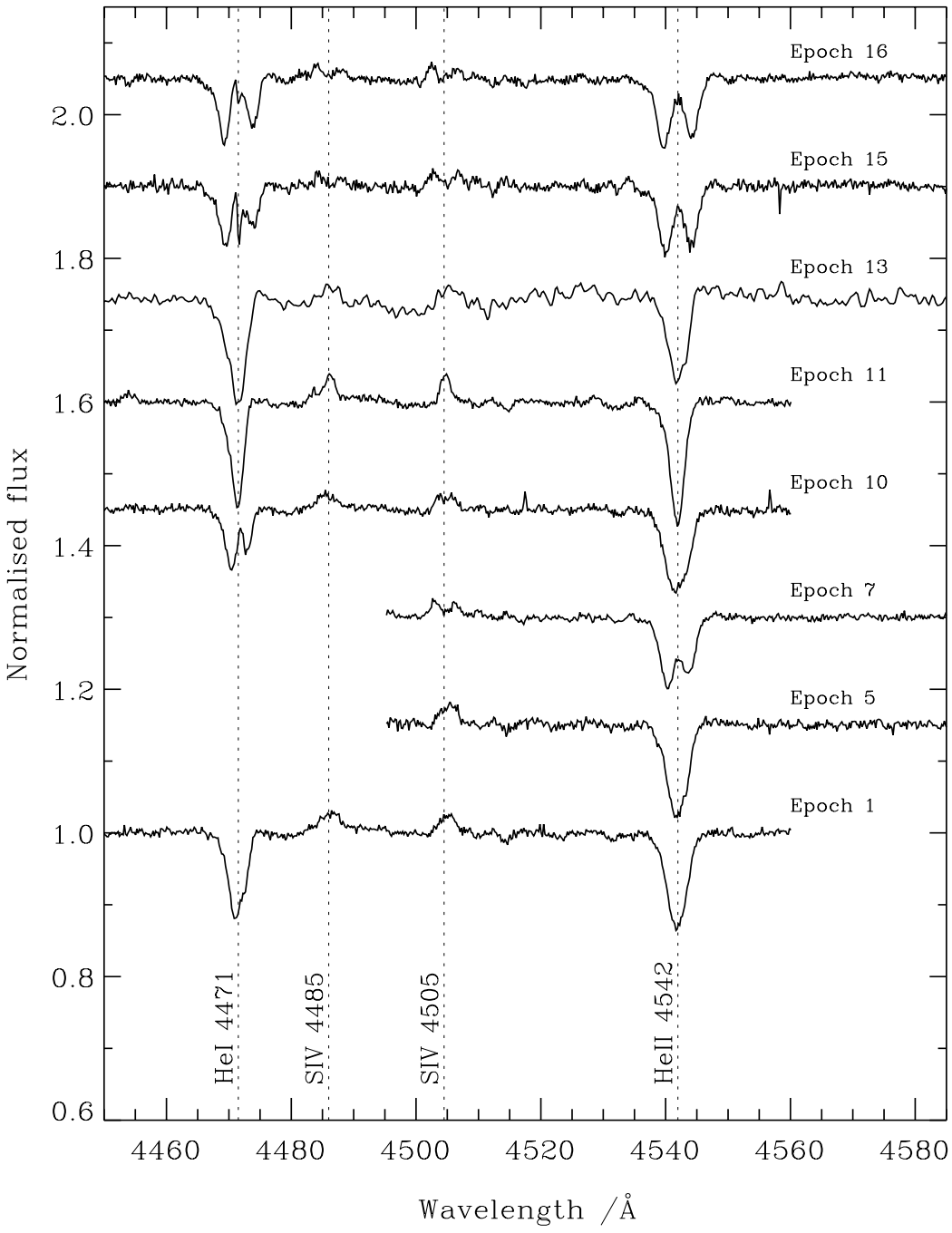

Figure 3.2: Normalised spectra of R139 for a number of different epochs, showing clearly the separation of spectral features. This region covers the overlap of the LR02 and LR03 FLAMES settings. Epochs #11 and #16 show the minimum and maximum observed separation, respectively. The He I λ4471 line profile in epoch #16 suffers from a slight nebular over-subtraction but does not prevent clear identification of the components.

3.4 Results

3.4.1 Spectral classification

Feast et al. (1960) described the spectrum of R139 as exhibiting 'O-type absorption plus weak W emission (4686, 4640)'. Walborn & Blades (1997) argued that R139 has very strong Of emission features, classifying it as O7 Iafp, while Schnurr et al. (2008b) adopted the spectral type WN9h::a.

Figure 3.3 shows a normalised spectrum of R139 in the oft-used λ4000 - 4900Å diagnostic region; this is a merger of the LR02 and LR03 frames. R139 is seen to exhibit emission in N III λ4643, He II λ4686 and H β. Since these features are the result of the superposition from two stars, when observed at lower resolution, this would have falsely suggested enhanced emission or broadening of the lines. It is likely this led to the suggestion that R139 is a late-type W-R.

There has historically been some debate about the naming of objects with both emission and absorption features. Indeed, Walborn (1982) introduced the naming system Ofpe/WN9 for such objects. Although, it should be noted that this was to describe the uncertainty in their classification, not as a description of an object which straddles the divide between O-type and W-R stars, such as O3 If*/WN stars. In attempt to bring order to these objects, Crowther & Walborn (2011) discuss a number of observable trends in the spectra and, from these, impose certain criteria. They state that for low-ionisation stars, where N IV λ4058 is absent, if He I λ4471 is in absorption,

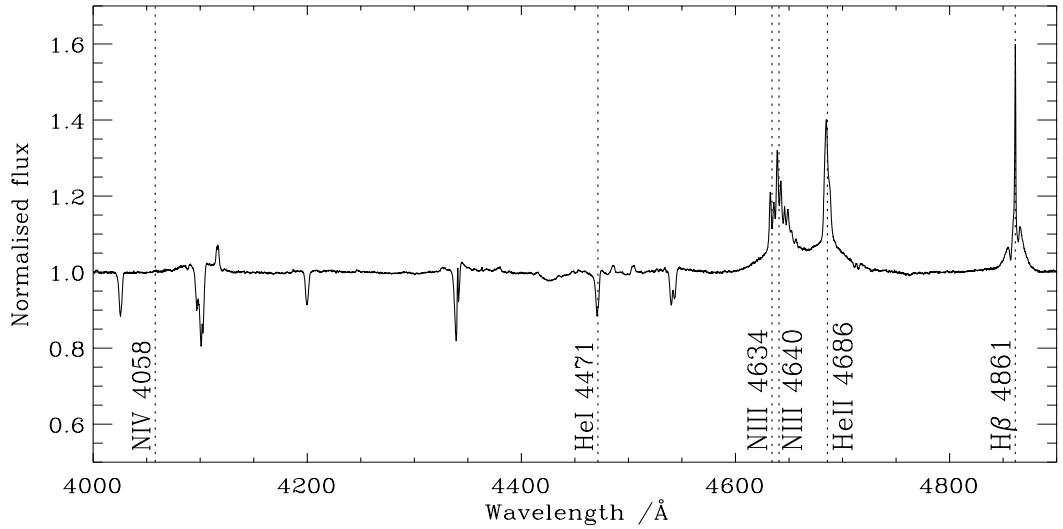

Figure 3.3: Normalised spectra of R139 between λ4000 - 4900. This region is used to determine what types of stars are present - the absorption lines are indicative of O-type stars.

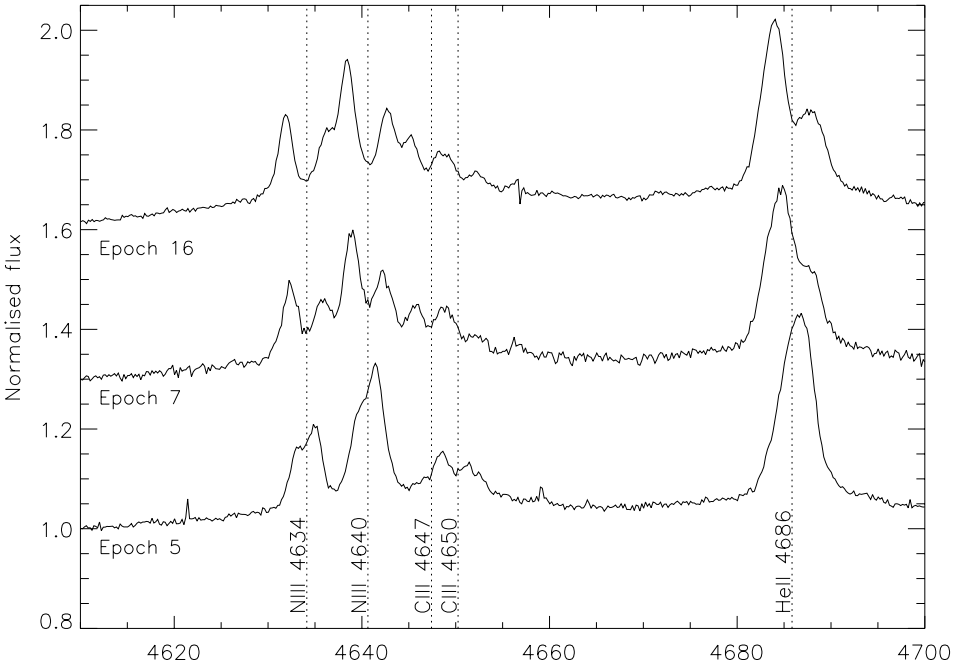

Figure 3.4: Normalised spectra showing the complex N III and C III emission region. Both of the N III emission lines and the He II λ4686 emission are comprised of two un-equal components, the stronger of which is associated with the primary. The C III emission lines show no separation, but exhibit radial velocity shifts in the same direction as the primary.

then the star should be treated as an O star. As can be seen in Figure 3.3, this is indeed the case for R139.

The epochs that display well-separated components have allowed a precise classification for each of the stars. The system consists of a massive, luminous primary, which is an O6.5 Iafc supergiant, and a slightly less luminous O6 Iaf companion. These spectral types are determined from visual inspection of the He II / He I absorption line ratios between λ4200 / λ4026 and also between λ4542 / λ4471, the latter of which can be seen in Figure 3.2.

The 'f' suffix in the classifications indicate that the stars show N III λ4634-40 emission, while the 'a' indicates that the stars are luminous supergiants. The 'c' classification of the primary arises from emission of C III λ4647 and λ4650-4652. This relatively rare feature led to the recent introduction of the Ofc category in the morphological framework used to classify O-type spectra (Walborn et al. 2010). Figure 3.4 clearly illustrates that the N III emission lines separate into two distinct components, whereas the two C III emission lines show no evidence of separation, but merely shift between epochs in the same sense as the primary. The Ofc feature

has previously been associated with the O5 spectral type (Walborn et al. 2010); this therefore, is an interesting example of the phenomenon in a later-type star, albeit in the LMC.

Where possible, the relative shift of the components was identified through the C III emission and also He I λ4922 emission, which are only present in the primary. In the LR02 observations, the Si IV λ4116 emission line was used as the main diagnostic for the relative shift of the components. The Struve-Sahade effect (e.g. Linder et al. 2007) has been seen to alter the relative strength of emission/absorption lines in a binary system as the components move towards and away from the observer. However, this effect is strongest for objects which are close together and so can likely be neglected in R139 given its relatively long period.

3.4.2 Radial velocity analysis and lower mass limits

A global χ^2 fitting approach was used to determine the radial velocity shifts of the different epochs. This technique fits double Gaussian profiles to a number of lines: He I λ4026, Si IV λ4116, He II λ4200, S IV λ4485, S IV λ4505, He II λ4542, He II λ 4686, and He I λ4922. This therefore avoided any of the lines which had shown evidence of nebula contamination: Hδ, Hγ and He I λ4471.

Examples of the fits to the LR03 data are shown in Figure 3.5 for epochs 5 and 7. The global-fitting method means that the radial velocity shift for all the lines are fitted at the same time. This has the advantage that a single profile shape is therefore used for all the fits, which is especially advantageous when the separation between the components is low, as is seen in the right-hand panel of Figure 3.5. This approach improves the disentangling of the contribution from each star for the data sets with limited phase coverage, but it does ignore the possibility of line-profile variations. The formal errors on the measurements for each component are a few km s^{-1}.

Figure 3.6 shows the measured velocities for the two components, indicated by the closed and open circles. Since the observations span a long time period, and therefore originate from different orbital cycles, they have been plotted here relative to their orbital phase, ϕ. The period was calculated through Fourier analysis of the measured radial velocity shifts using the methods of Gosset et al. (2001). The dominant signal indicated a period of 153.9 days; the formal errors on this are $\pm$ 0.1 days, but since this is a Fourier analysis, the real error could be larger. The corresponding orbital solution over-plotted on the data, was determined through the methods of Sana et al. (2006a), where the measured velocities for each component are solved as if each system were an SB1, using the well-established techniques of Wolfe et al. (1967). A full list of the fitted orbital parameters is given in Table 4.2. For a relatively eccentric system such as

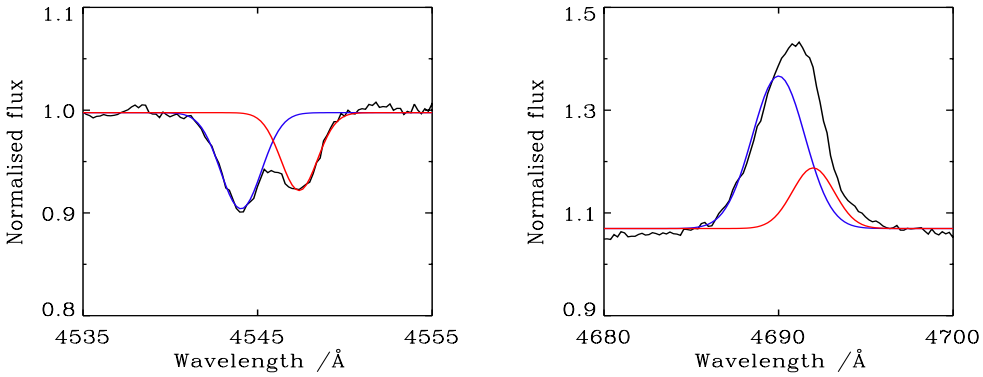

Figure 3.5: Examples of fits to the LR03 data using two independent Gaussian profiles. The left-hand side shows He II λ4542 for the well-separated epoch 7, while the right-hand side shows the poorly-separated emission feature of He II λ 4686 from epoch 5.

this, the fitting procedure is sensitive to the behaviour of the system around periastron: additional observations of this stage in the orbit would help to confirm these results.

The mass ratio of the two components in the system can be found from the ratio of the primary and secondary radial velocities: since the observed velocities are independent of any kind of system modelling, this is a direct measurement. For R139 the mass ratio is found to be $M_1/M_2 = 1.20 \pm 0.05$. The inclination of the system cannot be determined without an eclipse, therefore, it is only possible to put lower limits on the masses of the two components, these are found to be: $M_1 \sin^3 i = 78 \pm 8\,M_\odot$ and $M_2 \sin^3 i = 66 \pm 7\,M_\odot$. This suggests that R139 is the most massive evolved O-star binary system yet discovered.

Table 3.2: The parameters associated with the best-fit orbital solution. The errors quoted are the formal errors on the best-fit from the Fourier analysis, and therefore may not be fully representative of the uncertainty in the parameter values.

Property	Best-fit value
Period, P	153.9 ± 0.1 days
Eccentricity, e	0.46 ± 0.02
Argument of periastron, ω	106.9 ± 5.0 deg
Date of $\phi = 0$ (HJD - 2450000), T_0	6035.9 ± 1.3 days
Maximum velocity of primary, K1	$107.8 \pm 3.8\,\mathrm{km\,s^{-1}}$
Maximum velocity of secondary, K2	$127.0 \pm 4.5\,\mathrm{km\,s^{-1}}$
Projected semi-major axis for primary, $a_1 \sin i$	$290.6 \pm 10.8\,R_\odot$
Projected semi-major axis for secondary, $a_2 \sin i$	$342.3 \pm 12.8\,R_\odot$

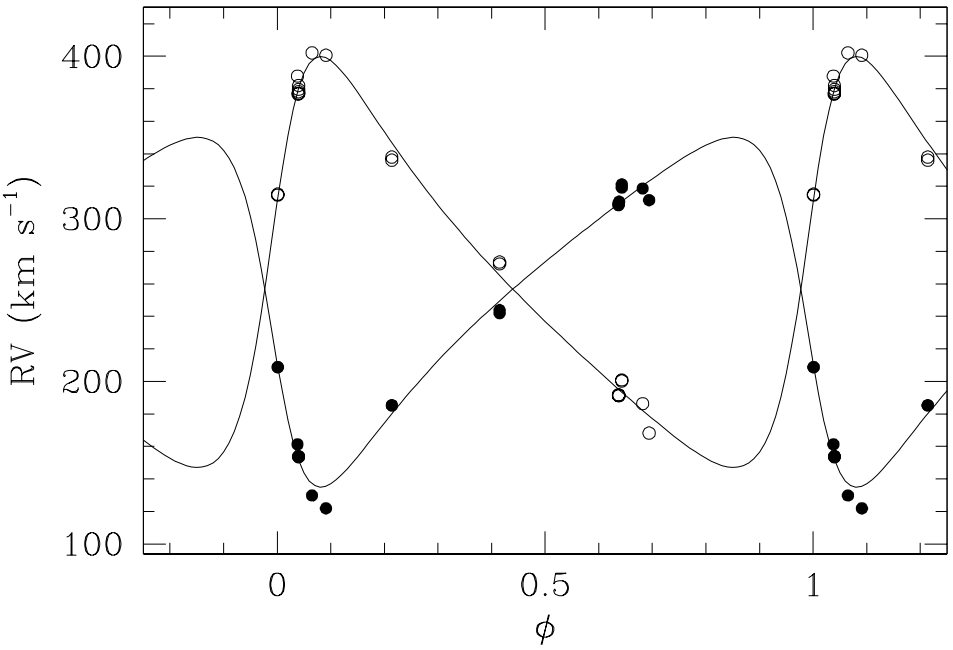

Figure 3.6: Best-fit orbital solution from the measured radial velocities of the components, indicating a 153.9 day orbit. The closed circles denote the velocities of the primary and the open circles the secondary.

3.4.3 The luminosity of R139

To estimate the intrinsic luminosity of the system, it is first necessary to determine the temperature of the star. This has historically been done through analysis of the line ratios of features in the spectrum - indeed, stellar classification is a primitive form of temperature assignment. The more sophisticated method now available is to use model atmospheres to simulate the observed spectrum of the star. To model R139, CMFGEN was used (Hillier & Miller 1998); this is a non-LTE (local thermodynamic equilibrium) radiative transfer code that includes spherical outflow of material and also the effects of line blanketing from the lines of many species.

For R139, the simulation was performed on an epoch with minimal separation of the components, as if the system consisted of only one star; this removed any uncertainty from disentangling the spectra. Metal abundances were adopted from Asplund et al. (2005), with appropriate scaling for the LMC. CMFGEN models were used to constrain the effective temperature ($T_{\rm eff}$) consistent with certain key spectral features:

1. the absence of N IV λ4058 emission;
2. the presence of N III λ4640 emission;
3. the intensity of the He I λ4471 absorption.

The models gave an estimated $T_{\rm eff}$ for both components of 34 ± 2 kK.

Using this temperature estimate, the luminosity can be determined by matching the expected spectral energy profile against photometric data. Optical and infrared data were used from Selman et al. (1999) and 2MASS (Skrutskie et al. 2006), respectively. Any extinction that would affect the photometric values must be corrected for. The visual extinction $A_V = R \times E(B-V)$ was determined for each model based on the relation $R = 1.12 \times E(V-K)/E(B-V) + 0.02$ from Fitzpatrick (1999). The resulting luminosity for the composite system is $\log(L/L_\odot) = 6.4 \pm 0.1$ (with R in the range 3.4–3.9). The luminosity of each star can be found from the mass ratio and mass-luminosity relationship $L \propto M^\alpha$, where for massive stars $\alpha = 2.5$. The luminosities are found to be $\log(L/L_\odot) = 6.1$ and $\log(L/L_\odot) = 5.9$.

3.5 Photometric variability

R139 was identified as showing slight photometric variability by Feitzinger & Isserstedt (1983). They observed a 0.3 magnitude dimming in the V band over a 25 day period. However, this was from only three observations taken with a wide (18") aperture.

An additional component of the VFTS has been photometric follow-up of the 30 Doradus region with the 2 m Faulkes Telescope South (FTS). The FTS is an extremely useful outreach project; it is a research-quality telescope in Australia, which is run remotely by school groups, who carry out the observations requested by astronomers. The FTS camera has a $4.7' \times 4.7'$ field-of-view, and was used to monitor seven fields in the 30 Doradus region, using Bessel B and V, SDSS i', and Pan-STARRS Y filters. The default mode of the camera is 2×2 binning of the CCD pixels, giving an effective pixel-scale on the sky of 0.278". The central FTS pointing included R139, providing an opportunity to investigate its photometric variability.

Fifty-four epochs of the relevant field were obtained, spanning dates throughout 2009. The seeing ranged from to 0.9" to 3.1", with a mean value of 1.5". The FTS data are reduced automatically following observations, but are not calibrated photometrically. The APPPHOT package in IRAF was used to obtain instrumental V-band magnitudes of R139 from aperture photometry. Five 'check' stars of similar brightness were selected from the frames for comparison: R133, R137, R138, Mk 11, and R146[1]. From these, differential residuals (ΔV) were calculated for R139 compared to the mean magnitude of the check star for each epoch (see equation 3.1). The deviation on these residuals was found to be consistent with that calculated between the check stars themselves, indicating that R139 shows no photometric variability. These results

[1] VFTS 333, 431, 424, 641, and 695, respectively.

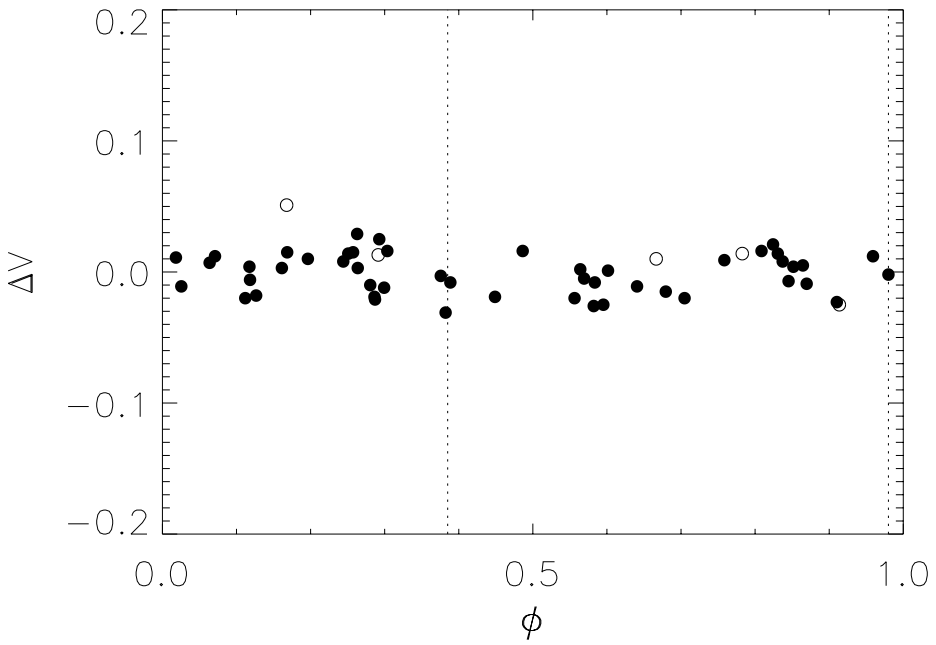

Figure 3.7: Differential V-band residuals for R139 compared to the mean of the five check stars, phased to the 153.9 day orbit. Open circles denote the five epochs when the seeing was in excess of 2."0. The dotted lines indicate the expected mid-point of any possible eclipses: $\phi = 0.39$ and 0.98 for the eclipses near apastron and periastron respectively.

are shown in Figure 3.7, where the observations have been phased to the 153.9 day orbit.

$$\Delta V \;=\; (V_n^{\mathrm{R139}} \;-\; V_n^{\mathrm{Chk}}) - \frac{1}{54}\sum_{n=1}^{54}(V_n^{\mathrm{R139}} \;-\; V_n^{\mathrm{Chk}}) \tag{3.1}$$

Although the photometry obtained with FTS gives relatively good coverage of the full period, there are some gaps. The timings and durations of the possible eclipses were therefore calculated through geometrical arguments. This was done by assuming that the stellar radii could be estimated from the luminosity, the temperature and the Stephan-Boltzmann law; this gave radii estimates of $30\,\mathrm{R}_\odot$ and $24\,\mathrm{R}_\odot$.

Figure 3.8 shows the expected luminosity profile for R139 for various different inclinations, i, of the binary system. The expected timings of the eclipses near apastron and periastron are found to be $\phi = 0.39$ and 0.98 respectively. This model has assumed the stars are at equal temperatures and consequently the depths of the eclipses if $i = 90^\circ$ are the same. It suggests that the maximum eclipses that could occur would lead to a 0.35 drop in magnitude. The positions of the eclipses are also overlaid on Figure 3.7,

but this shows no sign of variation at these points, even though observations were taken near to the possible events.

If $i < 85°$ then the eclipse near apastron will not be visible, and below 80° neither would be visible. Since no eclipses are seen, this could tentatively be used to constrain the lower limits on the stellar masses further, although the correction would not be significant. Also it would be desirable to conduct a more thorough search for an eclipse using the above estimates of their timings. An attempt was made to do this using the FTS in April 2012 to observe the periastron eclipse, but unfortunately only one observation was obtained due to poor weather.

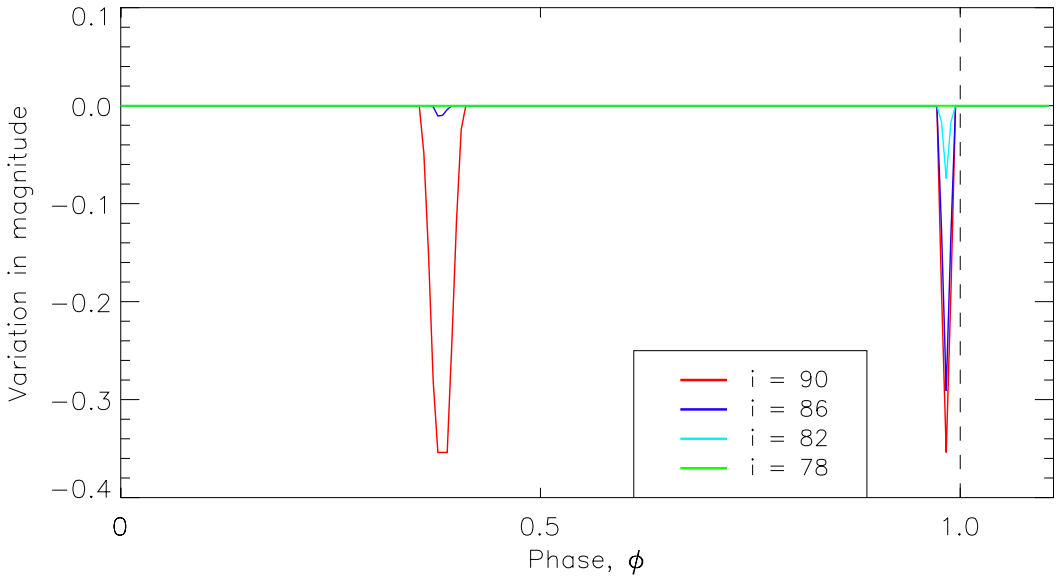

Figure 3.8: Predicted light curves for R139, at different inclinations.

3.6 X-rays

O stars are known to have intrinsic X-ray emission. Its origin is not entirely understood, but it is believed to originate in shocks that occur between different density regions of the star's wind. The X-ray luminosity and the bolometric luminosity of massive O stars are linked by the relationship $L_X \approx 10^{-6.9} L_{bol}$ (Sana et al. 2006b). Therefore, with a luminosity of $\log(L/L_\odot) = 6.4$ for the combined system, an X-ray luminosity of $1.2 \times 10^{33}\,\mathrm{erg\,s^{-1}}$ would be expected.

R139 was detected by Portegies Zwart et al. (2002) as an X-ray source in the 30 Doradus field observed with the Advanced CCD Imaging Spectrometer on the *Chandra X-Ray Observatory*. Further analysis of the *Chandra* data was carried out by Townsley

et al. (2006) and more recently by Guerrero & Chu (2008). These studies found R139 to have a relatively low X-ray luminosity compared to W-R stars in the study. Guerrero & Chu (2008) also considered data from the Röntgen Satellite (*ROSAT*), but it did not detect R139 due to its lower sensitivity.

Guerrero measured a luminosity for R139 of $2.7 \times 10^{33}\,\mathrm{erg\,s^{-1}}$ in the 0.5 - 7.0keV range. This is slightly higher than that expected solely for the intrinsic O star emission estimated above - even considering the possible 25% error in the detected X-ray count rate. This small excess emission might be associated with X-rays generated through the interaction of the system's stellar winds. There is no evidence, however, for phase-dependent line profile variations, which would have also suggested colliding winds; again observations near to periastron would be of particular interest.

3.7 Evolutionary masses

Figure 3.9 shows evolutionary tracks for a range of stellar masses from Friedrich et al. (in prep.), computed analogously to the models of Brott et al. (2011). The tracks indicate how a star starting with the initial mass shown on the left would evolve with time, moving to cooler temperatures along the track. For instance, without knowledge that R139 is a binary, its current temperature and luminosity would place it on the diagram at the position indicated by the red circle, i.e. it would be inferred to have started life with an initial mass a little over $125 M_{\odot}$ - note that due to mass loss, the current mass would be lower than this.

Evolutionary models were run to try and fit the luminosity and temperature of both the stars. These are based on a χ^2 fitting method to the four known observed system parameters: the luminosity, the mass ratio and the temperatures of the two stars. Two stars are evolved until they most closely resemble the observed parameters (note that in this model there is no interaction between the stars). The initial mass of the two stars can be varied, as can the length of time for which they evolve. The best fit results are plotted in Figure 3.9 and give estimates for the current masses of $75 \pm 14 M_{\odot}$ for the (cooler) primary and $62 \pm 11 M_{\odot}$ for the (hotter) secondary. These estimated masses are in relatively close agreement with the lower-mass limits from the orbital solution, this implies that the system has a high inclination. The best fit corresponds to an age of 2 - 2.5 Myr and implies that both stars have significantly evolved off the zero-age main sequence. This age is also supported by the observed spectral types.

Examples of the rate at which the temperature of a star decreases with age are shown in Figure 3.10 for a number of different initial masses (calculated by Brott, private communication). As is clear, the more massive the star, the faster the decrease in temperature. This leads to the question for R139 that, for two coeval stars of different

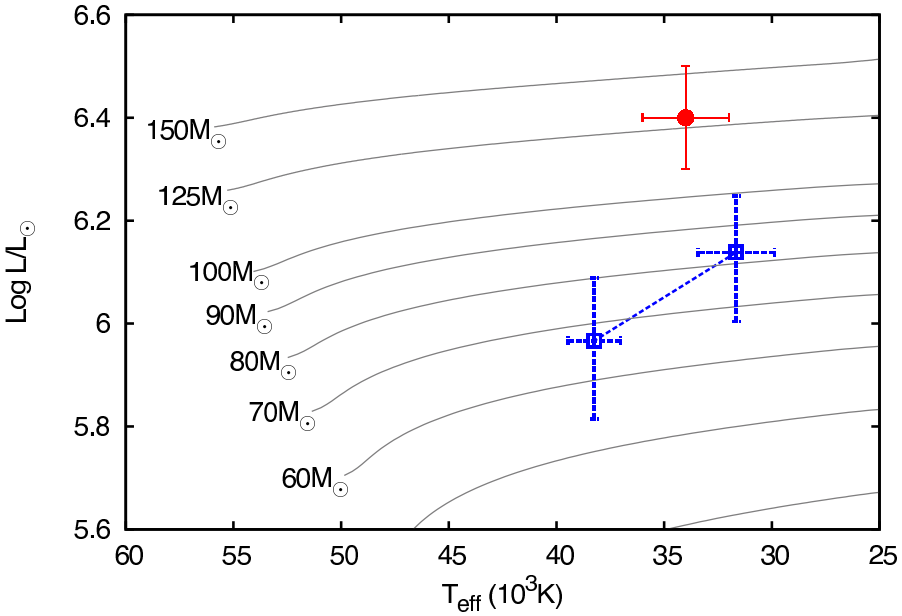

Figure 3.9: Hertzsprung-Russell diagram showing mass estimates derived from luminosity fits to evolutionary tracks (Brott et al. 2011; Friedrich et al. in prep.). The red circle indicates the best fit for the total luminosity of the R139 system, while the blue squares show the fit for the luminosity of the two components based on the mass ratio and assuming the objects are coeval. From these it is possible to infer the initial masses, see text for further details.

masses, how can they have such similar temperature? This paradox is reflected in the best fit values of Figure 3.9, which show a clear difference in the expected temperatures of the two stars.

The effective temperature of 34 ± 2 kK was initially found through the CMFGEN fit to the 'single' star, while the temperature difference for an O 6 and O 6.5 is only expected to be 1 kK (Martins et al. 2005). It is not immediately clear how this discrepancy can be resolved. If the stars were not coeval, this would resolve the problem. It is possible that the two stars formed independently at slightly different times and have since become trapped in the binary system. However, the similarities in the spectra would be a remarkable coincidence if this were the case. There is also the possibility of some interaction between the two stars, but this is not expected for the observed separation.

Another option that was considered could be the effects of rotation. As can be seen in Figure 3.10, very high rotation rates of 300 km s^{-1} can prolong the decay in temperature of the star. However, for both the R139 components the measured $v \sin i$ value is, not only very similar, but also around 110 km s^{-1}. Without the presence of extremely strong winds, the rotation rates of stars are not expected to significantly slow with time, so the current models for rotation cannot explain the situation.

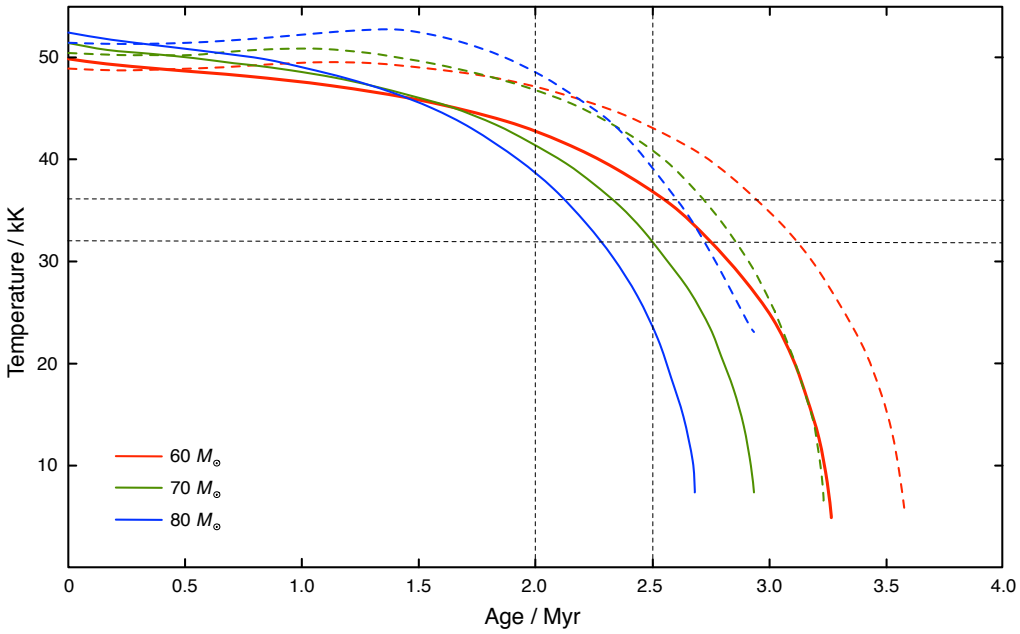

Figure 3.10: A graph showing how the temperature of a star decreases with age, modelled for stars with an LMC metallicity. More massive stars are seen to cool more quickly. Two sets of models were run with initial equatorial velocity rates of 100 $\mathrm{km\,s^{-1}}$ and 300 $\mathrm{km\,s^{-1}}$, shown by the solid and dashed lines respectively. The more rapid rotation is seen to 'hold up' the star's evolution, keeping it at a higher temperature for longer. The expected age and temperature ranges are shown by the dotted vertical and horizontal lines.

Within rotational models, there is an 'overshooting' parameter used to describe how the convective regions within the core interact with the radiative envelope. This parameter influences the mixing within the star and thus the impact of the rotation on the expected temperature. Due to the historically-limited sample sizes this parameter is not well characterised for O stars, especially those as massive as the stars discussed here. A better understanding of this overshooting might help explain the R139 case. Again this is an area where the VFTS data-set is expected to provide feedback into current theoretical models.

3.8 Discussion

3.8.1 Previous observations

Since this study has found such a clear signature of a binary companion, it was interesting to consider again the earlier work of Schnurr et al. (2008), who found

an insignificant radial velocity shift. A number of the VFTS epochs were therefore degraded to the same resolving power as Schnurr's ($R \sim$ 1000) and a number of lines were fit with a single Gaussian function. The radial velocity variation on these measurements was found to be only 10.3 $\mathrm{km\,s^{-1}}$, while the FWHM of the profiles varied by around 40 $\mathrm{km\,s^{-1}}$. This suggests that even if the system had been observed near periastron, it would have been difficult for Schnurr to confirm its binary nature.

3.8.2 Comparison systems

R139 is one of the most massive binaries discovered, and it is interesting to compare it with its high mass brethren. The largest known 'weighed' binary system where the exact masses have been determined is NGC-3603-A1, this is comprised of two W-R stars, a 116$\mathrm{M_\odot}$ primary and a 89$\mathrm{M_\odot}$ star (Schnurr et al. 2008). This makes the primary star in the NGC-3603-A1 system the most massive star with an accurate mass determination, thus providing an important calibration point for stellar modelling. The next most massive system is WR20a, an 83$\mathrm{M_\odot}$ and 82$\mathrm{M_\odot}$ binary (Rauw et al. 2004). There is also the famous case of η-carinae, where the primary star is believed to have a mass in excess of 100$\mathrm{M_\odot}$.

More direct analogs of R139 are systems with a pair of massive evolved O-stars, such as the Cyg OB2-B17 system (Stroud et al. 2010), where the component stars are O7 and O9 supergiants and Cyg OB2-#5 in which the primary is an O6-7 supergiant (Rauw et al. 1999). Unfortunately without observations of an eclipse, the masses for R139 will remain lower limits, which means they are not as informative to the models as an exactly determined mass would be.

3.8.3 Conclusion

The high-quality, time-sampled VFTS observations have revealed that R139 is a binary system. The data suggest that it is the most massive evolved O-star binary system yet discovered: a result which additional observations around periastron would help to confirm. As demonstrated here, such a massive system has already presented challenges for theoretical models to reproduce its observed properties and it will likely provide a crucial test for evolutionary and atmospheric models in the future.

Chapter 4

Searches for binary companions around massive stars with bipolar nebulae

...and in the darkness bind them.

J. R. R. Tolkien, qtd. in Nathan Smith

4.1 Author's note

This chapter reports the results of a study into the presence of binaries around LBV stars with intriguing nebulae, using techniques analogous to those described in the previous chapter. The nebulae are of particular interest due to their similarities with the famous triple-ring structure surrounding SN1987A.

4.2 Introduction

4.2.1 Luminous Blue Variables

LBVs, also known as Hubble-Sandage or S-Doradus variables, form a rare and heterogeneous group of objects that represent a poorly-understood phase of massive-star evolution. Rather than the traditional grouping of objects through spectral similarities, the defining characteristic of LBVs is evidence of significant photometric and spectral variations. They have been seen to exhibit changes of magnitude over timescales of decades or even years, with variations as large as 1-2^m. During such outbursts the stars cool dramatically as they appear to expand in size (Lamers 1995), with drops in effective temperature as large as 20,000K.

LBVs have generally been considered to be among the most massive stars ($> 50 M_\odot$); they correspondingly have extremely high luminosities, which approach the Eddington

limit for stability against radiation pressure. It is possible that their proximity to this limit gives rise to the instabilities in the star, and this is perhaps connected to the observed Humphreys Davidson limit of high-mass stars (Humphreys & Davidson 1979). Recently lower-mass candidate LBVs have also been identified that have masses as low as $10M_{\odot}$ (Stahl et al. 1990). It is believed that these lower-mass objects may have already passed through a RSG phase, before becoming LBVs on a blue-ward loop across the HR diagram, perhaps having lost up to 50% of their initial mass in the process.

It is believed that the LBV phase is a relatively short phase of stellar evolution: de Koter (1993) predicted that it will last only 1% of the star's main-sequence lifetime. As a consequence of this, coupled with the rarity of such massive stars, it is believed that there are probably only tens or hundreds of LBVs present in the Galaxy at any one time. There are currently only 13 confirmed galactic LBVs (Vink 2009), although there is debate about some of these. Vink also considered a larger number of 'candidate LBVs' that have been seen to undergo either significant rapid photometric variation *or* spectral variation, but not both, which he defines as the requirement for full LBV membership.

The limited sample size and the wide range of objects classed as LBVs, increase the difficulty of understanding what exactly is the mechanism behind their variability. It is not even entirely clear what evolutionary role they play: it has long been believed that LBVs occupy only a transitionary period as a massive star evolves across the HR diagram. However, there is increasing evidence that LBVs may themselves be the immediate progenitors of some supernovae (Kotak & Vink 2006).

Compelling evidence for this theory came from SN2006jc. The SN was deficient in H and He suggesting that the progenitor was a W-R star. However, two years prior to the SN the star was seen to experience a large eruption, which was initially reported as a SN (Nakano et al. 2006). No W-R star has been seen to experience eruptions of this LBV-type and consequently it has been proposed that the system may be a binary composed of a W-R and an LBV (Pastorello et al. 2007). A more simple solution would be if the outburst and the SN originated from a single star.

Another interesting piece of evidence comes from the double P-Cygni absorption features seen around some LBVs, for instance the Hα profiles of AG Car and HD 160529 (Leitherer et al. 1994). These arise due to absorption as light passes through material ejected from the star in multiple previous eruptions. The emission from SN 2005gj has extremely similar features to these stars, with Trundle et al. (2008) suggesting that it too had experienced eruptions in its relatively recent past. These shells are found to be expanding at velocities of order 200-300km/s. Such speeds are considerably faster than those associated with RSG winds and slower than those of W-Rs.

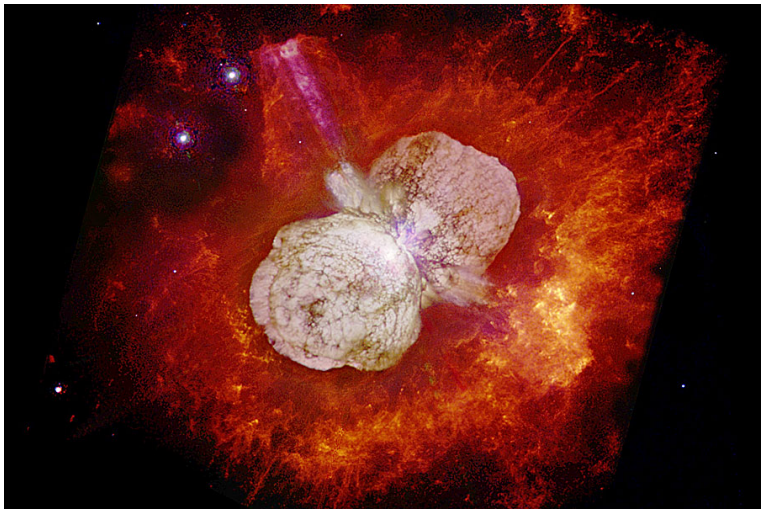

Figure 4.1: The Homunculus nebula surrounding Eta Carinae.

4.2.2 LBV nebulae

In the 19th century the star η Carinae was seen to undergo a dramatic increase in brightness of 3^m. It has subsequently been discovered that during this period material was shed from the star forming the now famous Homunculus nebula, which is shown in Figure 4.1; estimates for the nebula's mass vary considerably but it is believed to be at least $10M_\odot$ (for a discussion of the nebula and its mass, see Smith (2009)). A similar giant eruption occurred in the 17th century when the star P Cygni appeared to significantly increase in brightness, with a resultant nebula also left behind.

AG Car is often considered a good example of a LBV as it has displayed spectral and photometric variations on numerous occasions (Groh et al. 2008). It is also surrounded by a nebula that contains $\sim 4M_\odot$ of material which appears to have originated from the star a few thousand years ago (Nota et al. 1995). Other LBVs show evidence of surrounding nebulae, with similar ages, and it is therefore believed that giant, nebula-forming eruptions are another part of the LBV stage.

An intriguing aspect of the LBV nebulae is that they are often highly bipolar, with material thrown off along the star's axis of rotation. The Homunculus is perhaps the most famous example of this, but others are known, such as the star Sher25; a B-type supergiant that is also an LBV candidate (Vink 2009), found slightly to the northwest of the OB association NGC 3603 (Sher 1965). The nebula was discovered by Brandner et al. (1997) and, as can be seen later in Figure 4.3, it consists of a well-defined central ring surrounding the star, with two asymmetric lobes of material on either side.

4.2.3 SN1987A and Sher25

In 1987 the blue supergiant Sk −69°202 in the LMC exploded as a type II supernova. This surprised the astronomical community as theory did not predict that an apparently normal, stable BSG would undergo a supernova explosion. Subsequent *HST* observations of the remnant have revealed that the progenitor star was surrounded by a pre-existing bipolar nebula (Burrows et al. 1995). This is also shown in Figure 4.3; again there is a well-defined central ring, with two larger rings along the proposed rotation axis. Sk −69°202 was a B0.7-B3 supergiant when it exploded (Walborn et al. 1989) and it is thought to have had a mass of around $20M_{\odot}$. The star showed evidence of chemically-processed material suggesting it had passed through a RSG phase with the corresponding CNO products. However, it has also been suggested that core dredge-up could have led to the observed abundances, perhaps occurring at the same time as the turbulent process which created the rings.

Sher25 is a B1.5 supergiant and Hendry et al. (2008) suggested from comparisons with FASTWIND model atmospheres that it had an initial mass of around $50M_{\odot}$. This is rather too high to be sure that it would have undergone a RSG phase. They also showed that its N and He abundances are at the lowest end of those expected for a post-RSG phase.

The relatively close spectral types and the similarities in their nebulae has led some to argue that Sk −69°202 was an LBV, and that the famous triple-ring structure is another example of an LBV giant eruption. Again, this would suggest that the LBV phase can be the end-point of a star's life rather than the previously believed transitional phase. A number of other competing theories have been put forward for the generation of the rings in SN1987A; these are briefly outlined in the next section.

4.2.4 Forming triple-ring systems

One of the most popular formation theories proposed is that of a binary merger (Morris & Podsiadlowski 2007, hereafter MP). Their starting system consists of a $15M_{\odot}$ star and a smaller $5M_{\odot}$ companion. After leaving the main sequence, the larger star evolves and expands to become a RSG, engulfing its companion in the process. During the merger a large disk-like common envelope is formed. Due to the build up of pressure as the stars spiral into the centre of the disk, material is preferentially lost at around 45° from the plane of the disk. After the merger, the envelope shrinks and the star begins to resemble a BSG. During this shrinking, matter from the outside edge of the disk, which has the highest angular momentum, is lost from the equatorial region, forming an over-dense region. In time the stellar wind of the BSG 'sweeps' up these over-dense regions into the well-defined triple-ring structure.

Smith & Townsend (2007, hereafter ST) dispute the binary merger simulation for SN1987A, arguing that there is insufficient time after the merger for the star to have returned to an apparently normal BSG. They also contend that Sk $-69°202$ was not rotating rapidly enough to fit the binary merger evolution. Finally, and perhaps most conclusively, evidence has been found to suggest a much larger bipolar nebula beyond the visible rings (Sugerman et al. 2005). If this was so, it would rule out the possibility of a binary merger: this multiphase process can not have happened twice.

ST have instead looked to the homunculus of η Car: it is highly bipolar and has certainly not evolved through a RSG phase. They present a method for generating the nebula which is based on a single star, as they argue that η Car's evolution will not have been significantly affected by its small binary companion. This is interesting in the context of the discussion of binaries in systems in this study.

An object rotating rapidly becomes oblate. Assuming the net flow of radiation is perpendicular to the surface, then since the star is effectively 'flatter' at the poles there is increased emission from these regions. Also since the radius of the star is smallest from the centre to poles, the surface gravity is stronger at the poles and they become brighter, a process known as gravity darkening (the equator is dimmed). This leads to a bipolar over-density of material near the poles, which when the star undergoes an eruption leads to an ejection of an object similar to the homunculus. The stellar wind would then get swept up into the 'corners' of the homunculus, which over time would create the over-dense regions seen in the triple-ring systems. Note that ST do not attempt to explain the origin of the eruption, but they highlight that the nebula of η Car has considerably more kinetic energy than that available from photons, and therefore it must have been formed from some kind of explosion, not just a solely wind blown phenomenon.

A third model involves the interaction of BSG winds with a spherical, stationary shell of material created during the RSG phase. This idea is illustrated in Figure 4.2, which shows the results of simulations from Chita et al. (2008). The wind of the BSG has an hour glass shape as a result of mass-loading at the equator of the star. As the outer lobes of the hourglass expand they collide with the stationary RSG shell and at the points of interaction compression and heating occurs, making these regions visible. It can be seen how the initial interaction with the shell would create a nebula similar to Sher25; later the compression regions change, leading to a nebula with rings that would more closely resemble those of SN1987A.

However, a problem with this theory is that it is not clear if Sher25 has passed through a RSG phase. Another challenge is that, although predicted by theory, RSG shells have not been observed, although it could be claimed that Sher25 itself is the first evidence for such a shell.

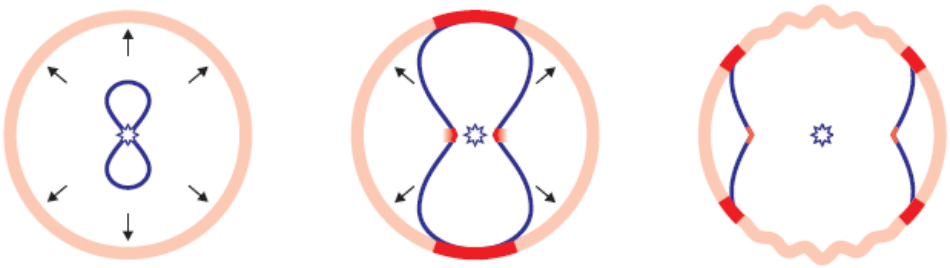

Figure 4.2: 2D simulations from Chita et al. (2008) of the interaction between the circular RSG shell and the hourglass shaped BSG shell. The darker regions show the areas under going compression that would be visible.

4.3 Objects under consideration in this work

While studying the abundances of Sher25 and its nebula, Hendry et al. (2008) detected radial velocity shifts of order $12\,\mathrm{kms}^{-1}$ in its spectrum. This was from only five spectroscopic observations, which were taken at different times, and was consistent with a 3 or 6 day orbit of a binary companion. Such an object would have a major impact on the formation theories of such nebula. A comprehensive set of follow-up observations was therefore acquired with FEROS on the MPG/ESO 2.2m telescope at La Silla.

Other close analogs of the SN1987A nebula have been discovered around some LBVs. In an attempt to see if binarity is common among these stars, two similar candidates were also observed: HD168625 (Smith 2007) and SBW1 (Smith et al. 2007), see Figure 4.3. HD 168625 is a B6 supergiant and has a luminosity more similar to Sk $-69°202$ than Sher25, and uncertainties in its chemical abundances also make it unclear if this star has passed through a RSG phase (Smith 2007). SBW1, a B1.5a supergiant, has an initial mass similar to that predicted for Sk $-69°202$, of $20M_{\odot}$. It has a solar N abundance, suggesting it cannot have been a RSG. This star is therefore potentially an example of a complex ring structure without having passed through a RSG phase.

This chapter reports the results of repeated observations of Sher25, SBW1 and HD168625. Section 4.4 details the observations and their reduction, while section 4.5 presents the results and considers the possible orbital solution they imply but also the importance of considering stellar pulsations. Finally, in section 4.6 conclusions about what can be learnt from this study are summarised.

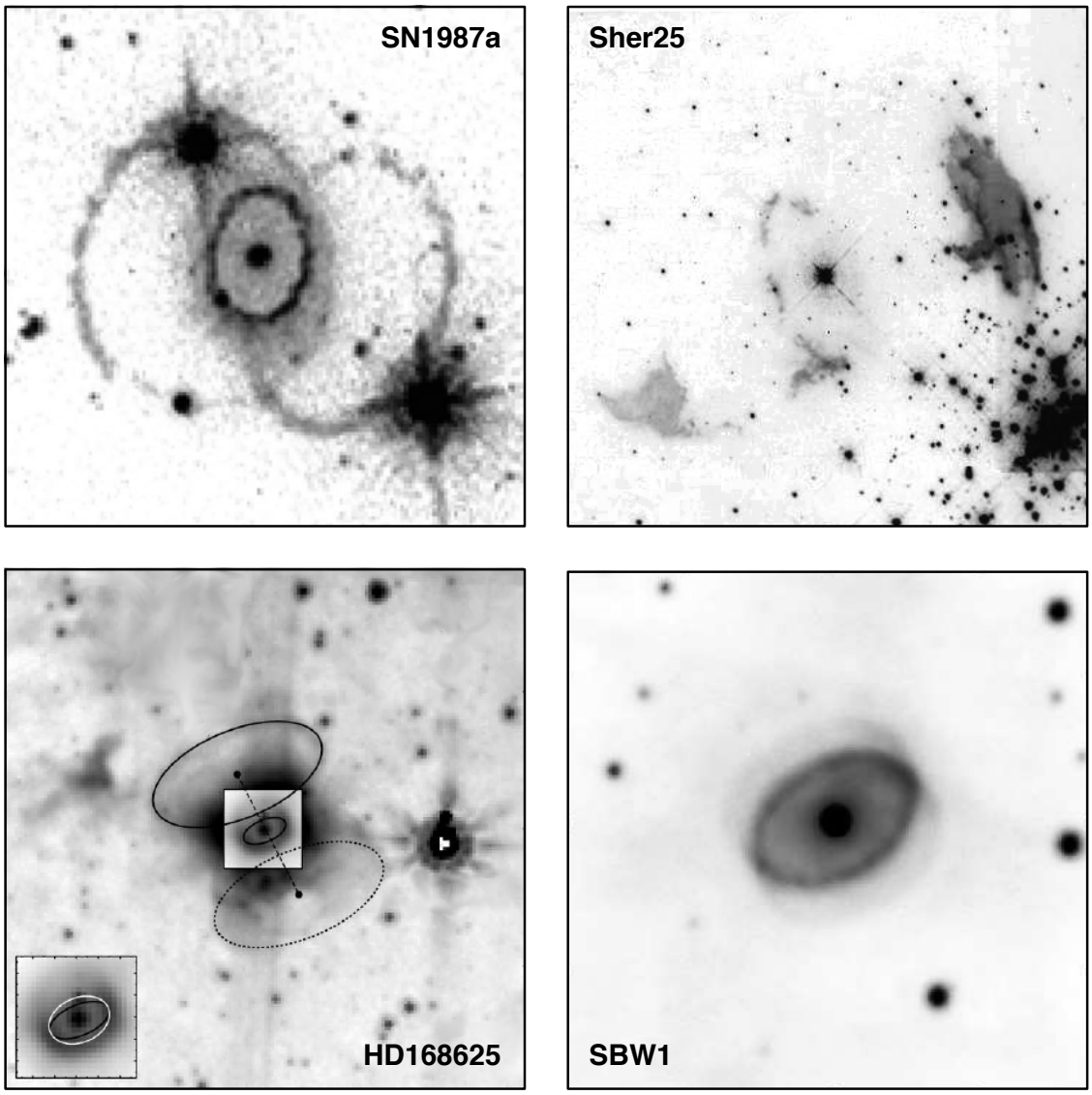

Figure 4.3: The top left image shows the famous triple ring structure of SN1987A, while the other images show the LBV candidates under consideration in this investigation. SBW1 is perhaps the closest analogue, with well-defined asymmetric rings; Sher25 has large lobes of material aligned along the axis of the central ring, while the rings of HD168625 are so faint they have had to be highlighted in this image. The SBW1 and HD168625 images are from Smith et al. (2007).

4.4 Data handling

4.4.1 Observations

The objects of interest were observed over six consecutive nights with FEROS on the MPG/ESO 2.2m telescope at La Silla, as part of the ESO programme 086.D-0997(A). FEROS is a cross-dispersed échelle spectrograph. It provides high-resolution (R $\sim$ 48,000) spectroscopy across almost the entire visual spectrum; λ3500 - λ9200. The spectrograph is fed by two 2.0 arcsec optical fibres, one for the object and one for the sky. The use of fibres allows the spectrograph to be bench mounted and thermally regulated, which ensures that it is very stable and day-time calibrations can be used.

Sher25 and SBW1 have V-band magnitudes of 12.3 and 12.7 respectively and consequently relatively long exposures were needed to achieve the required signal to noise. To avoid too much contamination by cosmic-rays, observations were generally obtained in pairs of back-to-back 2400 s exposures. HD168625 is a considerably brighter target with $V = 8.4$ and consequently this was observed at the end of the nights in a series of back-to-back shorter exposures ranging in length from 240s to 600s. The schematic representation of the observations can be seen in Figure 4.4, this highlights that the greatest number of observations were taken of Sher25 as it was the primary target that led to the study being undertaken.

The data were reduced using the in-house Data Reduction Software ESO pipelines. Further reduction techniques can be carried out which improve the regions where spectral orders are merged, however, this was not deemed necessary. Likewise, sky subtraction was not performed, as for the fitting of a relatively small number of lines it provided no significant advantage for these targets.

4.4.2 Preparation of the data

The relatively long exposures for SBW1 and Sher25 did suffer from cosmic ray contamination; this can clearly be seen in Figure 4.5. The first treatment of the data

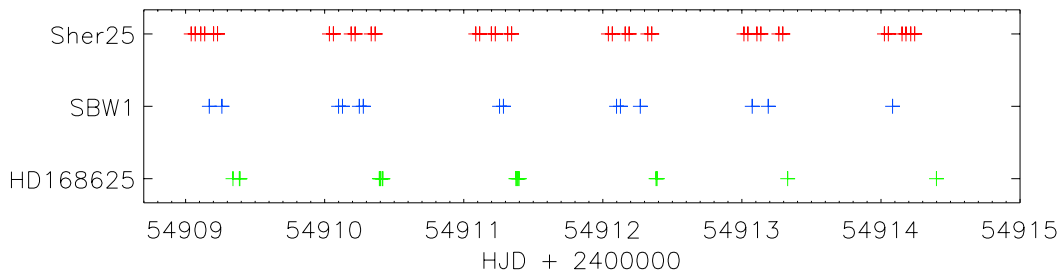

Figure 4.4: Dates of observations for the different targets during the observing run.

was to perform a rough normalisation of each frame by dividing through by the median value of that frame (note the median was used, as the mean would be unduly affected by the cosmic ray contribution). A "Master Profile" (MP) was then created by taking the median of all the observations for that particular object. The ratio between the MP and each spectrum was then calculated and a boxcar 5-sigma clip was applied over 100 element wavelength bins. This method highlighted any feature present only in the spectrum and not the MP. Such a feature must be a cosmic ray and can therefore be replaced with the value of the MP appropriately scaled by the ratio of the surrounding region. The success of this treatment is displayed in Figure 4.5.

Note that since the MP is created through a median stack, if the RV shifts between frames were large, shifted regions could have been flagged as "suspect" pixels and removed. To prevent this, only suspect pixels with a value greater than the local continuum were removed; this ensured that the absorption features used in the fitting were left untouched.

A number of sharp features were still present in the spectra after cosmic ray corrections, for instance those at λ4509 and λ4695; these are residuals from the merging of spectral orders. As the location of these features was the same in every frame, they were interpolated across.

Finally all the spectra were rectified; this was performed by dividing through

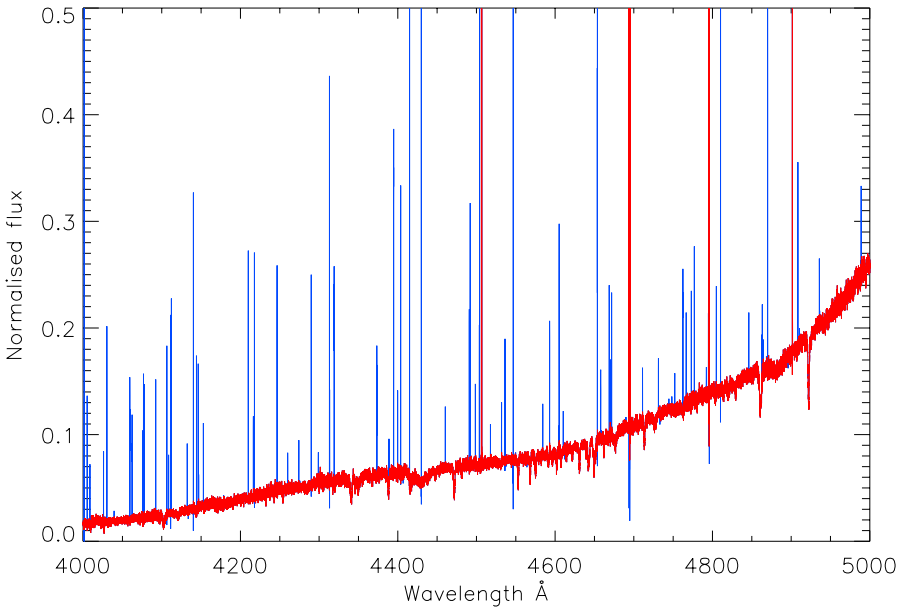

Figure 4.5: Spectrum for an example Sher25 observation showing the effect of cosmic ray clipping: the blue indicates the original spectrum, with the overlaid red showing the cleaned spectrum.

by a continuum which was made through spline fitting through a large number of known continuum points. Any back-to-back exposures were then co-added to increase the signal-to-noise (S/N). In the case of HD168625, where the epochs were taken in quick succession, the frames for each night were coadded, effectively giving only six measurements. This strategy gave typical S/N values of $\sim$50, 50 and 120 for Sher25, SBW1 and HD168625 respectively. The final spectra for the three stars are shown in Figure 4.6.

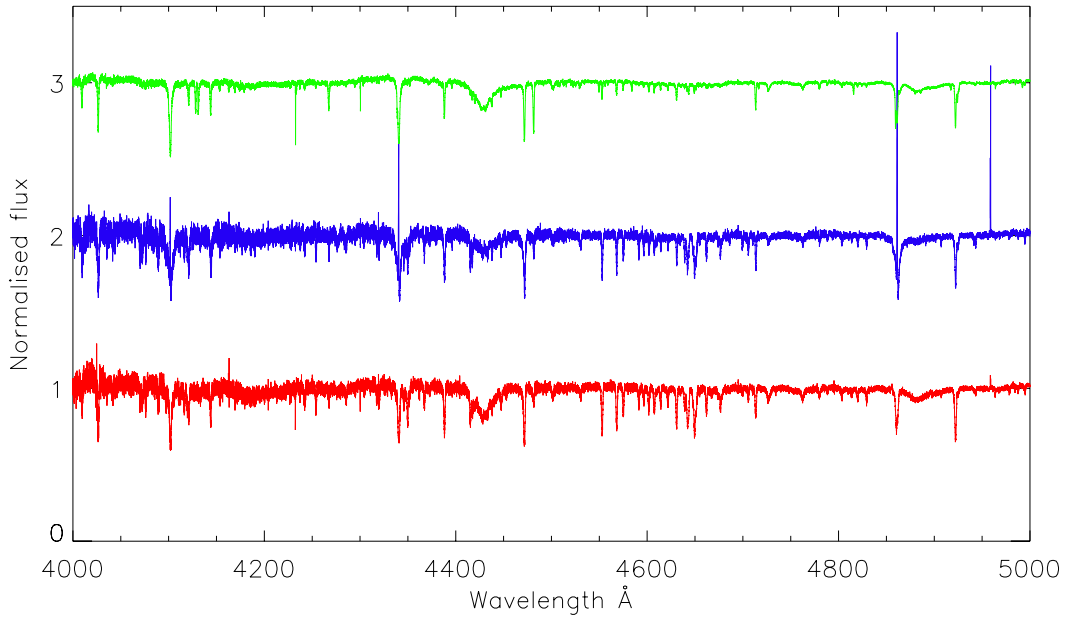

Figure 4.6: Spectra of the LBV candidates studied here. From top to bottom: HD168625, SBW1 and Sher25. The similarities between the spectra are obvious as they are all early-type B stars.

4.4.3 Radial velocity measurements

Radial velocity measurements were made in two different ways: profile fitting of absorption lines and cross-correlation of the spectra. For both methods, measurements were made using features from different parts of the spectrum. This ensured that any measured signal was derived from different spectral orders of the FEROS spectrum, thus reducing the possibility that any observed signal could be instrumental - although for an instrument as stable as FEROS, this would be unlikely.

Small regions on either side of the expected line centres were first used to make a localised correction of the continuum. The plots in Figure 4.7 show examples for a selection of the fits. The data shown are after the local rectification, but the local correction continuum fit is shown in orange for each region.

The lines were first fit using the MP, this gave a median width and depth of each line that could then be held constant for all the other fits. Since the S/N is not that high, allowing only the centre of the line to vary, greatly improved the accuracy of the fits. For each line the deviation in the chi-squared value for the fit was then assessed; if the deviation was found to be large - it was assumed the fit was not reliable for that line and it was rejected from the analysis. For instance in SBW1 the Paschen lines were weak, and therefore yielded poor results and so were not included. The final lines used in the radial velocity measurement for each object are indicated in Table 4.1.

As an additional measurement, cross-correlation was also used to assess the magnitude of any radial velocity shifts. As will be discussed in section 4.5.2, errors can be introduced into Gaussian fitting measurements if the profile shape of a feature varies, rather than a true radial velocity shift. Cross-correlation techniques are less sensitive to such variations and consequently additional measurements were made. Three different spectral regions were checked for shifts via cross-correlation: λ4500 - λ4700, λ5650 - λ5750 and λ8580 - λ8680 Å.

Figure 4.8 shows the results of the measurements for the three different objects. The black crosses indicate the mean radial velocity shifts for each epoch derived from the line-fitting method while the error bars indicate the standard deviation of all the measurements for that epoch. These values are relative to the mean shift for all the epochs. Overlaid on these, in the coloured crosses, are the radial velocity shifts found through the cross-correlation technique. Note that for the SBW1, the red-region was not included as the lines are too weak.

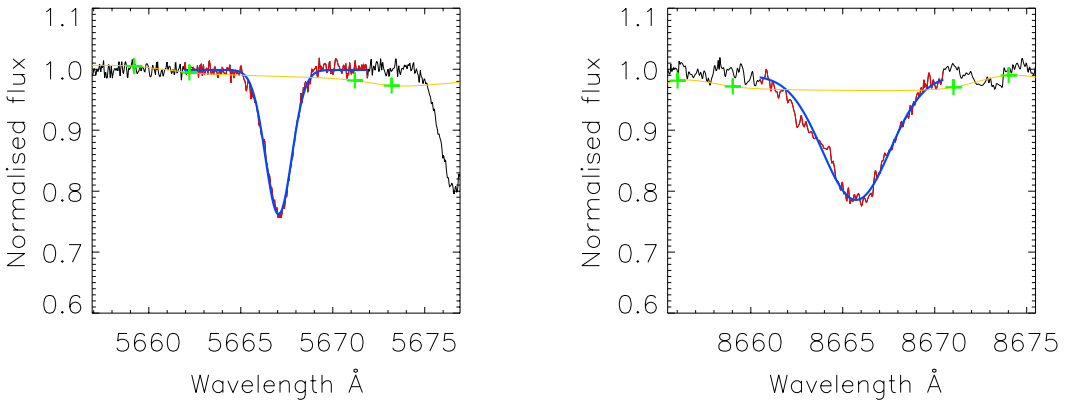

Figure 4.7: Examples of the Gaussian-profile fitting performed on the Sher25 data. The red region of the data denotes the part that was actually fitted, whilst the blue line shows the best-fit profile. For reference, the green crosses mark some of the nearby points used for the local rectification, with the orange line showing the continuum fit to those points that was used.

Table 4.1: Lines used for the different objects to measure any radial velocity variation.

Line	Wavelength	Notes	Sher25	HD168625	SBW1
He I	4026.1799		n	y	n
He I	4143.7598		n	y	n
He I	4387.8300		n	y	n
Si III	4552.6200	Silicon triplet	y	y	y
Si III	4567.8400		y	y	y
Si III	4574.7600		y	n	y
O II	4590.9750		y	n	n
N II	4607.1500		y	n	n
N II	4621.3900		y	n	n
N II	4630.5400		y	n	n
O III	5010.6200		y	y	y
N II	5668.2020		y	n	y
C I	5676.0200	Blend?	y	y	y
H	8598.3916	Paschen lines	y	y	n
H	8665.0186		y	y	n

4.5 Results

From Figure 4.8 it is clear that there is an observed radial velocity variation for Sher25. This is matched by the measurements taken through cross-correlation. The magnitude of the variation and the observed period are consistent with that observed by Hendry et al. (2008). Due to the large time difference between the two observations no attempt has been made to combine these data sets.

For the other two stars the results are less clear. HD168625 does appear to show slight evidence of a shift in its observed radial velocity, but the shift is within the observed errors, so care should be taken about drawing strong conclusions from the result. SBW1 appears to show no evidence for variation.

There are two primary ways in which the RV shifts of Sher25 could be generated: either the presence of a binary companion or from pulsations of the stellar atmosphere. The most common method arises from binary companions, which as has been discussed previously, are common in massive stars. Consequently, an orbital solution for the system is derived below, with corresponding considerations of the properties of such a binary system. However, it should be noted that the presence of pulsations has led some authors to place thresholds on the RV shift required to classify as a likely binary detection. Both Sana et al. (2012, in press) and Ritchie et al. (2009) place a lower limit of $\Delta 20\,\mathrm{kms}^{-1}$ for a detection. The results for Sher25 clearly fall below this and, consequently, an assessment of possible pulsations is also made section 4.5.2.

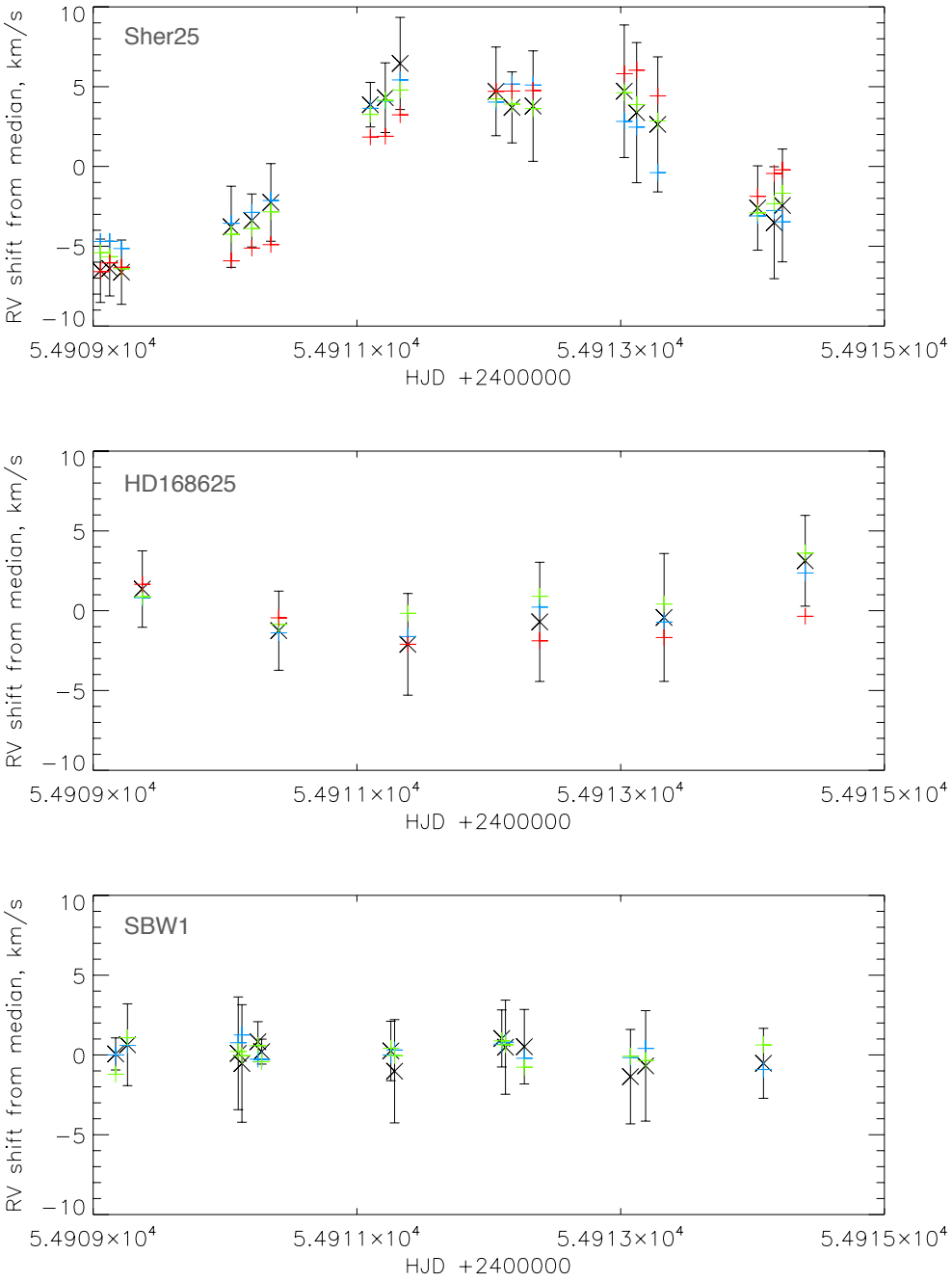

Figure 4.8: Radial velocity measurements for Sher25, HD168625 and SBW1. Black crosses mark the mean RV shifts measured from Gaussian-fitting to spectral lines, with the error bars associated with the deviation on these measurements. The coloured crosses mark the measured shifts from the cross correlation measurements for the blue, green and red regions of the spectrum.

4.5.1 Orbital analysis for Sher25

The observed variation in Sher25's radial velocity has two possible origins. The most common form of RV variation is due to the presence of a binary companion, and therefore, in this section, an orbital solution is explored. However, oscillations in the stellar atmosphere can also cause variations in RV; this is considered in the next section.

A rough period of ∼6 days was found for the Sher25 system using a basic Fourier analysis. This value was then used as an estimate to feed the Liege Orbital Solution Package (see Sana et al. 2006a, for a description), which fits an orbital solution to the data of the SB1 system using the well-established techniques of Wolfe et al. (1967). A full list of the fitted orbital parameters is given in Table 4.2, with a fit to the data shown in Figure 4.9, where the measurements are plotted as a function of orbital phase rather than date.

The mass function, f_{mass}, shown in Equation 4.1 is used to describe the relationship between the mass of two objects in a SB1 binary. The symbols are those defined in Table 4.2.

$$f_{mass} = \frac{m_2^3 \sin^3 i}{(m_1 + m_2)^2} = \frac{PK^3}{2\pi G}(1 - e^2)^{3/2} \tag{4.1}$$

For most SB1 systems it is not possible to do much with this equation, but the rings of Sher25 allowed Brandner et al. (1997) to calculate the inclination of the system to be $i = 65°$. Using the Geneva evolutionary model tracks of Meynet et al. (1994), Hendry et al. (2008) estimated the initial mass of Sher25 to be $50M_{\odot}$. The current mass is hard to determine, as it depends on whether the star has passed through an RSG phase or not. Hendry et al. (2008) argue that this is unlikely, due to the relatively low CNO abundances and because the star is above or near the expected H-D limit. They therefore estimate the current mass of the star to be $40 \pm 5M_{\odot}$. With the values of the m_1 and i coupled with the fits to the orbital solution, it is possible to make an estimate of the mass of the secondary to be $\approx 0.68M_{\odot}$. The error on this value is considered below.

Through Keplerian arguments it can also be shown that $a_2/a_1 = m_1/m_2$. As a result, it is trivial to calculate that the orbital separation of the two components is $43R_{\odot}$. Intriguingly the radius of a B1.5 supergiant is expected to be $60 \pm 15R_{\odot}$ (Meynet et al. 1994). It would therefore appear that if the observed radial-velocity shift of Sher25 is due to the presence of a companion, this much smaller star lies very close to, or even in, the envelope of the primary. As an immediate check, a number of similar calculations were performed for a range of different masses for the primary

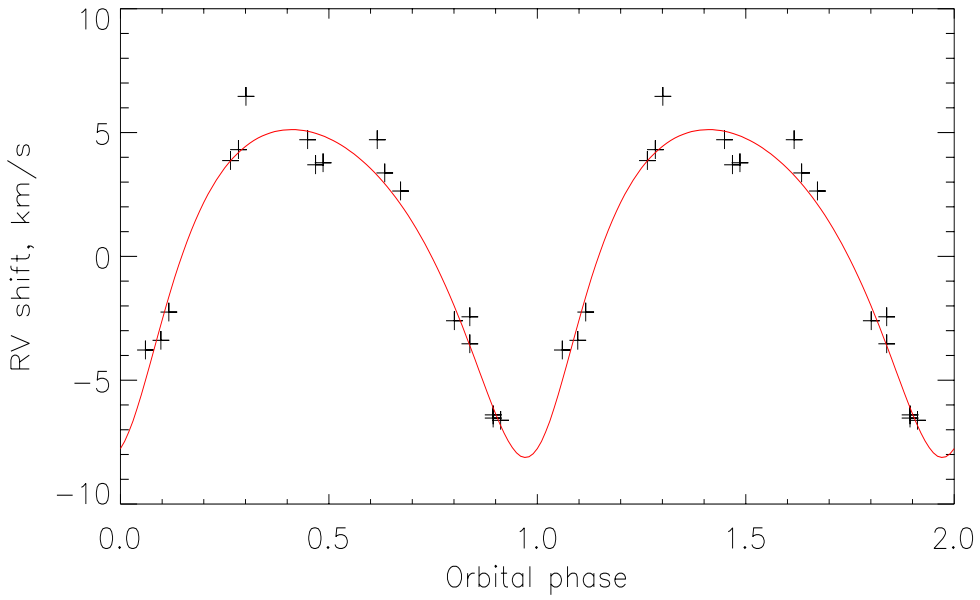

Figure 4.9: The orbital model derived from the Liege Orbital Solution Package analysis of the measured RV values. The measurements have been re-ordered to the appropriate phase value and also replicated for a second phase period to show more clearly the fitted orbital solution. This reveals a 5.4 day orbit.

and also different inclinations. It was found that although the exact values vary, even a significant variation in the mass estimate, does not affect the principal finding of a small companion very close to or even within the primary star's radius.

Table 4.2: The parameters associated with the best-fit orbital solution to investigate the binary scenario. The errors quoted are the formal errors on the best-fit from the Fourier analysis, and therefore may not be fully representative of the uncertainty in the parameter values.

Property	Best-fit value
Period, P	5.4 ± 1.6 days
Eccentricity, e	0.28 ± 0.05
Argument of periastron, ω	198.9 ± 10.4 deg
Date of $\phi = 0$ (HJD - 2400000), T_0	54915.0 ± 0.1 days
Maximum velocity of primary, K	$6.62 \pm 0.53\,\mathrm{km\,s^{-1}}$
Projected semi-major axis for primary, $a \sin i$	$0.677 \pm 0.056\,R_\odot$

4.5.1.1 Possible binary models for the Sher25 system

The proximity of the two stars and the high mass-ratio make a binary system in Sher25 appear relatively unlikely, however, the presence of the nebula shows that this is not a typical supergiant and therefore an unusual binary system should not necessarily be ruled out. Some different formation scenarios have been considered that could create this system.

In a binary scenario, the most likely situation is that the two stars began life separated by a larger distance, and at some stage the smaller object has been 'dragged' inwards. One possible cause of this could have been the larger star passing into a RSG phase, at which time the envelope would have swollen considerably, perhaps interacting with the smaller companion and dragging it in. Another scenario might be that mass has been stripped from the companion, leaving this small remnant, and during this process the stars could have moved closer together.

It is also interesting to consider that the system could have been a triple, with two larger stars and a smaller companion. The two larger stars could have undergone a merger. During this time the common envelope of the stars would have expanded and drawn in the smaller companion, perhaps stripping some of its mass in the process. Intriguingly, such a scenario would fit with the merger hypothesis of MP for the ring formation.

A puzzling aspect of this system are the timescales involved: the pre main-sequence lifetime of a smaller companion would be expected to be roughly equivalent to the *entire* lifetime of a star as large as Sher25. The companion should therefore still be relatively bright in X-rays, and yet Nazé et al. (2012) found no evidence of any significant X-ray emission for Sher25. This makes the argument for the mass-loss scenario perhaps the most compelling.

4.5.2 Line profile variability checks

Hendry et al. (2008) indicated that there is variation present in the Hα P-Cygni wind profile of Sher25. Figure 4.10 shows that a similar variation is also seen in the new observations. This could be caused by inhomogeneous large-scale structure within the star's wind, which leads to variation in the absorption profile (Markova et al. 2005). It is clear from the figure that the change in profile does not show any periodic behaviour during the six nights of recorded observations. This suggests that the observed RV shifts are occurring on a different time-scale to the properties of the stellar wind.

Many OB-type supergiants are known to shown small-scale evidence of photometric and spectral variability. Lucy (1976) suggested that such variations could arise from pulsations within the star's envelope. More recent studies have shown that Line Profile

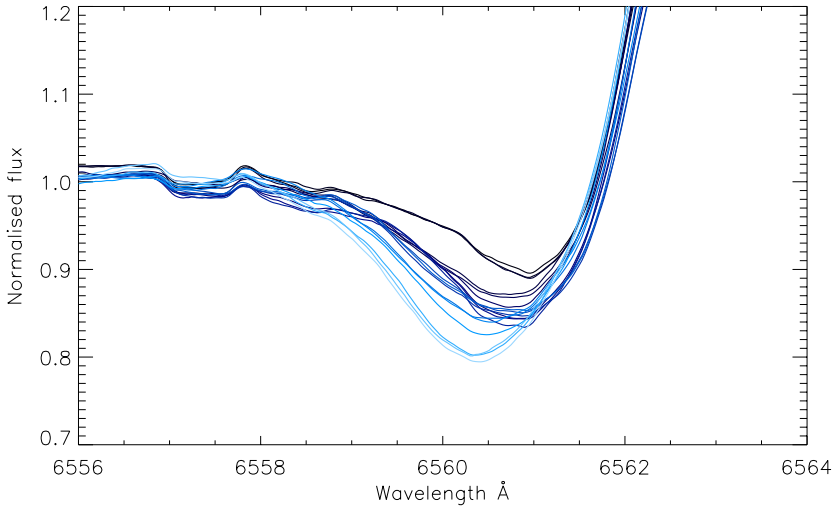

Figure 4.10: A close up section of the P-Cygni profile of the Hα line for Sher25, showing variation in the wind profile. The colour denotes the date of the observation with the darkest lines indicating the earliest frames, and the lightest the most recent. The data have been smoothed for increased clarity.

Variability (LPV) can be linked to the macroturbulence of the star, i.e. to non-radial oscillations within the stellar envelope (Simón-Díaz et al. 2010).

Ritchie et al. (2009), studied RV shifts of massive stars in Westerlund 1, rejecting a number of luminous stars due to apparent variation in profile shapes. They suggest that varying shapes of absorption profiles are a strong indicator of pulsations - these primarily arise due to the dynamical motion of the stellar atmosphere during a pulsation, but also on longer time-frames can be due to the marginal cooling effect associated with an expansion of the stellar atmosphere. Figure 4.11 shows the Silicon triplet for Sher25. This is a relatively strong feature and a commonly used diagnostic in B supergiants. For clarity the data has been binned into one observation per night. It can be seen that there is slight variation in the depths of the lines. A trend in the change is not as clear as it is in the Hα wind structure; the deepest profile is from the first night, the line subsequently appears to get shallower until the final night when the pattern reverses. This hints at a periodic behaviour in the line-profile variation.

The moments of a distribution are defined by equation 4.2. The first moment describes simply the mean, while the second is the width of the distribution and the third describes how asymmetric the distribution is.

$$< v^n >= \int_{-\infty}^{\infty} x^n f(x) dx \tag{4.2}$$

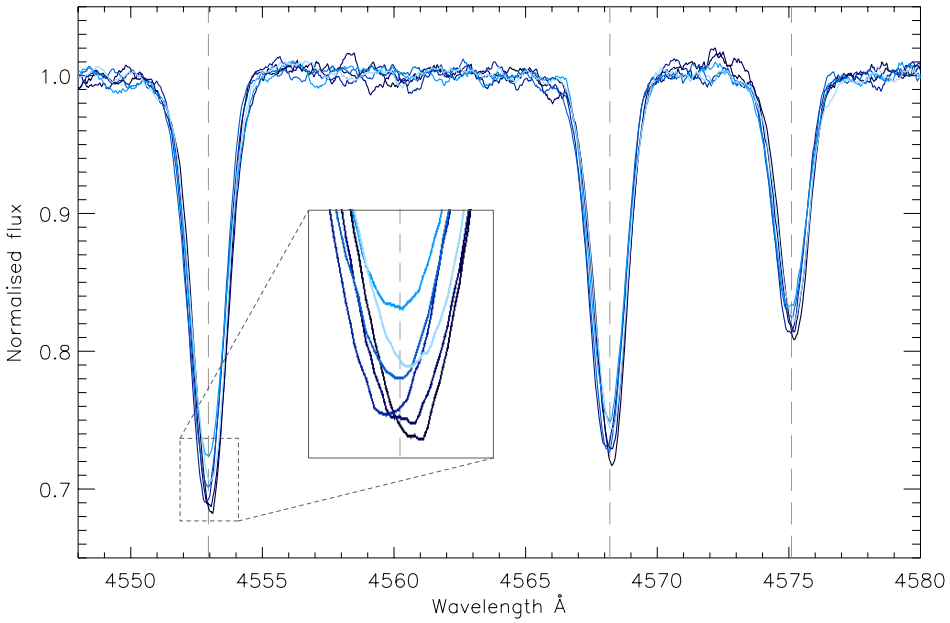

Figure 4.11: Variation in the profile shapes for the Silicon triplet, with a close-up of the λ4553 Å line to highlight the change in profile shape. The colour sequence is the same as that used for Figure 4.10 and the data has been smoothed for clarity.

Balona (1986) proposed that the first three moments could be used to describe features in stellar spectra; specifically the centroid velocity from the first moment while the third moment, or skewness, gives a measure of any 'wobble' in the lines. This last idea is of particular relevance here, if a line is truly shifting due to motion of the star, any asymmetry in the line will remain the same for a SB1 system. Simón-Díaz et al. (2010) showed that for a number B supergiants, which show very small RV oscillations, there appears to be a direct correlation between the first and third moment, i.e. the line centre is 'wobbling' and consequently the measured velocity of the line also appears to move.

For Sher25 the order of magnitude of the RV shift is similar to those described by Simón-Díaz et al., although none of the stars in that study show such a clean periodic behaviour. The skewness of the three Silicon lines shown in Figure 4.11 was therefore assessed. To match the work of Simón-Díaz et al., this analysis was performed using the software package FAMIAS[1], which employs the moment analysis techniques of Briquet & Aerts (2003). The results are shown in Figure 4.12 and clearly suggest that there is periodic variation in the skewness of the line, which shows a very similar pattern to that of the measured RV shifts.

[1]Mode identification results obtained with the software package FAMIAS developed in the framework of the FP6 European Coordination Action HELAS (http://www.helas-eu.org/)

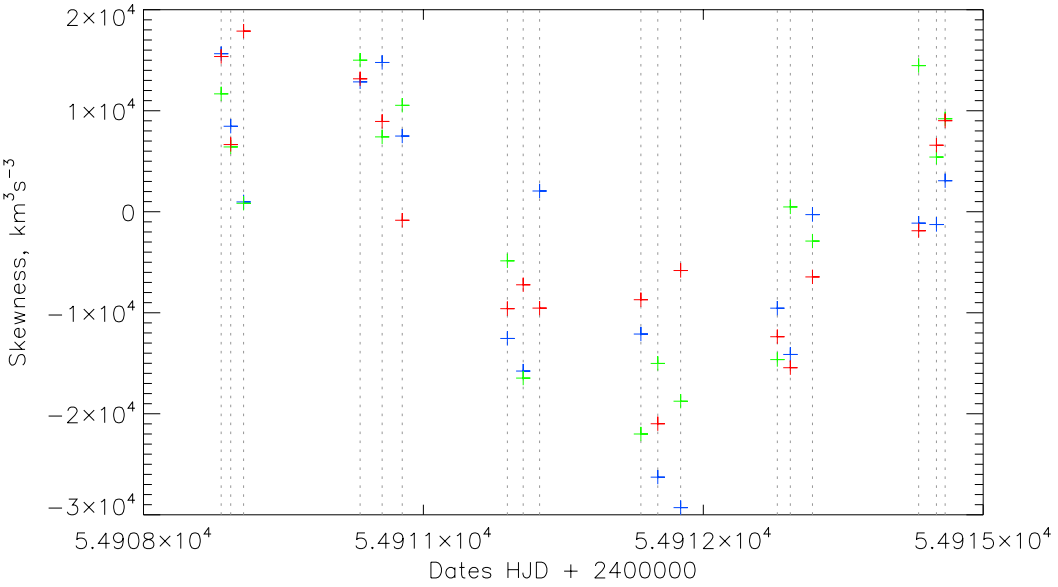

Figure 4.12: Skewness analysis for Sher25, for the Silicon triplet lines: λ4553, λ4568, λ4575 Å; shown by the blue, green and red crosses respectively.

4.6 Conclusion

Due to its similarities to the mysterious SN1987A, Sher25 is an excellent example of a very interesting breed of stars. This work strongly suggests that the star is pulsating in a regular periodic way, which mimics the RV signal of a small binary companion. Such a companion is believed to be unlikely for two reasons; firstly, the variation in the skewness of the line profiles matches the period of the RV shifts, and secondly, any binary system with these orbital parameters would be relatively unphysical.

This work therefore lays to rest the possibility of a short-period companion raised by Hendry et al. (2008). Also of note, is that the period of 5.4 days rules out their speculation that the combined mass of the two stars would need to be $136 M_{\odot}$, which had arisen from Keplerian dynamics based on their estimate of a 3 day orbit.

Looking at the possibility of any other binary companions in Sher25, it is interesting that Nazé et al. (2012) found no evidence of X-ray emission from Sher25, and were only able to place a (relatively low) upper-limit on any potential emission. The authors therefore argued that it is unlikely that Sher25 has any large binary companion, as the colliding winds of the two stars would likely lead to X-rays, as was discussed for R139 in the previous chapter. Combined with the findings of this study, it would appear unlikely that Sher25 has a close binary companion of any size, although this does not rule-out the possibility of a more distant companion with a long period. However, such

a distant companion is unlikely to have affected the evolution of Sher25 and therefore for models attempting to generate the ring structure of Sher25, the star can most-likely be treated as single. More accurately, it should be said that it is likely to be *currently* single; indeed the results of Sana et al. (2012b) described in the introduction, which suggest that ∼70% of massive stars are born as binaries, instead raises the intriguing question of whether Sher25 was initially a binary system which has now merged?

The pulsations of Sher25 are interesting but they are in no way unique amongst B supergiants. However, of the stars studied by Simón-Díaz et al. (2010), none showed such a distinct period as Sher25. Although only one cycle was observed, the results do appear to match the signal of Hendry et al. (2008), which suggests the pulsations have been occurring relatively stably for at least a decade. To study these pulsations further, it would be best to try and obtain a prolonged set of observations with an instrument such as X-Shooter on the VLT, which could acquire much higher S/N than that used here, in relatively short observations.

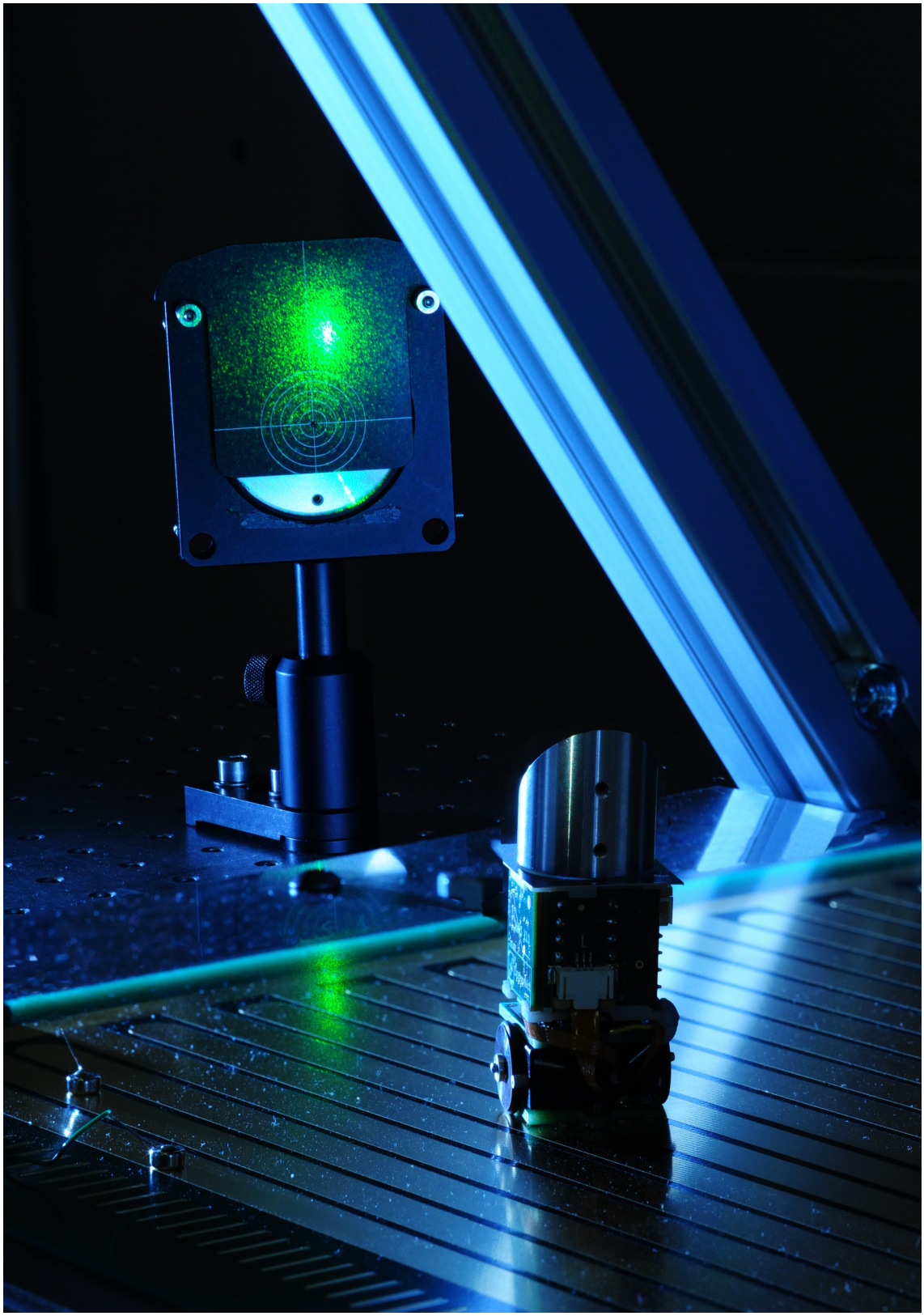

A micro autonomous robot reflecting a laser (photo - Stuart McIntyre).

Chapter 5

A Micro Autonomous Positioning System

The question should be, is it worth trying to do, not can it be done.

Allard Lowenstein

5.1 Author's note

This chapter introduces the concept of a Micro Autonomous Positioning System (MAPS), with comparison to other mirror placement systems and also other miniature robot systems. Part of this chapter has been modified from a 'Requirements Specification' document, which details a system engineering approach to defining the requirements of MAPS (Taylor et al. 2010b). The chapter also introduces aspects of the current design for the various sub-systems of MAPS. The work here has been presented in annual reports delivered to STFC's Centre For Instrumentation, whose 'Responsive Bid Funds' have been funding the MAPS research. An attempt is made to steer the unfamiliar reader through the system engineering approach with use of small comments at the start of many sections.

5.2 The road to MAPS

It was outlined in the introduction that the initial idea for a system to position mirrors on the focal plane of a telescope arose from EAGLE, the multi-object spectrometer proposed for the E-ELT. As Figure 1.5 (in Chapter 1) indicates, this aspect of the EAGLE design is not unique: there are two other projects planning to use pick-off mirrors. What is also apparent, is that no instrument currently employs pick-off mirrors for target selection. This is due, in part, to the difficulty of positioning optical components within an instrument, however it is also largely because there has not been the need for such a system before. It is only with the relatively recent introduction

Figure 5.1: The focal plane of KMOS, surrounded by the 24 robotic arms, each of which has a pick-off mirror mounted on its tip. The arms drive the mirrors into any required configuration across the focal plane.

of the image slicer (e.g. Krabbe et al. 1997), that selection of a complete sub field has been required.

It is possible to form an IFU by grouping together a bundle of optical fibres and using an array of microlenses to couple the light into the fibres, as is discussed in Chapter 2 with reference to the FLAMES instrument. Fibre-fed systems suffer the disadvantage that spatial information is lost as light passes through the fibres. This loss of spatial information, makes it impossible to recreate the pupil image that is required for AO. For this reason, the FLAMES equivalent instrument that has been proposed for the E-ELT, OPTIMOS-EVE, is seeing limited (Navarro et al. 2010). Future instruments such as EAGLE and a similar concept, IRMOS, being developed for the Thirty Metre Telescope (Eikenberry et al. 2006), must look to Pick-off Mirrors (POMs) for target selection - the only current example of this is KMOS.

5.2.1 KMOS and EAGLE

The K-band Multi Object Spectrometer (KMOS) is a second generation instrument for the VLT, which is currently being built by a UK and German consortium (Sharples et al. 2006). It has 24 POMs, each of which will feed light onto an IFU; the light from the channels is then combined to feed three identical spectrographs. It has recently passed acceptance testing and will be installed on the VLT later in the year. Like

EAGLE it has primarily been designed to make dynamical studies of high redshift galaxies ($z \approx 2$).

In KMOS the POMs are located at the tips of robotic arms and reflect the light back through this arm into the rest of the optical system (see Figure 5.1). Each arm can move in r and θ, thus providing wedge-shaped coverage of the focal plane, with the greatest overlap in the field centre. To give greater configurability and reduce the risk of collisions, the arms operate in two planes, which are equal distances above and below the focal plane.

The entrance window of KMOS acts to collimate the beam, thus ensuring that the rays incident on the focal plane are telecentric and therefore the focal plane is completely flat. If this were not the case, light reflected off the POMs would not be parallel to the focal plane and could therefore not be coupled back through the robotic arm. This is a key feature of KMOS which, unfortunately, cannot be scaled-up for EAGLE: the focal plane of KMOS is 35 cm in diameter, but for EAGLE it is likely to be 2 m x 1.5 m. It would be extremely challenging and expensive to produce an entrance window for EAGLE which would provide a telecentric beam over so large a field, consequently EAGLE will have a curved focal plane. This is schematically represented in Figure 5.2. It would also be technically difficult to manufacture arms which extend up to 1 m

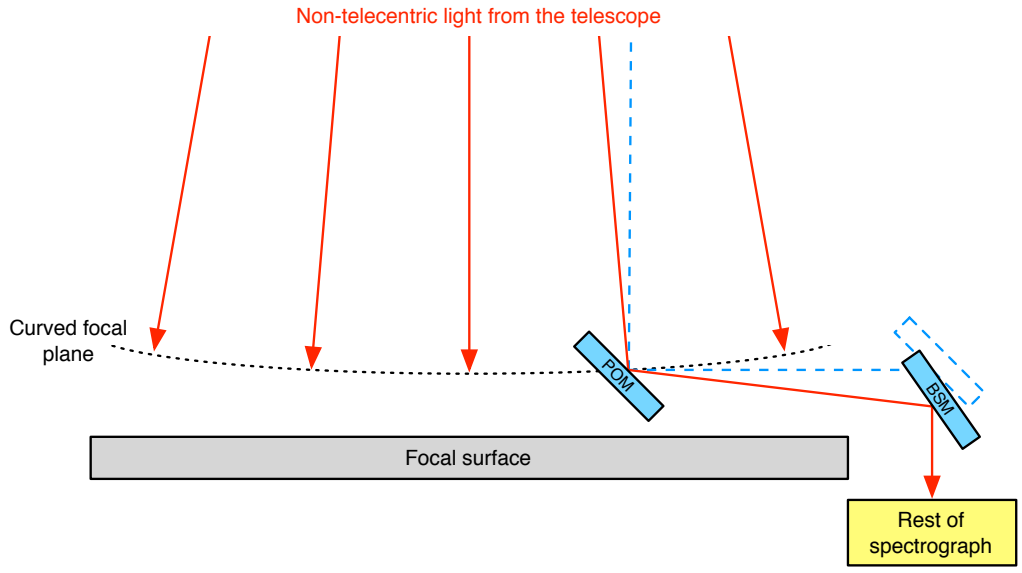

Figure 5.2: The exaggerated effect of a non-telecentric field from the E-ELT. The blue dashed line, indicates the idealised telecentric light path, which is reflected off the POM parallel to the surface. For the real light path, shown in red, the beam reflects at an angle greater than 90°. This results in the Beam Steering Mirror (BSM) having to translate in z and tip to ensure the light enters the spectrograph at the correct angle.

across the focal plane without sagging under their own weight. Consequently EAGLE has had to develop a different method to couple the light from the POM to the rest of the instrument.

5.2.2 Other pick-off designs

The current design of EAGLE uses free-standing POMs positioned across the focal plane, each of which reflects the relevant sub-field of light to a Beam Steering Mirror (BSM), from which it is then reflected into the rest of the instrument. The BSM must rotate to line up with the POM, but in order to compensate for the non-telecentricity of the incoming beam, it must also move up and down, and tip and tilt. A discussion of some focal plane coverage considerations for EAGLE is given in Appendix B.

It is proposed that EAGLE's POMs will be positioned by two pick-and-place robots. These will be able to move in x and y across the plane, with each operating on its own half of the focal plane. Although pick-and-place machines are used widely in industry, the positional tolerances on the POMs in EAGLE are extremely demanding. A prototype pick-and-place device, Starpicker (Hastings et al. 2006), was built at the UK ATC and is shown in Figure 5.3. Although not specifically designed for EAGLE, Starpicker successfully demonstrated many of its requirements.

Figure 5.3: The Starpicker robot, built at the UK ATC as an example of a high-precision pick-and-place machine; it can position POMs to within $\leq 5\,\mu$m, on a curved focal plane.

One drawback with pick-and-place systems, is that they are relatively slow if a full re-configuration of a field is required - every POM has to be sequentially picked up and re-positioned. One of the obvious drivers for a new type of positioning system would be to allow all the POMs to reposition themselves simultaneously. The advantage for EAGLE, with only 25 mirrors, would not be necessarily that large, however, if hundreds of POMs were required in future instruments, the saving would be significant. Such a problem has been faced in FLAMES, where the OzPoz positioner can take up to twenty minutes to position a full field of 135 fibres. The solution for FLAMES is to employ two focal plates, one of which can be observing, while the other is being populated by OzPoz ready for the next observation (Gillingham et al. 2000). In EAGLE, where the focal plane is so large, such an interchange mechanism would not be feasible. This also highlights another slight drawback of the pick-and-place system: it is not possible to reposition any POMs whilst others are being used for observations. It would clearly be a major advantage if, in future systems, unused POMs could be repositioned during observations.

Another major aspect which should be considered is that of weight and size. Many of the instruments which have been proposed for the E-ELT are vast, weighing tonnes and occupying many cubic metres. Any aspect of an instrument's design which can reduce its weight is therefore an advantage; with a pick-and-place system there is certainly a slight inefficiency in a bulky multi-kilogram robot, positioning mirrors which only weigh a few grams.

One other idea that was considered early in the EAGLE design process was to tile the focal plane completely with small mirrors which could be tipped and tilted to act as POMs at the desired positions. However, such a system would dramatically reduce the flexibility of the POM arrangements, and consequently it is likely that many of the desired sources would always fall on or near the edge of the POM. A study was carried out to investigate the 'Allocation Efficiency' of different pick-off systems (Taylor et al. 2008). The allocation efficiency was defined as the percentage of objects which can be observed when the desired number of objects matches the number of observing channels. This study found that for a number of randomly selected fields the allocation efficiency for the tiled plane could be as low as 75%. In addition, a comparison was made between a normal pick-and-place system, which will always require a region surrounding the POM for the gripper jaw to pick it up, with an ideal POM placement system, where the mirror placement system allows the POMs to be placed right next to each other. It was found that such a system would improve the allocation efficiency for observations of clustered fields.

A large number of motivations for a new positioning system have been laid out here; simultaneous positioning, repositioning during observations, clustering potential

and physical properties such as weight and size. The ideal version of the proposed MAPS would meet all of these requirements. It should also be noted, that many of these motivations become stronger for higher-multiplex instruments than EAGLE, MAPS is therefore quite possibly a technology for the future rather than today - but it is necessary to start somewhere.

5.3 A Systems Engineering approach

The concept of systems engineering arose in the early 1950s in the US (Schlager 1956), and developed in order to meet the ever-increasing complexity of 'systems'. According to the International Council on Systems Engineering (INCOSE)[1] "Systems engineering is an interdisciplinary approach and means, to enable the realisation of successful systems. It focuses on defining customer needs and required functionality early in the development cycle, documenting requirements, then proceeding with design synthesis and system validation while considering the complete problem."

Perhaps the first question to address from this is, what is meant by a system? The Oxford English Dictionary defines a system as "a set of things working together as parts of a mechanism or an interconnecting network; a complex whole." This is in keeping with the descriptions found in system engineering textbooks (e.g. Stevens et al. 1998), where the emphasis lies on the concept of integrated components, none of which would individually achieve the 'required functionality' of the system.

The aspect of the 'required functionality' is a key tenet of the system engineering process. When designing a product, be it a piece of computer software or a micro autonomous robot system, it is clearly very important to recognise at the outset, exactly what the product needs to do. System engineering provides a framework through which the user's desires can be identified and turned into quantifiable, assessable 'Requirements'. In the context of MAPS, it is its application within EAGLE that leads to a large range of requirements; these must be met in order for the system to be considered 'successful.'

There are a number of different lifecycle models for the development of successful systems, with one of the most popular being the V-model shown in Figure 5.4. This description separates onto the left-hand wing, the early stages of the designing process and on the right, the build and testing phase of the project. A key component of the process is the 'verification' which occurs between the stages to ensure that the requirements are met. Stevens et al. (1998) argue that the better the work on the left-hand side, the easier the work on the right. With that in mind, this chapter will look in more detail at those processes on the left-hand side: it will explore how EAGLE

[1] http://www.incose.org/

(the would-be 'User') places particular constraints on the design of MAPS, and how the System Requirements can be derived from these. In chapter 6, those items on the right-hand side of the V-model will be detailed.

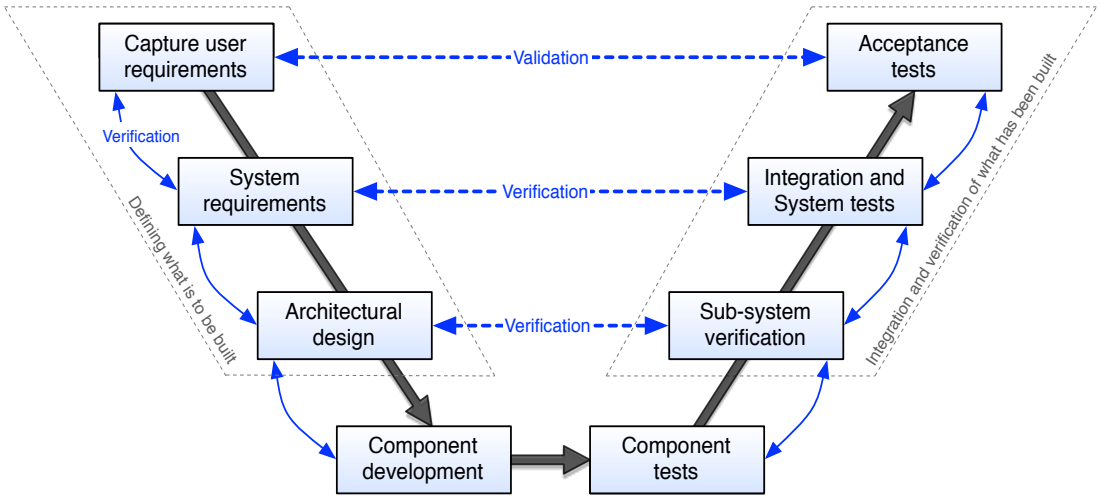

Figure 5.4: The V-model simple life cycle. This illustrates how the design process of project should evolve, taking as a starting point the functions demanded of the system, leading through to a detailed design, and finally the finished product, which through consistent and repeated verification testing, should meet the requirements identified during the design process.

Another important role of systems engineering is to define how a system can be split into smaller, more manageable sections, which are defined as 'sub-systems.' For instance, in EAGLE there is the target pick-off sub-system, a pupil re-imaging sub-system where the light is corrected on the DM, and then there is the spectrograph sub-system itself. Each sub-system can be split into smaller units known as a modules, for instance a detector in the spectrograph sub-system. This use of a structural hierarchy constitutes the architecture design stage in the V-model. It is the role of the system engineer to ensure that the interfaces between the different sub-systems are well defined and these can therefore lead to separate sub-system requirements. This further simplifies the process of verification and ensures that the system will work as required. It is interesting to note that MAPS in its current form is defined as a system, but if it were integrated into EAGLE it would become a sub-system.

Since MAPS is a relatively small system, it is unnecessary to deploy the full arsenal of system engineering tools for its development, but there are still some advantages to treating different sections separately. Consequently, this chapter concludes with a definition and discussion of the various MAPS sub-systems.

5.4 Defining the MAPS system

The idea of a robot-based positioning system is ambitious: the MAPS project has thus far, therefore been that of a 'Technology Demonstrator.' The aim has been to develop a self-contained system which demonstrates much of the required functionality that would be needed if MAPS were employed in EAGLE. There are four basic functions which this stand-alone system must perform; these are described below and their interaction is shown in Figure 5.5.

- **Movement of robot and POM:** The primary function of MAPS is to drive mirrors into position.
- **Command handling:** A user interface is required to allow control of the robots and provide feedback about their status to the user.
- **Metrology of robots:** Measuring of the robots' positions is required to ensure they are properly located.
- **Analysis of alignment:** A simulated light path is needed to show that MAPS can accurately align a source.

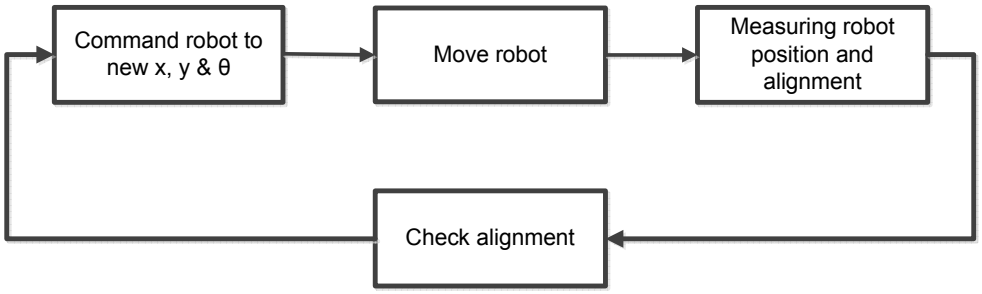

Figure 5.5: The most basic functions that a self-contained MAPS demonstrator needs to perform.

System Characteristics

The different categories of 'Characteristics' detailed below are intended to cover all possible aspects of a system's design. Through rigorously listing all behaviours, the system engineer is able to ensure that no required feature has been overlooked. It also provides an excellent tool for being able to trace the origins of requirements, which will be defined later.

For clarity, the coordinate system is defined in Figure 5.6, i.e. the focal plane extends in the x and y directions, while the height of the robot extends in the z direction.

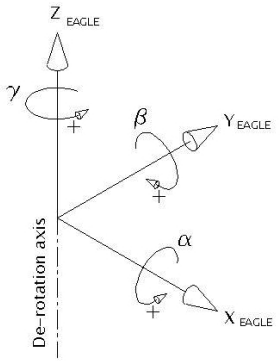

Figure 5.6: Coordinate definition for MAPS.

5.4.1 Functional characteristics

These can be considered as things the system must 'do.' In the case of MAPS, these are often linked with movement and positioning.

5.4.1.1 Positional accuracy in x-y

In order that the correct on-sky field of view can be selected and also re-observed at a later date, the x-y positional accuracy of the POM on the focal surface must be extremely precise. For EAGLE, this is determined by the requirement that any positional error must correspond to less than one quarter the width of an IFU slice (McGregor & Schnetler 2009). As was discussed in section 1.4.2.1, the on-sky slice width arises primarily as a result of the EAGLE science cases and particularly the desire to study structural features in galaxies at $z > 2$. These features are of order 75 - 100 mas and consequently a slice width of 37 mas has been adopted, which allows two resolving elements to sample each feature. This basic property of distant galaxies strongly influences the performance of the MOAO system required for EAGLE, while for MAPS it determines the required x-y positional accuracy. Since the plate scale for EAGLE is 3.8 mm per arcsecond, one quarter of a slice-width corresponds to 35 μm. This is one of the most challenging aspects of MAPS.

5.4.1.2 Rotation in γ

This is the angular accuracy with which the POM would have to be lined-up with a BSM. This is determined through ensuring the pupil image on the DM is not out by any

more than the spacing between actuators. It gives the requirement of 1 mrad rotational accuracy about z.

5.4.1.3 Rotation in β and α

Ideally there would be no rotation of the POM about α or β, as both of these would lead to alignment problems further down the optical train. In practise it is not possible to ensure *no* rotation, so a limit of ± 5 mrad of tilt is set for each axis of rotation. However, it should be noted that due to the ability of the BSM to tip and tilt, if the robot were to be tilted in the direction it is facing, the BSM could, in theory, compensate for this. This could only be achieved though, if the tilt of the POM was known.

5.4.1.4 Configuration Time

The configuration time for the robots must be less than the allowed setup time for the telescope so as to not impact on the scientific observing efficiency. The time allotted for repositioning all the POMs has therefore been set as 5 minutes in EAGLE's planned observing schedule (Evans & Cuby 2009). Since in MAPS the POMs can be positioned simultaneously, this is also the time limit to position each POM.

5.4.1.5 Drive speed

The robots are required to move at a minimum speed of 10 mm/s. At this speed, a POM moving from one end of the focal plane to the other, could do so in 3 minutes. Note however, that it is very unlikely POMs would have to travel this distance, as they are more likely to operate in smaller patrol areas.

5.4.1.6 Alignment speed

The time allowed to make the small motions needed to precisely align the robot once it has travelled roughly to the correct position. Due to the possible travel time described in the previous requirement, this must be achieved in less than 2 minutes.

5.4.1.7 Positional measuring accuracy

It would not be wise to assume that a robot can be driven into position with sufficient accuracy purely through dead-reckoning. With such precise positioning, even a small piece of dust could throw the robot off-course and thus cause an unknown error in its position. It is therefore necessary to have some form of positional assessment, which continually monitors the robots: this is called the Metrology sub-system. It must be able to measure the position of the robots to an accuracy that is a minimum of 5 times

finer than the required positional accuracy. This therefore corresponds to being able to measure the robot's position to 7 μm.

5.4.1.8 Turning circle

In order to simplify the alignment process it will be necessary for the robot to be able to turn on the spot, in practise this would mean rotating whilst not violating the x-y positional requirement.

5.4.1.9 Clustering

For EAGLE the requirement is that two POMs can be placed within 18 mm of each other. Each pick-off mirror is 20 mm in diameter and this clustering requirement means that it would be possible to 'tile' a large area of the sky by placing the POMs in a grid 18 mm away from each other, and then repointing the telescope to fill in the blank regions, without repositioning the mirrors. This clustering requirement would impact observations of any dense grouping of objects, but the need to 'tile' a region would likely be more apparent for stellar science cases rather than for the sparser galaxy populations. Consider looking back to Figure 2.3; this shows the ARGUS pointings from the VFTS that were employed across the central arcminute of R136. If the twenty POMS of EAGLE were arranged in a grid and the telescope repointed sixteen times to 'tile' this area, this would provide coverage of almost the entire region shown in the figure. Likewise similar maps could be employed to cover the entirety of more distant stellar clusters, providing datasets analogous to VFTS for regions in other galaxies.

5.4.1.10 Collisions

Collisions clearly must not occur. The metrology system must continually monitor the position of the robots, if two are found to be closer than 18 mm, then they will be stopped. On-board collisional sensors could potentially also perform such a task.

5.4.1.11 Power

The MAPS robots must be powered by some way which does not require cables. The exact requirements for power delivery depend on the chosen locomotion method, but any system must be capable of running continuously. However, it is possible that if the power system required charging time, more than one fleet of robots could be deployed. This therefore lowers the requirements on continuous operation, as long as the charging time is less than the duration of time a fully charged robot can run for.

5.4.1.12 Wireless communications

Again to avoid cabling, the robots must receive their commands through a wireless method. Wireless commands, if coupled with the use of an external metrology subsystem, mean the robots need to have very little on-board intelligence. However, they must be designed to be able to also transmit wireless signals as well as receive them, in order to report their status.

5.4.1.13 Graphical User Interface

A Graphical User Interface (GUI) needs to be provided which can perform two different tasks: it needs to be of use to the technician who wants to perform experiments, and also a common user who wishes to only move a robot in a simple way. These two aspects are discussed more in the following chapter.

5.4.2 Physical characteristics

These characteristics are the measurable properties of the system, such as sizes.

5.4.2.1 POM dimensions

The field-of-view of each IFU has been chosen to be 1.55 arcsecs as this corresponds to the likely on-sky dimensions of EAGLE's target galaxies. This represents ∼6 mm on the focal plane. It is envisaged that the astronomer may want to tile a region of the sky by repointing the telescope, but leaving the POMs in place. When doing this, the same Natural Guide Stars (NGS) would be used for the AO correction but to select these after repointing, the NGS POMs must either be moved or they need to be oversized such that they still gather light from the NGS. For simplicity it was decided that the POMs for the science channels and the NGS should be identical, so they are all oversized. The final POM is a 45° mirror, which has a base diameter of 20 mm.

5.4.2.2 Robot load mass

The estimated mass of the POM the robot must carry is 20 grams. This influences the torque output of the robot's drive mechanism.

5.4.2.3 Robot footprint

In the ideal version of MAPS, the robot would sit directly underneath the POM, however, for now, the footprint limit has been set as 30 x 30 mm.

5.4.2.4 Robot height

There is no requirement limiting the height of the robot, but it simply must be stable when carrying the POM, therefore a height-to-width ratio of 2:1 is advised (this is excluding the POM).

5.4.2.5 Robot mass

The limit on the robot's mass is set by the choice of locomotion method, i.e. there is no constraint imposed by the design of EAGLE's focal plane.

5.4.2.6 Focal plate dimensions

For this demonstrator the operating area will be only 400 x 300 mm. There are no restrictions on the height or the composition of the focal plane surface, these can be entirely dictated by the choice of pick-off system. In EAGLE the envisaged focal plane will be considerably larger at approximately 2 x 1.5 m. It is these dimensions that have set the speed requirements for MAPS detailed above. The dimensions of the EAGLE focal plane are a result of a wide range of properties. While most science cases would demand as large a field-of-view as possible, in reality the performance of the MOAO system and the impact of vignetting caused by the six Laser Guide Stars limits the effective useable field-of-view to a diameter of between 5 and 10 arcminutes. The plate scale of 3.8 mm per pixel delivered from the telescope then sets the final dimensions for the focal plane. For more information about the real EAGLE focal plane dimensions see Appendix A.

5.4.2.7 Focal plate smoothness

In order to meet the requirements of rotation about β and α, the root mean squared flatness must be less than 10 μm.

5.4.2.8 Wireless interface range

The distance over which any wireless transmission must work is 2 m to the centre of the focal plate.

5.4.3 System characteristics

These characteristics cover a wide range of more practical design aspects. In a larger system, these could be split in to smaller, more detailed sets of characteristics, but this is not necessary for MAPS.

5.4.3.1 Lifetime

For the MAPS demonstrator, it is hard to characterise this property as the robots continually undergo modifications and adjustments. It is important that the parts are sufficiently robust to undergo many weeks of testing without malfunction or deterioration in performance. It should be noted that the cost of producing these robots lies primarily in the design development, therefore manufacturing many would not be prohibitively expensive and the robots could be replaced relatively regularly. For actual use in EAGLE the robots would have to demonstrate a longer lifetime, of order years.

5.4.3.2 Environmental conditions

MAPS operates at standard room temperature and pressure. It had been considered that the pick-off system of EAGLE would be cooled, however, to do this, a large entrance window would be required to enclose the cooled area. This idea was abandoned because, as mentioned before, construction of such a large optic would not be straightforward. The first stage of cooling is therefore immediately after the BSMs.

5.4.3.3 External interfaces

As discussed above, for now MAPS is designed as a stand-alone system and it therefore has no external systems with which to interact with. If MAPS were deployed within an instrument, other factors would have to be considered - e.g. size of the whole system, power constraints and accessibility.

5.5 Sub-system Definition

As discussed earlier, it can be advantageous to break complex systems down into smaller sub-systems. For MAPS there are four distinct areas which can be identified: the robot itself, the power delivery or charging sub-system, the command and control sub-system and finally the focal plane surface on which they operate. These sub-systems can themselves be broken down into smaller 'Modules'. In Table 5.1 the function of each of these different modules is described; note that, at this stage, these are relatively independent of any design constraints.

Using the system characteristics, the system requirements can be identified in Table 5.2. Note that for some areas, To Be Confirmed (TBC) has been entered. This is because some requirements depend on the choice of design, and cannot be finalised until later. In such cases, the ambiguity is discussed in the relevant characteristic section, but these are generally not critical requirements.

Table 5.1: System, sub-system and module definitions and their functions.

Sub-systems and modules	Functional Description
0: MAPS	• To transport mirrors into desired configuration with micro autonomous robots.
1: Robot	
1.1: Chassis	• Carry POM to any required position on the focal surface.
1.2: Pick-off mirror	• Reflect vertically incident light at 90° from the side of robot.
1.3: Drive electronics	• Interpret commands and generate appropriate drive signals. • Relay status reports to command and control sub-system.
1.4: Power unit	• Receive power from power delivery module. • Deliver necessary power to on-board robot sub-systems.
2: Power Supply	
2.1: Power delivery	• Deliver power to the robot.
3: Command and Control	
3.1: Command interface	• Transmit commands to the robots. • Receive status reports from the robots.
3.2: Control software	• Provide a GUI to inform user of current system properties • Translate user inputs into commands for robots.
3.3: Metrology system	• Determine robot positions. • Relay positional information to the software control. • Identify the different robots
4: Focal Plane	
4.1: Operating surface	• Provide a flat, smooth and stable surface on which the robots move.

Table 5.2: Requirements for the MAPS demonstrator, with assignment to the appropriate sub-system. The deriving characteristic is also referenced.

Number	Description	Requirement	Origin
0: MAPS			
0.1	Lifetime	1 month	5.4.3.1
0.2	Operating environment	Room temperature and pressure	5.4.3.2
1: Robot			
1.1	x-y position	$\leq$35 μm	5.4.1.1
1.2	z rotation	$\leq$1 mrad	5.4.1.2
1.3	Speed	$\geq$ 10 mm/s	5.4.1.5
1.4	Turning circle	x-y deviation $\leq$ 35 μm	5.4.1.8
1.5	Clustering	$\geq$ 18 mm	5.4.1.9
1.6	Footprint	$\leq$ 30 x 30 mm	5.4.2.3
1.7	Height (excluding POM)	$\leq$ 60 mm	5.4.2.4
1.8	Power duration	Continuous	5.4.1.11
1.9	Load mass	$\leq$ 18 grams	5.4.2.2
2: Power supply			
2.1	Charging time	TBC	5.4.1.11
2.2	Delivery voltage	TBC	5.4.1.11
3: Command and Control			
3.1	GUI interface	Basic operation must not require any specialist instruction	5.4.1.13
3.2	Command transmission range	$\geq$ 2 m	5.4.2.8
3.3	Accuracy of metrology reading	$\pm$7 μm	5.4.1.7
3.4	Collision warnings	$<$ 18 mm separation	5.4.1.10
4: Focal plate			
4.1	Focal plate size	$\geq$ 0.4 x 0.3 m	5.4.2.6
4.2	Focal plate smoothness	r.m.s smoothness $<$10 μm	5.4.2.7

5.6 Micro robotic systems

Outside astronomy micro robots are an active area of research, and it was therefore important to see if any of the current projects could meet the requirements of MAPS.

A number of the projects use small, but ultimately conventional, motors to drive the robots. An excellent and early example are the 'Alice' robots (Caprari 2000). These small robots, which run off watch batteries, have been through numerous different design iterations, which have seen increased functionality added such as inter-robot communications and sensing of the surroundings. The robots run quickly at 30 mm/s, but are not designed for high precision work such as MAPS.

The family of different Alice robots have been used in a number of different applications, including educational programmes, however, they are not designed for any particular purpose. This is a common trait of many micro-robots projects: the challenge simply is often to build a small robot, but not necessarily with any goal in mind. The other two areas where some of these micro robots have an intended use is for manipulation of small objects within a microscope, and in the study of group behaviour. One early example of such a group system are the 'Ants' robots. These too are driven with small motors, but this is a group of the robots which are intended to work together to achieve certain goals (McLurkin 1995).

Two other motor-based projects of note are the Sandia Robot and Epson's Monsieur. Both of these were built, in part, as publicity for their companies, and therefore the company websites form reference points for the information about the robots. The Sandia robot is of note as it uses small tank-like tracks, while Monsieur is remarkable because of its very small size - 12 x 12 x 17.5 mm. Neither is capable of very long operating times - especially Monsieur - nor are they designed for high precision work.

A summary of the properties of these robots, and the others to be discussed, is given in Table 5.3; it is not intended as a comprehensive list of all projects, but it does include examples of a number of different types of micro-robots.

The other type of micro robot which needs to be considered are those driven by piezoelectric actuators. Piezoelectric materials deform when an electric charge is applied to them; through careful arrangement of the actuators, motion can be generated. This can fall into two loosely separated categories: robots which have actuators that would be recognised as 'legs' and robots where the actuators are arranged to generate a stick/slip drive system, where the robot moves along the surface in a way which is not that dissimilar to a caterpillar.

A well-known example of the legged robots is that of the Nanowalker (Martel et al. 2000), this is shown in Figure 5.7, as are some of the other robots. Nanowalker also employs a vibrating floor, which effectively throws the robot momentarily into the air,

Table 5.3: Key characteristics of other micro-robot projects, see text for references.

Project	**Drive method**	**Application**	**Step size**	**Speed (mm/s)**	**Dimensions (mm)**
Alice	Motors with wheels	Research and education	n/a	30	30x40x30
Sandia	Motors with tracks	Promotional	n/a	8	25x25x25
Ants	Motors with wheels	Research into group behaviour of robots	n/a	150	50x40x30
MiCRoN	Piezo-electric pads	Research, with planned use in a microscope	0.3 μm	2.1	12x12x17.5
NanoWalker	Piezo-electric legs	Research	0.3 μm	25	33.7x33.7x31
Monsieur	Ultrasonic motors	Promotional	n/a	15	11.0x12.4x10.8
Imina	Piezo-electric pads	Commercially available, inspection of chips	40 nm	2.5	20.5x20.5x13.6
iSwarm	Piezo-electric legs	Research into group behaviour of robots		1.5	3x3x2
Ramona	Piezo-electric pads	Research	0.15 μm	10	22x22x6

at which point it takes its step and therefore lands in a marginally different place. By this method it moves across the surface with very high accuracy and quite high speeds. However, as a consequence of its motion, it would not be suitable for carrying loads such as a POM.

Another legged robot system, which is in the early stages of development, is the iSwarm project (Valdastria et al. 2006). As is clear from the image in Figure 5.7, these robots are extremely small, and are mounted on a single 3-legged piece of piezo-actuator. They have such low power consumption that they are powered through a small solar panel on the top of the robot. They are designed to be operated in large numbers, again with the intention to make all the robots perform a task as a group. They are too small to carry the mass of a POM, but perhaps if the system ever reached its envisaged potential, a swarm of robots could move a POM into position.

The Imina robots provide one of the very few commercially available micro-robot systems[1]. These robots are extremely similar to the Ramona project (Fatikow et al. 2011) in that they both use an actuated pad, which generates the stick/slip motion across the floor. These robots both meet many of the requirements of MAPS, and have a profile which would be very suitable. However, they are both tethered robots that receive power and commands through a small trailing wire.

Perhaps the project that most closely meets the MAPS requirements is the MiCRoN project (Estaña & Wörn 2007). This robot is based again on a small piezo pad on its base, but it has no trailing wires. It receives its power through an inductive coupling link with the floor, which continually charges small on-board batteries. The robot

[1] http://www.imina.ch/

however, does not meet the speed requirements of the MAPS robot and it is also not clear if it could carry the required mass.

5.6.1 Astronomy related projects

There is one other astronomy related micro robot project to be considered, which is the Starbug project based at the AAO in Australia (Goodwin et al. 2010). The very idea of using robots to populate a focal plane actually originated with the Starbug team back in 2004 (McGrath & Moore).

The Starbugs are designed to carry fibres into position across the focal plane, and they consequently have a very different set of requirements to the MAPS project. Since the Starbugs must carry an optical fibre across the surface, they are already trailing a 'cable' and consequently power and commands are also delivered through this tether. The robots use miniature piezo actuators to crawl along the base of a piece of glass, and they are held in place by a magnet on the upper surface of the glass. The fibre and cable then hangs down from the robot, with the light coupled through the piece of glass into the fibre. Starbugs are planned for use in Manifest (Saunders et al. 2010) instrument which has been proposed as a multi-object instrument for the Giant Magellan Telescope - one of the other ELT projects.

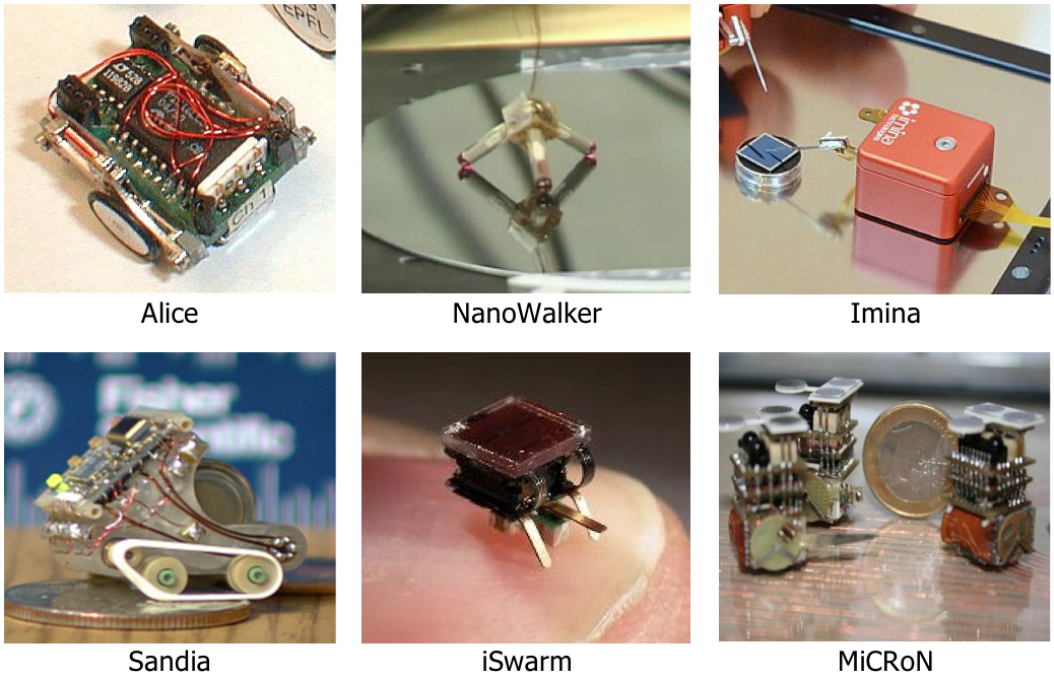

Figure 5.7: Examples of other micro-robotic systems: the images on the left show motor driven robots, the middle shows "legged" robots, and on the right, stick/slip piezo-electric pads.

5.6.2 Applicability for MAPS

There are numerous ongoing micro robot projects; between them they cover all of the requirements of MAPS, but there is no individual system which does so. With regard to locomotion, one of the major balances to be struck is that between precision and speed - many of the existing systems would require a choice between the two.

Power is another issue which would affect the suitability of many of the robot systems; they either don't deliver power for long enough or have adopted the use of cables. The only system that has successfully addressed the problem is the MiCRoN project, which utilises a wireless link. Due to this system's potential, an approach was made to form a collaboration to work with the MiCRoN team and adapt the robots to meet the needs of MAPS, however, for a number of reasons, this was not possible.

5.7 Fulfilling the MAPS functions

This section discusses in more detail the primary functions of MAPS, as outlined in Figure 5.5 and Table 5.1. With the additional understanding of the different characteristics outlined above, it describes how these functions can be successfully performed. It looks at the options available at the design stage and shows the origin of some of the decisions which have been made in the current MAPS design. 'Decision trees' are used to illustrate this process, which again are a common system engineering tool; these show the options considered, and the reasons for rejection of different designs.

5.7.1 Movement

One of the earliest decisions made regarding the MAPS design, was to employ motors and wheels to drive the robots into position. This decision dictated many aspects of the design and placed requirements on nearly all other systems; the decision is critically evaluated in Chapter 7.

Piezoelectric actuators are now being used in many commercially available high-precision positioning systems. However, despite extensive research, commercial components could not be found that met the size requirements of MAPS. This was often as a result of the driving electronics: piezo actuators often require very high voltages and also holding currents to keep the actuator in position. In the early stage of the design, the powering method for the robots had not been identified - for a long time batteries were used - a piezo system would have drained the batteries very quickly.

Various robots have been described above which use custom-made piezo systems. However, one of the problems identified is that such systems are generally slower than that required for MAPS. The other problem was partially that of simplicity: with the

available budgets and time constraints at the outset of the project, it was deemed less of a risk to base the chassis on a motor design, as this greatly reduces the complexity of the chassis and the required driving electronics.

A great deal of time was spent studying the market for available motors which could meet the MAPS requirements. The motor which was finally selected was the Faulhaber Smoovy 030-B series[1]. It is a brushless DC motor, which means it can be stepped, in 48 steps per revolution. Crucially, this motor is supplied with an integrated 125:1 gearhead, which allows for 6000 steps per revolution - this remarkably small stepping size is essential for the robots to meet the positional requirements. The motor and the gearhead fit into a footprint which is only 15 mm in length and 3 mm in diameter. The motors are driven by a simple 3-phase signature and come supplied with ready-made drive chips. These chips are relatively small (10mm x 10mm x 5mm), but their influence on the design of the electronics modules will be mentioned below.

Initial testing of the motors showed that they delivered the advertised torque of 0.88 mNm, which was believed sufficient to drive at least 100 grams of mass. The motors were found to exhibit a small amount of backlash, which was measured to be 14 μm (this is to be expected for all geared systems, unless the gearhead is spring-loaded, which is not possible on these scales). This can be accounted for in the robot's motion, but it does also make it essential to have a positional feedback system. One other element of the motors which should be noted was that the motor shafts could take very low lateral force; anything above 0.2 N resulted in damage to the gearhead. This influenced the design of the chassis, and eventually led to the development of specialised tools for mounting components onto the motor shafts.

5.7.1.1 Chassis design

Figure 5.8 highlights the options that were considered for the chassis. Once the principle of using motors had been decided, the next aspect of the design was how to mount them. A number of different designs were considered. There are other small robot projects that use 'tank tracks' for motion. These have the advantage that they give a stable platform on which the robot sits and they are have a large contact area with the ground, which helps with traction for such small masses. However, turning a tracked robot requires higher torque than other systems due to the higher friction associated with the tracks; this also leads to less accuracy in turning. There were also some concerns about the side load which a track system might exert on the motor shafts.

A simple direct-drive version of the robot was built, where the wheels were mounted onto the shafts of the motors. Such a system would have benefitted from a very simple

[1] http://www.faulhaber.com

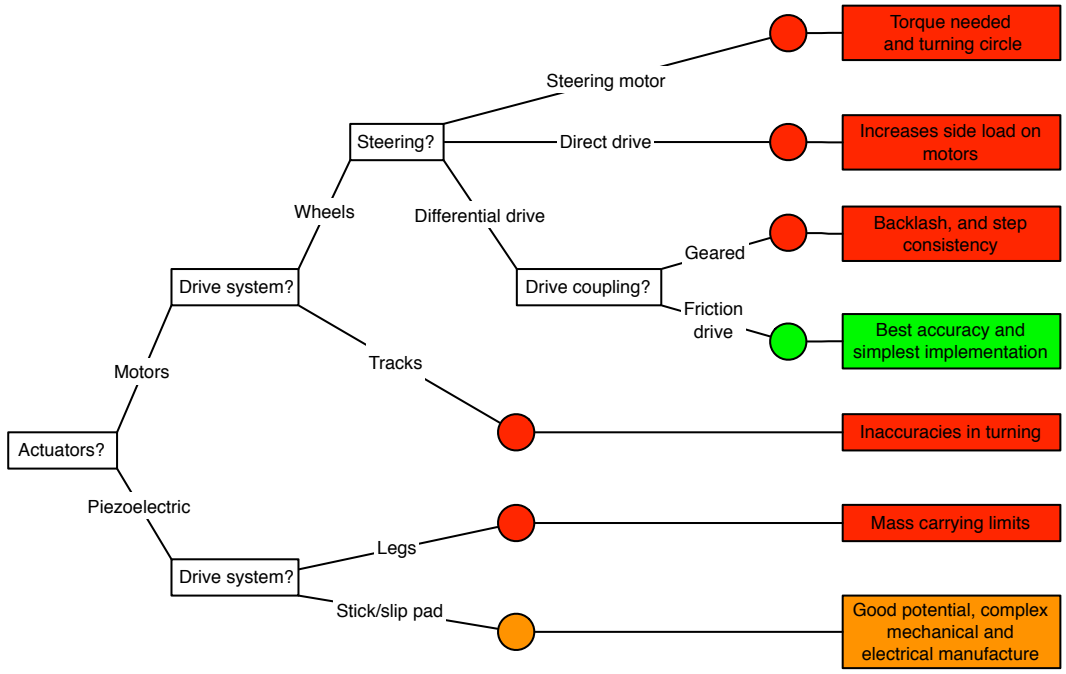

Figure 5.8: Decision tree showing the selection of the drive mechanism. The green indicates the selected option, the orange a viable but unexplored option, and the red, rejected options.

design and manufacturing process. However, it was found that the side-load on the motor shafts was too much as all of the weight of the robot acted through them. This design was therefore put on hold. To address the problem of side-load, discussions have been held with the motor manufacturers, Faulhaber, as to whether a tailor made set of micro-bearings could be installed onto the motor shaft. This would allow much higher forces to be applied to the shafts, but it would increase the size of the motors by around 5 mm in length. This idea is still being explored, and could lead to a wider range of different chassis designs.

The current design of the chassis is shown in Figure 5.9. It is based on a differential-drive method, where each wheel is independently driven by a motor; this allows on-the-spot rotation by driving the wheels in opposite directions. The wheels are driven through a friction drive between the pinion attached to the shaft of the motor and the O-ring which is used as a tyre. Note that the friction drive was selected as it overcame any problems of backlash. Each motor is mounted in a wing of the chassis that is itself, connected through a fine flexure point. A small tension spring is used to squeeze together this wing and keep the pinion in constant contact with the O-ring. Tests of this chassis design are discussed in more detail in the reports presented as part of the MAPS project (Taylor et al. 2010c).

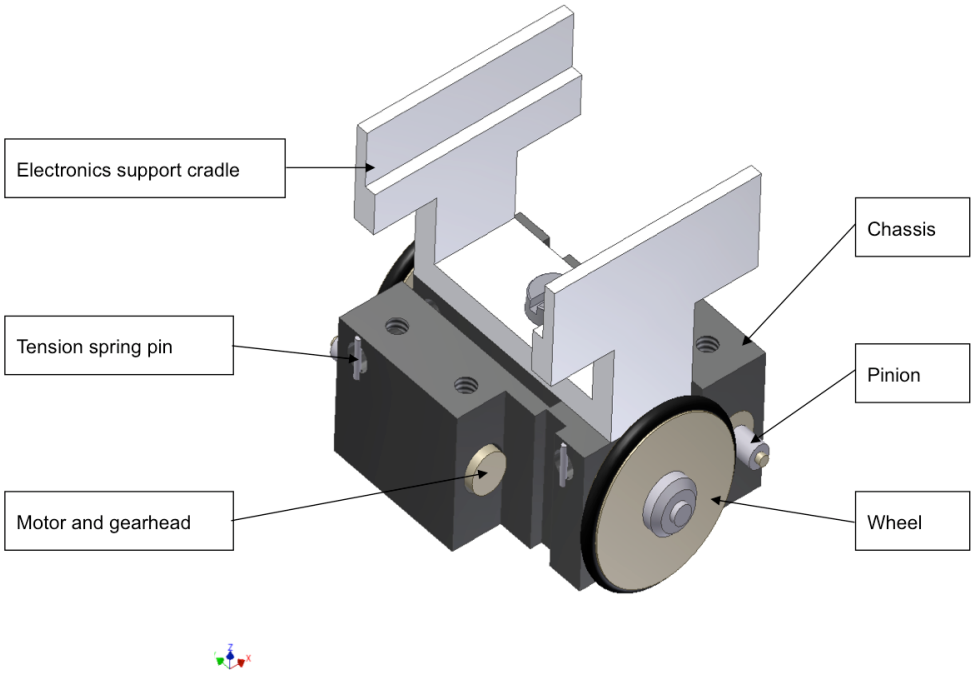

Figure 5.9: A CAD drawing of the MAPS chassis, this illustrates the spring-loaded flexures in which the motors are housed and also the friction drive system.

Testing of the chassis and the Smoovy motors has shown that the motor step size is slightly less than 1 μm and that over short travel distances the robot can be positioned to $\leq 7\,\mu$m. Details of these tests and other tests to assess the robot's performance are given in the next chapter.

5.7.2 Power delivery

The early versions of the robots were powered by a 3.7 V, 110 mAh Lithium polymer battery. These are lightweight batteries with a high energy density, which have been developed for use in model helicopters. Despite this, they still only last about 30 minutes during continuous operation of a robot. They are also 40 x 12 x 8 mm, which makes them hard to package in the robot footprint. Numerous other batteries were investigated, but anything smaller than these had correspondingly faster discharge times.

There are many options which could be considered to get round the problem of charging the robot; for instance, multiple fleets of robots could be used, so whilst some were observing others would be charging. However, this scenario works well for long observations, where the time for charging is long, but it is less effective if numerous short observations are performed in quick succession.

It was desirable to completely replace the battery, so inductive coupling was initially explored as a method to provide continual power. Here an oscillating magnetic field is generated by a high frequency current passing through a coil in the floor, and this field induces a current in a smaller coil on board the robot. Such systems are most efficient when the transmitting and receiving coils are in close contact and are relatively similar in size. For a robot system, with a large floor, it is therefore necessary to have a complex arrangement of tightly packed coils within the floor; this was the system employed by MiCRoN for their inductive powering system (Gao 2005).

Due to the inefficiencies of the power transfer in an inductive link, it would have been very challenging to transfer sufficient current to the robots to drive the two Smoovy motors, each of which can draw a maximum of 300 mA. Power which is not successfully transferred in an inductive system is often lost in the formation of eddy currents within any surrounding metals, this leads to the metal heating up considerably. Since EAGLE will operate in the infra-red, it would not be acceptable to have a pick-off system which might generate heat. With this is mind, the inductive coupling floor was not pursued.

The current version of MAPS operates using a continuous direct-coupling method, which is based on the mobile phone charging "Wildcharge" system[1]. Here the robot travels on a charged surface consisting of an inter-digital electrode pattern. This surface

[1] http://www.uk.wildcharge.com/

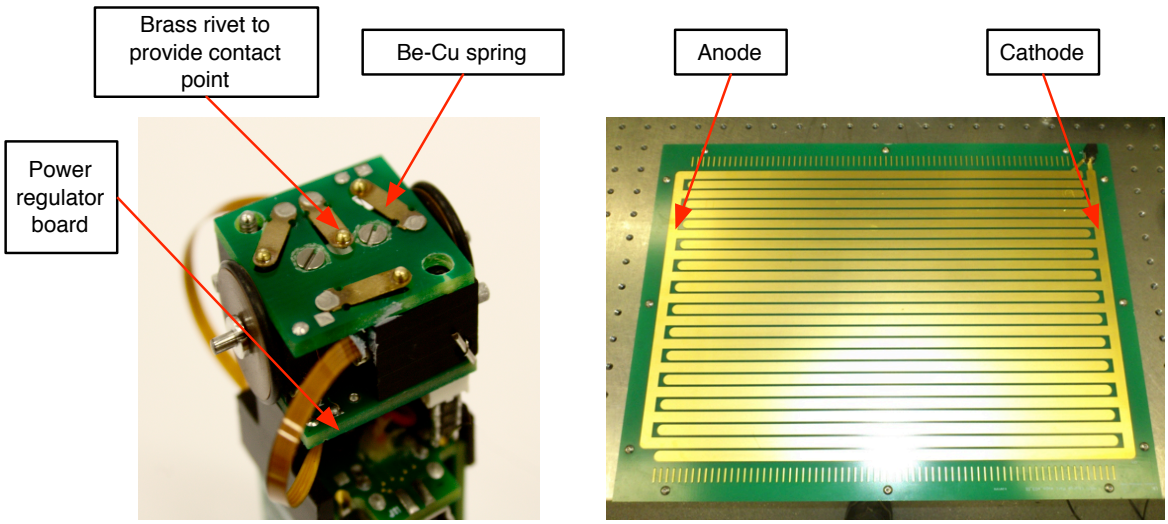

Figure 5.10: On the left is an image of the underside of the robot, which shows the four springs of the power pick-off system. There is one contact directly in the centre, and three at an equal distance from the centre, separated by 120°. On the right is the power floor, showing the two inter-locking contacts.

has been manufactured from a conventional Printed Circuit Board (PCB). A series of carefully arranged, spring-loaded electrode couplers mounted on the base of the robot continuously supply the power. Both the power floor and the power pick-off board are shown in Figure 5.10.

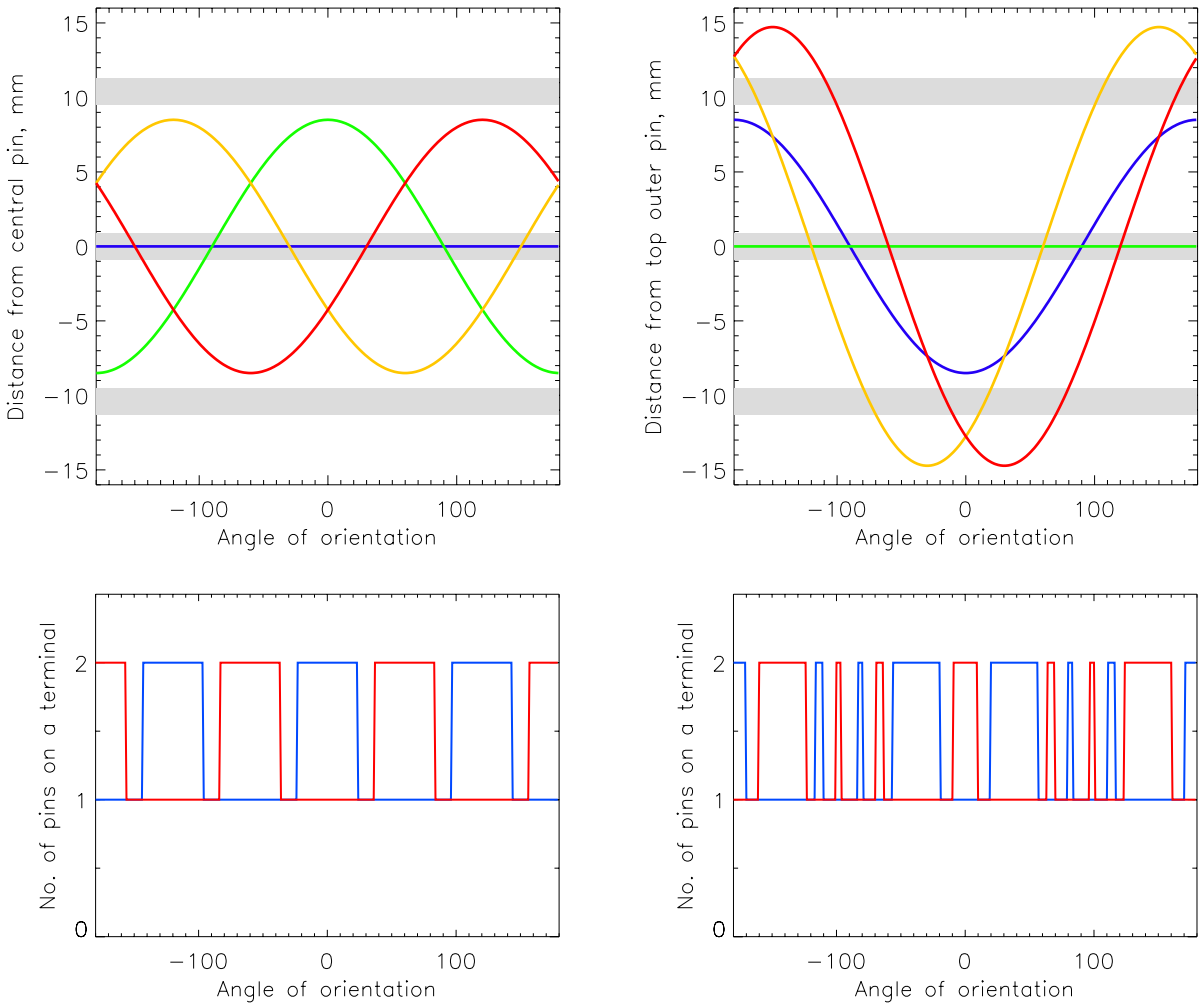

Figure 5.11: This diagram demonstrates that it is possible to always draw power from the power floor with the arrangement of four pick-off pins shown in Figure 5.10. The coloured lines in the top two panels show the positions of the four pins on the power floor as the robot is rotated. The grey bands on the figures, indicate the 'dead' regions of the board, which lie between the power terminals; the alternating positive and negative terminals are indicated on the plots also. The bottom panels show the cumulative number of pins on either the anode or the cathode as the robot rotates, shown by the red and blue lines respectively. There is always at least one pin on each of the anode and cathode. A fuller discussion is given in the text.

The geometrical design of the pick-off springs and power floor ensures that at least one contact is touching the anode and one touching the cathode, irrespective of position and rotational orientation. Proof of this concept is given through the use of the diagram in Figure 5.11. Consider if the central pick-off contact was on a dead region, between the anode and the cathode: is it possible that for a particular orientation power could be lost? On the left hand side of Figure 5.11, this scenario is played out. The top panel shows the position on the pins relative to the central pin as the robot is rotated through 360°. The graph below, shows the number of pins on the anode in red and the number of pins on the cathode in blue. It is clear that at no point is there less than one pin on each of the two terminals.

The right hand side of Figure 5.11 shows a similar scenario, but this time for the situation where one of the three outer pins lies on the dead region of the floor. The robot is again rotated through 360°, but this time about the 'dead' pin, rather than the centre. As can be seen, there is still no point at which the there is less than one pin on each terminal. Since the arrangement of pins on the base gives the system threefold symmetry, this does not have to be repeated for the other outer pins. The two examples illustrated in Figure 5.11 are the 'worst case' scenarios, where one of the pins is continually out of action, and yet the floor still works. This therefore demonstrates that the pick-off system will work for all positions and orientations.

The pick-off springs require supporting circuitry on the robot to couple, manage and deliver the power from the charged surface to the robot drive electronics. Specifically, two additional PCBs are attached: one below the chassis and one above it. The lower of these simply couples the power from the pick-off pins to the other board, where a diode network always ensures the polarity of the output power is constant. The contact springs are manufactured from a 0.1 mm thick Beryllium-Copper (Be-Cu) sheet, as shown in Figure 5.10. The electrode contacts themselves are made from miniature rivets soldered to the Be-Cu springs.

A fuller discussion of the performance of the power floor concept is given in the next chapter.

5.7.3 Electronics modules

Much of the design work for the electronics module was carried out by Dreampact, a small start-up electronics firm, which is based at the Heriot-Watt Research Park. There are four primary parts to the module - the motor driver chips, the wireless antennae to send and receive commands, the processor to interpret commands and a small power regulator system.

The wireless system is a 2.4GHz radio controller unit implemented on a Chipcon

SmartRF04EB evaluation board and its associated CC2510EM daughter module. An RS232 allows the control computer to interface with the evaluation board. This system was selected as it has a range of a few metres (which is more than adequate for MAPS), is low power and has a small footprint on the circuit board.

The system allows a range of commands to be sent to the robot, a full list of which is given in the MAPS user guide (Pooley & Thompson 2010). The commands can be sent individually and acted upon immediately, i.e. *Move forward 1000 steps*, or they can be stored in the on-board memory and acted upon on receipt of a *Go* command. The memory can store 40 commands. Each robot can be addressed individually or commands can be sent to them all at the same time, which is particularly useful for the *Stop* commands that force the robots to stop immediately. The software has been designed to operate in a python environment, and is platform independent.

The robot can also be told to report its current status, of which it has a number of different settings:

- IDLE: The robot is present and waiting commands.
- READY: The robot has commands stored and is ready to execute them.
- RUNNING: Motors are moving.
- DONE: Last command has been performed successfully.
- ABORTED: Last command was interrupted by the Stop command.
- LOW: Battery needs recharging.

The electronics modules were developed in three stages; these are roughly shown in Figure 5.12. The first version of the electronics allowed two motors to be driven, which did not have the wireless enabled and were therefore programmed via an RS232 connected directly to the computer with only preset programmes transferred to the module. In the second iteration the hardware was kept mainly the same, but the wireless control was implemented. Both of these systems were designed to operate from a battery and were designed so that the circuits boards relatively neatly enclosed the battery, as can be seen in Figure 5.12. As they were used for development, they also contained a mini USB connection to allow the processor to be easily reprogrammed.

The third, and currently final, iteration of the electronics design, allows control of three motors. Some of the redundant components from the first design have been removed, and so the whole arrangement has been repackaged into a much smaller 18 x 18 x 18 mm cube. This is formed from four small PCBs that have a flexible internal layer which connects the boards and allows them to be folded into the cube. The addition of the third motor driver allows for the potential addition of another motion stage for the robots. For instance, work has been done to develop a rotation stage, which allows the mirror to rotate independently to the rest of the chassis.

One of the limiting factors for the size of the modules is the drive chip of the motors; these have a through-hole mounting, which limits how the boards can be arranged. It is conceivable that the signals from this drive chip could be generated by the module's processor itself, thus bypassing the need for the driver chips. Indeed, the whole driving electronics could be dramatically reduced in size by designing and manufacturing an Application Specific Integrated Circuit (or as they are more commonly known, an ASIC). This would reduce the whole electronics module to a single circuit board, but, while it would form an interesting area of further study, ASIC design and manufacture is expensive, and generally only becomes financially viable when a large number of units is required.

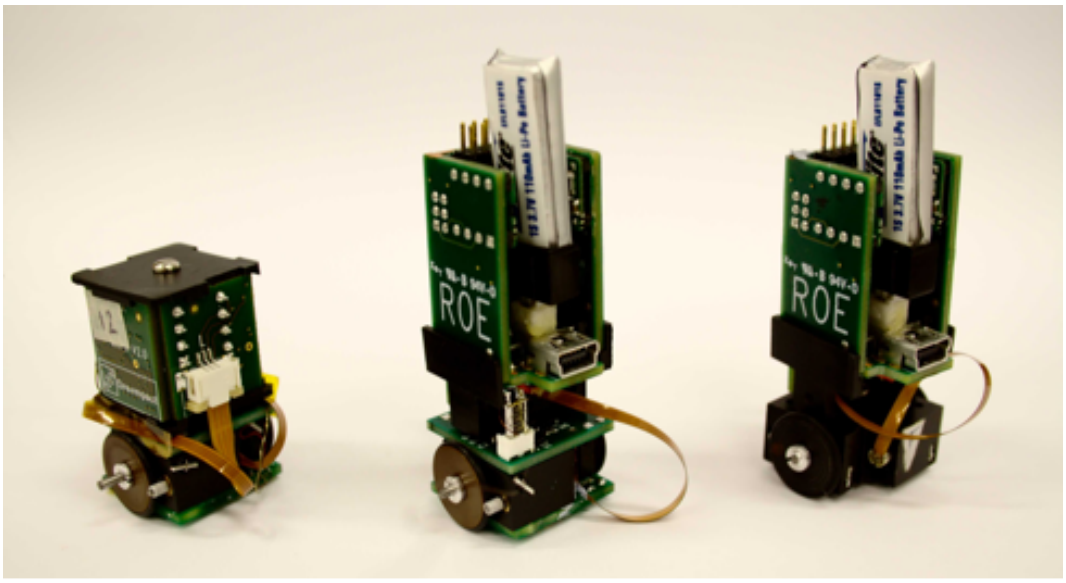

Figure 5.12: The three primary different versions of the robot. On the right, the first electronics powered by a battery, in the middle the same electronics, but with the power floor electronics delivering power. Finally on the left, the most recent version of the electronics module, also with the power floor electronics.

5.7.4 Metrology

Numerous methods were considered to determine the position of the robots; a particular issue being whether the positional determination should be done on or off the robot. A schematic representation of the decision process is shown in Figure 5.13. Although there was promise in some of the onboard ideas (particularly a mouse-like imaging system which analyses the floor), in general all the on-board systems require considerable additional space and power. For this reason it was decided to not use on-board systems.

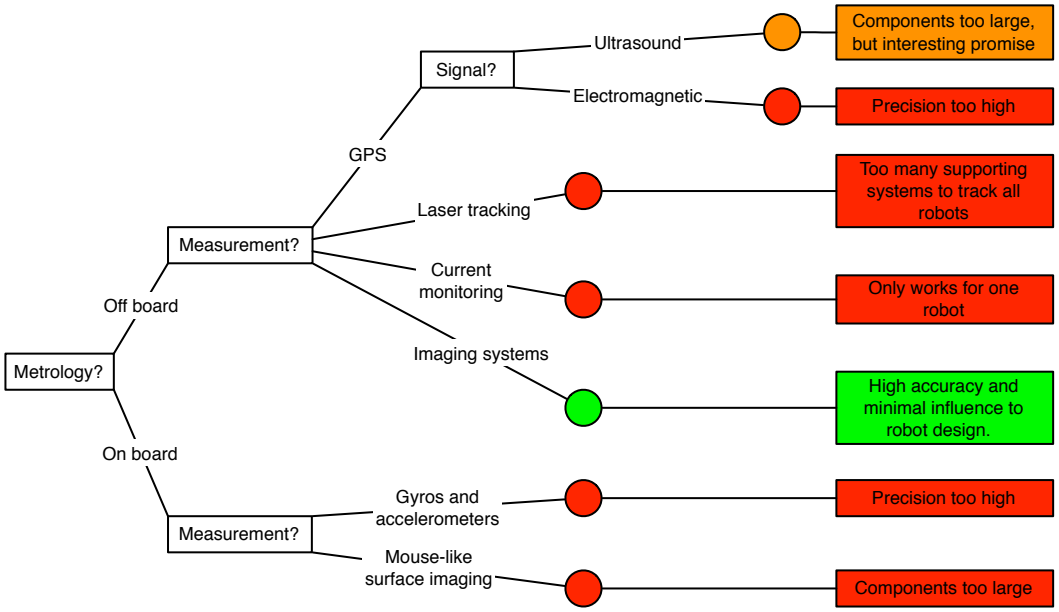

Figure 5.13: Decision tree showing selection of metrology system. All the ideas that were considered are shown here, including some of the more ambitious, such as monitoring the position of the current being drawn from the power floor. Not all these ideas are discussed in the text, but the reason for rejection is shown in the red boxes.

One appealing idea was to use a triangulation system, like a miniature GPS. To achieve micron precision over such a short distance is not possible with conventional electromagnetic systems, so ultrasound was investigated. This would require each robot to have an ultrasound transmitter that would be detected by numerous receivers around the operating area. These systems are available commercially[1] but, not for the MAPS size regime: the transmitters are a few centimetres cubed and the best precision is of order hundreds of micrometers, not tens of micrometers. It might well be possible to improve these characteristics, but this would be a separate investigation.

MAPS has currently adopted an imaging system to monitor the position of the robots. High resolution targets are attached to the top of each robot, and the whole operating area is then imaged by a camera, with the position determined through an analysis of the robot's targets. Such systems have been shown to work to extremely high accuracy in other robotics projects, for instance the MiCRoN project measured positions to an accuracy of 5 μm (Estaña & Wörn 2003). The design for MAPS would have to be different due to the presence of the POM, but this does show that in principle imaging can deliver the required accuracy.

[1]There are many companies offering such systems; one of the closest to meeting the MAPS requirements is http://www.hexamite.com

The metrology system must achieve three primary purposes:

- Determining the position of robots;
- Identifying which robot is which;
- Proximity warnings.

All the robots are visually identical so it is necessary to identify which is which. To do this a dedicated start-up algorithm could be used. This would command one of the robots to turn on the spot, whilst all the others remained stationary, this would then identify that particular robot. The process would then be repeated for all the other robots.

There are admittedly two drawbacks to the imaging system, which will be discussed in greater detail in the Chapter 7. Although one camera is sufficient for the current version of MAPS, if it were ever deployed in a larger operating area such as the proposed 2 x 1.5 m focal plane of EAGLE, a number of cameras would have to be used. The other, is that the camera has to be mounted above the focal plane, which inside EAGLE could potentially be difficult.

5.7.5 Analysis of alignment

To assess the behaviour of the MAPS system it is necessary to have some simulation of the light path of the telescope. This would not be an integral part of MAPS, and would be the only aspect of the design which would not be needed if the system were to be used in EAGLE. The test could simply be carried out by mounting a laser light source above the focal plane, the robot could then be driven into position below this light source and used to reflect the light onto a detector camera, it should be possible to manoeuvre the robot to get this light source perfectly aligned with the centre of the CCD. This test, and ways in which it could be extended to also include assessment of the tip and tilt of the robot, is discussed in more detail in Chapter 6.

5.8 Conclusions

This chapter has explored the various design characteristics of an independent MAPS system; from these it has been possible to identify quantifiable requirements that the system must meet. With an early investigation into the possible design of the sub-systems, a system architecture diagram can be produced. This diagram, shown in Figure 5.14, details the different sub-systems and their interactions. The two primary sub-systems are the robot and the command and control; and both of these are split into a number of very different modules.

In the next chapter the performance testing of many of the sub-systems and modules is described. This allows comparisons with the requirements outlined here to be made and therefore an assessment of the current status of MAPS can be given.

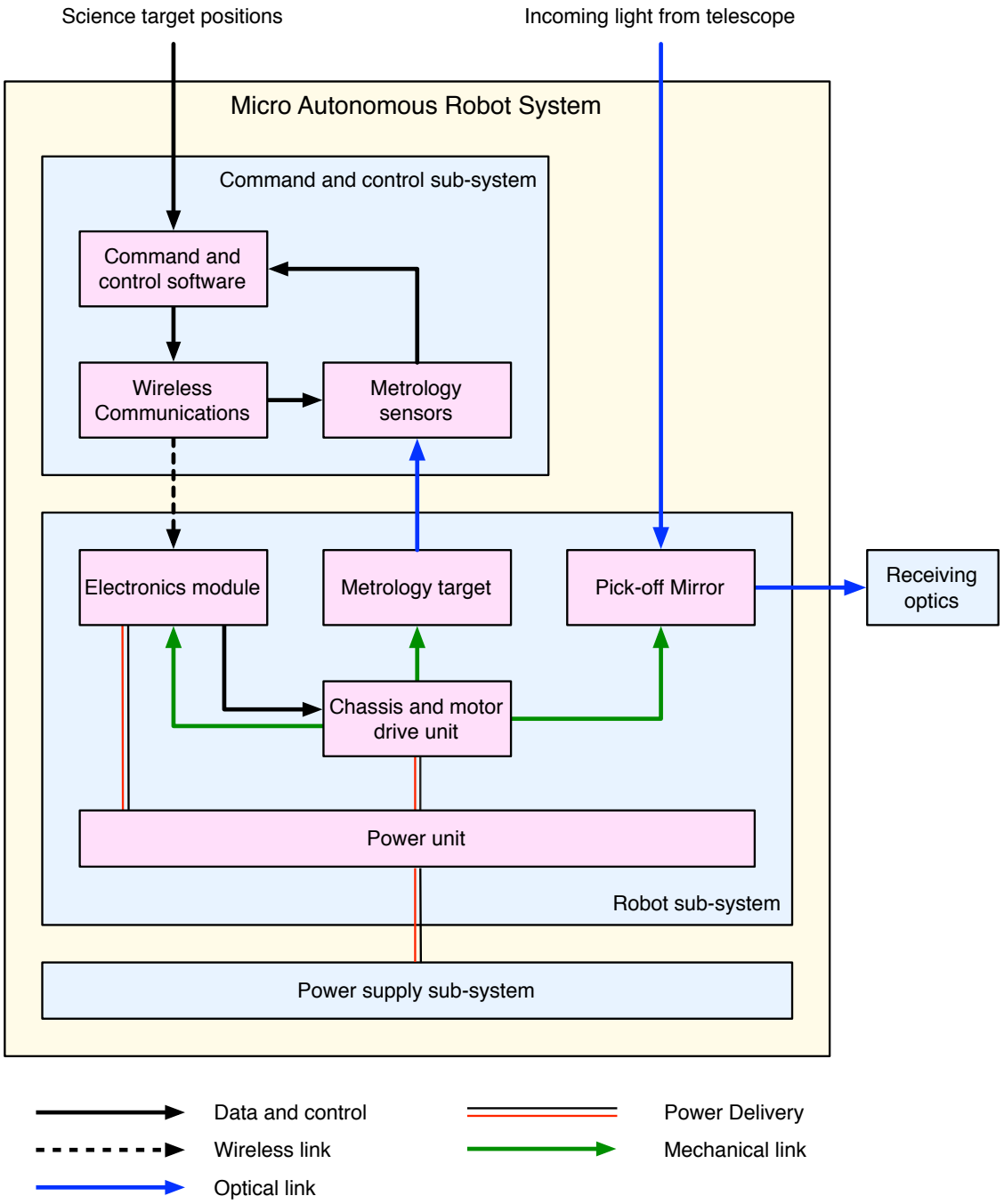

Figure 5.14: System Architecture Diagram.

Chapter 6

Characterisation of MAPS

Good decisions come from experience, and experience comes from bad decisions.

Anon

6.1 Author's note

This chapter presents a more detailed description of the MAPS sub-systems and illustrates some of the design's evolution. It goes on to show the quantitative testing which has been carried out on various aspects of the design. Particular focus is given to the metrology methodology used to determine the positions of the robots - some of this work is taken from a paper delivered to the SPIE Astronomical Instrumentation conference in Amsterdam earlier this year (Taylor et al. 2012). There are also elements from the software documentation delivered to accompany the command and control system. First though, the chapter begins by reporting the development of the design for the power delivery sub-system.

6.2 The power floor

The robots draw their power from the floor on which they operate; this concept was described in detail in the previous section 5.7.2 and shown in Figure 5.10. Here the actual implementation of the design is discussed: it follows a fairly temporal layout, detailing the changes to the design as they happened.

6.2.1 Testing the design

The power floor was first demonstrated to work using a version of the pick-off electronics that powered an LED when placed on the surface. These tests showed that, in principle,

the concept worked extremely well: wherever the LED unit was placed, it always drew power.

The power pick-off sub-system was therefore integrated onto a robot, which at the time, used the phase 1 electronics module. It was quickly found that as the robot moved across the floor, it would momentarily lose power; this was due to the contacts effectively 'bouncing' along the surface as the robot moved. This problem had been anticipated and the design of the electronics allowed for addition of a capacitor to provide power for the moments when contact was lost.

A version of the robot was therefore set up which was run from a battery, but also incorporated the power floor electronics, with the output from the floor being dissipated through a resistor. Small trailing leads were connected between the power points on the robot to an oscilloscope to measure the voltage across the resistor. Through this system the duration of the power losses could be monitored, while the robot would still keep on moving.

First the robot was commanded to move 10000 steps forward, this equates to roughly 1 cm of travel; this was then repeated 40 times, with the cumulative frequency of different power loss events being recorded. The same procedure was then repeated for 10000 steps backwards, 100000 steps in each direction and also rotation tests. The combined results from these different tests are shown in Figure 6.1.

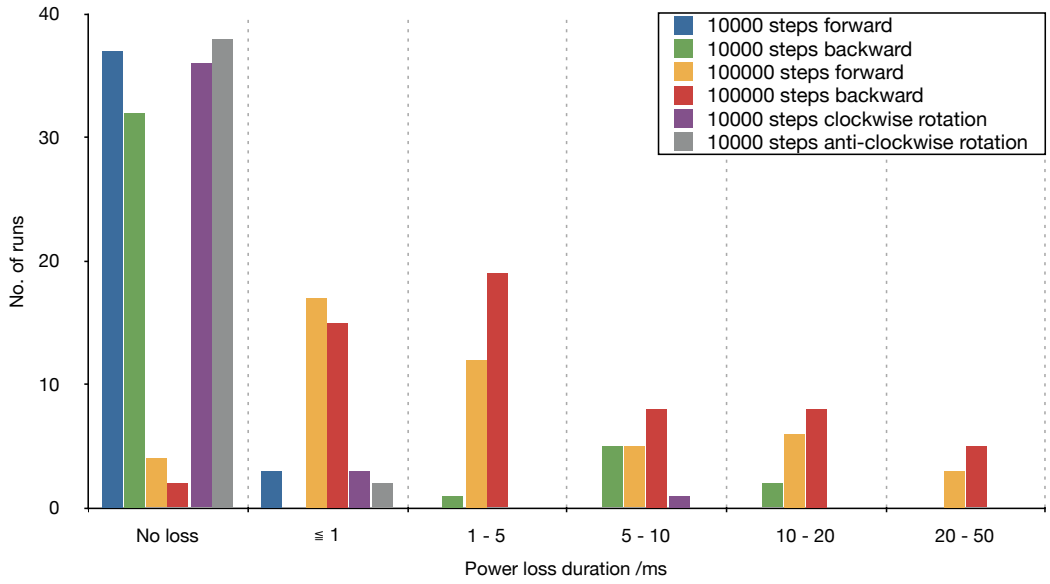

Figure 6.1: Variation in the duration of power losses with the power floor. The robot performed each of the six different motions 40 times, with the frequency and duration of power loss events being recorded. For some of the longer runs, more than 1 event was recorded, hence the cumulative number of runs can appear to exceed 40.

The majority of short movements (10000 steps) do not show any power loss, both for straight runs and rotations. However, for the longer runs power outages occur in over 90% of runs, and often more than one event occurs per run. The most important measurement is the duration of the longest power loss as this dictates the size of the capacitor. It is clear that numerous events can be expected which last for up to 50 ms, however, no longer power losses were recorded. One other interesting aspect is that there is a discrepancy between the forward and the reverse motions - this is especially noticeable for the short runs. It was found that this was due to the positioning of the stabilisers on the robot's base, as described below.

The capacitance (C) required can easily be found using: $C = It/V$. The maximum current (I) that can be drawn at one time is 0.7 A, that is 0.3 A per motor and 0.1 A for the control electronics. The voltage required (V) is set by the power floor, which is 9 V. Assuming a maximum power loss duration of 50ms, this would require capacitance of 4 mF. It was not possible to find a 9 V capacitor which had this capacitance and a suitable footprint for MAPS. However, 'Cellergy' produce 5.5 V capacitors that have a capacitance of 8 mF (part no. CLG05P0008L12); combining these in series to give sufficient voltage therefore yields the required 4 mF.

Ideally a capacitor that could bridge a longer time gap would have been employed, but again the size constraints of the robot would not allow this: even the Cellergy capacitors that were used have dimensions of 12.5 x 12 x 3.1 mm. It was possible to fit two of these inside the folded electronics module, and consequently, the introduction of the capacitors had no impact on the overall dimensions of the robot. With respect to the capacitance, it is important to note that in testing of the current drawn by the electronics module, at no time did it exceed 0.2 A. This therefore increases the potential time lag of the capacitors to over 150 ms.

At the time the capacitors were selected, a number of other improvements to the pick-off design were planned. These were to address the fact that the addition of the Be-Cu contact springs reduced the robot's ability to move in a straight line. The actions taken to improve the robot's performance are discussed in the next sections.

6.2.1.1 Change of stabilisers

The robot has two stabilisers to maintain balance on the floor; the off-centre mass of the POM ensures that the robot will always tip backwards onto a rear stabiliser and thus the three same points are always in contact with the floor - the base of each wheel and this stabiliser. Before the addition of the power board, the stabilisers were fitted within the footprint of the chassis and were placed an equal distance from each wheel. However, the positions of the contact springs meant it was not possible to keep these

positions and so the stabilisers were placed off-centre; this is shown in Figure 6.2. This made the robot rather unstable, and it is believed that this was responsible for the observed discrepancy between the forward and reverse motions. A new pick-off circuit board was therefore designed that allowed the stabilisers to be in symmetric positions, again shown in Figure 6.2. This change improved the robot's performance, removing many of the erratic stops and starts, but the straight line performance was still poor.

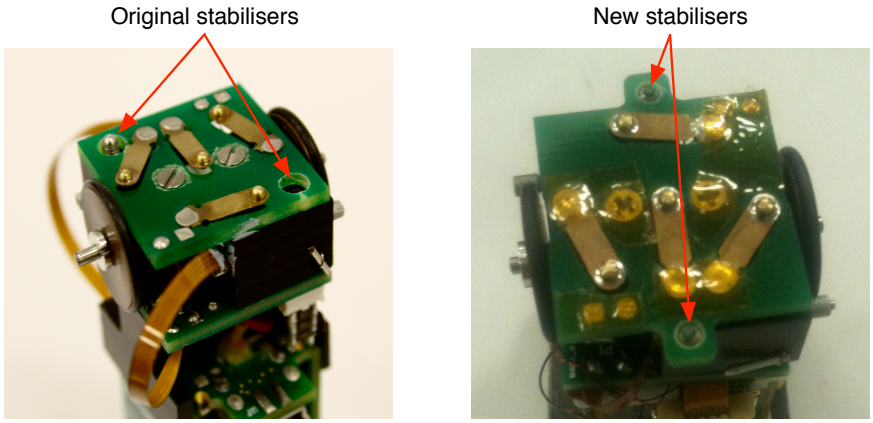

Figure 6.2: Repositioning of stabilisers: on the left can be seen the position of the original stabilisers, while on the right are the new on-axis stabilisers. These significantly improved performance, however they increased the footprint by 6 mm in one direction. The power board is still within the 30 x 30 mm footprint requirement

6.2.1.2 Spring modifications

It was identified that the poor straight line performance was due to the downward force of the pick-off springs lifting the robot slightly from the surface. This caused the wheels to effectively slip as they momentarily lost contact with the floor. Since this happened to each wheel at different times, the robot would turn during these moments.

Equation 6.1 shows how much force, F, is required to cause a deflection, δ, in a cantilevered beam, which is an accurate description of the pick-off springs (from Gere & Timoshenko 1991). The beam is assumed to have a width w, a length l, and a thickness t in the direction of the deformation. From Budynas & Nisbett (1980) the Young's modulus E of the beryllium copper springs is $1.24\times10^{11}\mathrm{Nm}^{-2}$.

$$F = \frac{\delta E w t^3}{4l^3} \tag{6.1}$$

With the force known, the mass required to depress the spring can easily be calculated. The initial design of the pick-off system had the springs mounted such

that the deflection needed would be only 0.1 mm, this would therefore require a mass of 39.5 grams. However, it was found that such tiny deflections were not sufficient to keep good electrical contact with the floor. Small shims were therefore added between the base of the chassis and the pick-off spring board, which brought the springs nearer to the floor, thus increasing the deflection. Since δ is proportional to the mass, it meant the robots were not heavy enough to deflect the springs, and keep the wheels in contact with the floor.

An attempt was made at this stage to improve the contact with the floor by adding small rare-earth magnets above each of the pick-off springs. The power floor was then placed on a metal surface with the intention that the additional downward force provided by the magnets would improve the power continuity, even for small deflections of the pick-off springs. In a test setup using a dummy chassis this appeared an excellent solution, however, upon assembling the complete robot, it was found that the magnets were attracted to the motors inside the chassis more strongly than the floor. It might have been possible to modify the chassis to include shielding of the motors from the magnetic flux, but it was decided that this could not be practically investigated at the time.

A new sheet of reduced-thickness beryllium copper springs was purchased which was only 0.1 mm thick. For a robot weighing 50 grams, these new springs should, in theory, not lift the wheels from the ground even for spring deflections as large as 1 mm.

6.2.1.3 Weight addition

Despite the improvements outlined above, there were still problems with the power floor. The issue of wheels spinning and therefore turning during motion were significantly reduced by the replacement of the power springs, but there were still problems with straight-line performance (believed to have a different origin and discussed in more detail in section 6.5.2). Also, the robot did occasionally lose power, but the addition of weight to the robot helped improve the continuity. This might at first seem strange - surely there should be a point at which, once the robot has reached a certain mass, the springs will be deflected such that the wheels and the stabilisers are in contact with the ground and even if more mass is added, it would not deflect the springs anymore. However, as mentioned earlier, the robot was designed to rest on the rear stabiliser only, and therefore the front stabiliser is slightly shorter than the rear one. This means that during motion, the robot actually rocks forward and will not rest on either stabiliser, but is instead supported by the springs themselves. It is at these moments that the additional weight is an advantage and improves the continuity.

The first tests of the floor were carried out using trailing wires and an oscilloscope,

but it was later found that the power behaviour of the robot could be monitored more remotely. The potential difference between the positive and ground track of the floor is 9.06 V. It was found that when the robot is sitting stationary on the surface this drops by 20 mV; when the robot starts to move; there is an additional drop of another 20 mV. This therefore gave an excellent way to monitor the motion of the robot, and the regularity and duration of power losses. A PicoLogger 1000 (a digital voltmeter) was therefore connected to the floor, an example of a typical observed signal is shown in Figure 6.3

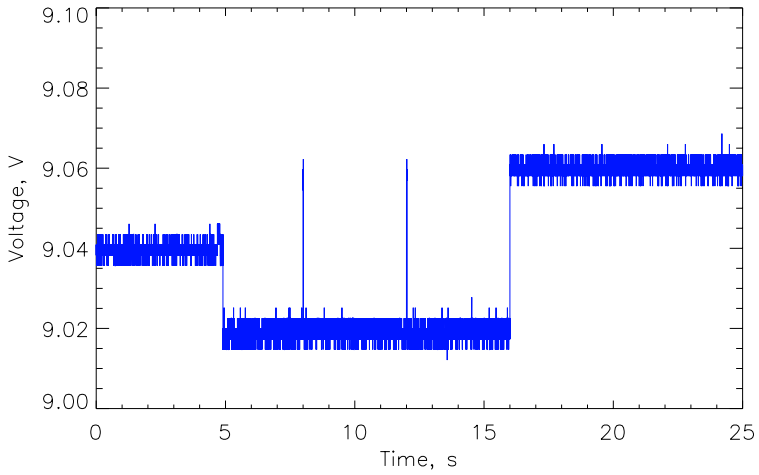

Figure 6.3: An example of the PicoLogger results showing the voltage across the terminals of the power floor. At the start the robot is stationary, drawing some power to listen for commands. At 5 seconds, it begins to move and the voltage drops. At 8 and 12 seconds it loses electrical contact with the floor, but regains it sufficiently quickly that the capacitors bridge the gap. At around 16 seconds the robot loses power completely.

Tests were carried out to determine the variation in power losses while various different mass weights were added to the robot. The addition of around 30 grams improved the performance and beyond this there was little further benefit to adding more weight. It was therefore necessary to find a way to add weight to the robot without increasing the size significantly. The ideal solution would be to re-manufacture the chassis using a dense metal rather than the current Delrin (a plastic); this would also have the advantage of lowering the robot's centre of gravity. However, the fine flexure point required to keep the motor housing in contact with the wheel would be very hard to reproduce using a metal. The current intention is therefore to manufacture the retainers which hold the electronics unit in place from a metal, these too are currently a lightweight acrylic. Materials such as Densimet, a tungsten alloy, could be used which has a density of 18.5 gcm^{-3} - this is 1.5 times that of lead.

6.2.1.4 Floor smoothness

The tests of the weight performance also highlighted a concern with the power floor: the PCB board on which the power tracks were manufactured is not completely smooth. Measurements using a Coordinate Measuring Machine showed that there is a height difference of as much as $50\,\mu m$ between the electrical surface of the track and the surrounding silk-screen layer between the tracks. It was found that when moving perpendicular to the tracks the springs have to overcome these height differences, which leads to vibration in the spring and power loss. It was found that the robot was much less likely to lose power when moving parallel to the tracks.

The current version of the board is the third iteration of the design. In PCB manufacturing, a layer of solder resist is placed over the surface of the board to properly isolate different non-conductive top surfaces. Attempts were made to build up the layers of solder resist such that they were brought up to the same level as the tracks, but this was not successful. Another method used was to coat the board with a hard-setting epoxy resin and then to sand the surface back down to the level of the tracks. This gave an extremely flat surface, but it also damaged the thin layer of gold which coats the top surface of the tracks, and thus contact between the springs and the floor deteriorated. There are other methods which could be used to manufacture the surface such as techniques used in ceramic PCB manufacture; however, those are prohibitively expensive for such a large PCB.

6.2.2 Conclusions

The power floor has, in principle, been shown to work relatively well, but not faultlessly. The design has been through many different iterations to bring it to its current technical readiness level. There are, however, outstanding problems which have not yet been fully addressed. One of these is the manufacture of a flat floor, although with greater funds, it is believed solutions are available. This would certainly improve the continuity of the power delivery. The capacitance of the capacitors is another major factor which influences the system's performance. Capacitor technology is continually changing and developing and it is likely that in a short space of time it will be possible to purchase capacitors with a similar space envelope but higher storage capacity. As the early tests showed, the discharge time of the current capacitors is very close to the longest observed power losses; a small increase in capacitance could therefore significantly improve the floor's performance.

Another idea would be to incorporate a small battery onto the robot which would provide power during the power losses, the battery could then be recharged when the robot was stationary. This system would require an independent battery-

powered circuit to be continually monitoring the input from the floor, such that it can supply power immediately when power is lost. Small capacitors would probably still be required on the main electronics to bridge the small gap before the back-up started working. Whether such a system can be developed that still meets the space requirements, despite the battery, the capacitors and additional circuitry needed for both the monitoring and recharging the battery, is an area of ongoing research.

6.3 Metrology

As was discussed it section 5.7.4, it was decided that a visual system would be the most appropriate method for determining the positions of the robots, and thus providing the closed-loop control feedback. This sub-system comprises: a camera, optical targets on-board the robots, the power floor and finally, the algorithms to process the images. This section reports on the evolution of the design, the reasons for certain design choices and provides a quantitative analysis of the system's performance.

6.3.1 Background

Many of the other robot systems discussed in section 5.6 require feedback of their positions - although some, such as the Imina robots (for use in microscopes) assume that positional feedback will be determined through inspection by the robot operator. Imaging the operating area is a common technique for many systems. For instance the Starbugs described earlier, rely on three measurement points on the robot's surface to determine their position (Goodwin et al. 2010).

The MiCRoN project uses a novel positioning technique (Estaña & Wörn 2003), where a series of concentric circles on top of the robot are imaged. This real image is then compared to a 'virtual' image of a large set of finely-spaced circles which cover the whole operating area. This generates a Moiré pattern at the points where the two sets of circles intersect, and from this the position of the robot can be found to an accuracy of $\pm 5\mu$m across a 25 x 25 cm operating area. The technique is not directly applicable to MAPS, as the mirror sits at the position where the optical targets should be mounted. An attempt was made, though, to recreate a similar system, and it was found that this technique ultimately relies on the generation of a large number of measurement points at the Moiré fringes. It was considered that other methods could be used to generate many measurement points, which might better suit the MAPS design.

Fibre positioning systems such as OzPoz on FLAMES (Gillingham et al. 2000) use a camera which is mounted with the gripper that moves the fibres. This means the camera does not require a large field-of-view, and consequently high-precision measurements

can be made. In larger optical fibre systems, such as China's LAMOST instrument, more interesting solutions have to be considered (Yonggang et al. 2010). Here, 4000 fibres need to be imaged across a focal plane which is 1.75 m in diameter, a scale that is not dissimilar to EAGLE's. The proposal by Yonggang et al. is to mount a series of linear CCDs on a rotating arm which swings over the tops of the fibres, thus precisely recording their position. The challenge of imaging numerous fibres on large focal planes is going to be a common one in years to come as there are a number of high-mulitplex, fibre-positioning systems being planned for telescope facilities around the world. This was discussed extensively at the SPIE conference in Amsterdam in 2012, e.g. MOONS, 4MOST, BigBOSS, WEAVE and PFS (see conference proceedings for as-yet, unpublished papers).

Centroiding on sources in an image is a common technique for astronomers, as it is essential for precise astrometry. Often this is for finding the positions of point sources, whose shape is dictated by the PSF of the telescope. Sub-pixel accuracy is not uncommon, with authors such as Niwa et al. (2010) claiming precision of $1/1000^{th}$ of a pixel. As will be discussed in the following section, the targets that are used in MAPS will not be point sources, but the shape will be an approximately Gaussian profile, which is similar to the PSF of many telescopes. Some of the common techniques available for centroiding on such sources are discussed in Shortis et al. (1994).

6.3.2 Target imaging

The requirement for the metrology system given in Table 5.2 is for measurement accuracies of $\leq 7\mu$m. In order to achieve this, it is necessary for the measurement to give sub-pixel accuracy, a concept which is discussed later with reference to the camera selection. This level of precision is often achieved by centroiding on a point source, such as an illuminated pinhole. The exact centre of the pinhole is found by performing a 'centre of gravity' measurement on the flux levels detected in a small region surrounding the pinhole. This method works best with well-illuminated pinholes where it is easy to obtain a high signal-to-noise ratio. A conceptual design which was considered would be to mount a series of LEDs around the mirror and to place a set of pinholes over this, thus providing a set of precise measurement points. This would require additional wiring and was deemed to be another layer of complexity which should be avoided.

An alternative concept to centroiding on pinholes is to generate a high-precision printed target, which is imaged solely through light reflected off the surface. In such a design, any pattern could be printed on the surface, but the best pattern is the most simple: a circularly symmetric spot, as it allows accurate, simple centroiding. To ensure sufficient light is reflected from the spot, it must be larger than the pinholes used with

an LED - these are typical tens of microns in diameter, whereas spots need to be over a millimetre. This presents an opportunity: by generating the spot as a 2D Gaussian profile, rather than merely a circle, it was found that the fitting procedure can be more accurate. Also finding the moments of Gaussian profiles is a commonly-used tool, and therefore fast and accurate algorithms are readily available.

In the comparison by Shortis et al. (1994) they found that Gaussian fitting generally out-performs centre-of-gravity fits; this is due, in part, to the increased amount of data provided by the wings of the Gaussian. This is especially true when the background contribution is non-negligible.

It was determined that the targets should therefore be comprised of a series of these Gaussian spots, nestled around the outside edge of the mirror, all at a fixed radius from the mirror's centre. It is then possible to further improve the measurement accuracy by fitting the centres of the measured spots to an ellipse - note that the spot centres actually define a circle, but since the target is nearly always viewed from an angle, it is necessary to fit to an ellipse instead.

6.3.2.1 Target evolution

The natural position for the target is right on top of the robot. Since most of the top surface is covered by a mirror, there is little room for mounting a target. The original design was therefore to mount the target on a small raised section immediately behind the mirror, thus not blocking the theoretical light path of the telescope. This design can be seen in Figure 6.4. Also of note in this design, is that the spots are red; this was to aid the process of target identification and will be discussed in more detail in section 6.3.3.

Figure 6.4: The different designs for the targets: the original on the left, the second iteration in the middle and the final design on the right.

Initial testing of this target found that good centroiding could be performed on the spots. However, since the spots were only on one side of the mirror, the ellipse fitting introduced a large error; this can be seen in Figure 6.5. In this test the target was aligned such that the mirror was facing along the y-axis; the measurement in y is therefore considerably worse than x, as there was only a small range of points in the y direction to constrain the fitted centre. It would potentially have been possible to use only the spot measurements to determine the position, but this would have involved complex analysis on the geometry of the system, and might not be able to accurately account for the distortion introduced by the target being towards the edge of the field and therefore viewed at an angle.

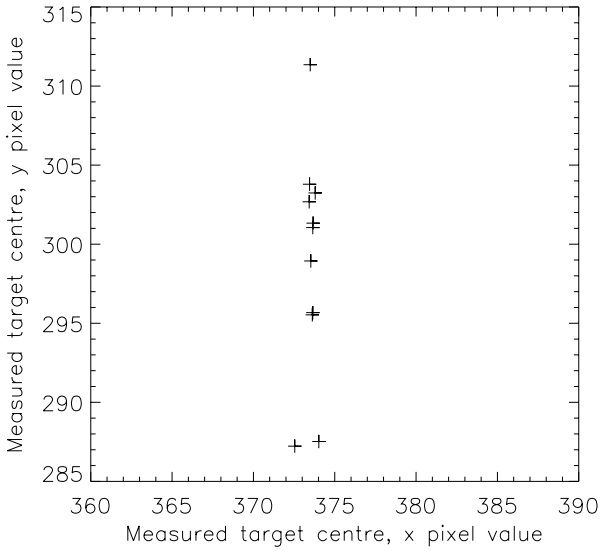

Figure 6.5: Calculated centres of a stationary robot measured repeatedly using the top-mounted target. These are the x-y positions in camera pixel units. The measurement precision in x is clearly better than it is in y.

The next iteration of the target is also shown in Figure 6.4. Drawing on the conclusions of the first design, this target had points on either side of the mirror and there is also an asymmetry in the design to help identify the pointing direction. This target was used a great deal in some of the development stages of the control software, with the target simply attached to the top surface of the robot as shown in the photo. This target could not be mounted on top of the robot as it would block the light path, so the plan would have been to mount it below the mirror, with the spots on either side. However, there would always have been the problem of the mirror itself obscuring many of the spots if the target was viewed even at a slight angle.

The current design of the target is again shown in 6.4. This has a ring of 29 spots distributed around the base of the mirror. This design still suffers the problem of some

spots not being visible due to the mirror. However, as there are such a large number of spots, even with a few missing the fit can still be sufficiently good. Also, the spots are marginally further from the mirror's centre than earlier designs - they sit on a radius of 12.5 mm - this has the advantage that fewer spots are blocked by the mirror. The spots are evenly spaced, except for two spots at the front; these two provide the necessary directional information, this can be seen later in Figure 6.11.

The current size of this target is 29 mm in diameter. This is much larger than the 20 mm mirror, but still within the 30 x 30 mm footprint. Due to concerns surrounding electrical insulation, and the fragility of the robot's design, it was decided to place the robot inside a cover, which enshrouds the chassis, wheels and electronics. This cover is 29 mm square, and it was this size that led to the final acceptance of these larger targets.

6.3.2.2 Target manufacturing

The target must be printed to the highest possible accuracy. The first two designs of the target were produced on a normal inkjet printer from files created using the vector drawing tool, Inkscape. It was difficult to accurately reproduce the Gaussian profile in these formats and the fitting accuracy suffered as a result. For the final target, a program was written in IDL whereby targets could be created to any desired pixel scale.

The pixel scale is determined by the limits of the target production technique. For conventional inkjet printers it is commonly measured in dots-per-inch (DPI), which defines the proximity with which ink drops can be placed by the printer head. Continuous tone printers were also employed, where the ink is deposited onto a photographic substrate, on which it can disperse and blend with adjacent drops, leading to a less pixelated image.

Targets were also made using two photolithography techniques, which, in theory, offer higher resolution than traditional printers. In photolithography a material is deposited on a substrate and then removed from the desired regions. The first method used Chrome deposited on a substrate of quartz glass and then etched away chemically. The second method, used a photomask on film, with high-intensity light used to remove the regions of the spots.

The best printer available to MAPS had a DPI of 1600, which equates to drop sizes of 16 μm, whereas the chrome deposition could achieve a pixel scale of 1.5 μm. For the photomask it was nearer to 6 μm. Photolithography, however, cannot recreate different shades of colours in pixels, like a normal printer. Instead the image is 'rastered' where varying density of 'on/off' pixels are used to recreate the desired colour gradients. This unfortunately does effectively increase the pixel size.

A visual comparison between a model spot and an imaged spot can be seen in Figure 6.6. In order to assess the quality of these various different versions of the targets, a 'Quality parameter', Q, was defined such that:

$$Q = 1 - \frac{X_{spot}}{X_{background}}, \tag{6.2}$$

where X_{spot} is the chi-squared fit of the imaged spot against a model spot of the same width and peak intensity, and $X_{background}$ is the chi-squared fit of the model spot against a blank background, i.e. the worst case 'fit' if there was no spot to fit against. Q is defined such that for the perfect fit it has a value of 1 and for no fit, it is 0. The results for all the spots are shown in Table 6.1. Also included here is the spot width, W (in pixels), as this is also an important criteria; if it is too low, the spot centroiding accuracy will decrease.

The first clear result from the analysis of the Q values, is that the two more precise manufacturing techniques did not reproduce the Gaussian pattern well, and there is also a relatively large deviation in the values. It is believed that this arises from the difficulty of recreating the subtle graduations in colour required to produce the wings of a Gaussian. Since these techniques do not use conventional image formats, it is also possible that the problems arose in the conversion of the original bitmap files. In future it would be interesting to explore other techniques to raster images tailored for a particular production technique, coupled with more direct access to these facilities to allow greater experimentation.

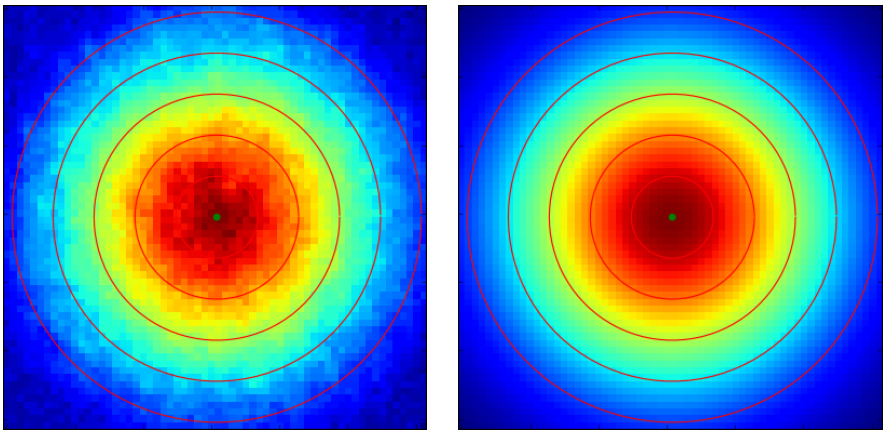

Figure 6.6: On the left is a close-up image of a spot from the best manufactured target. On the right is a model 2-D Gaussian, which has the same peak intensity and width as the imaged Gaussian. The overlaid red circles are merely to ease comparison of the two images. Note that the picture was taken with the camera at the lowest height above the focal plane possible, and therefore the pixel scale is the finest used.

The images produced on professional continuous tone printers offer very good reproduction of the model Gaussian, but suffer from high variation in width measurements. This is not surprising, a continuous tone printer is capable of providing well-graduated colours - the ink droplets merge - and so the Q value is high. However, since the precision of the drop placement is not that high, the deviation on W is poor. Again, access to better continuous tone printers might lead to better results.

The very best Q value came from the 'Plain' settings on the photo inkjet printer, with an image scaling of 2.5, although this did suffer from relatively large variation in the width of the peaks. Consequently, the printing process selected was that of the *'semi-gloss' settings, on heavy duty matt paper*. A test where the same, semi-gloss target was imaged thirty times, showed a deviation in the measured centre of 0.0017 and 0.0016 pixels in x and y respectively: this suggests the accuracy is extremely good. This paper target can then be mounted on a thin metal substrate before being attached around the base of the mirror.

Table 6.1: Comparison of the spot quality for the different manufactured targets. The 'quality' parameter, Q, of the spots compared with a model 2-D Gaussian function. The mean value is shown for all 29 spots in single target, along with the standard deviation. The width, W, of the spots is also given in pixels. The standard deviation of W gives an indication of the repeatability of the manufacturing process.

Target printing method	Mean Q	σ Q	Mean W	σ W
Chrome deposited on quartz	0.54	0.265	11.432	0.868
Photomask on film	0.75	0.067	7.764	0.454
Gloss settings on gloss paper	0.94	0.010	14.319	0.149
Gloss settings on matt paper	0.92	0.011	12.844	0.161
Jpeg on normal paper	0.88	0.011	11.164	0.130
Continuous tone printer small	0.92	0.012	13.345	0.531
Continuous tone printer broad	0.92	0.012	14.466	0.519
Matt settings on matt paper	0.93	0.007	13.975	0.157
'Plain' settings (scaling 1.0) on normal paper	0.88	0.012	11.266	0.258
'Plain' settings (scaling 1.5) on normal paper	0.92	0.006	14.513	0.219
'Plain' settings (scaling 2.0) on normal paper	0.94	0.006	17.766	0.293
'Plain' settings (scaling 2.5) on normal paper	0.95	0.007	20.464	0.599
'Plain' settings (scaling 2.0) on matt paper	0.95	0.005	16.936	0.232
Semi-gloss on matt paper	0.95	0.009	12.476	0.121

6.3.3 Camera selection and evaluation

The term 'pixel scale' is used to define the physical size on the robot's operating surface that is imaged by a single pixel by the metrology camera. To achieve the greatest

measurement resolution it is necessary to minimise this value. There are clearly two ways to do this: to decrease the field-of-view of the camera or to increase the number of pixels.

For initial testing of the system a 10 Megapixel UEye USB camera was purchased; this was a relatively small and inexpensive colour camera. It is primarily designed for use with microscopes, and consequently has small pixels of only 1.67 μm across. Since it is not yet possible to build detectors which are truly sensitive to the wavelength of the incident light, any colour camera is, in reality, a monochrome camera with an arrangement of finely spaced red, green and blue filters placed directly in front of the detector's pixels. The camera purchased employed a Bayer matrix, which is the most commonly used system of filters. The sampling of colours through filters effectively degrades the absolute accuracy of the quoted number of pixels: in reality the figure is probably nearer to one quarter of that quoted. However, this colour camera allowed a wider range of experiments to be performed during the early stages of the MAPS development.

For the next stage of testing, a monochrome camera was therefore sourced. The camera was required to have as many pixels as possible, a minimum read-out speed of a few frames per second and to be able to provide both 8-bit and 12-bit frames.

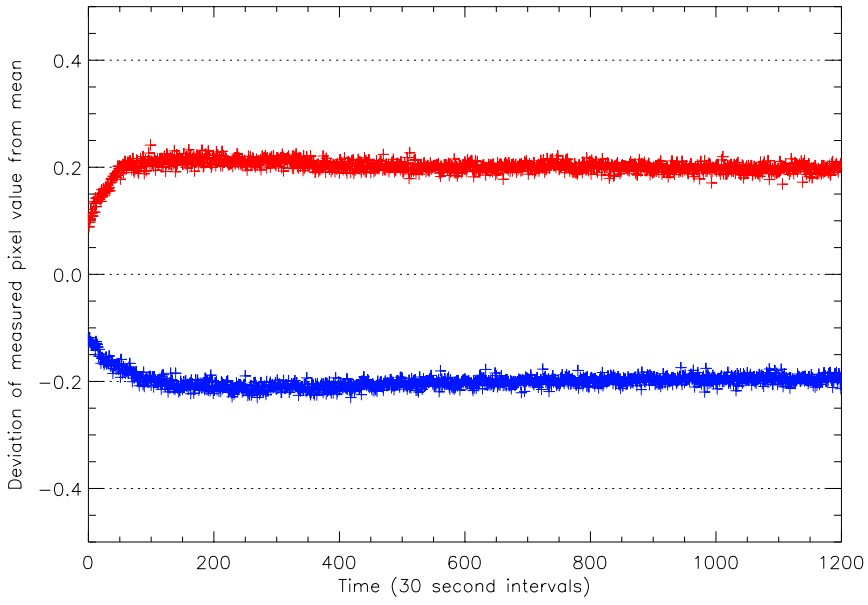

Figure 6.7: Measurement for the centroid of a spot recorded in 30 second intervals throughout one night. The red shows the x position of the spot centre and the blue the y position. The results have been offset from the mean of 0 by +0.2 and -0.2 for easier viewing.

A Lumenera Lw11059M USB 2.0 camera was selected as this met many of these requirements. The camera has a 10.7 megapixel Kodak KIA-11002 sensor (3648 x 2670 pixels), which has a full frame format with 9 μm square pixels. These sensors are often used in amateur astrophotography as they have very low noise and high sensitivity, two features which are excellent for this application.

The first test of the camera was designed to determine its stability, i.e. is there variation in its behaviour over a relatively long period of time? The camera was bolted securely to an optical table and used to image a 100 μm pinhole placed 50 cm away, which was illuminated by a known, stable light source. Images of the source were then recorded at 30 second intervals over the course of a night. The results are shown in Figure 6.7. It is clear that there is an initial warm-up time of nearly 2 hours. It is common for many cameras to experience such a shift (Handel 2007); this often arises due to the thermal expansion of mechanical components in the camera. Note that the shift is of order one-tenth of a pixel, which corresponds to 0.9 μm of expansion - a very small amount. This warm-up time is perhaps longer than might be expected (Handel 2007), but frames were taken only every 30 seconds, which might explain this. Following this test, it was ensured that the camera had always been left running in video mode for minimum of an hour before measurements were taken.

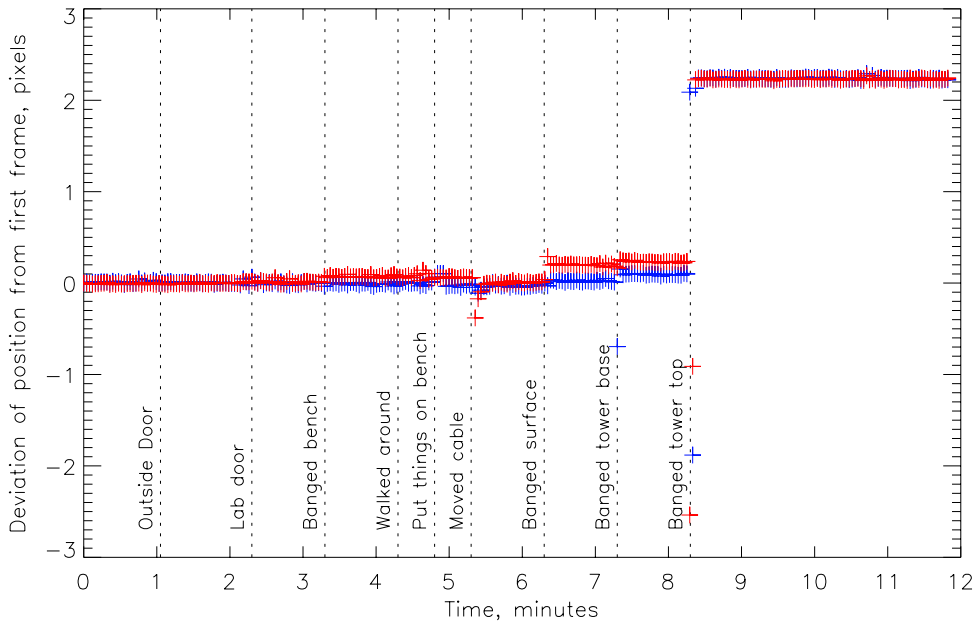

Figure 6.8: Testing for the influence of various 'events' which might occur in the lab and their effect on the measurement stability of the camera. The measured x position is shown in blue and the y positions in red. The time at which the different 'events' occurred is indicated by the dotted lines.

After the warm-up time, the behaviour of the camera was excellent, showing only a very slight drift in the x direction of roughly 1/100th of a pixel over the course of 8 hours. This is a reflection on the quality of the camera being used. There is deviation in the measurements which is larger than the underlying drift, but it is believed that this is more due to inaccuracies in centroiding on the light source, than any inherent property of the camera. It is important to note that, in general, the camera in MAPS is used to take measurements in very quick succession, so small drifts over the course of hours are acceptable. It is reassuring, though, to know that the drifts are so small.

Having established that the camera did not suffer from any significant drift, the next test was to analyse the effect of mounting the camera on an optical tower, located above the MAPS focal plane. A similar test was performed to that described above, imaging a light source now placed on the robots' operating surface with the camera mounted looking down. Experiments were again run overnight and it was found that the standard deviation of the measurement was 0.015 μm, which compared to the value of the 0.017 μm found for the camera on the table, showed that there was no significant deterioration in accuracy when mounted on the tower.

To assess the impact of normal behaviour in the laboratory, a test was devised whereby a number of 'events' would occur, which might cause vibration in the tower: these included allowing the lab doors to slam, placing objects on the surrounding optical table, and more direct action, such as striking the tower itself. For these tests the camera was read out every second, with the 'events' occurring at pre-defined intervals. These results are shown in Figure 6.8, with the time stamp associated with each event indicated by the dotted lines. It is clear from this that any direct impact on the tower

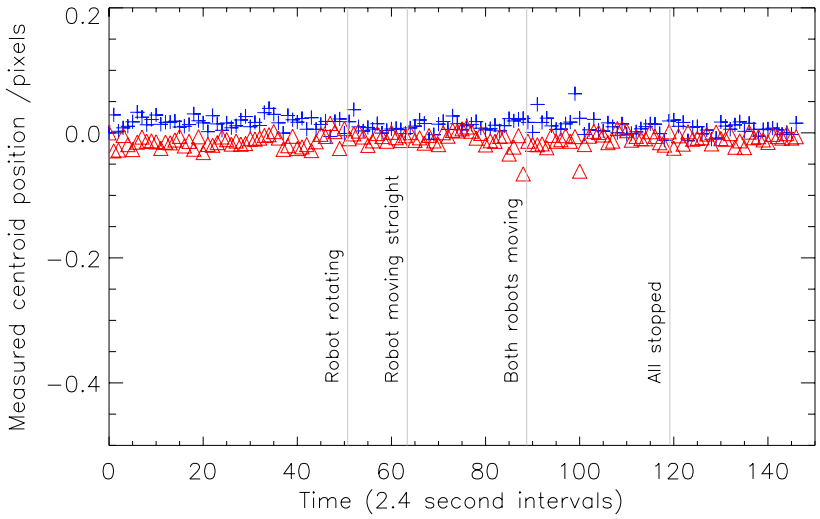

Figure 6.9: The effect of robot motion on the measurement stability of the camera.

can affect the stability, especially if that impact is near the top of the tower.

Figure 6.9 is analogous to Figure 6.8 and shows the stability of measurements when the robot is moving around on the focal plane. It suggests that there is no significant vibration introduced by the robot's motion. The robots did lose power on a few occasions, which meant they had to be replaced on the floor; it is likely that this is the cause of the few jumps seen in the data around the 90 second mark. After these tests were performed, additional care was taken when placing the robot down on the operating area to minimise any such effects.

6.3.4 Target analysis technique

For the first targets, which had red spots, the process of isolating the spots was greatly speeded up through manipulation of the colour camera's red, green and blue frames. Figure 6.10 shows an image of the target and the processed image to find the spots. Although this technique is no longer possible with the monochrome camera, it was a very fast way to locate the spots.

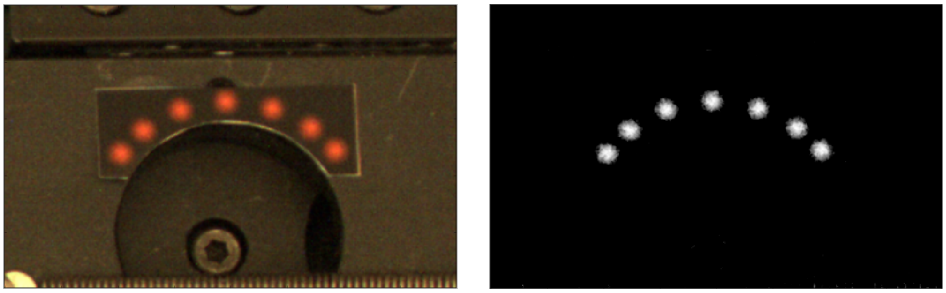

Figure 6.10: Analysis of the red targets using the colour camera. Through manipulation of the RGB frames the red features can be isolated, thus making spot identification considerably easier.

Attempts were made to recreate the red frame selection process with the monochrome camera and a red filter, however, without the additional information provided by the green and blue frames, the improvement in the signal was not as dramatic. The spots were therefore found using the following procedure:

1. Sub-region of the image is selected either through motion of robots, from known position or from user selection
2. First spot roughly found by searching for the best chi-squared fit to a model spot anywhere in the sub-image
3. First spot precisely fit using 2-D Gaussian fitting package built into Python
4. Next spot found by searching appropriate surrounding region - knowledge of pixel scale required

5. Spot is then fitted by a Gaussian profile
6. Process repeated for 20 spots (not full 29 in case of obscuration by the mirror)
7. Temporary ellipse fitted to spot centres
8. Angle of orientation found
9. If more spots will be visible, find and fit these
10. Refit ellipse and calculate final coordinates (x, y, θ)

A robust ellipse fitting routine proposed by Halíř & Flusser (1998) was employed. This technique is based on a non-iterative least squares minimisation, which is particularly effective even when the data is noisy. It is also extremely quick for a small number of data points ($\ll 1\,\mathrm{s}$), which is an advantage for the real-time control of MAPS. An image of the target, with the overlaid measurements is shown in Figure 6.11. A comparison between the repeatability of measuring the centre of a given spot compared to fitting and measuring the centre of the ellipse is shown in Figure 6.12; it is clear that there is an advantage to using the ellipse.

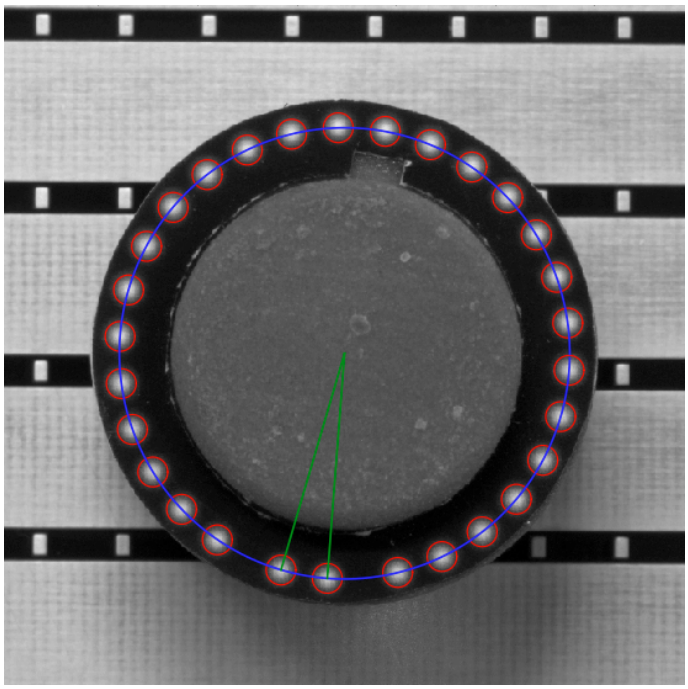

Figure 6.11: The target with overlaid measurements. The red circles show the centroid fit on each spot; the blue circle, the fitted ellipse; and the green lines indicate the front spots, used for assessment of rotation.

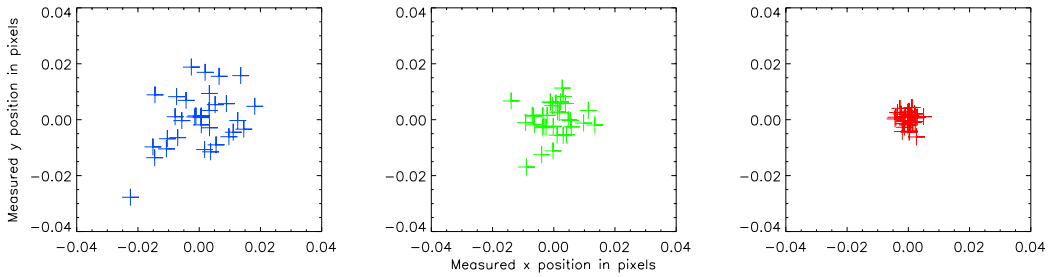

Figure 6.12: Thirty repeated measurements for a stationary target. Left: centroiding accuracy of the spot showing the highest standard deviation. Centre: centroiding accuracy of the spot showing the lowest standard deviation, i.e. the 'best' spot. Right: the centre of the target found through fitting an ellipse to all 29 spots.

6.3.5 Floor analysis technique

The analysis described thus far will only provide measurements of the target positions in the pixel coordinates of the camera, i.e. without any reference to the "real world" physical position and the actual distances involved between measurements. To make this correction points with known positions (or fiducials) are required. As discussed previously the power floor has a very distinctive pattern of marks (seen in Figure 6.11 and 6.13), which can potentially be used as fiducials.

Again through Python-based image analysis, the centres of the floor markings are analysed and a measurement grid can be defined, as shown on the right of Figure 6.13. This is again done through a multi-step process:

1. Pixel positions of a number of points are entered manually (these are stored in log files for the different relative positions of the camera and the power floor).
2. A centroid position of these first positions is obtained, and from these the positions of the other fiducials are predicted. The pixel positions of all the robots must be known, so that the surrounding regions can be avoided.
3. All the other available fiducials are found and centroids performed to get accurate positions of a complete grid of points.
4. A second-order polynomial is independently fitted for each row and column of fiducials. This relates the pixel positions to the known real positions (in mm). This fitting can also take into account gaps left in the grid of fiducials due to the presence of robots.
5. The coefficients of the polynomial fits are themselves then fitted to find how they vary across the image.
6. For any measured pixel value, the real positions can now be found.

As an example of this process, if the measured position is at pixel (450,950), the coefficients describing the pixel-to-real relationship for x-column 450 can be obtained from the calculations in stage 5, and then the real y position corresponding to pixel 950 can be found. The repeat pattern is then performed for row 950 to obtain the real x position of x-pixel 450.

The code to perform this assessment has been implemented, but it has not yet been fully characterised. The scaling is made more complicated by the fact that the power floor and the robot's target are at different planes, and therefore an additional height correction must be applied to the measurement grid to account for this offset. In order to apply this height correction, the camera's viewing angle must be known, as must any angular misalignment in the power floor, i.e. is it tilted with respect to the observer?

The height correction would introduce a large additional element of uncertainty into the measurements. As an alternative, a scaling image could be taken of a grid placed in the same plane as that in which the targets are moving. This image would have to be recorded prior to the robots being placed on the surface. The camera could not then be moved, as this would mean the scaling relationship would no longer be valid.

These two different ideas are still being explored, and form a large part of the ongoing MAPS research. The results that follow are therefore based on measurements in pixel space only.

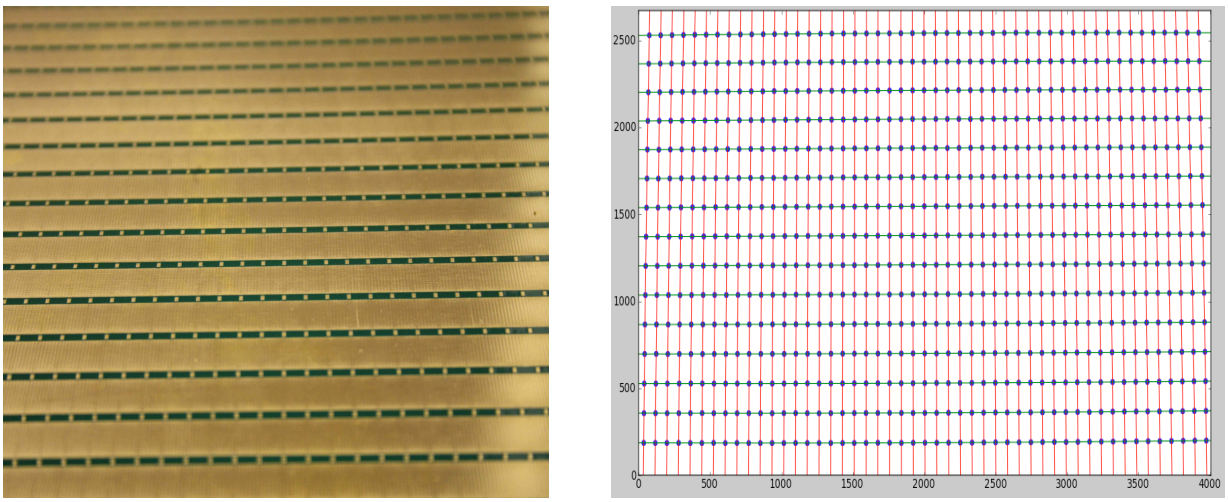

Figure 6.13: Left: image of the power floor on which the robots operate and draw their power. On the right, the measurement grid derived through analysis of all the markings on the surface of the floor, the axes on the grid show the camera pixel values.

6.3.6 Quantitative analysis and results

A large number of tests have been carried out to assess the performance of the metrology system. To do this a test rig was constructed that gave a range of different ways in which the camera can be mounted, as shown in Figure 6.14. The rig has a base made from 6 mm thick mild-steel which provides a completely flat surface on which to mount the charge mat. Each test and its results are documented below, they are each assigned a reference, e.g. A1 or B2. Since MAPS is an ongoing research project, a number of these tests are yet to be carried out, but they are included here for completeness, together with a brief outline of the intended plan.

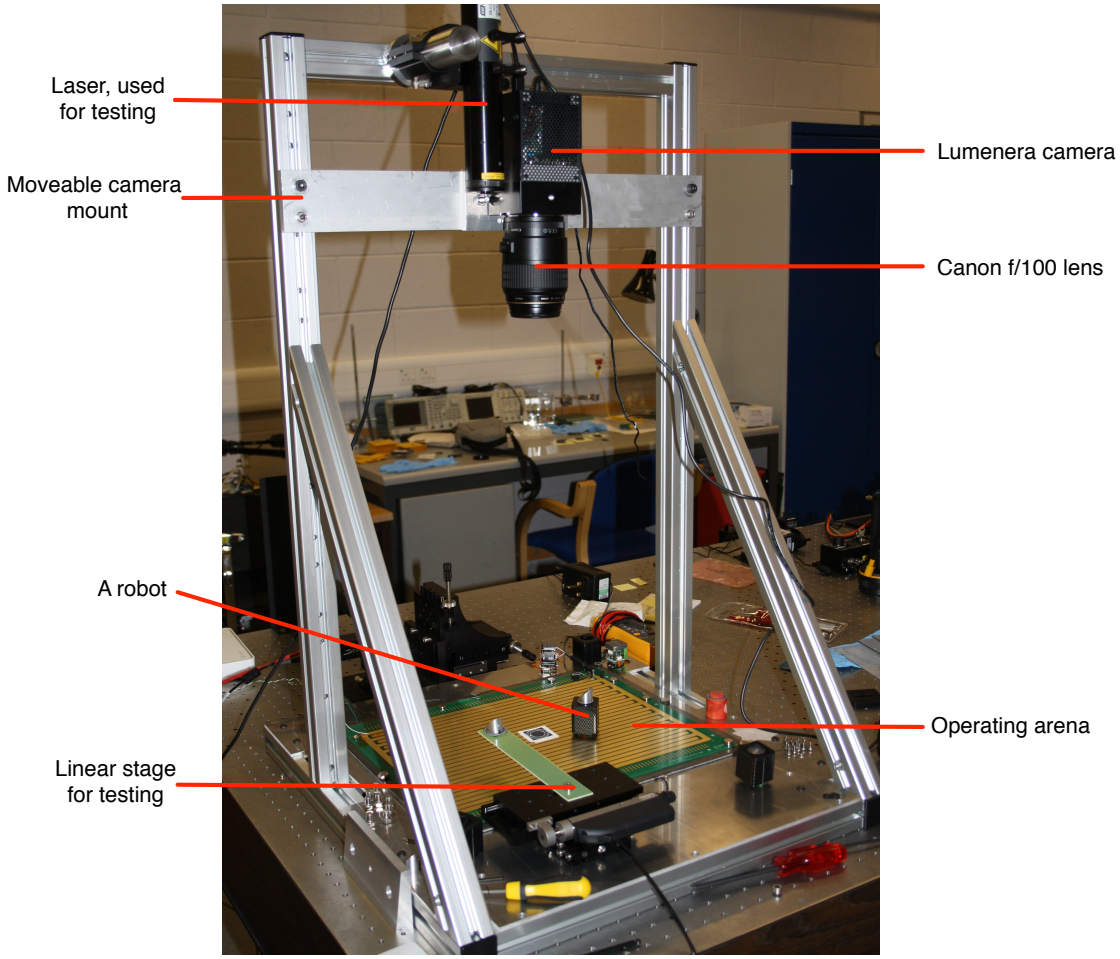

Figure 6.14: An image of the tower constructed to provide a range of mounting positions for the camera. Also visible is some of the test equipment, such as the laser for alignment tests and a high precision linear stage.

A: Repeatability of measurements for a non-moving target (pixel based)

1: Different locations in the field

The target was moved to various places in the field to assess if this affected the repeatability of the measurements. For the camera mounted at the top of the optical tower, using the 100 mm lens, it was found that there is no significant variation at different points across the field - this is a reflection on the quality of the optics and the camera used.

2: Different S/N

By varying the size of the camera's aperture it was possible to adjust the amount of light incident on the CCD, and thus change the signal-to-noise ratio. Figure 6.15 shows how the standard deviation of 16 measurements of a stationary target vary as the intensity on the image decreases. It is clear that the peak value needs to be above 200 for the best results. Since the camera was being read out in 8 bit mode, it saturates at 255 counts; if this occurs it too will lead to a deterioration in the measurement, as can be seen on the graph. Also of note is that below 100 counts the code occasionally failed to correctly identify all 29 spots.

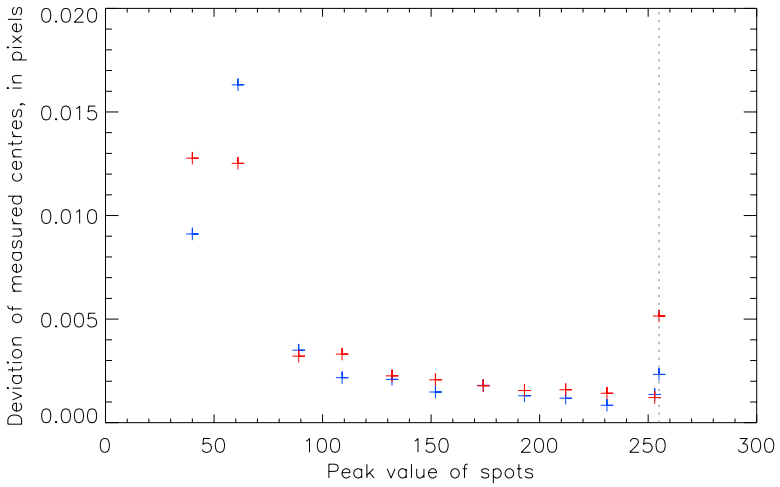

Figure 6.15: Variation in measurement accuracy as the signal-to-noise is increased. The blue and red show the measured x and y position respectively.

3: Different field sizes

By moving the camera up and down on the tower, different field sizes are obtained. The target was measured in the centre of the field 16 times. The results of this test are shown in Table 6.2. As can be seen, there is a slight variation in the measurement precision, with the smallest field having the best results, which is to be expected.

Table 6.2: The standard deviation of 16 repeat measurements of a stationary target for different field sizes, created by moving the camera to different heights.

Field size (mm)	Camera height (mm)	Peak counts	Standard dev (pixels)
Big (236 x 157)	674	212	0.0016
Medium (195 x 130)	560	220	0.0012
Small (155 x 103)	440	231	0.0010

4: Different number of spots

At certain positions the mirror always obscures some of the spots on the target. To test for the impact of this on the measurement accuracy the target was imaged 10 times. The centre of the target was then found and the deviation on the ten measurements calculated. The analysis was repeated on the same set of images, but with an increasingly large number of spots not included in the analysis. The results are recorded in Table 6.3. It is clear that there is a deterioration after 5 spots are obscured. In the current design up to 9 spots can be obscured if the robot is positioned at the edge of the field, but in general it will be lower than this. Where possible the robots should be arranged to avoid spot obscuration.

Table 6.3: Measurement accuracy for different numbers of obscured target spots.

Number of missing spots	Δ centre (x)	Δ centre (y)	σ (x)	σ (y)
0	-	-	0.0016	0.0010
1	0.0000	-0.0003	0.0016	0.0011
3	0.0055	0.0093	0.0017	0.0012
5	0.0467	0.0566	0.0019	0.0011
7	0.0441	0.0579	0.0025	0.0013
9	-0.0928	-0.0076	0.0024	0.0017
11	-0.1855	-0.0316	0.0046	0.0015

B: Moving target

1: Variation in xy plane

To test the possible measurement accuracy, a target was mounted on two orthogonally-aligned high-precision linear drives, which are capable of sub-micron precision. The target was then driven in x and y in 1 μm steps, and after each step it was measured five times. The results are shown in Figure 6.16, and these clearly indicate that 1 μm steps can be distinguished. This also highlights another technique that can be employed to improve the measurement accuracy. The stacking of multiple frames to improve the signal-to-noise is a very common technique in astronomy, and it is quite possible

that employing a similar method in these measurements would significantly improve accuracy. However, this would slow down the analysis, so perhaps this could be done for a final 'high-precision' setting after the robot has finished moving.

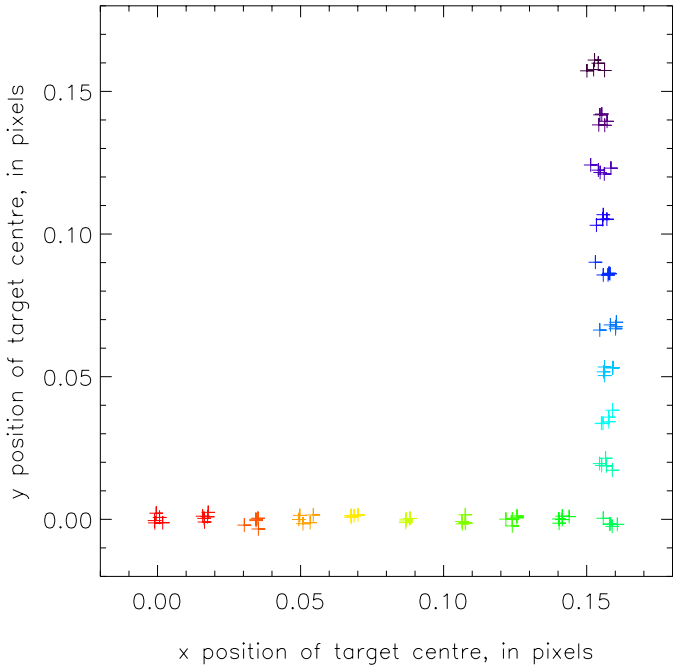

Figure 6.16: Tests showing the motion of the target in 1 micron increments: first 10 steps along the x-axis, then 10 steps along the y-axis. Note that the axis of the drives are not perfectly aligned with those of the detector.

2: Rotation

In order to assess the precision of the rotation measurements, the target was mounted on a high-precision rotation stage. It was initially commanded to make turns of 90°, and, as can be seen in Table 6.4, the measurement accuracy appears to be very high indeed (accurate to ∼0.001°). It also should be noted that the rotational measurements are

Table 6.4: Results for turning the target through 360° and measuring at every 90° interval. All the measurements are in degrees.

Angle commanded to turn	Measured turn
0	0.010
90	90.021
180	180.004
270	270.000
360	360.013

real measurements of angle, which are relative only to the orientation of the camera's field-of-view, they do not need to be scaled to the power floor in any way.

To further assess this, the rotation stage was driven in smaller steps. Initially it was driven in steps of 1 mrad, but as can be seen in Figure 6.17, the deviation on measurements was so precise that the process was repeated for steps of 0.1 mrad. These again can be distinguished, although there is much greater deviation within the results. Again, taking multiple images would potentially have led to much higher precision measurements.

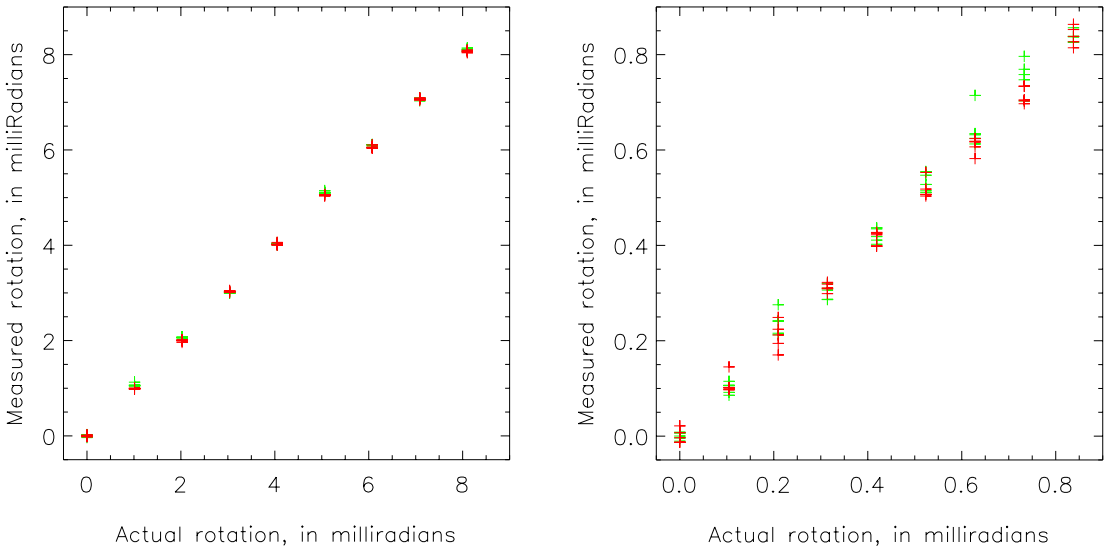

Figure 6.17: Graphs showing the measured angle of the target after rotation on the rotation stage. On the left the target was rotated in steps of 1.0 mrad, on the right, 0.1 mrad. The target was imaged five times after each step. For both graphs the green points indicate the measured angle when the camera was focused on the floor - so the target itself was not perfectly in focus - the red shows the same step sizes but with the camera focused on the target.

C: "Real" measurements (floor and target combined)

A large number of tests and measurements will need to be carried out to verify the scaling accuracy of the power floor.

1: Stability of measurements

The first tests will be to assess the stability of real measurements. As with the first tests of the metrology system (i.e. those recorded in Figure 6.12), this will involve repeated measurements of a stationary target.

2: Moving target around the field
It will be necessary to check the accuracy of the metrology's measurements with comparison to another measurement system. This will be achieved using a FARO laser tracker, which is described in more detail in section 6.5.2.

D: Closed loop tests

The final stage of this work will be to implement the closed-loop control of the robots. This has already been done using a rough scaling factor between real positions and pixel positions. It has been decided that due to the computational time required to assess the targets, there will be an open-loop aspect to the control. The system currently calculates where the robot is and the commands required to get it into the next desired position. The system then sends the robot small parts of the full command required, i.e. if the robot is required to move 15 cm, it will only be instructed to move 2 cm at first. The robot is then left to carry out this command and only once it has completed it, will the metrology system acquire a new image. It will then reassess the robot's position and calculate the new commands needed to get it to the desired position.

Through this iterative process it will be possible to get the robots into position, but at the final alignment stage the chassis design will mean that carefully ordered patterns are needed. This is illustrated in Figure 6.18 and it arises from the fact that the robot

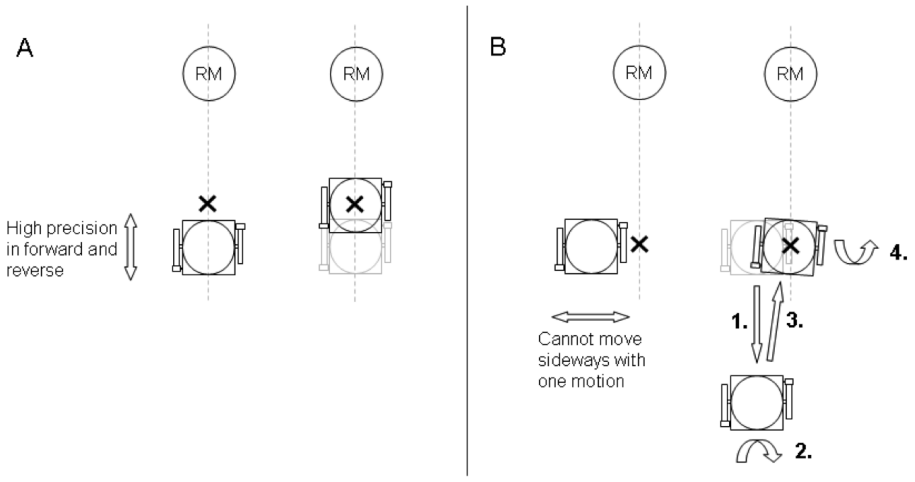

Figure 6.18: In both image A and B the robot is trying to align with the X and direct light along the dotted line to the receiving mirror (RM). In A, whilst the robot is initially misaligned along the direction of travel, this can be easily corrected through moving forward. In B, the misalignment must be corrected by first reversing (1), turning through a small angle (2), moving forwards (3) and then finally rotating once again to line up with the RM (4).

has high precision moving backwards and forwards, but cannot move to the left and right without rotating through 90° first. A more convenient solution to the problem is illustrated in the Figure 6.18.

There are two other important aspects of the command and control system, linked with the positional information of the metrology system. Path analysis will initially attempt to avoid intersection of the different routes for each robot from its starting to its end position. If this cannot be achieved, the analysis must estimate the temporal aspect of when each robot will be at each point along its route. With only a small number of robots this will not be too complex an algorithm, however, even for EAGLE with 25 robots, this would start to require some careful planning of routes and travel times. Proximity warnings will also have to be determined through continual assessment of each robot's position relative to the other robots. If any two robots are found to be getting too close together a stop command will have to be sent and their paths recalculated.

6.3.6.1 Sources of errors

Different errors could affect the measurement accuracy. These fall into two categories: systematic errors, which can be calibrated out of the system, and random errors which cannot be accounted for. The exact position of the target mounting relative to the mirror is unlikely to be accurate to within a few microns, such that the centre of the fitted ellipse exactly matches the mirror's centre. Likewise, if the target is not completely flat, or is tilted, there will be a mismatch between the observed and the real centre. These misalignments would have to be measured once for each robot, and will be corrected for in the software.

If the target were not properly secured and moved relative to the mirror during motion, this could not be corrected for and would affect the measurements. It is conceivable that datum points within the system could be used to periodically check the alignment of the mirror and the target.

6.3.7 Metrology system conclusion

The metrology system shows great potential to be able to meet the requirements of the MAPS system. Testing has shown that the system can clearly distinguish linear motion at the micron level, while rotation can be determined to sub-mrad precision. This is an excellent start to the system's design. The system is still in a development stage and will soon incorporate the scaling from pixel positions to real-world coordinates. This is needed before the full closed-loop performance of the metrology system can be properly assessed.

6.4 Command and Control Sub-System

As was outlined in Table 5.1 and Figure 5.14, the metrology sensors forms only one part, or 'Module', of the Command and Control sub-system. This sub-system provides the interface between the user, the cameras and the robots themselves, via the wireless communications. A detailed flow diagram showing the logic employed to control the system is given in Figure 6.19. A brief explanation follows for the key functions that are shown in the flow diagram.

Initialise systems: The first task is to set up the both the Lumenera camera and the Chipcon wireless transmitter. Both of these are USB driven devices and can be operated through Python. Upon initialisation, the wireless controller searches for live and available robots. This function then reports to the user the status of both the camera and the controller, and also the presence of all the available robots.

Locate: The next task is to find the position of the robots. This can be done through the metrology system, as discussed previously, or the user can input values.

Centroid: This is the process whereby the spots of the metrology target are located.

Ellipse: The fitting of the ellipse to the target spots to give the robot centre in pixel space. At this stage all the calibration corrections required to compensate for any offset between the position of the target and the mirror would be included.

Scale: The conversion of the pixel position to a real position. Note that this cannot be done earlier, as the floor cannot be analysed until the position of the robots is known.

Calculate path: When the desired coordinates are given, the software must calculate the shortest route for the robot to get from its current location to the next.

Proximity issues: On calculating paths, overlap of the paths must be considered. If the overlap will cause collisions, alternative paths should calculated.

Send commands to robots: This process sends the commands to the robots. It must also interpret the status of the robots to ensure that the commands have been received.

Rough centroid: Precise fitting of the centroid is currently time-consuming, so a quicker, less accurate centroiding can be performed. This is needed whilst the robots are in motion.

Proximity alert: The code will work in discrete time steps. As the robots move, the position of each robot will be found through the Rough Centroid. Once the position of all robots is known, a proximity check will be made to ensure no two robots are too close together.

Calculate correction: If the robot is found to be deviating from the intended path, a new path must be calculated.

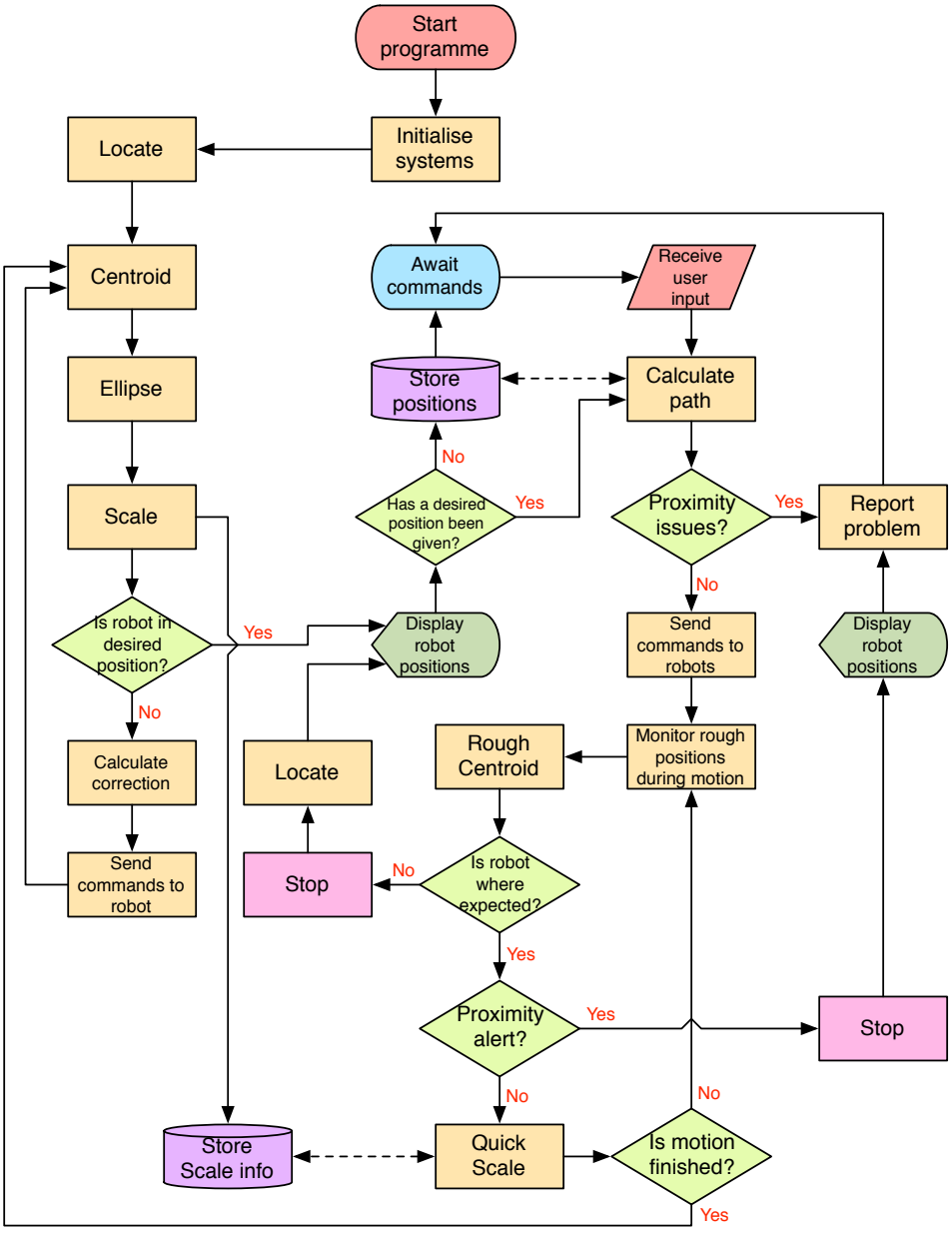

Figure 6.19: Flow diagram for the command and control sub-system; the different functions and statements are described in the text.

6.4.1 Software architecture

There are a number of different methods that have been proposed to try and formalise the development lifecycle of software engineering, an excellent discussion of which can be found in Pressman (2005). The MAPS software has followed a 'Spiral Development Model'. In this model the code development proceeds rapidly through planning, design, construction and deployment, to produce a simple first version of the system that can be tried and assessed. Learning from the experience of the first system the design then passes through another lap of the design process, but this time with increased functionality; this can continue ad infinitum as the design grows and responds to users feedback. The MAPS GUI is now in its third iteration, thus it has indeed passed through a 'Spiral Model' of development.

The Unified Modelling Language (UML) is a graphical tool which has been developed to both help design software and to document it for others to be able to interpret it. UML encompasses a range of different diagram types to meet different needs, for instance: there are State Diagrams that show the change in state of a system as information is passed from section to section; there are Sequence Diagrams that show the flow of events within a code - Figure 6.19 is loosely an example of one of these. There are many others, a fuller discussion of which, and UML in general, can be found in Fowler (2008).

One of the most common UML diagrams is the Class diagram. This design methodology is particularly relevant in object-orientated coding languages such as Python, where groups of common functions and tasks can be grouped together to form a 'Class'. The class diagram for MAPS is shown in Figure 6.20, note that this is concerned only with the functional control of the robots - it includes none of the GUI. The benefit of the class system is that any form of Sequencer script can be bolted onto the front end of these classes to control the robots in a variety of ways, without altering the core system classes. Each class has a list of 'Attributes', which store state information, and a list of the 'Methods', which control the state behaviour.

6.4.2 User interaction

The 'Use Case Diagram' is another of the design tools in the UML arsenal. It describes the different 'Actors' that interact with the system and the manner of their interaction. In the case of MAPS, there are only two possible actors, the 'Generic user' and the more experienced 'Technician'. As can be seen in the MAPS use case diagram, shown in Figure 6.21, there are a number of functions which the general user does not have access to.

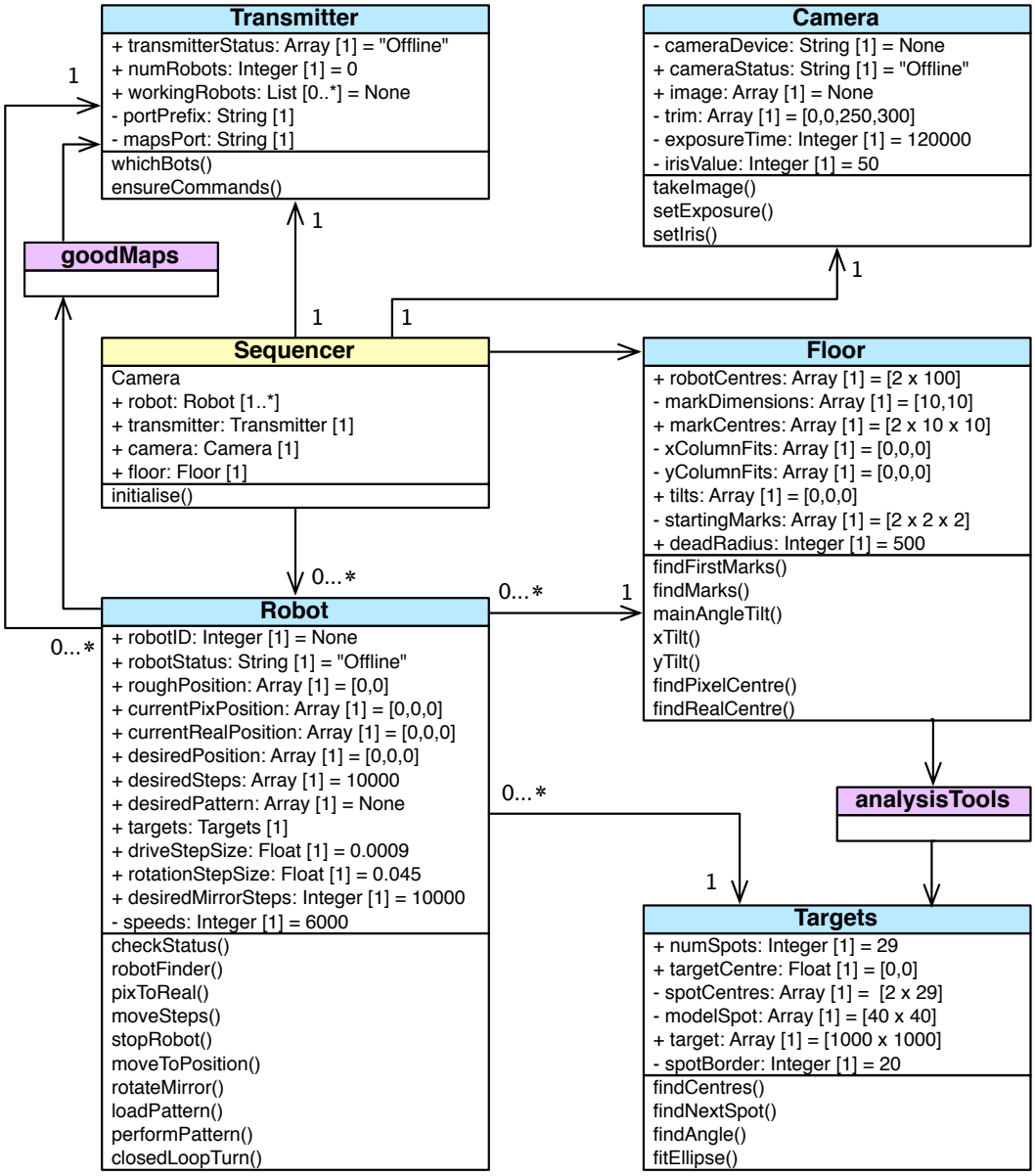

Figure 6.20: Class diagram describing the control software's architecture. The blue boxes define the main classes, with the top-top half contains the Attributes, with the Methods in the bottom-half. The purple boxes are additional Python packages which contain a few basic functions that are not listed here. The Sequencer could be used as a stand-alone script to control the system, but in reality is part of the larger GUI software, which is not described in detail here.

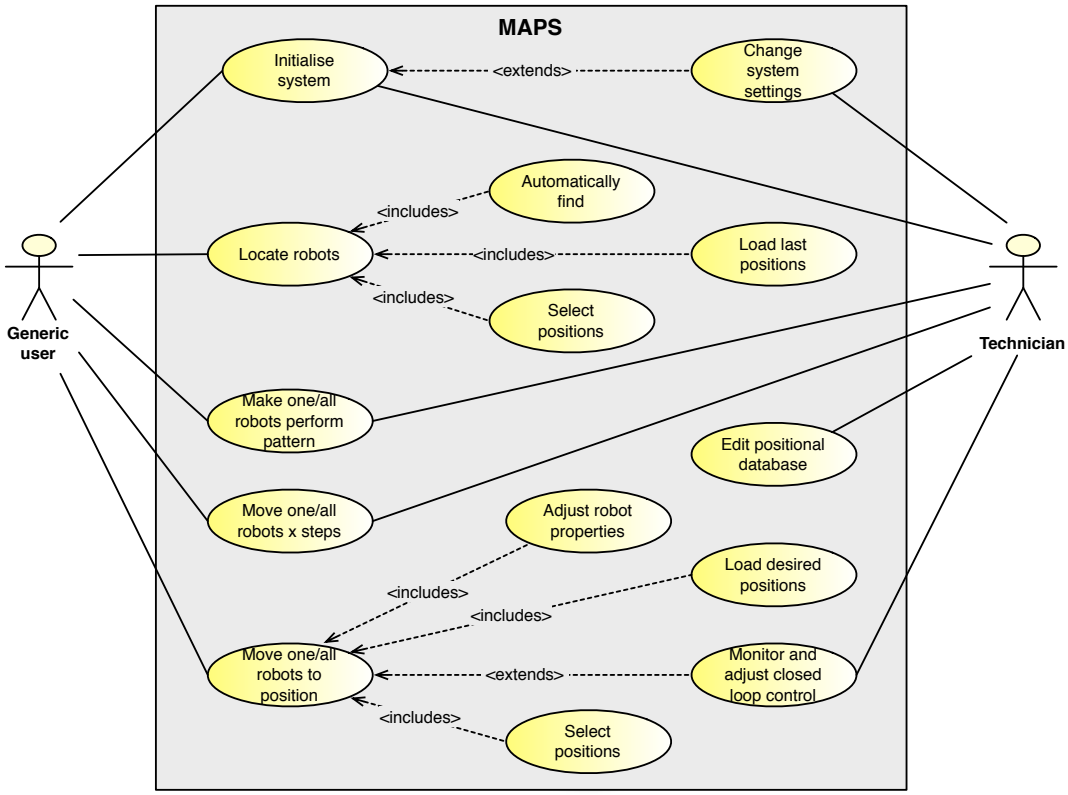

Figure 6.21: Use Case diagram for the MAPS software.

The use case diagram is a useful tool as it helps to highlight what functions are needed and what should be available to different users. This can be particularly useful when designing the GUI for a system. Two screenshots of the software that has been developed for MAPS are shown in Figure 6.22, with some of the functions from the use case diagram highlighted.

The opening screen of the software is shown in the top half of Figure 6.22. The user must first initialise both the camera and the transceiver. On doing this a picture will be recorded and the main screen will be updated. The transceiver searches for all available robots and creates a list of these complete with their status. The program simultaneously creates the additional individual control-panel pages (bottom half of Figure 6.22), which can be accessed through clicking on the tabs across the top of the page. Once into the control panel the user can control the robot by using the large joy-stick to simply send it in a particular direction, or the user can enter a desired position and command the robot to go there. This panel also allows control of features such as the speed of the robot.

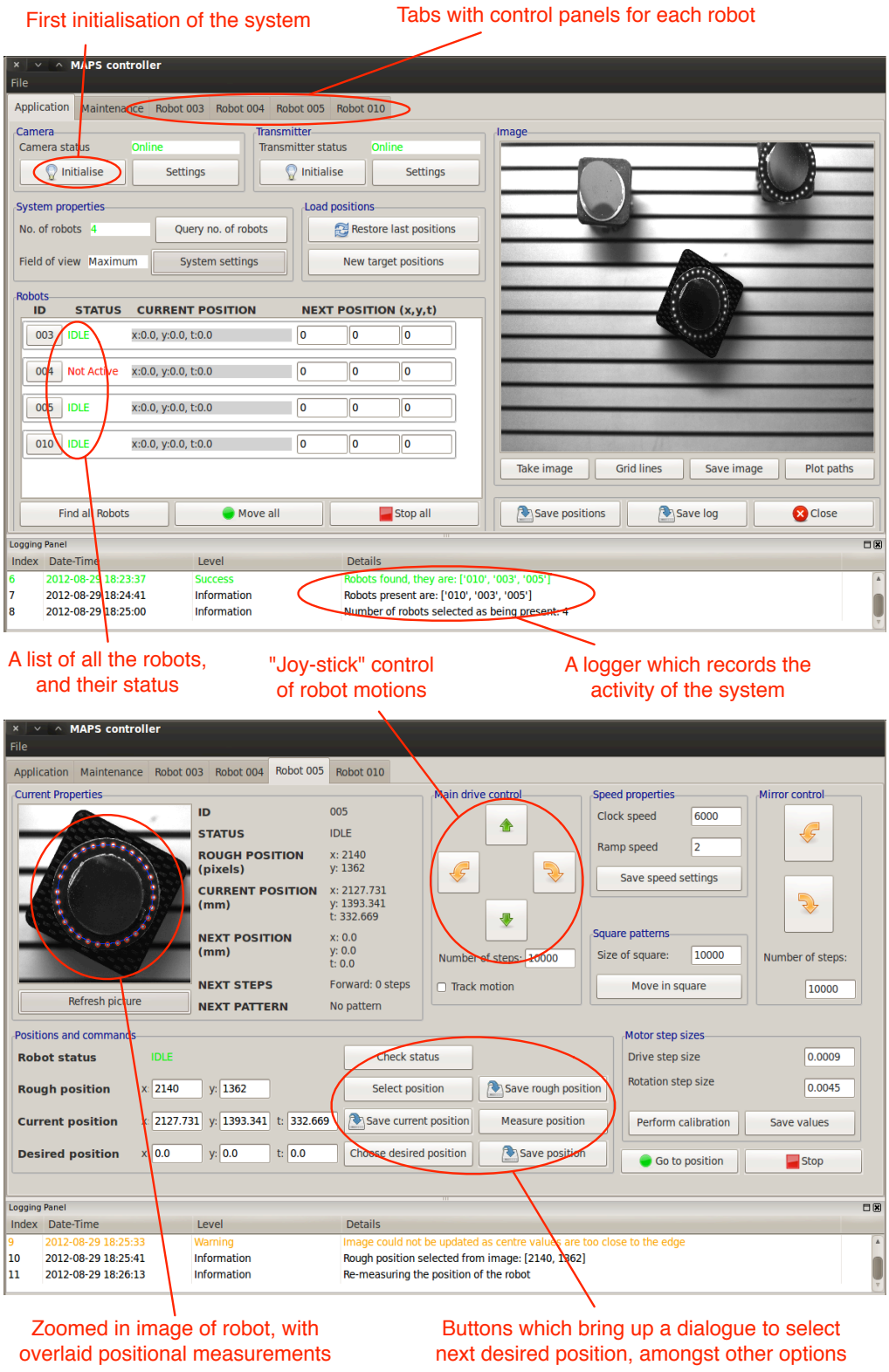

Figure 6.22: Screenshots of the two main GUI panels, with some highlighted features.

6.5 Positional performance

A number of tests have been performed to assess the accuracy with which the robots can be positioned. These are detailed here, although work is ongoing that will in time supersede these results.

6.5.1 First generation tests

The first tests were carried out using the phase one design of the robot, powered with a battery. These tests provide an excellent indication of the repeatability and precision of the chassis and the motors as the results are not clouded by other potential factors, such as the behaviour of the power floor.

These tests were performed with a Nikon measuring microscope. This device has a 75 mm diameter glass viewing area, which can be driven in x and y through two digitally encoded micrometer drives. The surface was moved into position until a recognisable feature on the robot could be lined up with the cross hairs of the viewing scope. The robot was then commanded to move a small distance and the scope re-centred, this therefore showed the exact distance the robot had moved. The scope has a measurement accuracy of $\leq 5\,\mu$m. This process was then repeated for a wide range of motions across the surface.

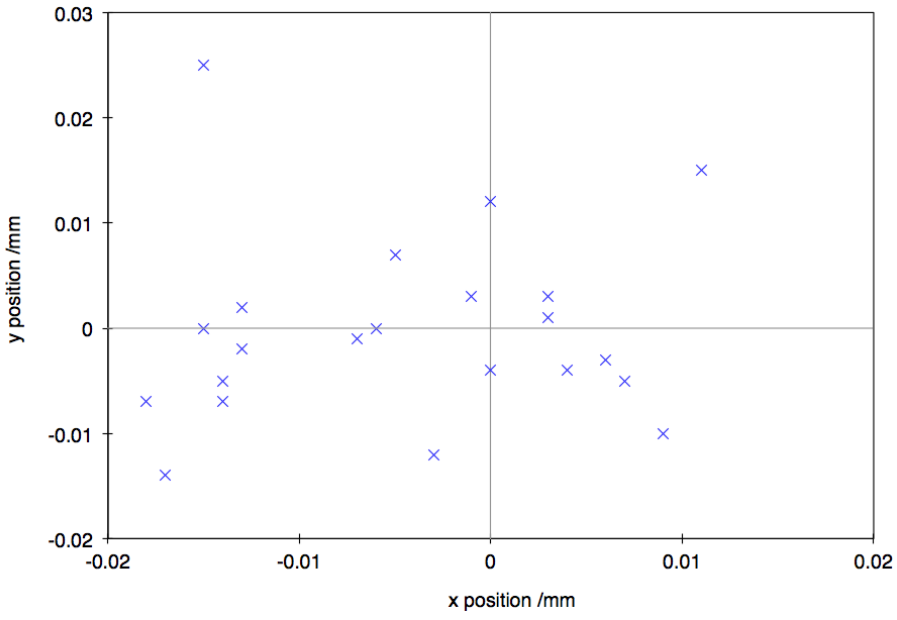

Figure 6.23: The robot was commanded to move 1000 steps in one direction and then 1000 steps in the opposite direction. The measured positions should ideally be all centred at 0,0 but the motion naturally introduces errors. In this test the positional errors were less than the x-y precision requirement of 35 μm.

Figure 6.23 shows the results for driving the robot forward through 1000 steps and then backwards through 1000 steps. As can be seen the robot does not return exactly to zero, but all the results are within 30 μm, which meets the requirements. Tests were performed for motions with a much smaller number of steps, i.e. only 1 step at a time, but with this measurement system it was difficult to determine how the robot was performing. However, it did not appear to move very regularly when commands of 1 step were sent. It is believed that there is a certain amount of inertia which must be initially overcome, which is not achieved when very small numbers of steps were attempted. It should also be noted, that while brushless motors such as those selected can be stepped, they will not do so as reliably as a dedicated stepper motor. It was not expected that the motors would ever be accurate to the 1 step level, but since the chassis has been designed to deliver steps sizes of roughly 1 micron, this precision is not needed.

In Figure 6.24 the results for repeatedly driving the robot 1000 steps forward in the same direction are shown, where the distance is relative to the finishing point of the previous motion. For this test two points were measured on the robot so that the angle of the robot could also be determined. Again, all of these results show that the robot has travelled to a precision of $<35\,\mu$m after travelling a distance of $\sim 850\,\mu$m, indeed the standard deviation on the differences of the travelled distance is only 12 μm. The angle it turned through can be as much as 1.5°, which for only $\sim 850\,\mu$m is quite large; further discussion of angular turning precision is given below. This test gives a more accurate estimate of the step size of the motors to be 0.85 μm per step, however, as mentioned above this does not mean that the robot can be stepped at this precision.

The results presented here are some of the best results that were obtained and serve as a proof-of-concept. These tests were repeated on a number of occasions, and with different robots. On some occasions the deviation on the travelled distance was seen to be outside the acceptable precision, with some tests showing deviations of order 75 μm. It was found that the performance of the robot was sensitive to the manner in which it had been assembled, with the exact alignment of the driving pinion and the wheels being crucial. As was mentioned in the previous chapter, it would be ideal if bearings could be added to the motor's drive shaft, thus allowing higher side loads to be applied. This would make the robot more robust and less susceptible to slight variations in the manufacturing process.

6.5.2 Second generation tests

The next generation of positional tests have been performed on the current version of the robot, which runs on the power floor. These have been carried out using a

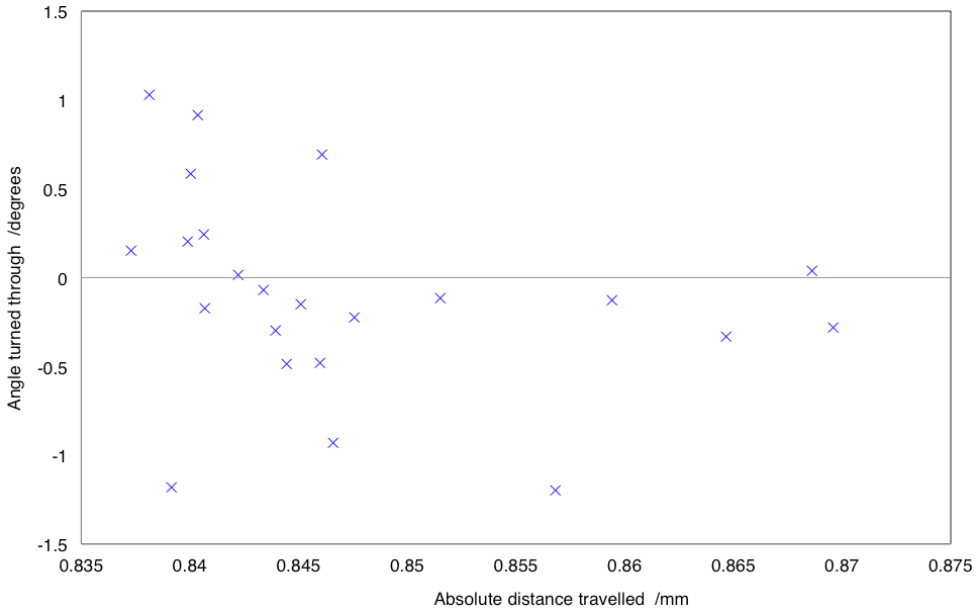

Figure 6.24: The robot was commanded to move 1000 steps in one direction, with the absolute distance travelled recorded. The figure also shows the angle through which the robot turned during the motion.

FARO laser tracker, which measures the position of an object through reflection of laser light from a retro-reflective target. The FARO can calculate a relative three-dimensional position of an object through the rotation and angle of the laser, with distance determined through time-of-flight measurements of an infra-red laser; it has a measurement resolution of 10 μm. For the purposes of the tests a 12 mm diameter retro-reflector was mounted on top of the robots.

These tests were designed to measure larger motions of the robots, since this was not possible on the small microscope stage. The robot was commanded to move 240000 steps, which took it fully across the power floor. This motion was repeated ten times and it was found that the deviation in the absolute distance travelled was 306 μm, which is quite good considering the distance travelled. However, the robot was clearly seen to deviate from a straight path, turning strongly to the left as it travelled forwards.

The test was repeated for the same distance but with the journey split into smaller sections of twelve 20000 step motions. The measurements of one such sequence, and its return journey, are shown in Figure 6.25. Again, repeat readings were taken and the deviation in the total distance travelled was decreased to 132 μm by shortening the runs. The curving motion is still clearly apparent and, perhaps more interestingly the degree of turning appears to depend on the direction of travel. The turning could be due to inaccuracies in the manufacturing process, while the variation in turning

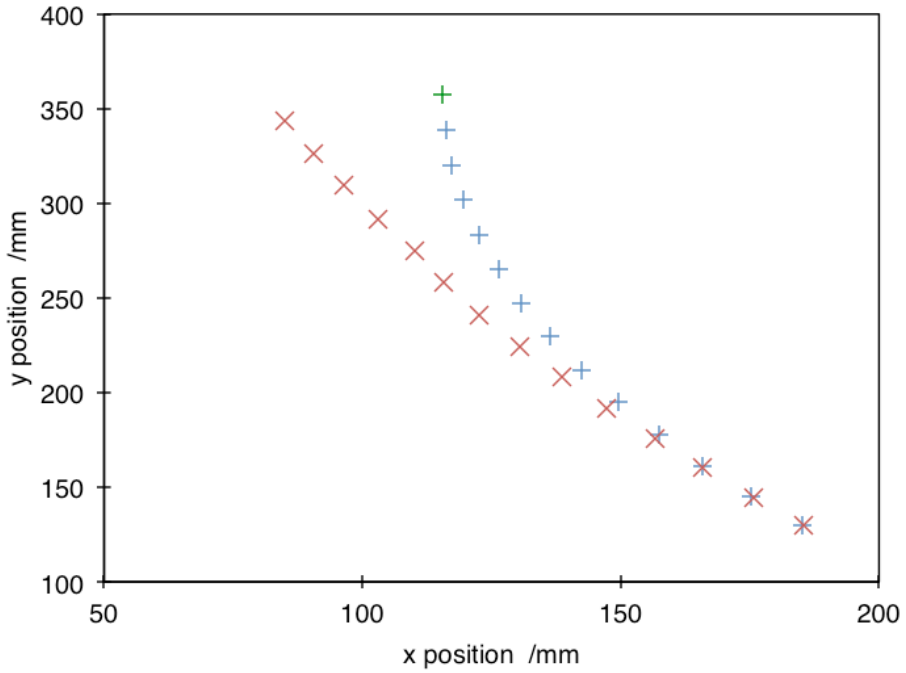

Figure 6.25: The robot was moved in runs of 20000 steps across the surface, with a measurement recorded at the end of each motion. After 12 motions it was then commanded to move in the opposite direction. The starting point is shown by the green cross, with the outward steps shown by the blue crosses, and the return motion with the red x marks. Note that the axes have different scales which exaggerates the turning of the robot.

amount could arise due to the relative difference in the position of the centre of mass for different travel directions - leading to extra pressure being placed on one motor at a time. Other chassis have demonstrated better straight line performance, and this aspect of the robot's design is still being explored.

6.5.3 'Tip-tilt' performance

As the robot moves across the surface it is seen to very slightly rock backwards and forwards as a result of slight eccentricities in the O-ring tyres and also the influence of the power pick-off springs. From section 5.4.1.3 it can be seen that only ± 5 mrad of tilt can be accepted. Although quantitive data is not available on this element of the robot's performance, observation would suggest that the robot will not meet this requirement.

New wheels have been designed that have an additional outer edge that overhangs the O-ring, thus providing a more consistent contact point with the ground. Further to this, investigations have began into developing a small tilt stage for the mirror, which

could sit atop the robot and potentially provide some correction for any misalignment; this is discussed further in the concluding chapter. A quantitive assessment of the tilt error and therefore the required motion of any tilting stage, will be determined by the tests described below.

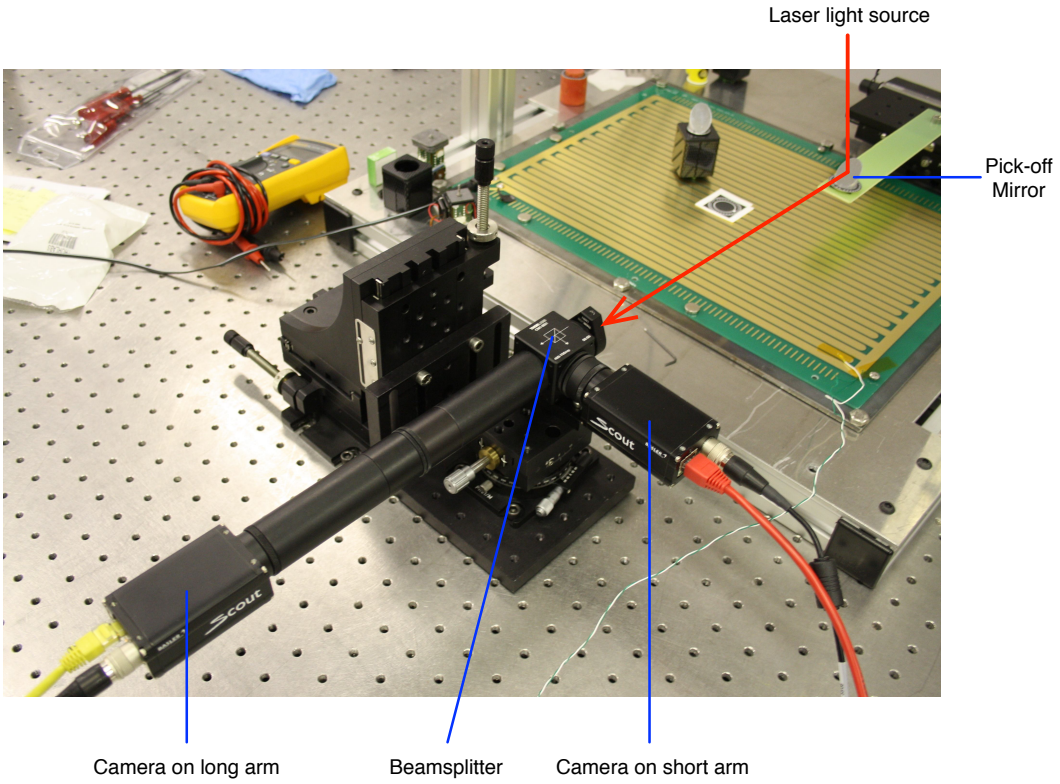

Figure 6.26: An image showing the apparatus of the laser test performed to assess the robot's alignment. Light passes from the laser, off the POM and into a beam splitter. It then passes onto two cameras which are different distances from the beam splitter; this gives information about any misalignment of the robot.

6.5.4 'Complete' system behaviour

A test has been devised which will allow both the positional alignment and also the metrology system's closed-loop behaviour to be assessed. For this, a laser is suspended above the operating area, thus simulating the light path of the telescope. As is shown in Figure 6.26, the laser is reflected off the pick-off mirror onto a beam splitter, from which the beam passes to two different cameras. The path length from each camera to the POM is different and this means that different types of misalignment of the robot can be distinguished by inspecting the relative positions of the laser spot on the CCD of the cameras. The impact of different misalignments is described in Figure 6.27.

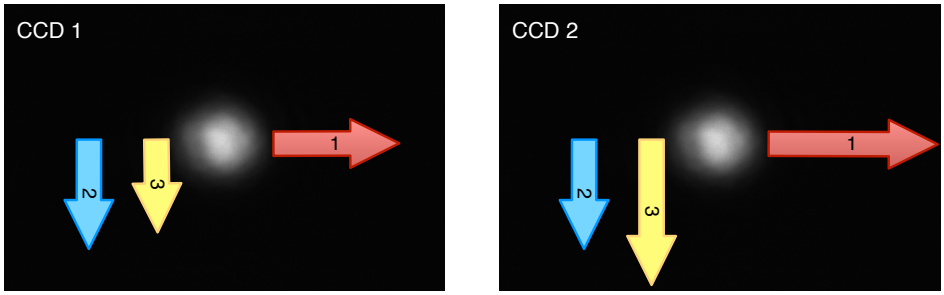

Figure 6.27: An example real image from both cameras shown in Figure 6.26. When the robot is perfectly aligned the laser spot will be in the centre of the image. If the rotational alignment of the robot is wrong, the spot will be misplaced by an unequal amount in the long dimension of the CCDs (arrow 1). If the robot is misaligned in y on the floor, the spot will be off centre by an *equal* amount in each CCD (arrow 2). Finally, a tilt in the robot, causing the mirror to lean forward or backwards, leads to an *unequal* movement of the spot (arrow 3).

The intention is to use this test setup in a number of different ways. The most basic test is to see if the robot can be driven precisely into the required position, with feedback from the two cameras. This is, in many ways, a key test of the robots - given enough time, and enough commands can they direct a light source to the required position on a CCD? If they can't, then they have not met the positional requirements laid down in chapter 5.

The next test which will be carried out is on the control loop software. The robot will first be aligned, and then its position measured and recorded. The robot will then be driven away from the laser source. The test will be to see if the command and control system can return the robot to the correct position without any feedback given by the two test cameras. This will bring in another side to the experiment: if the robot is correctly aligned in x, y and θ, is the laser aligned with the centre of the both CCDs? If not, this suggests a misalignment due to a tip or tilt of the robot.

The conclusions that can be drawn from all the work presented in this chapter can be found in Chapter 7.

Chapter 7

Conclusions

A cow is a very good animal in the field; but we turn her out of a garden.

Attributed to Samuel Johnson

7.1 Author's note

The aim of this short chapter is to review the work of this thesis objectively. Since some of the assessments and opinions are those of the author, I will at times write in the first person and enjoy the liberty that this affords.

7.2 Tomorrow's technology?

A great deal of progress has been made with MAPS in the last four years. An idea which was nothing more than a concept, has been developed into a working prototype that displays many aspects of the functionality required for EAGLE. It is timely to now assess the system's performance and how well it meets the requirements that were laid down in Chapter 5. Table 7.1 provides a summary of the main requirements, with an indication of how well they have been addressed.

The decision to use conventional motors has dictated many elements of the robot's design and performance, in particular the key aspect of positional accuracy. The Smoovy motors that were selected have been extremely reliable and provide very good performance when used as stepper motors. Their only major drawback has been that they are not very robust and cannot take large side-loads. Informed, in part, by the experience with these motors, one of the designs for the fibre-positioning system for the VLT-MOONS study (Cirasuolo et al. 2011) utilises a similar motor also manufactured by Faulhaber.

The robots have shown that they are capable of sufficiently precise positioning

Table 7.1: The final column indicates how well the MAPS requirements have been met. No stars: the requirement has not been met; one star: met but with caveats; two stars: fully met; three stars: exceeding expectations. TBD applies to properties that have not yet been well quantified.

#	Description	Requirement	Status
1.1	x-y position	$\leq$35 μm	$\star$
1.2	z rotation	$\leq$1 mrad	$\star$
1.3	Speed	$\geq$ 10 mm/s	
1.4	Turning circle	x-y deviation $\leq$ 35 μm	TBD
1.6	Footprint	$\leq$ 30 x 30 mm	$\star\star\star$
1.7	Height (excluding POM)	$\leq$ 60 mm	$\star\star$
1.8	Power duration	Continuous	$\star$
1.9	Load mass	$\leq$ 18 grams	$\star\star\star$
3.1	GUI interface	Basic operation must not require any instruction	$\star\star$
3.2	Command transmission range	$\geq$ 2 m	$\star\star\star$
3.3	Accuracy of metrology reading	$\pm$7 μm	$\star$
3.4	Collision warnings	$<$ 18 mm separation	TBD
4.1	Focal plate size	$\geq$ 0.4 x 0.3 m	$\star$
4.2	Focal plate smoothness	r.m.s smoothness $<$75 μm	

($<$35 μm) in simple testing. To date, this has only been demonstrated in conditions where the robot needs to move in straight lines; before firm conclusions can be drawn, positional tests involving turning and aligning will be required as described in the laser tests discussed in chapter 6. This will form part of the on-going MAPS research.

A more demanding outside goal of the project has been to achieve a positional accuracy of $<$10 μm. While the $<$35 μm requirement has been met in many of the tests, the more demanding goal has only been achieved in some. There are areas in which improvements could be made (e.g. the manufacturing of the wheels and the pinions could be more precise) but I would argue that to improve the robots' performance to this next level would require the use of a different propulsion system. It is interesting that many of the other, non-astronomy, micro-robot systems employ piezoelectric actuation of some kind. So far, the MAPS study has attempted the design of the whole system; including propulsion, powering and metrology. A future project might be to focus solely on developing a finer, more precise drive system that is suitable for MAPS, but draws on other pre-existing research.

The power floor has been a very interesting part of the MAPS project. It consumed more time than had originally been envisaged, but it does present an elegant solution to the problem of powering lots of randomly-distributed objects without the use of wires. This system would work particularly well with static objects - it was the motion of the robots that created many of the initial problems. There are outstanding

issues surrounding the performance of the system, but it is believed that these could potentially be solved with a smoother floor and the addition of extra weight to the chassis.

As the project has developed the importance of the command and control subsystem has become more apparent. It has to integrate many different aspects of the system: the metrology, the communication to the robots and the GUI. This complexity made the controlling software considerably more involved than I had personally anticipated. The software has been written using the object-orientated flexibility of Python, which will provide a good foundation from which to add on the next layers of complexity. For instance, there is currently no treatment of path analysis or proximity sensing and these are key parts of the complete system.

The metrology algorithms used to determine the position of all the robots show great promise at achieving the required measurement accuracy. However, they have not been fully combined with the required 'real-world' scaling. This is the next stage for the metrology-side of the project. Nevertheless, the potential to measure motions of one micron over a relatively large area is an exciting achievement, and it will be interesting to see if some of the techniques used could be employed in other applications requiring metrology, such as the fibre-positioner systems being developed for MOONS.

In addition to the requirements laid out in Chapter 5, it has also been possible to identify two other requirements that should be considered as part of the MAPS design. Section 5.4.3.2 considered the environment in which MAPS must operate, but did not consider the impact of MAPS itself on that environment. The motors used have been found to heat up slightly during operation. Although this is not likely to be a major concern, an additional requirement should be placed on how much heat can be dissipated by the robots in any given time period. Likewise, any final assessment of the suitability of MAPS must also consider the Allocation Efficiency of the complete system (as discussed in section 5.2.2), i.e. given the same number of desired scientific targets as POMs, on average, what percentage of the targets can be observed?

7.2.1 MAPS and the ELT

Since beginning this investigation, the E-ELT has undergone a major design review. The telescope was originally meant to provide two gravity invariant Nasmyth focal stations, one of which would have housed EAGLE, thus providing the flat focal surface on which MAPS could operate. However, as part of the reduction in costs, these focal stations have now been removed from the E-ELT design and consequently the focal plane of EAGLE must be vertical. For MAPS this is a very serious problem as the robots will now have to effectively run up walls to get into position.

Ideas have been considered to solve this fairly major problem, such as the addition of magnets or the use of some of the novel 'Gecko' technologies for wall climbing. However, the current robot is simply not suited for this - it was deliberately designed to fit under a POM, so it is tall and thin, with a centre-of-gravity which is some way above the surface. MAPS would have to be radically redesigned to find use in an updated vertical EAGLE.

If the modifications to the E-ELT are briefly neglected, it is interesting to consider whether MAPS would have provided a credible solution for EAGLE; it is my opinion that it may not have done. MAPS addresses a problem of how to get mirrors into place. It does this through a system that, while very elegant, is not without some technical risks. For such a small number of POMs (only 25) the speed difference between MAPS and a pick-and-place machine is not significant and with the additional back-focal distance currently required for the metrology cameras, it cannot be claimed that MAPS has a considerably smaller footprint. It is therefore not immediately clear if the benefits of MAPS, in its current form, would have justified the uncertainties and perceived risks. That is not to say that a revised "mark-two" MAPS might not mitigate some of these current technical issues.

These observations should not detract from the work of MAPS. Considerable promise has been shown in this investigation and the technical readiness level of the autonomous POMs concept has certainly been raised. I think MAPS could provide potential solutions for a subsequent generation of instruments, when the multiplexing is that much larger and its benefits would really come to the fore. Technology development must start somewhere.

7.2.2 Further ideas

One concept that has grown out of MAPS is that of 'SmartPOMs'. These would be small, actuated mirrors that could be positioned on a surface using a pick-and-place machine. The SmartPOMs could be capable of small motions such as tip-tilt or rotation, or even small linear movements. As static devices, they could exploit the power floor and the wireless control from MAPS.

One of the advantages of this system could be the compensation for non-telecentricity of light entering EAGLE. This is currently achieved through the tip-tilt of the BSM accompanied by a translation in the z direction. A tip-tilt stage on the SmartPOM could instead correct for this with just one motion. Another use of SmartPOMs links back to the work carried out on differential atmospheric refraction effects in the VFTS survey (section 2.6). This problem would also have to be corrected for in EAGLE by small adjustments of the POM positions. This could be done very

efficiently using small linear motions on a SmartPOM. Some funding has been secured to investigate early ideas for these devices, and they can certainly draw on the expertise developed for MAPS.

The future of EAGLE itself might actually change slightly. It is probable that ESO will initially only require one MOS facility on the E-ELT and therefore research has recently begun to explore combining the capabilities of the OPTIMOS-EVE and EAGLE designs into one instrument (Evans et al. 2012). Both optical and IR channels could perhaps share the same focal plane; with fibres used to feed light into the OPTIMOS-EVE part of the instrument and POMs for the IR channels. For stellar work, this would have the interesting potential that the more sparsely populated outer regions of a target galaxy could be observed with the fibres of EVE, while the AO corrected IFU channels could probe denser areas towards the core. In this context it might be interesting to even investigate fibre-carrying robots.

7.3 Massive stars

There are, in my opinion, two reasons that the study of massive stars is fascinating. Firstly, it has wide and far-reaching consequences, which make a full understanding of these objects relevant in many others areas of astronomy. Secondly, it has the great habit of unearthing bizarre and intriguing objects that often defy explanation. Through some of its early discoveries, the VFTS has already provided a number of the latter cases. In time, as the full extent of the data set is used and interpreted, the survey will move on to address, in its small way, some of those other broader questions.

VFTS has made good use of the multi-fibre FLAMES instrument, and it has highlighted some of the limitations of such instruments. The problem of scattering within the instrument was exaggerated by the wide spread in magnitudes of the stars in the survey. With hindsight, perhaps some attempt should have been made to group the observation fields by magnitude, but the density of targets would not have made this possible in all cases.

The scattering investigation, which began as a result of the effects seen in the data, has given some early indication that a better model of the fibre profile might be able to accurately describe the background contribution across the detector. However, this work, while encouraging, is extremely preliminary and it is yet to be seen whether it can be used to explain scattering for the full range of possible modes and settings in FLAMES. The final aim of the investigation remains to try and retrieve the data of the stars rejected from VFTS due to cross-contamination. The early results suggest an attempt could be made to do this, but it is unlikely the data could be completely trusted and therefore it would be very premature to consider folding this scattering

description into the FLAMES reduction software.

The system of R139 encapsulates well the concept of a focussed result in one area but with broader impact. While its evolutionary conundrum is in itself intriguing, it is probably more in its use as a calibration point for evolutionary models that the system will be most valued. It is interesting to consider that while this system is not the most massive binary found, the few that eclipse it all contain W-R stars, whose mass cannot be obtained through spectroscopic methods. R139 is the highest mass system where this can be done for both components.

Observations of an eclipse would allow determination of the system's inclination and therefore exact masses could be obtained, which would make it an even better calibration point. Attempts will therefore again be made to try and detect any trace of an eclipse associated with periastron passage, after the weather-hindered observations last time. Linked with this, spectroscopic observations around periastron would help to further constrain the orbital period, and potentially better estimate the timings of any eclipses. Such observations would also provide even more precise estimates of K_1 and K_2, and with that, the mass ratio.

The search for short-period binaries around the three ringed stars Sher25, HD168625 and SBW1 found none. This has allowed rejection of the possible scenario proposed by Hendry et al. (2008). However, it unfortunately does not further constrain the mechanism behind the generation of the rings. Further observations over a different timeframe would be needed to rule out the presence of any larger, longer period binary companions.

The observations of pulsations in Sher25 is perhaps not surprising as many B-type supergiants are expected to undergo such oscillations. However, the detection and characterisation of such activity is relatively new. Further analysis of its pulsations, with higher S/N observations, could reveal more details about dynamics of its stellar atmosphere.

Some of the broader science results from the VFTS are beginning to emerge. The O star multiplicity paper has been accepted for publication (Sana et al. 2012a), and this now allows 'single stars' to be identified for use in evolutionary models and the dynamical cluster work. Intriguing early results hinting at isolated star-formation have been presented, while a recently submitted paper by Dufton reports an apparently bimodal distribution for the rotational velocities of B-stars. In time, further analysis of the data, combined with additional information provided by the on-going *HST* proper motion survey, will help to either confirm or deny these unexpected results.

The early evidence suggests that the VFTS is going to present as many questions as it answers and will no doubt provide many challenges for the surveys of tomorrow, whatever instruments they may be using.

Bibliography

Akiyama, M., Smedley, S., Gillingham, P., et al. 2008, in Society of Photo-Optical Instrumentation Engineers (SPIE) Conference Series, Vol. 7018

Appenzeller, I., Fricke, K., Fürtig, W., et al. 1998, The Messenger, 94, 1

Asplund, M., Grevesse, N., & Sauval, A. J. 2005, in Astronomical Society of the Pacific Conf. Series, Vol. 336, Cosmic Abundances as Records of Stellar Evolution and Nucleosynthesis, ed. T.˜G.˜Barnes III & F.˜N.˜Bash, 25

Bagnasco, G., Kolm, M., Ferruit, P., et al. 2007, in Society of Photo-Optical Instrumentation Engineers (SPIE) Conference Series, Vol. 6692

Balona, L. A. 1986, MNRAS, 219, 111

Bastian, N., Covey, K. R., & Meyer, M. R. 2010, ARA&A, 48, 339

Bestenlehner, J. M., Vink, J. S., Gräfener, G., et al. 2011, A&A, 530, L14

Bonnell, I. A., Bate, M. R., & Zinnecker, H. 1998, MNRAS, 298, 93

Bosch, G., Terlevich, E., & Terlevich, R. 2009, AJ, 137, 3437

Brandner, W., Grebel, E. K., Chu, Y.-H., & Weis, K. 1997, ApJ, 475, L45

Bressert, E., Bastian, N., Evans, C. J., et al. 2012, A&A, 542, A49

Breysacher, J. 1981, A&AS, 43

Breysacher, J., Azzopardi, M., & Testor, G. 1999, A&AS, 137, 117

Briquet, M. & Aerts, C. 2003, A&A, 398, 687

Brott, I., de Mink, S. E., Cantiello, M., et al. 2011, A&A, 530, A115

Budynas, R. G. & Nisbett, K. J. 1980, Mechanical Engineering Design (McGraw-Hill)

Burrows, C. J., Krist, J., Hester, J. J., et al. 1995, ApJ, 452, 680

Campbell, B., Hunter, D. A., Holtzman, J. A., et al. 1992, AJ, 104, 1721

Campbell, M. A., Evans, C. J., Mackey, A. D., et al. 2010, MNRAS, 405, 421

Cannon, A. J. & Pickering, E. C. 1918, Annals of Harvard College Observatory, 91, 1

Caprari, G. 2000, Intelligent Robots and Systems, 1, 793

Castor, J. I., Abbott, D. C., & Klein, R. I. 1975, ApJ, 195, 157

Chita, S. M., Langer, N., van Marle, A. J., García-Segura, G., & Heger, A. 2008, Astronomy and Astrophysics, 488, L37

Cirasuolo, M., Afonso, J., Bender, R., et al. 2011, The Messenger, 145, 11

Cochrane, W. A., Luo, X., Lim, T., Taylor, W. D., & Schnetler, H. 2012, International Journal of Optomechatronics, 6, 199

Cohen, M. & Jagourel, P. 2009, E-TRE-GEP-567-0031 TRAMS Analysis & Design Report

Crowther, P. A. 2007, ARA&A, 45, 177

Crowther, P. A., Schnurr, O., Hirschi, R., et al. 2010, MNRAS, 1103

Crowther, P. A. & Walborn, N. R. 2011, MNRAS, 416, 1311

Cuby, J.-G., Morris, S., Fusco, T., et al. 2010, in Society of Photo-Optical Instrumentation Engineers (SPIE) Conference Series, Vol. 7735

Cui, X. 2009, in Bulletin of the American Astronomical Society, Vol. 41, American Astronomical Society Meeting Abstracts 213, 226.01

Davies, B., Kudritzki, R.-P., & Figer, D. F. 2010a, MNRAS, 407, 1203

Davies, B., Lumsden, S. L., Hoare, M. G., Oudmaijer, R. D., & de Wit, W.-J. 2010b, MNRAS, 402, 1504

de Koter, A. 1993, Studies of the variability of Luminous Blue Variable stars., University of Utrecht (Netherlands)

de Mink, S. E., Langer, N., & Izzard, R. G. 2011, Bulletin de la Societe Royale des Sciences de Liege, 80, 543

Dekker, H., Delabre, B., & Dodorico, S. 1986, in Society of Photo-Optical Instrumentation Engineers (SPIE) Conference Series, ed. D. L. Crawford, Vol. 627, 339–348

Duchêne, G., Simon, T., Eislöffel, J., & Bouvier, J. 2001, A&A, 379, 147

Dufton, P. L., Dunstall, P. R., Evans, C. J., et al. 2011, ApJ, 743, L22

Dunstall, P., Sana, H., Dufton, P., et al. 2012, in press

Duquennoy, A. & Mayor, M. 1991, A&A, 248, 485

Eikenberry, S., Andersen, D., Guzman, R., et al. 2006, in Society of Photo-Optical Instrumentation Engineers (SPIE) Conference Series, Vol. 6269

Eikenberry, S., Bandyopadhyay, R., Bennett, J. G., et al. 2012, in Society of Photo-Optical Instrumentation Engineers (SPIE) Conference Series, Vol. 8446

Elmegreen, B. G. & Elmegreen, D. M. 2005, ApJ, 627, 632

Estaña, R. & Wörn, H. 2003, in Society of Photo-Optical Instrumentation Engineers (SPIE) Conference Series, ed. W. Osten, Vol. 5144, 431–442

Estaña, R. & Wörn, H. 2007, Autonome Mobile Systeme, 8, 334

Evans, C. & Cuby, J. 2009, E-TRE-ATC-567-0010: Operational Concept Document

Evans, C. J., Barbuy, B., Bonifacio, P., et al. 2012, ArXiv e-prints

Evans, C. J., Davies, B., Kudritzki, R.-P., et al. 2011a, A&A, 527, A50

Evans, C. J., Lennon, D. J., Smartt, S. J., & Trundle, C. 2006, A&A, 456, 623

Evans, C. J., Smartt, S. J., Lee, J.-K., et al. 2005, Astronomy and Astrophysics, 437, 467

Evans, C. J., Taylor, W. D., Hénault-Brunet, V., et al. 2011b, A&A, 530, A108

Fatikow, S., Edeler, C., Diederichs, C., Meyer, I., & Jasper, D. 2011, 13th World Congress in Mechanism and Machine Science, A12, 322

Feast, M. W., Thackeray, A. D., & Wesselink, A. J. 1960, MNRAS, 121, 337

Feitzinger, J. V. & Isserstedt, J. 1983, A&AS, 51, 505

Filippenko, A. V. 1982, PASP, 94, 715

Fitzpatrick, E. L. 1999, PASP, 111, 63

Fowler, M. 2008, UML distilled: a brief guide to the standard object modelling library (Addison-Wesley)

Gao, J. 2005, IECON, EM-3, 64

Gere, J. M. & Timoshenko, S. P. 1991, Mechanics of Materials (Stanley Thomas)

Gieles, M., Sana, H., & Portegies Zwart, S. F. 2010, MNRAS, 402, 1750

Gies, D. R. 1987, ApJS, 64, 545

Gillingham, P. R., Miziarski, S., & Klauser, U. 2000, in Society of Photo-Optical Instrumentation Engineers (SPIE) Conference Series, ed. M. Iye & A. F. Moorwood, Vol. 4008, 914–921

Goodwin, M., Heijmans, J., Saunders, I., et al. 2010, in Society of Photo-Optical Instrumentation Engineers (SPIE) Conference Series, Vol. 7739

Gosset, E., Royer, P., Rauw, G., Manfroid, J., & Vreux, J.-M. 2001, MNRAS, 327

Grebel, E. K. & Chu, Y.-H. 2000, AJ, 119, 787

Greggio, L., Falomo, R., Zaggia, S., Fantinel, D., & Uslenghi, M. 2012, ArXiv e-prints

Groh, J. H., Damineli, A., & Hillier, D. J. 2008, in Revista Mexicana de Astronomia y Astrofisica, vol. 27, Vol. 33, Revista Mexicana de Astronomia y Astrofisica Conference Series, 132–134

Guerrero, M. A. & Chu, Y.-H. 2008, ApJS, 177, 216

Gyllenberg, W., Ohlsson, J. B., & Ambolt, N. P. 1926, Katalog von 11.800 Sternen der Zone +35 deg. bis 40 deg. AG Lund (Lund: Scientia)

Halíř, R. & Flusser, J. 1998, Numerically Stable Direct Least Squares Fitting Of Ellipses

Handel, H. 2007, Analyzing the Influences of Camera Warm-Up Effects on Image Acquisition, Vol. 4844 (Springer Berlin / Heidelberg), 258–268

Hastings, P., Ramsay Howat, S., Spanoudakis, P., et al. 2006, in Society of Photo-Optical Instrumentation Engineers (SPIE) Conference Series, Vol. 6273

Hénault-Brunet, V., Evans, C. J., Sana, H., et al. 2012a, ArXiv e-prints, 1208.0825

Hénault-Brunet, V., Gieles, M., Evans, C. J., et al. 2012b, ArXiv e-prints, 1207.7071

Hendry, M. A., Smartt, S. J., Skillman, E. D., et al. 2008, MNRAS, 388, 1127

Herrero, A., Puls, J., & Villamariz, M. R. 2000, A&A, 354, 193

Hill, J. M., Angel, J. R. P., Scott, J. S., Lindley, D., & Hintzen, P. 1980, ApJ, 242, L69

Hill, J. M. & Lesser, M. P. 1986, in Society of Photo-Optical Instrumentation Engineers (SPIE) Conference Series, ed. D. L. Crawford, Vol. 627, 303–320

Hillier, D. J. & Miller, D. L. 1998, ApJ, 496, 407

Hook, I. 2009, in Science with the VLT in the ELT Era, ed. A. Moorwood, 225

Hubbard, E. N., Angel, J. R. P., & Gresham, M. S. 1979, ApJ, 229, 1074

Humphreys, R. M. & Davidson, K. 1979, ApJ, 232, 409

Hunter, I., Brott, I., Lennon, D. J., et al. 2008a, ApJ, 676, L29

Hunter, I., Lennon, D. J., Dufton, P. L., et al. 2008b, A&A, 479, 541

Karachentsev, I. D., Karachentseva, V. E., Huchtmeier, W. K., & Makarov, D. I. 2004, AJ, 127, 2031

Kotak, R. & Vink, J. S. 2006, A&A, 460, L5

Krabbe, A., Thatte, N. A., Kroker, H., Tacconi-Garman, L. E., & Tecza, M. 1997, in Society of Photo-Optical Instrumentation Engineers (SPIE) Conference Series, ed. A. L. Ardeberg, Vol. 2871, 1179–1186

Lada, C. J. 2006, ApJ, 640, L63

Lamers, H. J. G. L. M. 1995, in Astronomical Society of the Pacific Conference Series, Vol. 83, IAU Colloq. 155: Astrophysical Applications of Stellar Pulsation, ed. R. S. Stobie & P. A. Whitelock, 176

Le Fèvre, O., Saisse, M., Mancini, D., et al. 2003, in Society of Photo-Optical Instrumentation Engineers (SPIE) Conference Series, ed. M. Iye & A. F. M. Moorwood, Vol. 4841, 1670–1681

Lehnert, M. & Evans, C. 2009, E-TRE-GEP-567-0003 EAGLE Science Case

Leitherer, C., Allen, R., Altner, B., et al. 1994, ApJ, 428, 292

Leitherer, C., Schaerer, D., Goldader, J. D., et al. 1999, ApJS, 123, 3

Linder, N., Rauw, G., Sana, H., De Becker, M., & Gosset, E. 2007, A&A, 474, 193

Lucy, L. B. 1976, ApJ, 206, 499

Maeder, A. 1987, A&A, 178, 159

Markova, N., Puls, J., Scuderi, S., & Markov, H. 2005, A&A, 440, 1133

Martayan, C., Frémat, Y., Hubert, A.-M., et al. 2007, A&A, 462, 683

Martel, S. M., Saraswat, A., & Hunter, I. W. 2000, in Society of Photo-Optical Instrumentation Engineers (SPIE) Conference Series, ed. B. J. Nelson & J.-M. Breguet, Vol. 4194, 82–93

Martins, F., Schaerer, D., & Hillier, D. J. 2005, A&A, 436, 1049

Mason, B. D., Hartkopf, W. I., Gies, D. R., Henry, T. J., & Helsel, J. W. 2009, AJ, 137, 3358

Massey, P., Zangari, A. M., Morrell, N. I., et al. 2009, ApJ, 692, 618

McGrath, A. & Moore, A. 2004, in Society of Photo-Optical Instrumentation Engineers (SPIE) Conference Series, ed. J. Antebi & D. Lemke, Vol. 5495, 600–610

McGregor, H. & Schnetler, H. 2009, E-TRE-ATC-567-0030: EAGLE POS Analysis and Design Document

McKee, C. F. & Ostriker, E. C. 2007, ARA&A, 45, 565

McLean, I. S., Steidel, C. C., Epps, H., et al. 2010, in Society of Photo-Optical Instrumentation Engineers (SPIE) Conference Series, Vol. 7735

McLurkin, J. 1995, The Ants: A Community of Microrobots

Meynet, G. & Maeder, A. 2000, A&A, 361, 101

Meynet, G., Maeder, A., Schaller, G., Schaerer, D., & Charbonnel, C. 1994, A&AS, 103, 97

Moffat, A. F. J. 1989, ApJ, 347, 373

Mokiem, M. R., de Koter, A., Vink, J. S., et al. 2007, A&A, 473, 603

Morgan, W. W., Keenan, P. C., & Kellman, E. 1943, An atlas of stellar spectra, with an outline of spectral classification (Chicago, Ill., The University of Chicago press)

Morris, S. L., Cuby, J.-G., Dubbeldam, M., et al. 2012, ArXiv e-prints

Morris, T. & Podsiadlowski, P. 2007, Science, 315, 1103

Nakano, S., Itagaki, K., Puckett, T., & Gorelli, R. 2006, Central Bureau Electronic Telegrams, 666, 1

Navarro, R., Chemla, F., Bonifacio, P., et al. 2010, in Society of Photo-Optical Instrumentation Engineers (SPIE) Conference Series, Vol. 7735

Nazé, Y., Rauw, G., & Hutsemékers, D. 2012, A&A, 538, A47

Niwa, Y., Yano, T., Araki, H., et al. 2010, in Society of Photo-Optical Instrumentation Engineers (SPIE) Conference Series, Vol. 7731

Nota, A., Livio, M., Clampin, M., & Schulte-Ladbeck, R. 1995, ApJ, 448, 788

Parker, J. W. 1993, AJ, 106, 560

Parry, I. R. & Gray, P. M. 1986, in Society of Photo-Optical Instrumentation Engineers (SPIE) Conference Series, ed. D. L. Crawford, Vol. 627, 118–124

Pasquini, L., Avila, G., Blecha, A., et al. 2002, The Messenger, 110, 1

Pastorello, A., Smartt, S. J., Mattila, S., et al. 2007, Nature, 447, 829

Pfalzner, S. & Olczak, C. 2007, A&A, 475, 875

Pooley, S. & Thompson, P. 2010, MAPS Dreampact User Guide

Portegies Zwart, S. F., Pooley, D., & Lewin, W. H. G. 2002, ApJ, 574, 762

Preibisch, T., Weigelt, G., & Zinnecker, H. 2001, in IAU Symposium, Vol. 200, The Formation of Binary Stars, ed. H. Zinnecker & R. Mathieu, 69

Pressman, R. S. 2005, Software Engineering: a practitioner's approach (McGraw-Hill)

Ramsay, S. K. 2012, in Society of Photo-Optical Instrumentation Engineers (SPIE) Conference Series

Ramsay Howat, S. K., Todd, S., Leggett, S., et al. 2004, in Society of Photo-Optical Instrumentation Engineers (SPIE) Conference Series, ed. A. F. M. Moorwood & M. Iye, Vol. 5492, 1160–1171

Rauw, G., De Becker, M., Nazé, Y., et al. 2004, A&A, 420, L9

Rauw, G., Vreux, J.-M., & Bohannan, B. 1999, ApJ, 517, 416

Ritchie, B. W., Clark, J. S., Negueruela, I., & Crowther, P. A. 2009, A&A, 507, 1585

Rousset, G., Fusco, T., Assemat, F., et al. 2010, in Society of Photo-Optical Instrumentation Engineers (SPIE) Conference Series, Vol. 7736

Salpeter, E. E. 1955, ApJ, 121, 161

Sana, H., de Koter, A., de Mink, S. E., et al. 2012a, in press

Sana, H., de Mink, S. E., de Koter, A., et al. 2012b, Science, 337, 444

Sana, H. & Evans, C. J. 2011, ArXiv e-prints

Sana, H., Gosset, E., & Evans, C. J. 2009, MNRAS, 400, 1479

Sana, H., Gosset, E., & Rauw, G. 2006a, MNRAS, 371, 67

Sana, H., Rauw, G., Nazé, Y., Gosset, E., & Vreux, J.-M. 2006b, MNRAS, 372, 661

Saunders, W., Colless, M., Saunders, I., et al. 2010, in Society of Photo-Optical Instrumentation Engineers (SPIE) Conference Series, Vol. 7735

Schlager, K. J. 1956, Engineering Management, IRE Transactions, EM-3, 64

Schnurr, O., Casoli, J., Chené, A.-N., Moffat, A. F. J., & St-Louis, N. 2008, MNRAS, 389, L38

Schnurr, O., Moffat, A. F. J., St-Louis, N., Morrell, N. I., & Guerrero, M. A. 2008, MNRAS, 389, 806

Selman, F., Melnick, J., Bosch, G., & Terlevich, R. 1999, A&A, 347, 532

Sharples, R., Bender, R., Bennett, R., et al. 2006, New Astronomy Review, 50, 370

Sher, D. 1965, MNRAS, 129, 237

Shortis, M. R., Clarke, T. A., & Short, T. 1994, in Society of Photo-Optical Instrumentation Engineers (SPIE) Conference Series, ed. S. F. El-Hakim, Vol. 2350, 239–250

Simón-Díaz, S., Herrero, A., Uytterhoeven, K., et al. 2010, ApJ, 720, L174

Skrutskie, M. F., Cutri, R. M., Stiening, R., et al. 2006, AJ, 131, 1163

Smith, N. 2007, AJ, 133, 1034

Smith, N. 2009, ArXiv e-prints, 0906.2204

Smith, N. 2010, in Astronomical Society of the Pacific Conference Series, Vol. 425, Hot and Cool: Bridging Gaps in Massive Star Evolution, ed. C. Leitherer, P. D. Bennett, P. W. Morris, & J. T. Van Loon, 63

Smith, N., Bally, J., & Walawender, J. 2007, AJ, 134, 846

Smith, N. & Townsend, R. H. D. 2007, ApJ, 666, 967

Sota, A., Maíz Apellániz, J., Walborn, N. R., et al. 2011, ApJS, 193, 24

Stahl, O., Wolf, B., Klare, G., Juettner, A., & Cassatella, A. 1990, A&A, 228, 379

Stevens, R., Brook, P., Jackson, K., & Arnold, S. 1998, Systems Engineering: coping with complexity (Pearson), 5

Stroud, V. E., Clark, J. S., Negueruela, I., et al. 2010, A&A, 511, A84

Sugerman, B. E. K., Crotts, A. P. S., Kunkel, W. E., Heathcote, S. R., & Lawrence, S. S. 2005, Astrophysical Journal, Supplement, 159, 60

Taylor, W. D., Atkinson, D. C., Cochrane, W. A., et al. 2010a, in Society of Photo-Optical Instrumentation Engineers (SPIE) Conference Series, Vol. 7739

Taylor, W. D., Evans, C. J., Sana, H., et al. 2011, A&A, 530, L10

Taylor, W. D., Evans, C. J., & Schnetler, H. 2008, in Society of Photo-Optical Instrumentation Engineers (SPIE) Conference Series, Vol. 7017

Taylor, W. D., Schnetler, H., & Cochrane, W. A. 2010b, CFI-ATC-MAPS-01 Requirement Specification

Taylor, W. D., Schnetler, H., & Cochrane, W. A. 2010c, CFI-ATC-MAPS-04 Final Anlysis and Design Report

Taylor, W. D., Schnetler, H., Cochrane, W. A., Black, M., & McLay, S. A. 2012, in press

Townsley, L. K., Broos, P. S., Feigelson, E. D., Garmire, G. P., & Getman, K. V. 2006, AJ, 131, 2164

Tramper, F., Sana, H., de Koter, A., & Kaper, L. 2011, ApJ, 741, L8

Trundle, C., Kotak, R., Vink, J. S., & Meikle, W. P. S. 2008, Astronomy and Astrophysics, 483, L47

Uomoto, A., Smee, S., Rockosi, C., et al. 1999, in Bulletin of the American Astronomical Society, Vol. 31, American Astronomical Society Meeting Abstracts, 1501

Valdastria, P., Corradia, P., Menciassia, A., et al. 2006, Robotics and Autonomous Systems, 54, 789

Vink, J. S. 2009, ArXiv e-prints, 0905.3338

Vink, J. S., de Koter, A., & Lamers, H. J. G. L. M. 2001, A&A, 369, 574

Walborn, N. R. 1982, ApJ, 256, 452

Walborn, N. R. & Blades, J. C. 1997, The Astrophysical Journal Supplement Series, 112, 457

Walborn, N. R., Prevot, M. L., Prevot, L., et al. 1989, A&A, 219, 229

Walborn, N. R., Sota, A., Maíz Apellániz, J., et al. 2010, ApJ, 711, L143

Weidner, C., Kroupa, P., & Bonnell, I. A. D. 2010, MNRAS, 401, 275

Wolfe, Jr., R. H., Horak, H. G., & Storer, N. W. 1967, The machine computation of spectroscopic binary elements, ed. O. Struve & M. Hack, 251

Yonggang, G., Chao, Z., Xiaoxheng, X., & Jiaru, C. 2010, in Society of Photo-Optical Instrumentation Engineers (SPIE) Conference Series, Vol. 7014

Zinnecker, H. & Yorke, H. W. 2007, ARA&A, 45, 481

Appendix A

Analysis of NGS availability for EAGLE MOAO System

A.1 Purpose of investigation

To achieve AO correction for selected sub-fields across EAGLE's full field-of-view, five natural guide stars (NGS) are required (Rousset et al. 2010). This brief study investigated the density of NGS of varying brightness in a number of different regions of the sky, to determine the potential sky coverage of EAGLE observations.

A.2 NGS density calculations

Table A.1 lists a number of oft-studied regions (across a broad range of wavelengths) that may be of interest for future EAGLE studies. The targets were chosen due to their high galactic latitudes, meaning they are out of the plane of the galaxy. For those wishing to study faint objects, being out of the plane of the Galaxy is an advantage as it reduces foreground objects and obscuration. It is therefore likely that many deep

Table A.1: Regions mapped in recent deep extra-galactic surveys, which provide candidate areas of sky for follow-up studies of high-reshift galaxies with EAGLE.

Target field	RA	Dec	Galactic latitude
Elais S1	00:34:44.0	-43:28:01.2	+73.31
XMM-LSS	00:24:40.0	-04:30:00.0	-66.47
CDFS	03:32:28.0	-27:48:30.0	-54.44
NGS 1097	02:46:19.0	-30:16:29.0	-64.68
NGS 1365	03:33:36.3	-36:08:27.8	-54.60

E-ELT observations will point here. However, since the Galactic density of stars is dropping, it has the disadvantage that there are fewer potential NGS.

The analysis comprised a number of steps:

1. Sources were extracted from the USNO-B Catalogues[1] for a 1-degree diameter area of sky, centred on the coordinates of the target fields.
2. 100 random fields, each with an area that matches the focal plane of EAGLE, were selected randomly from across the 1-degree field.
3. A faint magnitude cut-off was imposed (e.g. $R < 17$) and a minimum number of required stars was fixed (x).
4. The percentage of the 100 fields with the number of stars x was determined.
5. This loop is repeated 10 times, each time using a different 100 fields.
6. The mean percentage of fields with x stars or more was calculated.

The focal plane of the current EAGLE design is shown in Figure A.1 relative to a 5' and 10' diameter field of view. Also shown are the footprints of the six laser guide stars (LGS), which vignette the 10' field. Early designs of EAGLE had a focal plane that exploited the smaller 5' field, but it was decided to increase this area as objects can still be observed in the regions in-between the LGS footprints. This larger focal plane has a field-of-view equivalent to a circular field with a diameter of 7'.

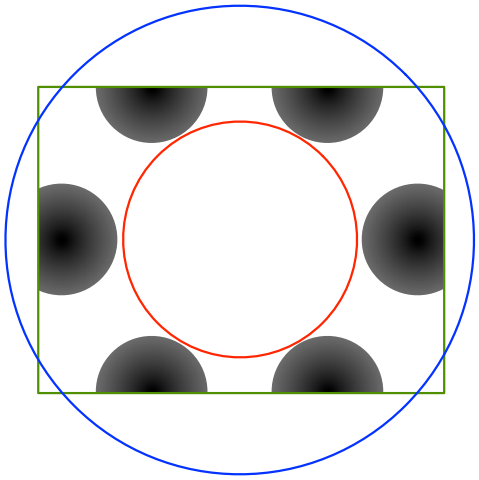

Figure A.1: EAGLE's focal plane shown by the green rectangle, in comparison with a 5' and 10' diameter field-of-view, shown in red and blue, respectively. The large black regions, mark the footprint of the LGS.

[1]The USNOFS Image and Catalogue Archive is operated by the United States Naval Observatory. It provides positions and magnitudes of billions of stars.
(http://www.nofs.navy.mil/data/fchpix/).

Initially results were calculated for all the possible EAGLE fields given in Table A.1; the mean values for each of the fields are plotted in Figure A.2. The methods used for analysis of the real target fields were then employed to consider 50 fields with randomly selected central pointings, restricted to Galactic latitudes (l) of $50 < l < 80$. The mean galactic latitude of the 50 fields was $\sim 66°$. The results were found to be in very close agreement with the data presented for the five target fields.

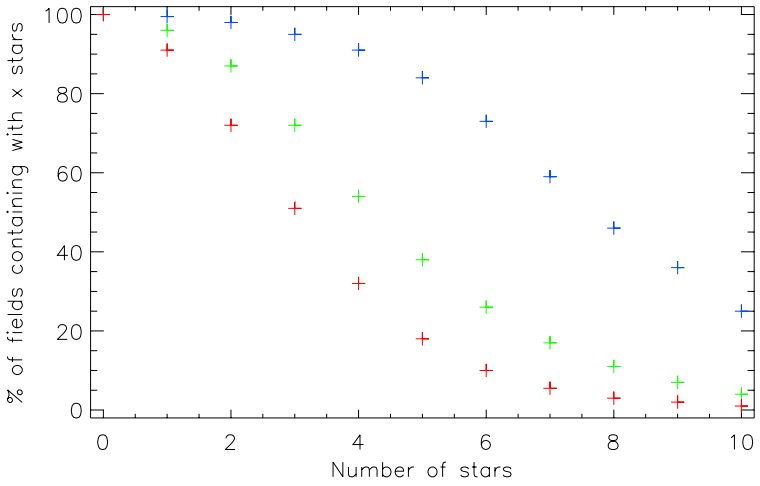

Figure A.2: NGS analysis for the regions surrounding possible EAGLE target fields. It combines two different forms of analyses: the blue and green data correspond to the 7' and 5' diameter fields respectively, and stars with a R-band limiting magnitude of $R < 17$. The red data show the results for the 7' field but with a limiting magnitude of $R < 15$.

A.3 Conclusions

This small study has shown that even at relatively high Galactic latitudes, if the full EAGLE focal plane is exploited, then there is a greater than 80% chance that five stars of magnitude $R < 17$ will be found in the field-of-view for any single pointing. It is also possible to estimate that there is a 90% chance that one of those five NGS will be a star with a magnitude of $R < 15$. This is good for the AO system as even one or two brighter NGS can significantly improve the performance. One aspect that this study did not consider is that a real pointing will never be completely 'random' as these simulated ones have been. In practise, it might be possible to slightly adjust the field centre so that it includes better NGS candidate stars.

Appendix B

Focal plane coverage of EAGLE

B.1 Background

EAGLE has been designed to be a highly modular instrument, with many aspects of the design repeated identically for each science channel. This technique saves both time and money at all stages of the project; through design, manufacture and even operation. As can been seen in Figure B.1, EAGLE will have ten identical modules surrounding the focal plane. Each will consist of a bank of three BSMs, two of which feed science channels while one feeds the NGS channels.

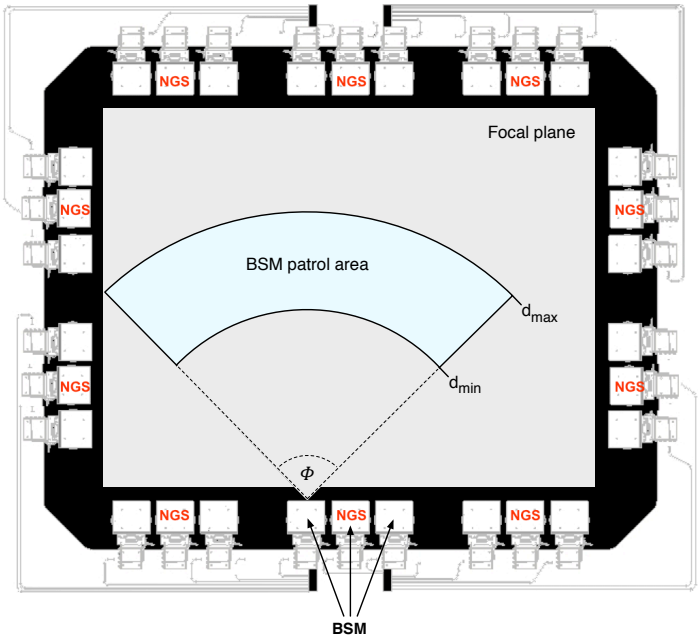

Figure B.1: BSMs mounted around the EAGLE focal plane, which is shown by the grey rectangle. The patrol area for one of the BSMs is shown in blue.

The BSM must be able to rotate so it can be aligned with its associated POM placed on the focal plane. The distance between a POM and its BSM (d) will vary depending on the position of the science object; this alters the path length of the optical system. The BSMs feed light into the Target Re-imaging and Magnification Sub-System (TRAMS), in which a trombone mechanism corrects for this varying path length. The travel range of the trombone defines the minimum and maximum value of d. For more information on the TRAMS see Cohen & Jagourel (2009).

B.2 Counting BSMs

If a limit is imposed on the angle (ϕ) through which the BSM could turn through, this, coupled with the restriction on d, defines a fixed patrol area on the focal plane from which a BSM can gather light, this is shown in B.1 for one of the BSMs.

This short investigation explored how many BSMs can observe each section of the focal plane, thus providing a check on target availability for science observations. This was similar to work carried out by Taylor et al. (2008), where the focal plane was split

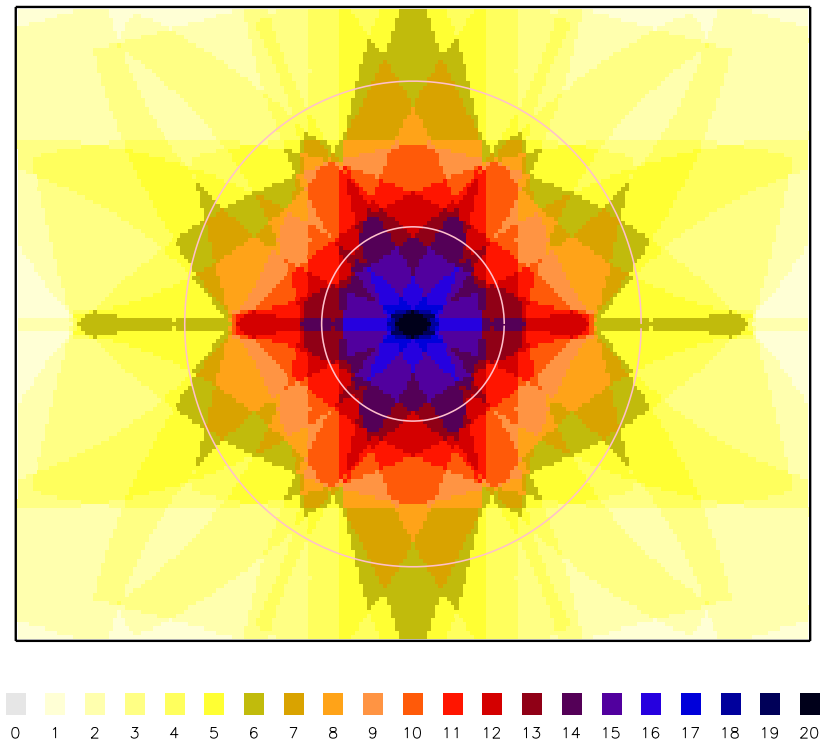

Figure B.2: Number of BSMs that can view different regions of the focal plane. The colours represent the numbers shown in the key. The two overlaid circles correspond to an on-sky observing diameter of 2 and 5 arcmins.

into discrete regions (or pixels) and for each pixel, the number of overlapping BSM viewing arcs was calculated. Figure B.2 displays a typical result for such an analysis using different colours to represent the number of BSMs covering each region.

Four different scenarios were considered for slightly different system designs, these are shown in Table B.1. If the viewing angle of the BSMs is restricted, it presents the question of which direction is the central point, i.e. are all the BSMs identical and do they look straight forward, regardless of their place in the field, or are they centred about different angles depending on their position relative to the field centre? The comparison of these results is shown in Figure B.3, which shows the varying field coverage for different numbers of BSMs.

Table B.1: The four different observing scenarios considered in the study.

Description	ϕ (deg.)	d_{min} (mm)	d_{max} (mm)	Colour
1: Identical BSMs all looking straight	90	1000	1450	Green
2: BSMs tailored to field position	90	1000	1450	Blue
3: No limiting restriction on angle	180	1000	1450	Orange
4: Increased d (hypothetical)	180	1000	1650	Red

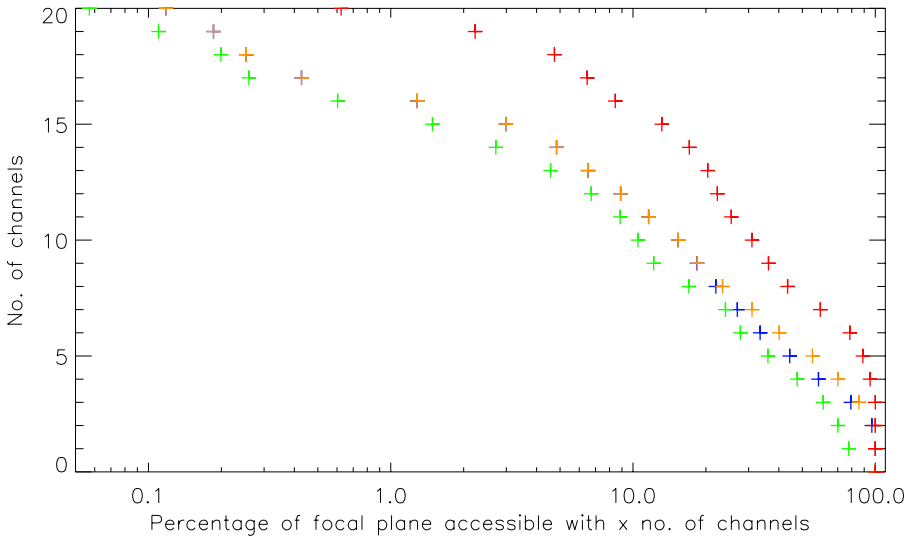

Figure B.3: Percentage of the focal plane that can be viewed with x number of channels, i.e. the entire focal is visible with at least one BSM, but only for a small region in the centre can an object be observed with any one of the twenty BSMs. The colours represent the four scenarios described in Table B.1.

B.3 Conclusions

A number of conclusions can be drawn from this work. Firstly there is clearly an advantage to tailoring the central viewing angles of the BSMs. However, this would mean that the modules containing the sets of the three BSMs would no longer be identical, which would be a drawback. To combat this, it would be simpler to remove any restriction on the viewing angle of the BSMs.

It is interesting to note that freeing the BSMs to point in any direction only improves performance marginally over scenario 2. This is because towards the central regions the greatest restriction is imposed by the limits on d. These are hard to change, as there are limits on the travel range of the trombone in the TRAM. There are also possible problems caused by the expanding beam leaving the POM. However, for interest, scenario 4 considers increasing d_{max} by 200 mm, which would mean an additional 100 mm of travel required from the trombone. It is clear that adjusting this restriction, even by a small amount, would have a significant benefit in terms of the field coverage. An analysis such as this would need to be combined with considerations of the target densities to determine whether the science benefits of such a change justify the additional complexity.

Publications

Refereed papers

Taylor, W. D., Evans, C. J., Sana, H., et al., "The VLT-FLAMES Tarantula Survey. II. R139 revealed as a massive binary system", 2011, A&A, 530, L10

Evans, C. J., Taylor, W. D., Hénault-Brunet, V., et al., "The VLT-FLAMES Tarantula Survey. I. Introduction and observational overview", 2011, A&A, 530, A108

Bestenlehner, J. M., Vink, J. S., Gräfener, G., et al., "The VLT-FLAMES Tarantula Survey. III. A very massive star in apparent isolation from the massive cluster R136", 2011, A&A, 530, L14

Bressert, E., Bastian, N., Evans, C. J., et al., "The VLT-FLAMES Tarantula Survey. IV. Candidates for isolated high-mass star formation in 30 Doradus", 2012, A&A, 542, A49

Dunstall, P. R.; Fraser, M.; Clark, J., et al., "The VLT-FLAMES Tarantula Survey. V. The peculiar B[e]-like supergiant, VFTS698, in 30 Doradus", 2012, A&A, 542, A50

Hénault-Brunet, V., Evans, C. J., Sana, H., et al., "The VLT-FLAMES Tarantula Survey. VII. A low velocity dispersion for the young massive cluster R136", 2012, ArXiv e-prints: 1208.0825

Hénault-Brunet, V., Gieles, M., Evans, C. J., et al., "The VLT-FLAMES Tarantula Survey VI: Evidence for rotation of the young massive cluster R136", 2012, ArXiv e-prints: 1207.7071

Evans, C. J.; Walborn, N. R.; Crowther, P. A., et al., "A Massive Runaway Star from 30 Doradus", 2010, ApJL, 715, L74

Cochrane, W. A. and Luo, X. and Lim, T. et. al., "Design of a Micro-Autonomous Robot for Use in Astronomical Instruments", 2012, International Journal of Optomechatronics, 6, p199

Society of Photo-Optical Instrumentation Engineers (SPIE) papers

Taylor, W. D., Atkinson, D. C., Cochrane, W. A., et al., "A prototype micro-autonomous positioning system for mirror deployment within multi-object instruments", 2010, SPIE, Vol. 7739

Taylor, W. D., Schnetler, H., McLay, S., et al., "MAPS: where have the robots got to?", 2012, SPIE, in press

Cochrane, W. A., Atkinson, D. C., Baillie, T. E. C., "Recent testing of a micro autonomous positioning system for multiobject instrumentation", 2012, SPIE, in press

Rousset, G., Fusco, T., Assemat, F., et al., "EAGLE MOAO system conceptual design and related technologies", 2010, SPIE, Vol. 7736

Cuby, J.-G., Morris, S., Fusco, T., et al. "EAGLE: a MOAO fed multi-IFU NIR workhorse for E-ELT", 2010, SPIE, Vol. 7735,

Selected conference proceedings

Taylor, W. D., Evans, C. J., Hénault-Brunet, V., et al., "The VLT-FLAMES Tarantula Survey", 2011, Société Royale des Sciences de Liège, 80, 430

Walborn, N. R., Sana, H., Taylor, W. D., et al., "Two Remarkable Spectroscopic Categories of Young O Stars from the VLT-FLAMES Tarantula Survey", 2011, Four Decades of Research on Massive Stars, arXiv e-prints: 1112.4435

Additional articles

Evans, C. J., Taylor, W. D., Sana, H., et al., "The VLT FLAMES Tarantula Survey", 2011, The Messenger, vol. 145, p. 33-38